Study of up & down conversion technique by all-optical sampling based on SOA-MZI

Hassan Termos

THÈSE / UNIVERSITÉ DE BRETAGNE OCCIDENTALE

sous le sceau de l'Université Bretagne Loire

pour obtenir le titre de

DOCTEUR DE L'UNIVERSITÉ DE BRETAGNE OCCIDENTALE

Mention : Photonics, Optoelectronics, Telecommunications

École Doctorale SICMA 0373

présentée par

Hassan TERMOS

Préparée au laboratoire Lab-STICC
UMR CNRS 6285
École Nationale d'Ingénieurs de Brest (ENIB)

Study of Up and Down Conversion Technique by All-Optical Sampling Based on a SOA-MZI

Soutenue le 27 Février 2017

devant le jury composé de :

Didier ERASME
Professeur, Télécom ParisTech, Paris / *Président*

Christelle AUPETIT-BERTHELEMOT
Professeur des Universités, ENSIL, Limoges / *Rapporteur*

Hong Wu LI
Professeur des Universités, Université de Nantes / *Rapporteur*

Ziad OSMAN
Professeur des Universités, BAU, Beirut /*Examinateur*

Ammar SHARAIHA
Professeur des Universités, Lab-STICC, ENIB / *Directeur de thèse*

Thierry RAMPONE
Maître de conférences à l'ENIB, Brest / *Encadrant*

Ali ALAEDDINE
Professeur des Universités, LU, Beirut / *Directeur de thèse*

Ali HAMIE
Professeur des Universités, LU, Beirut / *Encadrant*

This work was done within the project POETO “Étude- d'une technique de transPOsition de fréquence par Échantillonnage Tout-Optique pour applications en transmission de données radio sur fibre à haut débit” and has been supported by the Brittany Region by an ARED.

Acknowledgments

This dissertation is the result of three years of hard and persistent work that was performed at Lab-STICC (Laboratoire des Sciences et Techniques de l'Information, de la Communication et de la Connaissance) at ENIB (École Nationale d'Ingénieurs de Brest).

Working at Lab-STICC has been a wonderful experience. I thank Ammar SHARAIHA, Professor at ENIB, for introducing me to the laboratory and the unrestricted academic freedom he offered me. His scientific advice and his profound knowledge invaluably contributed to this work. His enthusiasm first inspired me to pursue research in this field. His advice and encouragement through the three years have kept me going.

I would like to take the opportunity to thank Thierry RAMPONE, Associate Professor at ENIB, for all the time he spent with me discussing my professional development. Our meetings have been very helpful and allowed me to develop high scientific and research capabilities. I am greatly indebted to him for his inspiring guidance, valuable advices, and endless support for work. He introduced me to the world of semiconductor lasers and integrated photonics. He has been an excellent ambassador for our research efforts. This work and publications could not been achieved without his discussions and suggestions.

Special thanks to Ali HAMIE, Dean of Faculty of Science and Fine Arts at the Arts, Sciences, and Technology University in Lebanon (AUL) and Professor at Lebanese University (LU), for giving me the opportunity to have my dissertation in such a developed laboratory in addition to the time, encouragement, and his time guidance and participation in all the stages of this thesis in which his efforts contributed to making my work successful to me and to all those concerned in the core of my work.

Moreover my most deep sense of gratitude and deep thanks to Ali ALAEDDINE, Professor at Lebanese University (LU), for giving me useful guidance, encouragement, and valuable suggestions in the work.

I sincerely thank Christelle AUPETIT-BERTHELEMOT, Professor at ENSIL, and Hong WU LI, Professor at University of Nantes, who accepted to be the reviewers of the thesis. I also express my sincere gratitude to Didier ERASME, Professor at Telecom Paris-Tech and Ziad OSMAN, Professor at Beirut Arab University (BAU), for accepting to be the examiners of this work.

I would like to thank the entire ENIB team: the professors, the technicians, and the administration, especially Viviane LARDEUR and Jean-Luc BERTHEVAS, for their help during the three years of the thesis.

Warm thanks are given to my family, especially my mother, for their tireless love, support, and encouragement.

Table of Contents

Introduction

In the last few years RoF networks have become the most important networks used as a solution to transmit high frequency signals for wireless applications [1]. Radio frequency (RF) signals in RoF networks modulate an optical carrier conveyed through the optical fiber link and subsequently carried towards a photo-detector which is used to convert the optical signal to the electrical one at the receiver. These networks can benefit from low loss, low complexity, wide bandwidth, and high immunity to electromagnetic interference of optical fibers. They can work to combine electrical and optical signals. Photonic implementation presents interesting advantages such as multi-wavelength treatment, optical amplification, wider bandwidth, capability of simultaneous conversions of several signals, high conversion efficiency, low input optical power requirement, good linearity and flexibility of integration with a wavelength division multiplexing (WDM) system compared to electronic one.

The frequency conversion is one of the main important function that was studied in RoF networks in the last few years. This function can either shift signals from an intermediate frequency (IF) domain to a RF one which is called frequency up-conversion or can convert RF signals to an IF domain which is called frequency down-conversion. Photonic or electro-photonic techniques are used in the previous years to perform the frequency conversion or frequency mixing function based on nonlinearities of several optical mixers such as a Mach-Zehnder modulator (MZM) [2], cascaded electro-optic modulators (EOM) [3], a photodiode (Pd) [4], an electro absorption modulator (EAM) [5], the direct modulation of a laser diode (LD), and a semiconductor optical amplifier (SOA) [6] [7] [8] [9] [10].

The conceptual diagram of the frequency mixing based on a photonic mixer is illustrated in Figure I.1. The frequency mixing is achieved when the local oscillator (LO) signal and the data signals are injected into the photonic mixer input.

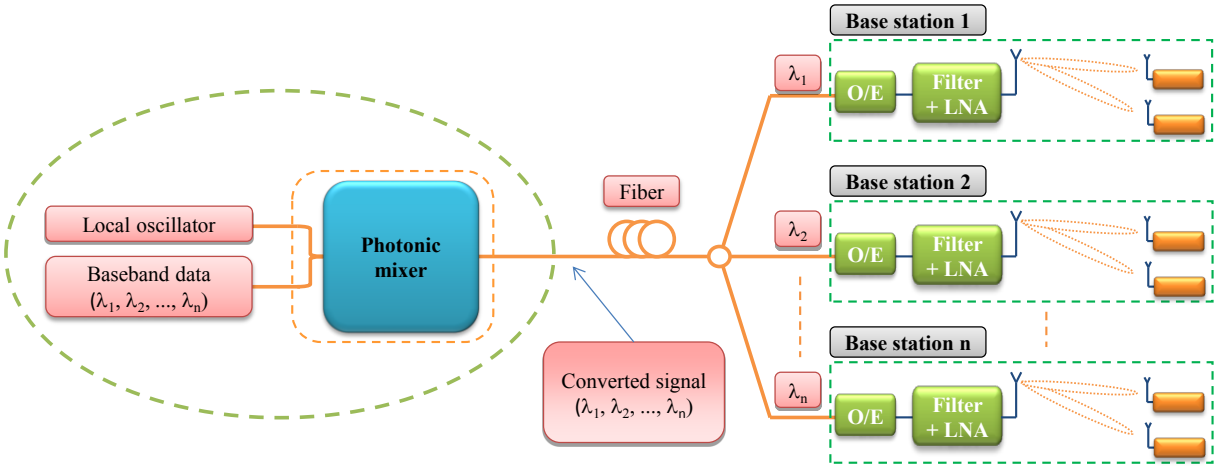

Figure I.1: Conceptual diagram of frequency mixing based on a photonic mixer.

The converted data signals obtained at the photonic mixer output are converted to the electrical one (O/E) by using a photo-detector. The detected signal is amplified by a low noise amplifier (LNA) as displayed in Figure I.1. This system could present an efficient support for a large number of base stations required to cover wireless service areas.

In Lab-STICC (UMR CNRS 6285) at ENIB, the SOA has been investigated through different architectures as a mixer [11] [12] in the range of radio frequency signals up to 10 GHz.

The objective of this work is to study the technique of a frequency conversion permitting the realization of frequency up-conversion and frequency down-conversion with the same device and the same configuration for RF signals up to 40 GHz with the transmission of data at high bit rates (BRs). In this study, we focus on Mach-Zehnder interferometers (MZIs) SOA structure (SOA-MZIs) for its capacity to operate at high BRs for different functions as wavelength conversion [13] [14] [15] [16] and frequency mixing [17] [18]. In addition, we exploit the spectral characteristics of sampled signals that permit to obtain up and down conversions with the same setup.

This work was done within the project POETO "Étude d'une technique de transPOsition de fréquence par Échantillonnage Tout-Optique pour applications en transmission de données radio sur fibre à haut debit" that was developed by the Lab-STICC at ENIB and that was supported by Brittany Region by an ARED "Allocations de Recherche Doctorale". It was also done within a co-joint PH.D thesis (co-tutelle de thèse) between ENIB (ED SICMA at University of Western Brittany, UBO) and Ecole Doctorale des Sciences et de Technologie (EDST) at Lebanese University.

The thesis is organized as follows: after an introduction, the chapter one gives the overview of the frequency mixing and its characteristics such as conversion gain and frequency range, implementation techniques of optical mixers for RF Signals, the up-conversion technique by periodic sampling and the down-conversion technique by bandpass sampling, the influence of the sampling pulse width and the origin of the receiver and sampling noise.

Chapter two presents the basic structure and operation principles of semiconductor optical amplifiers (SOAs) and their nonlinear properties. Static and dynamic characteristics of a SOA-MZI are also theoretically studied. Finally, the static and dynamic behavior of the used SOA-MZI are measured.

Chapter three describes the experimental characterizations for frequency conversion techniques by all optical sampling based on the SOA-MZI standard configuration. In this chapter, we present the principle of all-optical mixing based on a SOA-MZI, experimental setup of the all-optical mixer characterization, optical pulse source characteristics and its influence on the data signal at the SOA-MZI output, frequency up and down-conversion experimental spectrums, frequency up and down-conversion theoretical responses by small signal analysis, experimental

results of up and down-conversion gains, qualitative analysis of frequency up and down-conversion theoretical responses, and frequency conversion of complex modulated data.

Chapter four is devoted to experimental measurements based on the SOA-MZI differential configuration. We present in this chapter principle of all-optical mixing and frequency conversion based on the SOA-MZI differential configuration and experimental results of up and down-conversion gains of complex modulated data. This chapter is followed by a general conclusion and perspectives.

Chapter One

Optical and Electro-Optical Mixing Generalities

1.1 Introduction

In the present chapter, a brief survey of the mixing process for up-conversion and down-conversion and the characteristics of mixing function are presented. The emergence of optical mixing techniques for RF signals based on different optical mixers are discussed and compared. Finally, the main concepts of sampling methods, frequency conversion techniques to higher or lower frequencies, sampling pulse width, and receiver and sampling noise are studied.

1.2 Mixing Function

Mixing is a main process in RF design and technology. This process works as shifting signals to be converted to different frequencies. The frequency mixer is a three ports active or passive circuit as shown in Figure 1.1 with two input ports and one output port. The nomenclatures for the ports of the mixer are the local oscillator (LO), the radio frequency (RF), and the intermediate frequency (IF). RF and IF can be input or output signal according to the down-conversion process or up-conversion process.

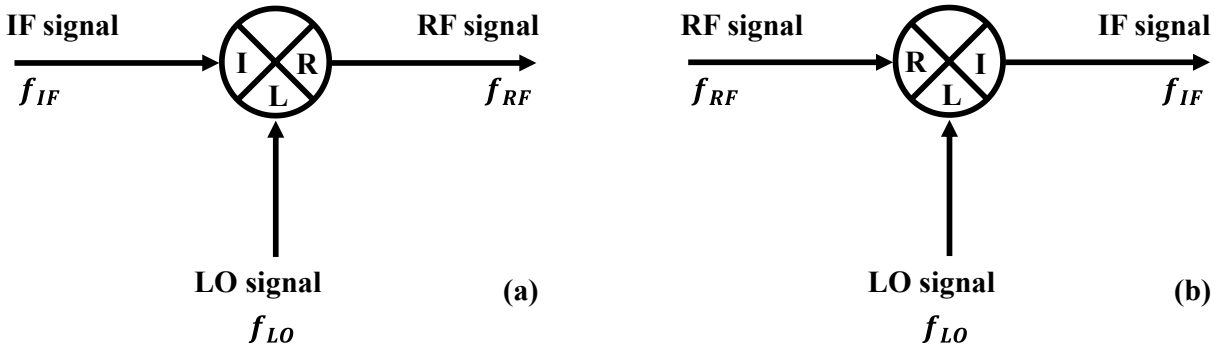

Figure 1.1: Definitions of mixing for the up-conversion process (a) and the down-conversion process (b).

The electrical spectrum for up-conversion and down-conversion at the output of a mixer is shown in Figure 1.2. The up-conversion process means that the IF signal is the input and the RF signal is the mixer output as shown in Figure 1.1(a). This implies that the IF signal at a low frequency is up-converted to a higher one, see Figure 1.2(a). In Figure 1.1(b), the down-conversion process means that the RF signal is the input and the IF signal is the mixer output. This leads to down-convert the RF signal at a high frequency to a lower one as displayed in Figure 1.2(b).

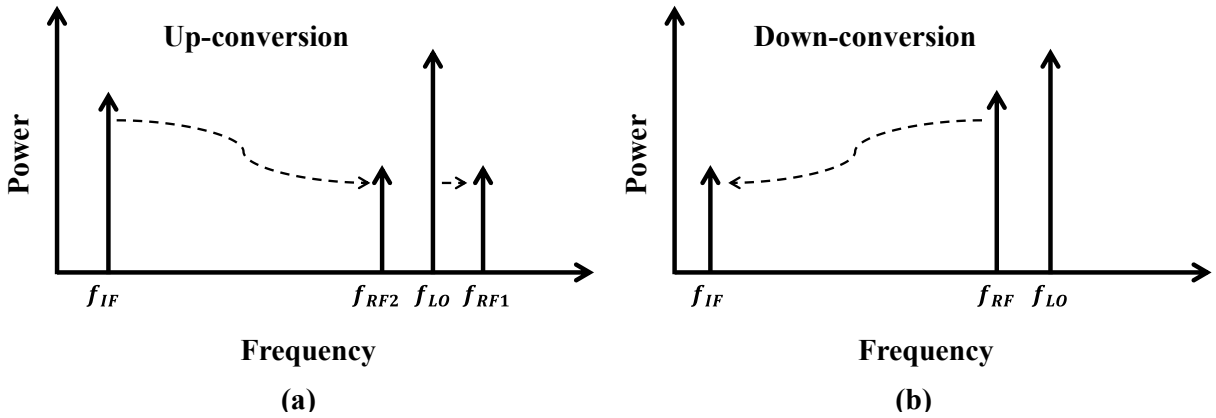

Figure 1.2: Mixing process for up-conversion (a) and down-conversion (b) in the frequency domain.

The relationship between input and output frequencies at the mixer output for the up-conversion process and down-conversion process is given by:

$$f_{RF_{1,2}} = f_{LO} \pm f_{IF} \quad \text{for up-conversion} \tag{1.1}$$

$$f_{IF} = |f_{LO} - f_{RF}| \quad \text{for down-conversion} \tag{1.2}$$

1.2.1 Mixing Process

There are several processes to implement the mixing function of mixers such as multiplication, sampling, and nonlinear processes.

1.2.1.1 Multiplication Process

A multiplier can be used for generating mixing terms at the mixer output when the IF/RF signal and the LO signal are injected into its input. We consider that $X_{IF/RF}(t)$ and $X_{LO}(t)$ are respectively the input waveform of the IF/RF signal and the LO signal of the mixer as defined in the equation below:

$$X_{IF/RF}(t) = X_{IF/RF}\cos\left(2\pi f_{IF/RF}t\right) \tag{1.3}$$

$$X_{LO}(t) = X_{LO}\cos(2\pi f_{LO}t) \tag{1.4}$$

Where $X_{IF/RF}$ and X_{LO} are the amplitudes of the IF/RF and LO input signals, respectively. The multiplication output of a mixer generates the mixing terms as defined in the equation below:

$$X_{LO}(t).X_{IF/RF}(t) = X_{LO}\cos(2\pi f_{LO}t)\,.X_{IF/RF}\cos\left(2\pi f_{IF/RF}t\right)$$
$$= \frac{1}{2}X_{IF/RF}X_{LO}\left[\cos\left(2\pi\left(f_{LO}+f_{IF/RF}\right)t\right)+\cos\left(2\pi\left(f_{LO}-f_{IF/RF}\right)t\right)\right] \quad (1.5)$$

1.2.1.2 Sampling Process

Sampling process plays a crucial role in signal processing. Obtaining the discrete time (DT) sequence to represent a continuous time (CT) function *x*(t) is known as sampling. An ideal sampling process can be modeled as a CT input *x*(t) multiplied by a sampling signal that corresponds to an infinite sequence of Dirac delta functions, see Figure 1.3.

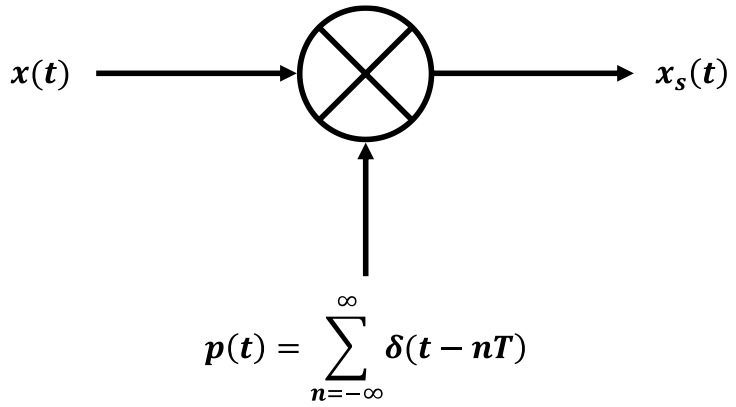

Figure 1.3: Ideal sampling process. *x*(t) is the CT input and $x_s(t)$ is the DT output.

The sampled signal $x_s(t)$ is given in Equation (1.6), where nT represents the sampling time instants. This equation corresponds to sampling between two input signals in the time domain.

$$x_s(t) = x(t).p(t) = x(t)\sum_{n=-\infty}^{\infty}\delta(t-nT) \quad (1.6)$$

The multiplication between the two input signals in the time domain corresponds to the convolution between them in the frequency domain. Hence, the spectrum of the sampled signal is defined as:

$$X_s(f) = \mathrm{X}(f)\otimes P(f) = \mathrm{X}(f)\otimes\frac{1}{T}\sum_{n=-\infty}^{+\infty}\delta\left(t-\frac{n}{T}\right)$$
$$= \frac{1}{T}\sum_{n=-\infty}^{+\infty}X\left(f-\frac{n}{T}\right) \quad (1.7)$$

We can observe from Equation (1.7) the shifting term or mixing terms of the sampled signal at the mixer output.

1.2.1.3 Nonlinear Process

Mixing can be obtained by using nonlinear characteristics of devices. The response of a nonlinear system is modelled by a high order polynomial equation as:

$$X_o(t) = a_1 X_i(t) + a_2 {X_i}^2(t) + a_3 {X_i}^3(t) + \cdots \tag{1.8}$$

Where $X_o(t)$ and $X_i(t)$ are respectively the output and the input of a device. Mixing terms can appear from the second-order product at the output $X_o(t)$ in presence of two input signals IF/RF and LO signals as shown in the equation below:

$$\begin{aligned} X_o(t) = {} & a_1\left[X_{LO}\cos(2\pi f_{LO}t) + X_{IF/RF}\cos\left(2\pi f_{IF/RF}t\right)\right] + \\ & a_2\left[X_{LO}\cos(2\pi f_{LO}t) + X_{IF/RF}\cos\left(2\pi f_{IF/RF}t\right)\right]^2 + a_3\left[X_{LO}\cos(2\pi f_{LO}t) + \right. \\ & \left. X_{IF/RF}\cos\left(2\pi f_{IF/RF}t\right)\right]^3 + \cdots \\ = {} & a_1\left[X_{LO}\cos(2\pi f_{LO}t) + X_{IF/RF}\cos\left(2\pi f_{IF/RF}t\right)\right] + \\ & a_2\left[X_{IF/RF}^2\cos^2\left(2\pi f_{IF/RF}t\right) + X_{LO}^2\cos^2(2\pi f_{LO}t) + \right. \\ & \left. X_{IF/RF}X_{LO}\left[\cos 2\pi\left(f_{IF/RF} + f_{LO}\right)t + \cos 2\pi\left(f_{IF/RF} - f_{LO}\right)t\right]\right] + \\ & a_3\left[X_{LO}\cos(2\pi f_{LO}t) + X_{IF/RF}\cos\left(2\pi f_{IF/RF}t\right)\right]^3 + \cdots \end{aligned} \tag{1.9}$$

Where $X_{IF/RF}$ and X_{LO} are amplitudes of the input IF/RF and LO signals applied at the device input, respectively. For high order product, mixing terms and multiples intermodulation products are produced.

1.2.2 Characteristics of the Mixing Function

The principle parameters required to characterize the mixer performance [19] [20] are conversion gain (G_c), frequency range, third-order intercept point (IP3), spurious free dynamic range (SFDR), gain compression, and isolation which are defined in the following sections:

1.2.2.1 Conversion Gain

Conversion gain G_c is defined as the ratio in powers between the output IF/RF power level and the input RF/IF power level. It can be a gain or a loss depending on the efficiency of the mixing process which is based on the type of the mixer.

1.2.2.2 Frequency Range

The frequency range is the range of frequencies over which the mixer will meet the specification parameters. The circuit construction of components inside a mixer will indicate the frequency range over which the mixer can run [21]. The frequency range of RF/LO signals is changed from a mixer to another one.

1.2.2.3 Third-Order Intercept Point

Two-tone third order intermodulation operates when two RF/IF signals enter simultaneously the RF/IF port of a mixer and they interact. Two-tone signals are used in predicting the nonlinear behavior of a mixer as the input RF/IF power increases.

We consider two-tone signals at frequencies f_1 and f_2 which have the same amplitude injected into the RF/IF port of a mixer and the LO signal injected into its LO port. Third order intermodulation occurs at the mixer output at frequencies $f_{LO} \pm 2f_1 \pm f_2$ and $f_{LO} \pm 2f_2 \pm f_1$ which are very close to $f_{LO} \pm f_1$ and $f_{LO} \pm f_2$ as shown in Figure 1.4. Third order products will increase by 3 dB for each dB increment at the input.

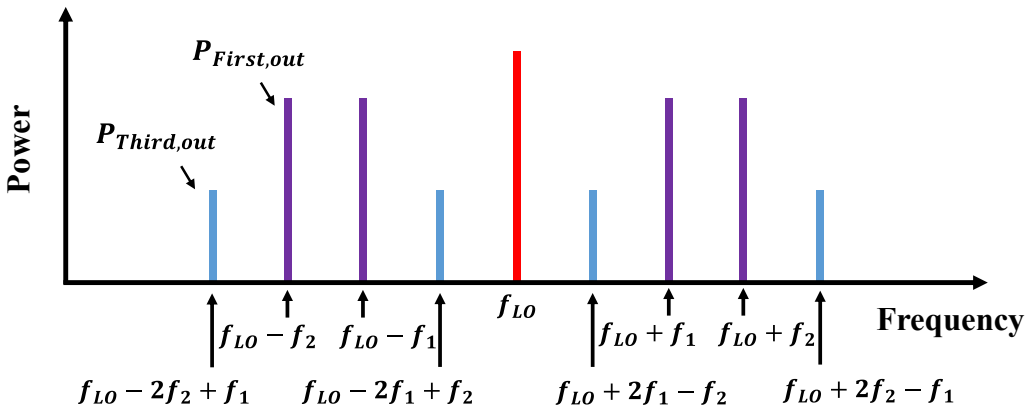

Figure 1.4: First and third order products at the mixer output around the fundamental harmonic of the LO signal. $P_{First,out}$ is the first order power and $P_{Third,out}$ is the third order intermodulation power of the output signal.

Third-order intercept point (IP3) is a theoretical location on the output versus the input curve. IP3 is obtained by linearly extending both the output signal curve and the third-order output signal curve until they intersect where the desired output power and the third order products power are equal as shown in Figure 1.5. The input of the IP3 (IIP3) is the input power at which the output power levels of the unwanted intermodulation products and the desired output are equal. The higher the output at the intercept point, the better the linearity and the lower the intermodulation product.

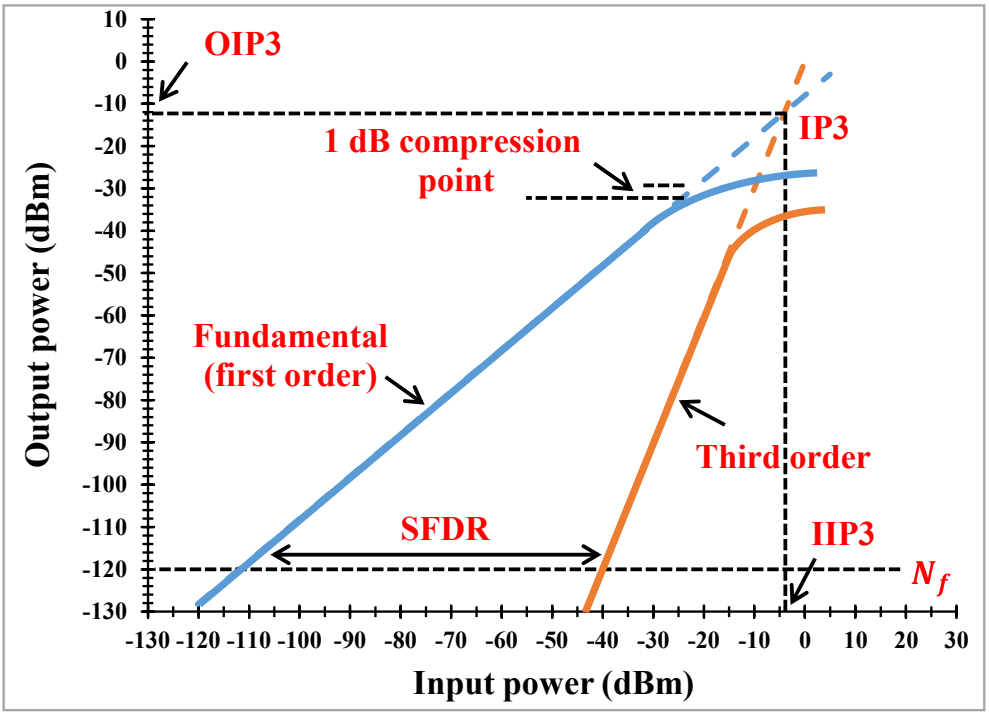

Figure 1.5: Third order intercept point (IP3) concept, N_f is the noise floor and SFDR is spurious free dynamic range.

The IP3 at the output of a mixer denoted OIP3 measured in dBm is calculated in the equation below:

$$OIP3 = P_{First,out} + \frac{C/IM_3}{2} \tag{1.10}$$

Where the parameter C/IM_3 denoted in dBc represents the carrier to third order intermodulation term at a given input power. The C/IM_3 parameter corresponds to ratio of power between $P_{First,out}$ and $P_{Third,out}$ that are respectively the first and third order of the output signal, see Figure 1.4.

1.2.2.4 Spurious Free Dynamic Range

The dynamic range of a mixer is defined as the range of power over which it provides useful operation. The spurious free dynamic range (SFDR) is commonly used to describe the dynamic range of RF systems. The SFDR denoted in $dB/Hz^{(2/3)}$ is the difference in powers between the first order output signal and the third order intermodulation products at the mixer output when they have the same power as the noise floor (N_f), see Figure 1.5.

1.2.2.5 Gain Compression

Gain compression is a measure of the linearity of the mixer which is the useful index of distortion generation. It is specified in terms of an input power level at which the conversion gain drops off by 1 dB as illustrated in Figure 1.5.

1.2.2.6 Isolation

Isolation (Iso) denoted in dB is a measure of the amount of power at the output port of a mixer. Iso is defined as the ratio of power between an IF/RF signal and a LO signal. Three types of isolation are quoted in mixers: LO-RF isolation, LO-IF isolation, and RF-IF isolation. The LO-RF isolation is the ratio of the LO power into the RF one as defined in Equation (1.11). It is important when the mixer is used as an up-converter. The LO-IF isolation is the ratio of the LO power into the IF one as given in Equation (1.12). It is important when the mixer is used for a down-converter. The RF-IF isolation is the ratio of the RF power into the IF one as written in Equation (1.13).

$$Iso_{LO-RF} = \frac{P_{LO}}{P_{RF}} \tag{1.11}$$

$$Iso_{LO-IF} = \frac{P_{LO}}{P_{IF}} \tag{1.12}$$

$$Iso_{RF-IF} = \frac{P_{RF}}{P_{IF}} \tag{1.13}$$

1.3 Optical Mixing for RF Signals

1.3.1 Implementation Techniques of Optical Mixers for RF Signals

Optical mixing can be obtained thanks to quadratic response and/or nonlinearities in photonic components like photodiode (Pd), electro-absorption modulator (EAM), Mach-Zehnder modulator (MZM), and semiconductor optical amplifier (SOA).

1.3.1.1 Photodiode

The photo-detector (Pd) is a device that permits the conversion from optical domain to electrical one by detecting the square of the incident optical field as defined in the equation below:

$$I_p = rP_o \propto r|E|^2 \tag{1.14}$$

Where the photocurrent I_p is proportional to the square magnitude of an incident optical field E as well as the incident optical power P_o and r is the responsivity expressed in A/W.

Thus, simultaneously illuminating the device by two optical signals modulated at two different frequencies will generate mixing terms [22] [23] by the quadratic response of the Pd. Mixing can also be obtained as a result of nonlinearity of the Pd when injecting a LO signal at its electrical port and simultaneously illuminating it by an optical signal [24] [25] [26]. For higher frequency range up to 100 GHz [27] and 300 GHz [28], uni-traveling carrier photodiodes (UTC-Pds) [29] can be used for mixing.

1.3.1.2 Electro-Absorption Modulator

The electro-absorption modulator (EAM) is a semiconductor device based on the electro-absorption effect. It can perform photo-detection as well as modulation in presence of an incident optical signal. Figure 1.6 shows the nonlinear static characteristic of the EAM that represents insertion loss as a function of the reverse bias voltage [30].

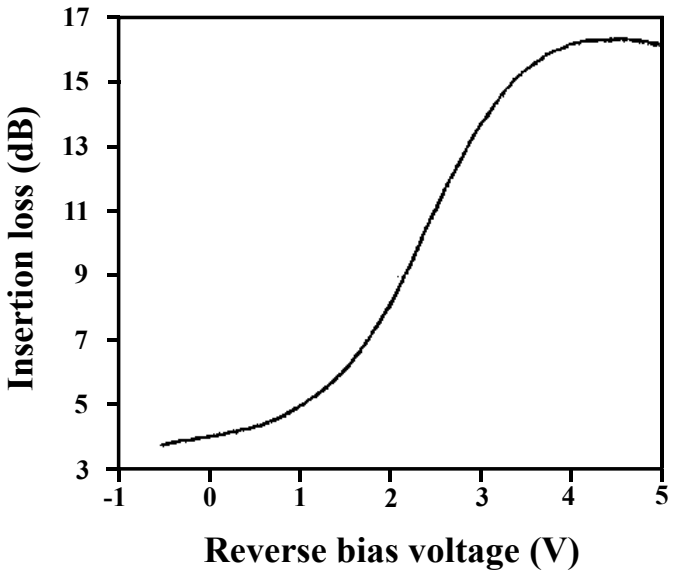

Figure 1.6: Static characteristic of an EAM showing insertion loss versus bias voltage [30].

The nonlinearities of electrical/optical response and cross absorption modulation (XAM) that represents nonlinear effects in an EAM can also be exploited for all optical signal processing including all-optical up- and down-conversion. Frequency mixing to obtain a down converted signal is achieved in an EAM due to its nonlinearities when the optical signal and the RF signal are respectively injected its optical and electrical ports [31]. Frequency up-conversion is accomplished by inserting two optical signals in an EAM due to XAM [5]. The up-converted and down-converted signals can be obtained at the same time by using an EAM [32]. Parallel EAMs are used to achieve mixing for down-conversion [33].

The EAM can be integrated with another optical mixer, such as semiconductor optical amplifier (SOA), to fulfill mixing [34]. In this case, cross-gain modulation (XGM) in a SOA and photo-detection in an EAM are used for frequency up-conversion, and EAM nonlinearity is used for frequency down-conversion.

1.3.1.3 Mach-Zehnder Modulator

A Mach-Zehnder modulator (MZM) is an interferometric component used for modulating the amplitude of an optical light. The characteristic of the MZM shown in Figure 1.7 represents the optical power as a function of a voltage.

The nonlinear transfer function enables the generation of mixing terms. The MZM driven by the LO signal is employed for frequency mixing due to its nonlinearities. The resulting optical field at its output contains the mixing between these signals [35]. The theoretical frequency response of the MZM used as an up-converter in [36] [37] shows clearly the up-converted signal at its output after mixing between the optical IF signal and the LO signal.

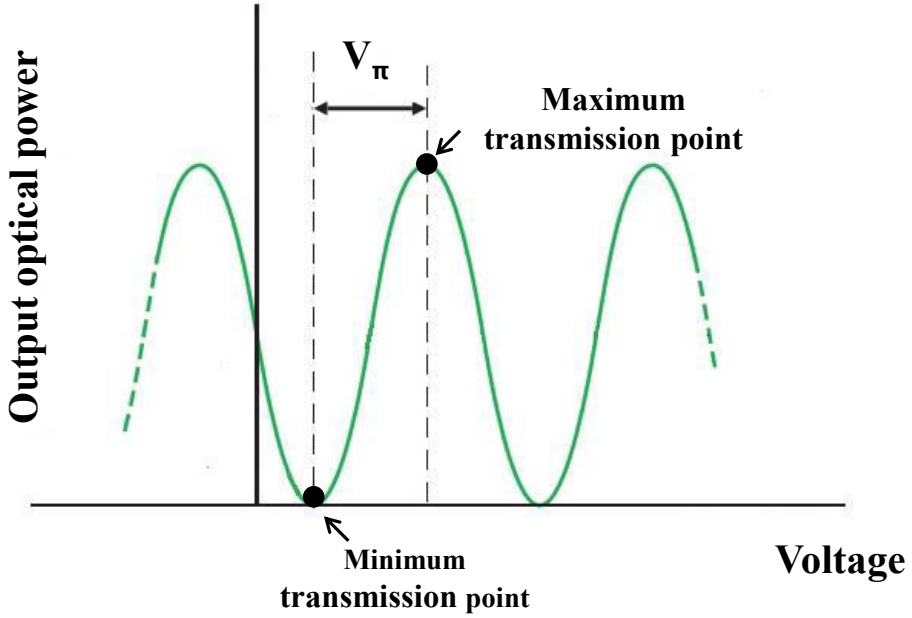

Figure 1.7: Nonlinear transfer function of a MZM, V_π is the voltage required to swing the modulator from its maximum transmission point to its minimum transmission point.

The frequency mixing is also implemented by cascading MZMs [38] [39] [40]. An optical carrier is modulated by the first MZM driven by an IF signal. Then, the modulated IF signal is also modulated with a LO signal by using the second MZM. The nonlinearity of the second MZM and the photo-detection operation generate up conversion mixing terms [40].

1.3.1.4 Semiconductor Optical Amplifier

The use of a semiconductor optical amplifier (SOA) as a multifunctional device permits to perform frequency mixing based on its nonlinearities such as cross gain modulation (XGM) [41], cross phase modulation (XPM) [42] [43], and four-wave mixing (FWM) [44]. The direct modulation of a SOA electrical port also leads to frequency mixing [45] [46]. SOA based on Mach-Zehnder interferometer (MZI) can be used for frequency mixing [47] [48] [49] [50].

1.3.2 Comparison between Different Techniques of Optical Mixers

Several frequency mixing techniques based on different optical mixers have been presented for applications in RoF systems. Table 1 gives the comparison of performances based on the experimental results for different optical mixers. This table is derived from the work used in [26] and developed by using the experimental results of the frequency conversion techniques based on other optical mixers such as an EAM [32], a MZM [2], a SOA [51], and a SOA-MZI [52].

Table 1: Comparison of efficiency of frequency mixing for different optical mixers.

	Pd	MZM	cascaded 2 MZMs	EAM	SOA-XGM	SOA-FWM	SOA-MZI
Conversion gain (dB)	-41	-7	-30	-6	10	5.8	13.2
LO power (dBm)	7	20	15	10	-13	-13	-12
Frequency range (GHz) for up-conversion	50 (300 UTC-Pd)	40	60	26	26 In theory (3-5 THz)	40	22.5
Frequency range (GHz) for down-conversion	60	40	60	60	3	28.5	22.5
Rejection of fundamentals	No	Yes	No	No	No	No	No
LO/IF isolation	Yes	No	Yes	Yes	No	No	No
Up-conversion	Yes	Yes	Yes	Yes	Yes	Yes	Yes
Down-conversion	Yes	Yes	-	-	Yes	Yes	Yes
Electro-optical	Yes	Yes	Yes	Yes	Yes	No	No
All-optical	No	No	No	Yes	Yes	Yes	Yes

1.4 Mixing by the Sampling Method

1.4.1 Up-Conversion by Periodic Sampling

Periodic sampling permits to represent a continuous signal x(t) with a sequence of discrete data values. Two conditions must be met; the first one is that the signal x(t) must be band-limited up to a maximum frequency f_{max}. The second one is that the sampling rate f_{sa} must be chosen to be at least twice f_{max}, which is defined as [53] [54] [55]:

$$f_{sa} \geq 2f_{max} \tag{1.15}$$

The minimum sampling rate allowed by the sampling theorem is $f_{sa} = 2f_{max}$ called the Nyquist rate.

In order to present the principle of the frequency up-conversion by a sampling method, we consider that an input signal is at an intermediate frequency (IF) f_{IF} as shown in Figure 1.8(a). It is considered as an analog signal x(t). This input signal is sampled by a pulse signal at a sampling frequency f_{sa} as given in Figure 1.8(b).

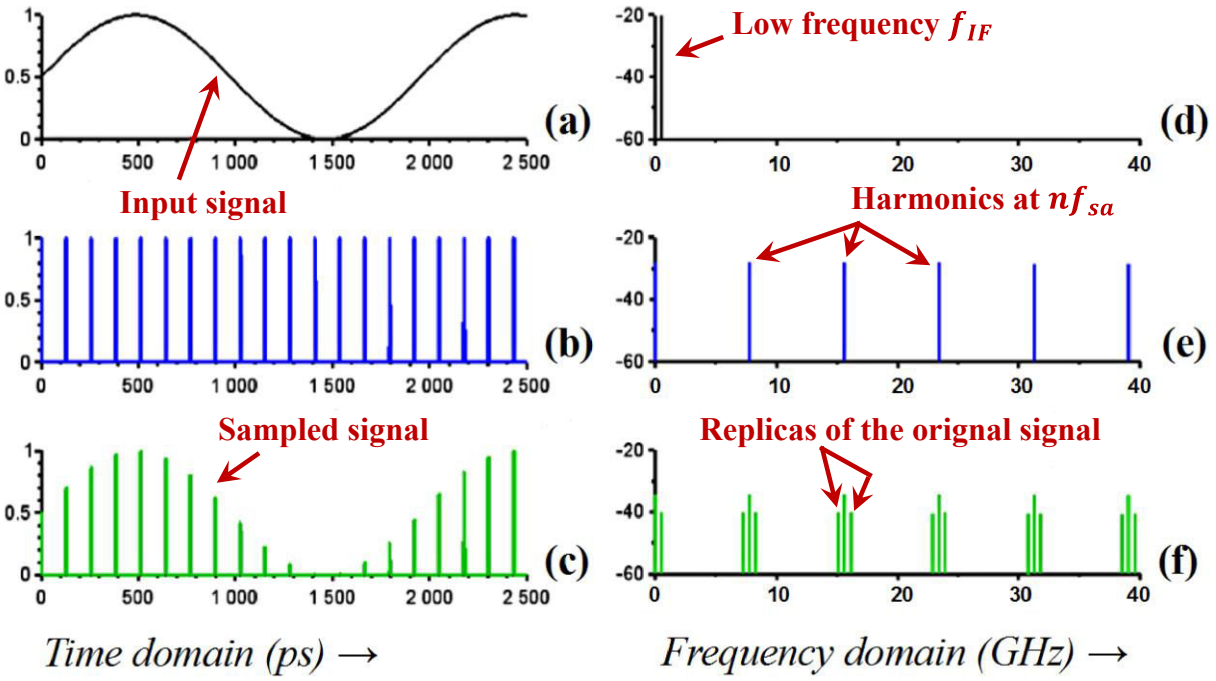

Figure 1.8: Time domain (a-c): an input signal (a) at f_{IF} is sampled by a sampling signal (b) at f_{sa}. As a result, we obtain the sampled signal (c). Frequency domain (d-f): the spectrum of the original signal at f_{IF} (d) is replicated around the harmonics of the sampling signal (e) leading to up-converted signals (f) at $nf_{sa} \pm f_{IF}$.

The pulse signal is supposed to be rectangular pulses of normalized amplitude and with a low duty cycle (α). This signal is used to sample an input signal at f_{IF} while respecting the Shannon theorem. The resulting sampled signal $x_s(t)$ in the time domain is shown in Figure 1.8(c) that represents the multiplication between the input signal and the sampling signal.

In the frequency domain, the input signal shows frequency component at f_{IF} as displayed in Figure 1.8(d). The spectrum of the sampling signal shows harmonics at frequencies multiple of the sampling frequency nf_{sa} given in Figure 1.8(e). Finally, due to the spectral property of sampling, the multiplication between the two input signals in the time domain corresponds to the convolution between them in the frequency domain. As a result of sampling, the spectrum of the sampled signal shows replicas of the original spectrum around each harmonic of the sampling signal at the frequencies $nf_{sa} \pm f_{IF}$, see Figure 1.8(f). Therefore, the original IF signal at f_{IF} is frequency up-converted at $nf_{sa} \pm f_{IF}$.

1.4.2 Down-Conversion by Bandpass Sampling

In bandpass sampling [56] [57] [58] [59] [60], the radio frequency (RF) of a bandpass signal is shifted to the intermediate frequency (IF) by using a sampling rate which is chosen below a range of frequencies of a bandpass signal. This sampling rate must respect constraints relative to the signal bandwidth to avoid aliasing and overlapping.

Let's assume a bandpass signal with a bandwidth BW, its spectrum is depicted in Figure 1.9(a). This signal is centered at a RF frequency f_{RF}. The spectrum of the sampled bandpass signal after bandpass sampling is shown in Figure 1.9(b). It is sampled at a sampling rate f_{sa1}, so spectral replicas of positive and negative bands just shift against each other at the lower frequency band. According to the bandpass sampling theory [61], the minimum sampling rate relies on the bandwidth (BW), not the maximum frequency f_{max}, of the bandpass signal. With an arbitrary number of Nyquist zones m in the range of the frequency $2f_{RF} - BW$ that is defined as follow:

$$1 \leq m \leq I_g \left[\frac{f_{max}}{f_{max}-f_{min}}\right] \tag{1.16}$$

And to avoid aliasing, this sampling rate is defined as:

$$f_{sa1} \leq \frac{2f_{min}}{m-1} \tag{1.17}$$

Where $(f_{max} - f_{min}) = BW$ is the bandwidth of the bandpass signal, f_{max} is the maximum frequency, f_{min} is the minimum frequency, and $I_g[X]$ is the floor function that returns the largest integer less than X [62].

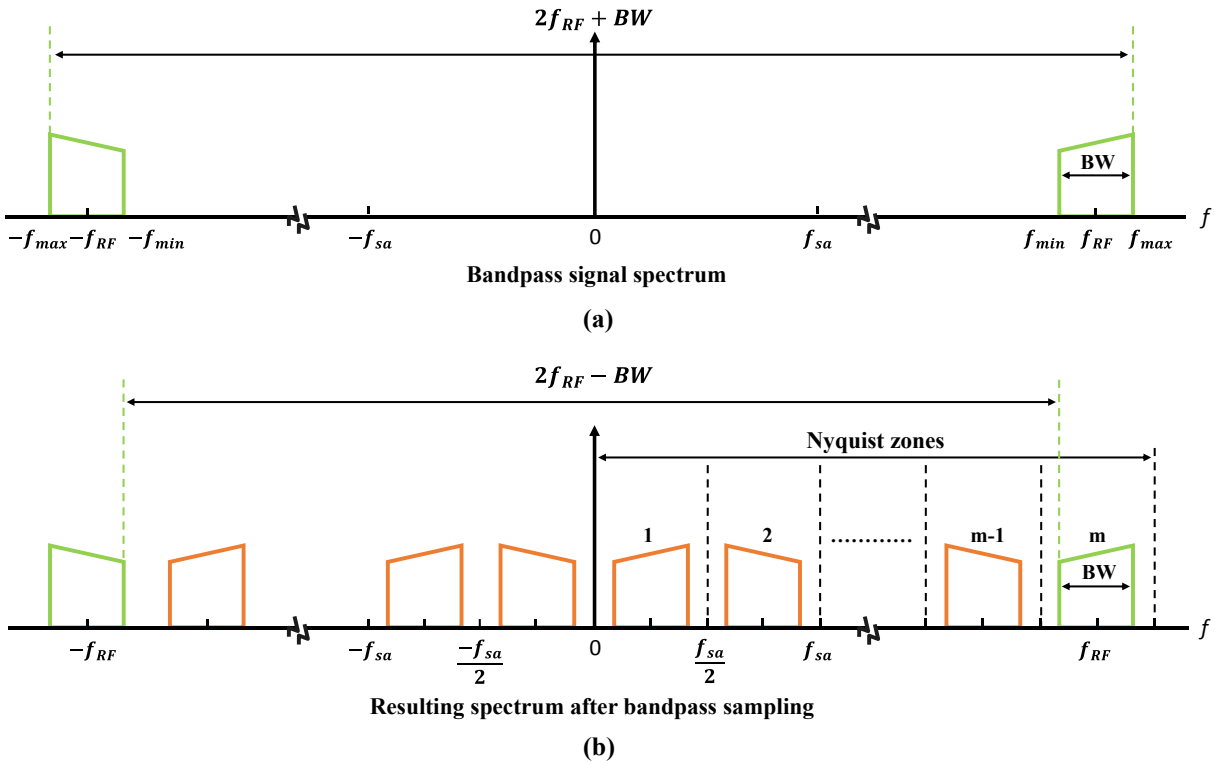

Figure 1.9: Bandpass signal spectrum: (a) original bandpass signal spectrum, (b) sampled signal spectrum replications after bandpass sampling. BW is the bandwidth of the bandpass signal and m is the Nyquist zones.

The spacing between replications will decrease when the sampling rate is minimized below f_{sa1}. The original spectra are fixed when the sampling rate is changed. The new sampling rate is f_{sa2}, where $f_{sa2} < f_{sa1}$, the replicas will just shift against the positive original spectrum centered at f_{RF}. With an arbitrary m and to avoid aliasing and overlapping, the new sampling rate is defined in the equation below:

$$f_{sa2} \geq \frac{2f_{max}}{m} \tag{1.18}$$

As a result, the sampling frequency or sampling rate f_{sa} may be chosen anywhere in the range between f_{sa2} and f_{sa1} to avoid aliasing that can be written by:

$$\frac{2f_{max}}{m} \leq f_{sa} \leq \frac{2f_{min}}{m-1} \tag{1.19}$$

or

$$\frac{2f_{RF}+BW}{m} \leq f_{sa} \leq \frac{2f_{RF}-BW}{m-1} \tag{1.20}$$

By virtue of bandpass sampling, many replicas of the bandpass signal, as shown in Figure 1.9(b), can be found at the IF frequencies. Therefore, a bandpass sampling gives rise to spectral replicas of the original signal spectrum in m frequency bands. These replicas correspond to down-converted signals.

Frequency down-conversion technique is based on bandpass sampling that allows an input signal at a high frequency to run at a lower one as illustrated in Figure 1.10. The sampling frequency f_{sa} is chosen well below the range of frequencies of the input signal to be sampled. We assume that an input signal at f_{RF} respects constraints relative to the signal bandwidth given in Equations (1.16) and (1.20). Hence, the bandpass sampling gives rise to spectral replicas of the original signal spectrum in multiple frequency bands centered at frequencies $|f_{RF} - nf_{sa}|$ as shown in Figure 1.10, where n that corresponds to the harmonic rank of the sampling signal is an integer chosen among the allowed values given in Equation (1.16). Selecting the appropriate frequency band provides the down-converted signals [62].

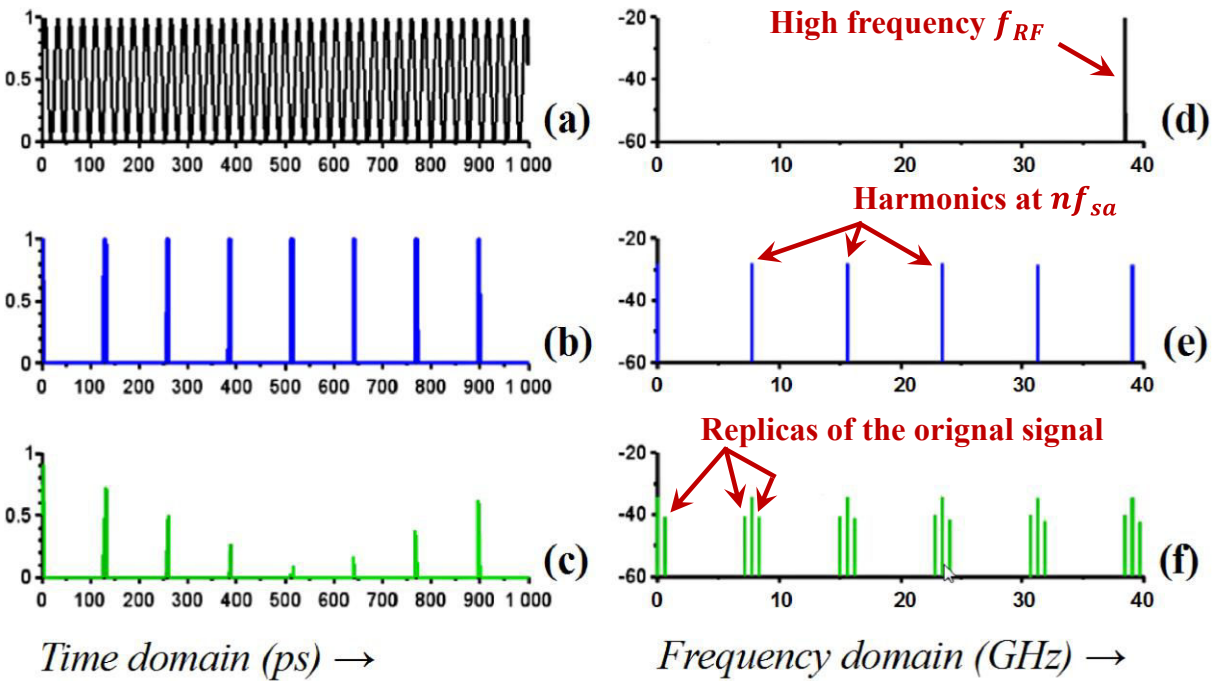

Figure 1.10: Time domain (a-c): an input signal (a) at f_{RF} is sampled by a sampling signal (b) at f_{sa}. As a result, we obtain the sampled signal (c). Frequency domain (d-f): the spectrum of the original signal at f_{RF} (d) is replicated on either side of the harmonics of the sampling signal (e) leading to down-converted signals (f) at $|f_{RF} - nf_{sa}|$.

Figure 1.10(a) and Figure 1.10(b) show respectively the input signal at a RF frequency f_{RF} and the pulse signal at a sampling frequency f_{sa}. The resulting sampled signal in the time domain is shown in Figure 1.10(c). The spectrum of the input signal is displayed in Figure 1.10(d)

which represents the power spectral density (PSD) of an input signal at f_{RF}. The harmonics of the sampling signal at nf_{sa} are observed in Figure 1.10(e). This signal is used to sample an input signal at f_{RF}. In Figure 1.10(f), the PSD of the sampled signal shows replicas of the original signal at f_{RF} apparent on either side of the harmonics of the sampling signal at $|f_{RF} - nf_{sa}|$ thanks to the bandpass sampling. Therefore, the original RF signal at f_{RF} is frequency down-converted at $|f_{RF} - nf_{sa}|$.

1.4.3 Sampling Pulse Width

In the time domain, a pulse has a power that is appreciable only within a short time interval and close to zero at all other times. The pulse duration, called its width δ_t, is defined at the full width at half maximum (FWHM) measured at the half of the pulse power. Periodic pulses form a sequence called a pulse train as shown in Figure 1.11, where the length of time from the beginning of one pulse to the beginning of the next one is called the pulse interval or period T_s. Pulses can have different shapes such as rectangular, triangular, Gaussian, etc. The pulse width δ_t and the period T_s are related by the duty cycle α defined as follow:

$$\delta_t = \alpha . T_s \tag{1.21}$$

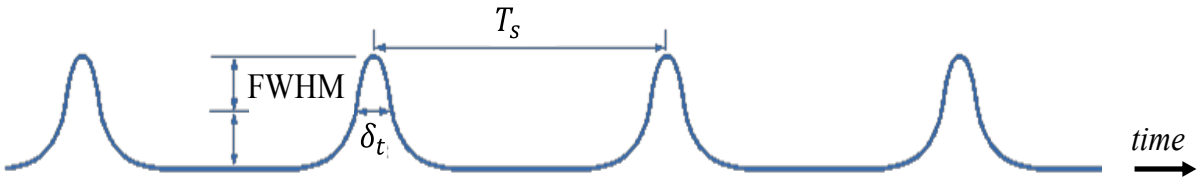

Figure 1.11: Pulse train of period T_s formed by pulses of width δ_t measured at FWHM.

The spectrum of an infinite pulse train formed by pulses of period T_s has harmonics at frequencies n/T_s, n is an integer. The amplitude of the harmonics depends both on the shape of the pulses and the duty cycle α. In the following, we compare two kinds of pulse train: a PWM pulse train (Pulse Width Modulation) and a Gaussian pulse train. The expression of a harmonic H_n of rank n is given for both kinds of pulse train as:

$$H_n = \frac{2}{n\pi}\sin(n\alpha\pi) \qquad \text{(PWM pulse train)} \tag{1.22}$$

$$H_n = \frac{\alpha T_s}{\sqrt{\ln 2}}\sqrt{\pi} \cdot \exp^{-\frac{\pi^2}{4\ln 2}(n\alpha)^2} \qquad \text{(Gaussian pulse train)} \tag{1.23}$$

The PWM pulse is used as a first approximation of a real pulse in order to analyze the effect of characteristics of the pulse on the obtained signals. The Gaussian one, due to its smoother shape, is closer to a real pulse.

As shown in Figure 1.12, the amplitude of harmonics depends on three parameters: the pulse shape, the duty cycle and the rank of the considered harmonic. The principle involved in sampling mixers is based on the convolution of an input signal with harmonics of the sampling signal. In order to keep the sufficient efficiency of the mixer, the amplitude of harmonics is an important point to address.

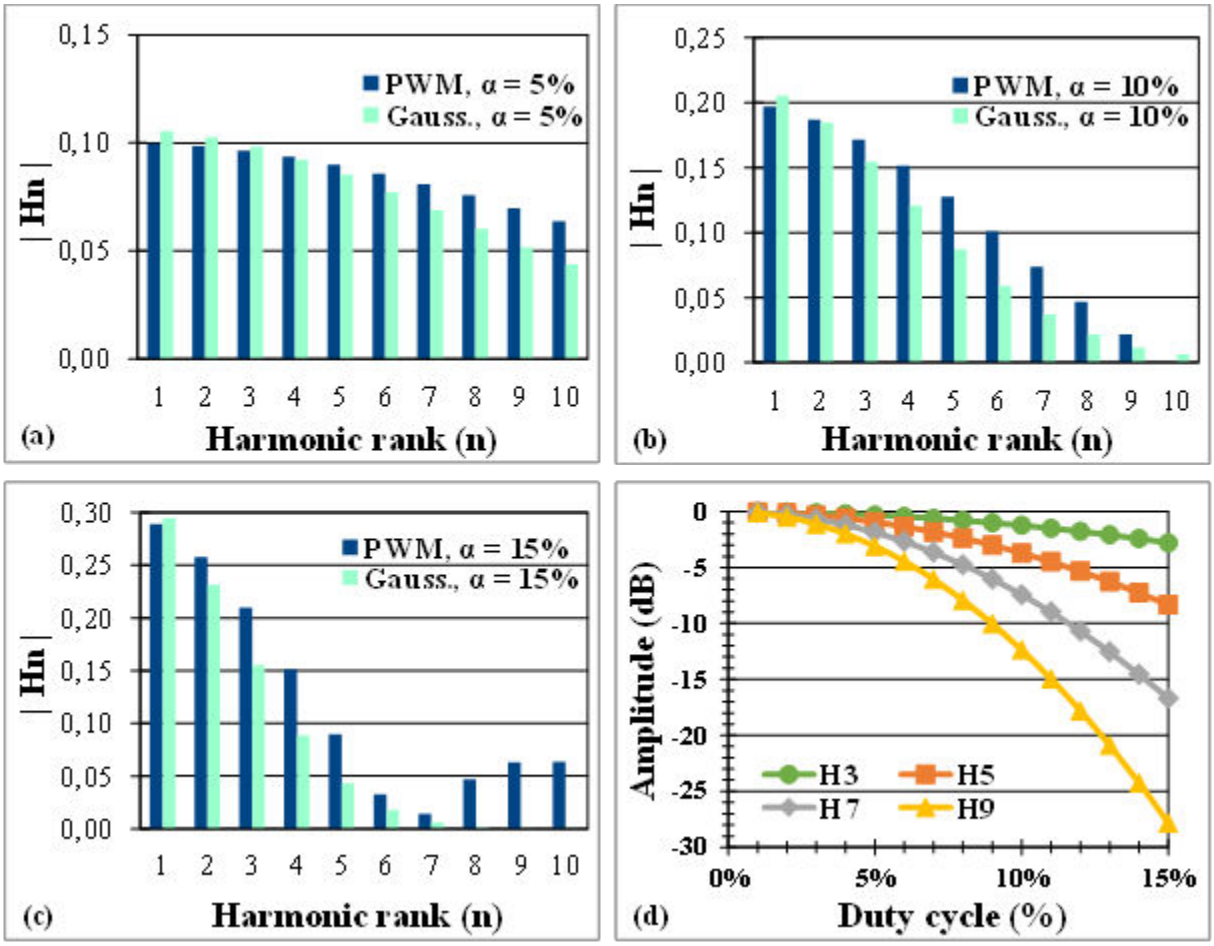

Figure 1.12: Amplitude of harmonics of PWM and Gaussian pulse trains for three different duty cycles (a) 5 %, (b) 10 %, (c) 15 % and as a function of the duty cycle for a Gaussian pulse train (d).

The Gaussian pulse train leads to lower amplitude of harmonics at high harmonic ranks n due to its smoother shape. The harmonics of the Gaussian pulse train monotonically decrease with the rank n. The duty cycle α plays on speed that the amplitude of harmonics changes with n. It means that an output signal of a sampling mixer involving a harmonic of a given rank must be driven by a sampling signal with a sufficiently low duty cycle to maintain an efficient mixing operation for this given harmonic. For example in Figure 1.12(a), the duty cycle of pulse train is 5 % leading, for Gaussian pulses, to an amplitude of harmonic H_9 that is half of the one of

H_1. When the duty cycle is doubled, the half of amplitude of harmonic H_1 is reached for H_4 as observed in Figure 1.12(b).

Figure 1.12(d) shows the value of the four first odd harmonics of a Gaussian pulse train relative to the fundamental as a function of duty cycle α. This figure helps to find the maximum value of α for a given normalized amplitude and a given harmonic rank. For example, an amplitude of -5 dB, normalized to the fundamental, is reached for the harmonic H_5 at $\alpha = 12$ %. The same relative value of -5 dB requires a duty cycle as low as 6 % for H_9.

As previously explained, the duty cycle α has to be small enough depending on the range of frequencies for which the mixer must work. However, α must not be chosen very smaller than necessary. Certainly the amplitude of harmonics varies slightly with n for low α but their absolute value is small, so a tradeoff has to be found.

1.4.4 Receiver and Sampling Noise

The noise in RoF systems is divided into two main types which are known as the optical noise and the electrical noise. The optical noise is affected by the optical origin such as relative intensity noise (RIN) of a laser and amplified spontaneous emission (ASE) of a SOA, and the electrical noise is affected by the electrical origin such as thermal noise. The shot noise is considered as both electrical and optical noise.

Relative intensity noise (RIN) describes the power fluctuations of an output optical signal generated by a laser. These fluctuations which can degrade the performance of RoF systems are due to quantum noise associated with laser gain. In a receiver, laser intensity fluctuations can cause noise that exceeds the thermal noise of the load impedance of the receiver photodiode (Pd). This noise augments with the optical power.

Photodiodes, such as p type intrinsic n type photodiode (PIN-Pd), generate two types of major noise which are called the thermal noise and the shot noise in the process of converting from optical domain to electrical one. In presence of optical amplifiers, such as a SOA, beating terms known as signal-ASE and ASE-ASE are added to the other sources of noise at the receiver.

In a sampling system, the spectrum contains noise combined into each of the sampling frequency over two $(f_{sa}/2)$ bands. Bandpass sampling is applied to shift a bandpass signal to lower frequencies. The sampled bandpass signal degrades due to the noise aliased from bands leading to degrade the SNR [63] [64] [65].

In addition to noise aliasing, the jitter noise and thermal noise are the prime sources of the sampling noise. Jitter noise is defined as the influence of sampling time uncertainty [66] [67]. There are two common categories of jitter processes known as aperture jitter [68] and clock jitter [66]. The time uncertainty in the state transition of the sampling circuit switches is called

aperture jitter noise. The clock jitter noise process is unstable in its nature which describes the variation of the sampling period duration caused due to the oscillator phase noise. The influence of jitter noise on the signal spectrum may create new components and produce frequency selective attenuation [69]. There are some techniques used in the mitigation of the sampling jitter [70] [71].

1.5 Conclusion

In summary, in this chapter we have presented the mixing function and its characteristics. We have pointed first the principal processes of mixing. Frequency mixing based on different optical components are then presented. We have developed afterwards the periodic and bandpass sampling process and we show that up- and down-conversion can be performed by this technique. We give next the influence of the pulse width for different signal shapes and duty cycles and finally we give the principal origin of noise at a receiver and in sampling process.

Chapter Two

Static and Dynamic Characteristics of a Semiconductor Optical Amplifier Mach–Zehnder Interferometer

2.1 Introduction

Semiconductor optical amplifier Mach-Zehnder interferometer (SOA-MZI) is a mature optical device. The optical sampling is performed by using the cross phase modulation (XPM) effect in a SOA-MZI used as an optical switch. SOA-MZIs have some attractive features of low power requirements, compactness, high extinction ratios [72] [73], and noise reduction [74]. Furthermore, the possibility of using the same experimental setup of the SOA-MZI [75] [76] to implement frequency up-conversion and frequency down-conversion, makes the scheme a very versatile choice. The large data bandwidth is fundamentally related to the carrier lifetime of SOAs [77]. Some functions, such as signal regeneration [78], wavelength conversion [79] [80], demultiplexing [81], have been demonstrated.

The architecture of a SOA-MZI is given in Figure 2.1. One SOA is located in each arm of a MZI. The phase shifter ($\emptyset_0$) located in the upper arm helps to provide phase optimization for both output arms. With this structure of the SOA-MZI, the input signals travel in the same direction, but they may travel in the counter-direction.

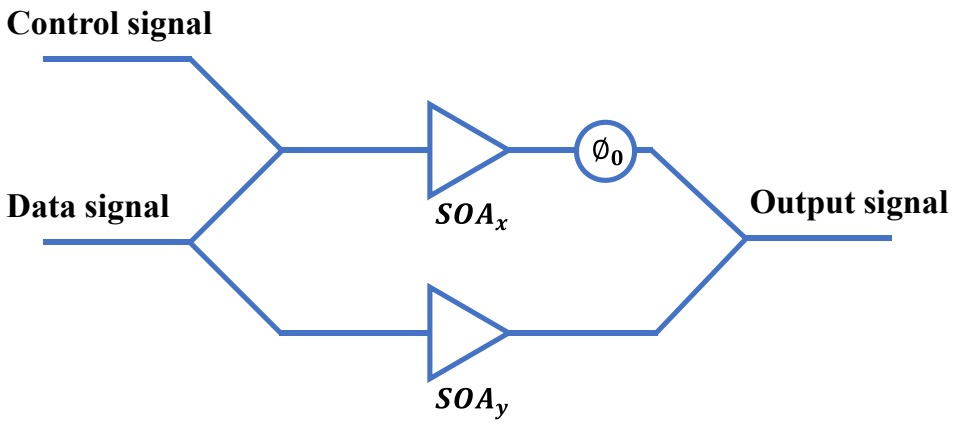

Figure 2.1: Architecture of a SOA-MZI including two SOAs and a phase shifter.

The data signal at the SOA-MZI input is divided into two signals, the first signal is injected into SOA1 at the upper arm and the other one is injected into SOA2 at the lower arm. When there is no control signal injected into the SOA-MZI input, both these signals amplified through SOA1 and SOA2 interfere in a destructive or constructive way at the SOA-MZI output depending on $\emptyset_0$. If a control signal is injected at SOA-MZI input, the carrier density in the SOA1 active region changes and then its refractive index leading to the XPM of the other signal carrying data. Hence, the interference at the SOA-MZI output may evolve from being destructive to constructive.

This chapter concerns the experimental and theoretical frameworks of the static and dynamic characteristics of the SOA-MZI discussed subsequently. In a first section, we investigate the architecture and the function of a SOA-MZI, we then review the use of a SOA and its nonlinearities and dynamic characteristic. Finally, we obtain the static and dynamic characteristics of a SOA-MZI by using a small signal study, the static characteristic of the used SOA-MZI is experimentally obtained with a high extinction ratio (ER). The SOA-MZI dynamic characteristic is also evaluated through its cutoff frequency.

2.2 Semiconductor Optical Amplifier

2.2.1 Introduction

Optical amplifiers which are not only used as a general gain unit include many functional applications [82] [83] [84] in photonic networks. They can be classified into two kinds known as waveguide amplifiers such as SOAs [85] and optical fiber amplifiers such as erbium doped fiber amplifiers (EDFAs) [86] [87] [88] [89] [90]. The main features of EDFAs are wide optical amplification bandwidth, simplicity, a high output saturation gain, low polarization sensitivity, low coupling loss, and low noise figure. They are utilized mainly for inline optical signal amplification. On the other hand, SOAs are used in many functional applications including all-optical switching, wavelength conversion, regeneration and optical logic signals due to their small size, a low switching energy, high stability, fast and strong nonlinear characteristics, and the potential of integration with other electronic and optical devices. The low cost SOAs are used as inline amplifiers for bi-directional transmission in local and metropolitan systems and networks [91]. For that reason, it is important to recognize the characteristics of the SOA and its functionality [92].

The SOA is also considered as a key component for optical gating and cascaded optical fiber systems [93] [94] [95] [96]. Optical gates are needed in all-optical network functions such as the wavelength conversion, the add-drop wavelength and time multiplexing, the clock recovery and the simple bit pattern recognition [97].

2.2.2 SOA Structure

An input optical signal injected into a SOA from its input facet side through the active region will experience gain implying amplification under certain conditions. The schematic diagram of a SOA is shown in Figure 2.2. An input optical signal is amplified along the SOA active region due to the stimulated emission process. The amplification of the optical signal through a SOA is due to the recombination of electrons and holes in a p-n junction. The p type and the n type semiconductor are put together in order to create the p-n junction that contains the recombination of electrons and holes. The electrons and the holes move in the active region when the external electric pump current is injected into the electrical part of the SOA. The amplification process produces noise with the optical amplified signal at the SOA output [85].

Amplification of an optical signal relies on the stimulated emission mechanism. Unfortunately, it is always accompanied by the spontaneous emission.

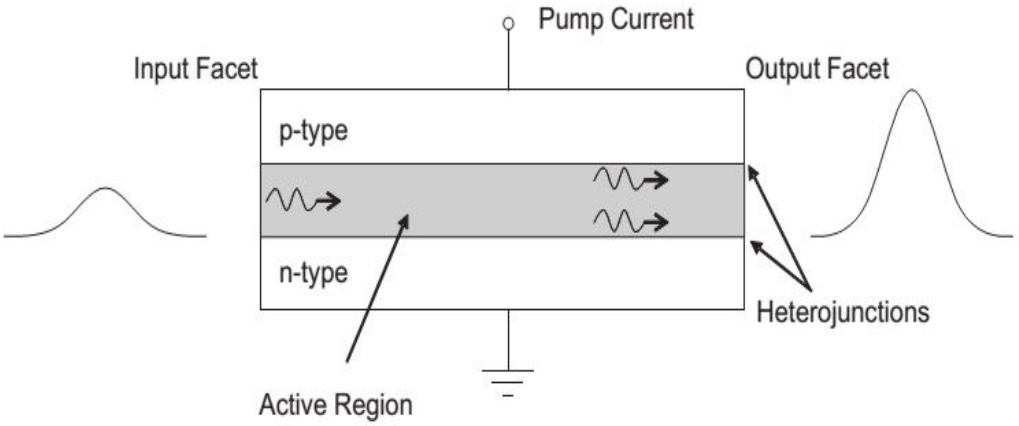

Figure 2.2: Schematic diagram of a SOA with the amplification process.

The spontaneous emission light is also amplified during the propagation inside SOAs and is considered as a noise source for the transmitted signal. The SOAs enhance the signal quality in terms of power but they also degrade the signal quality by adding amplified spontaneous emission (ASE) noise [98] [99] that cannot be entirely avoided during the operation.

2.2.3 Recombination Processes in a SOA

The SOA is biased with an external electric pump current that injects electrons to the SOA active region. An increase in the bias current enhance the number of excited electrons in the conduction band (CB). The recombination of electrons and holes in a radiative way is followed by the emission of a photon. There are three major radiative recombination mechanisms within the SOA active region known as spontaneous emission, stimulated absorption, and stimulated emission [85].

When an excited electron from the CB recombines to the valence band (VB), this leads to release a photon in the SOA active region. This process is called spontaneous emission considered as noise.

When an electron in the VB absorbs enough energy from an incident photon, its energy will be higher than the energy gap and this electron moves to the CB. This mechanism is known as the stimulated absorption process.

In the stimulated emission process, the transition of an electron from the CV to the VB can be stimulated by an incident photon. Therefore, the input photon entered the active region of the SOA via its input facet interacts with a number of excited electrons from the CB. This

recombination is accompanied by the emission of photons that have the same frequency, phase, and direction of the incident photon. A decrease in the SOA gain is achieved due to the reduction of excited electrons in the CB [100].

The carrier density rate equation of SOAs has a form as [101] [102]:

$$\frac{dN}{dt} = \frac{I_b}{qV} - R(N) = \frac{I_b}{qV} - \frac{N}{\tau_c(N)} - v_g \sum_i g_i(N) S_i(N) \quad (2.1)$$

Where N is the carrier density in the SOA active region, $\tau_c(N)$ is the carrier lifetime at the carrier density N, v_g is the group velocity, the index i stands for input signal, $g_i(N)$ and $S_i(N)$ are respectively the gain coefficient and the photon density at the carrier density N, I_b is the bias current, q is the magnitude of the electron charge, V is the volume of the SOA active region, and $R(\mathrm{N}) = R_{sp} + R_s$ is the carrier recombination rate. R_{sp} and R_s are respectively the spontaneous and stimulated recombination rates.

There are three terms given in Equation (2.1), the first term represents the carrier density supplied by external pump current injected into a SOA. The second one represents the loss of carrier density due to the spontaneous emission process and the last one represents the drop of carrier density due to the stimulated emission process.

2.2.4 SOA Fundamentals

Some parameters are used to characterize SOAs such as gain (G), gain saturation, noise figure (NF) and optical signal to noise ratio (OSNR), optical bandwidth, polarization sensitivity, and gain recovery time.

2.2.4.1 Gain

The useful parameter of a SOA is the optical gain. It is affected both by the input signal power, the ASE produced by the amplification process, and local beam intensity at any point inside the SOA. It also relies on the material structure used in the active region and operating parameters. The optical gain of a SOA is defined by the ratio of output power P_{out} to input power P_{in}. It is logarithmically related to the power ratio: $G(dB) = 10\,log\,G = 10\,log\,P_{out}/P_{in}$ measured in decibel (dB) where G is the single pass optical gain is determined by [103]:

$$G = e^{gL} = e^{(\Gamma g_m(\lambda,N) - \alpha_{int})L} \quad (2.2)$$

Where L is the SOA length, g is the net gain, Γ is the optical confinement factor, α_{int} is the internal loss coefficient, $g_m(\lambda, N)$ is the material gain at the wavelength λ and the carrier

density N. Equation (2.2) indicates that a high gain may be achieved with a high injection current. Then, a large optical confinement, a long cavity, or a combination of them.

2.2.4.2 Gain Saturation

One of the key factors affecting the SOA gain is the input signal power. When the input signal power increases, the carrier density in the active region of a SOA become depleted leading to a decrease in the optical amplifier gain. The gain saturation leads to a change in carrier density which results in a change in refractive index. The saturated output power ($P_{sat,out}$) is the key parameter defined as the output signal power when the amplifier gain is -3 dB from the unsaturated value. In general, the saturated output power depends inversely on the optical confinement factor. Additionally, it is increasingly beneficial to have a strong saturation since it results in a short carrier lifetime, thus, a wider bandwidth and in turn better dynamic performances [104].

2.2.4.3 Optical Bandwidth

Amplifiers with a large bandwidth are desirable for an optical communication system. This enables the optical gain to be as constant as possible over a large range of wavelengths. The optical bandwidth is defined as the wavelength range for which the SOA is operational. This parameter can be presented as 3 dB bandwidth for the wavelength range. Figure 2.3 represents the optical gain of a SOA as a function of the wavelength.

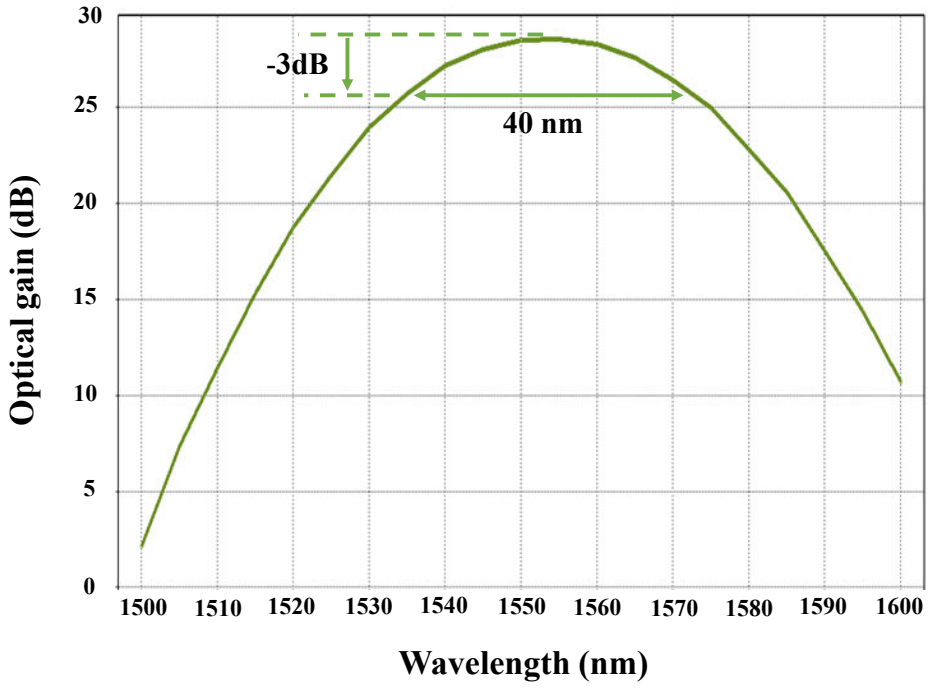

Figure 2.3: Optical gain of a SOA as a function of wavelength denoted nm [103].

The bandwidth depends inversely on the optical confinement and the cavity length [103]. Optical amplifiers have a significant gain over a wide bandwidth from 30 nm to 90 nm.

2.2.4.4 Noise Figure

The useful parameter for quantifying optical amplifier noise is the noise figure (NF) [105] [106] that is defined as the ratio of the input signal to noise ratio (SNR_{in}) to the output signal to noise ratio (SNR_{out}). The SNR of the amplified signal is degraded due to amplified spontaneous emission (ASE) that adds noise to the signal during the amplification process. SNRs are obtained when the input and output powers of the amplifier are detected by an ideal photo-detector. The sources that contribute to the noise are [107]:

(1) Shot noise due to signal and ASE
(2) Signal-ASE beat noise
(3) ASE-ASE beat noise
(4) Thermal noise

The signal-ASE beat noise dominates in the presence of an optical signal which has a high output power while the ASE-ASE beat noise prevails at the low output power. Shot noise is related to several parameters for an ideal photo-detector whose the performance is limited by this noise.

SOAs exhibit a high noise level due to their intrinsic internal loss, ASE, and the lower coupling efficiency on their input side. The SOA noise figure depends on the operating wavelength, the operating current, and the input signal power of an incoming signal. The NF can be defined as [108] [109] [110] [111]:

$$NF = \frac{2P_{ASE}}{hfGB_o} + \frac{1}{G} \tag{2.3}$$

Where B_0 is the optical bandwidth, f is the frequency of the injected optical signal, h is the Planck′s constant, P_{ASE} is the ASE noise power, and G is the SOA gain.

2.2.4.5 Polarization Sensitivity

The amplifier gain differs for the transverse electric (TE) and the transverse magnetic (TM) polarizations. Each one has different effective mode index. It depends on the polarization state of the input beam. This dependency is due to the geometrical form of the SOA active region. The polarization sensitivity of a SOA can be defined as the magnitude of the difference between the TE and TM mode gains.

2.2.4.6 Gain Recovery Time

The depletion in the carrier density will take place when an input signal power enters the SOA. As a result, the SOA gain saturates and recovers back within few tens or hundreds picosecond (ps) [84] [112] [113].

2.2.5 SOA Nonlinearities

In this section, we review the most promising techniques used to exploit the SOA nonlinearities. The used advantages of SOAs in applications, such as wavelength conversion, are widely used in high speed photonic networks. The changes of the carrier density induced by the input signals lead to nonlinearities in SOAs. The main types of nonlinearity are self-gain modulation (SGM), cross gain modulation (XGM), self-phase modulation (SPM), cross phase modulation (XPM), and four wave mixing (FWM).

The intention of this section is to highlight the practical devices exploiting the optical nonlinearities for high speed all-optical switching. The classification is depicted in Figure 2.4. We can distinguish the different concepts with respect to the techniques used to exploit the nonlinearity (XPM, XGM, and FWM) and to the configurations (MZI (Mach-Zehnder Interferometer) [114], MI (Michelson Interferometer) [115], single SOA).

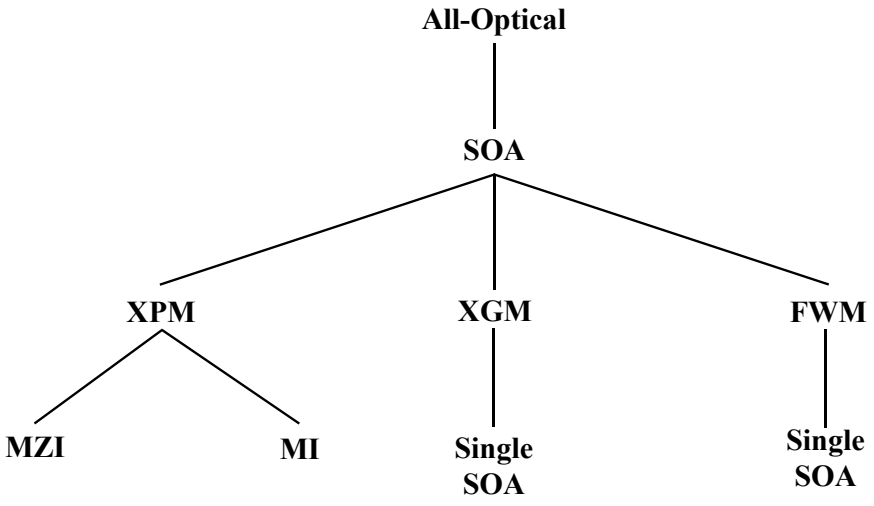

Figure 2.4: Classification of all-optical techniques to exploit the nonlinearities. They are exploited in different configurations.

2.2.5.1 Self-Gain Modulation and Cross Gain Modulation

The optical power variation of an input signal injected into a SOA induces a variation of the optical gain due to the SOA saturation. This process is called self-gain modulation (SGM).

Two input signals introduced into a SOA are affected by the carrier density alterations in the SOA active region due to the wide spectrum of the material gain. Cross gain modulation (XGM) is a technique that allows the conversion of an optical signal. In XGM devices, a strong control pulse signal at λ_1 is used to modulate the SOA carrier density and thereby to modulate a second signal at λ_2. Hence, the XGM imposes the control modulation on the second signal. Hitherto this technique, which inverts the control pulse shapes, has found applications mainly for wavelength conversion. This means that the SOA acts as a wavelength converter [116] [117] [118]. The information transposed from an input signal at λ_1 to a converted optical signal at λ_2 at the SOA output. Problems associated with XGM are extinction ratio (ER) degradation [119] and chirp produced by the phase modulation that accompanies gain modulation in a SOA [120].

2.2.5.2 Self-Phase Modulation and Cross Phase Modulation

The carrier density is changed by injecting an optical input signal into the SOA active region leading to alter the effective refractive index. This input signal modifies its own phase at the SOA output. This behavior is known as self-phase modulation (SPM) [121]. This nonlinear characteristic of the SOA can be used in several applications [122] [123].

In the cross phase modulation (XPM) technique, an optical control signal is used to modulate the phase of another input signal. The XPM will take place between the signals by changing the refractive index of the SOA active region depending on the carrier density. Among the interferometric configurations, we mention the Mach-Zehnder interferometer (MZI) with one SOA in each arm. Without a control signal, an input signal is directed towards the output port with amplification through SOAs. When a control signal is introduced into one arm of the MZI, the phase relations within the SOA on the respective MZI arm alter and the carrier density of the SOA active region also changes leading to the XPM on the input signal at the output port. A number of applications based on XPM, such as wavelength conversion, have been developed [124] [125].

2.2.5.3 Four Wave Mixing

Four wave mixing (FWM) is a coherent wave generation technique where nonlinearities are exploited to generate a new wave that has different frequency components from an optical input signal and a control signal. This technique is used for the conversion of an optical input signal. The FWM process is achieved by mixing an optical signal with a control signal. The nonlinear interaction between the input optical signals in a SOA generates signals at its output. There are three mechanisms known as carrier density modulation (CDM), spectral hole burning (SHB), and carrier heating (CH) which are used to generate FWM signals [85] [126]. FWM generated in SOAs can be used in many applications including all-optical wavelength converters [127] and dispersion compensator. FWM allows multi-channel operation [128] and provides phase conjugation. However, FWM in SOAs has some problems such as polarization sensitivity,

amplified spontaneous emission (ASE) noise from the SOA, and low conversion efficiency [104].

2.2.6 Dynamic Response

Many dynamic SOA models with varying degrees of complexity and accuracy exist [129]. The common approach to describe theoretically the behavior of frequency modulation response of a SOA consists of starting with the well-known carrier density rate equation shown in Equation (2.1) [130] [131]. The transfer function (TF) of a SOA displayed in Figure 2.5 is defined from the ratio between the power variations of an optical signal at the SOA output ΔP_{out} and the SOA input ΔP_{in} as given in Equation (2.4) [108].

$$TF = \frac{\Delta P_{out}}{\Delta P_{in}} = G_{opt} \frac{\tau_c}{\tau_{sat}} \frac{1+j\omega\tau_{sat}}{1+j\omega\tau_c} \tag{2.4}$$

Where G_{opt} is the mean optical gain at the high frequency, $\tau_c = 1/2\pi f_{unsat}$ is the carrier lifetime, ω is the pulsation, and $\tau_{sat} = 1/2\pi f_{sat}$ is the lifetime dependent on the SOA operating conditions.

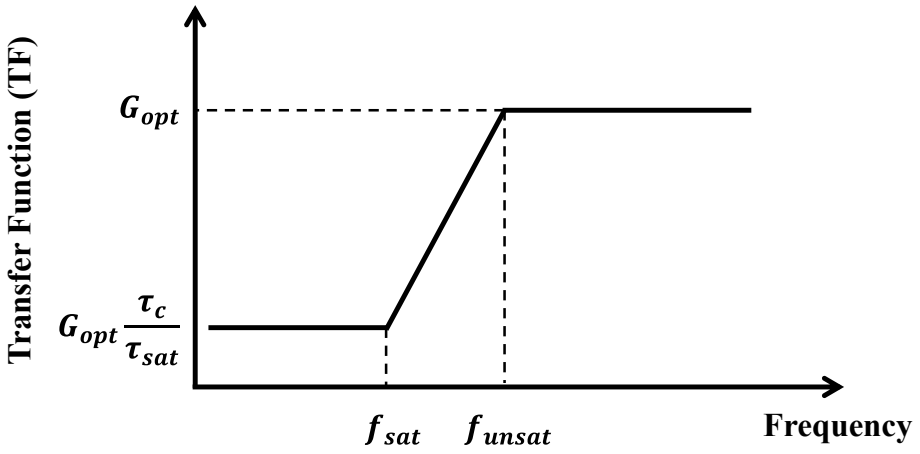

Figure 2.5: Asymptotic representation of frequency response model of the SOA to a saturating optical modulated signal [108].

The TF in Figure 2.5 shows that in presence of a modulated signal, the dynamic gain at low frequencies is lower than the one at high frequencies.

2.3 Characteristics of a SOA-MZI Structure

The static and dynamic characteristics of the proposed SOA-MZI configuration are studied as shown in Figure 2.6. A continuous wave (CW) optical signal with a constant power $\bar{P}_{CW}$ is

separated by using the first 3 dB optical coupler into spatial components propagating through the upper and the lower arms of the MZI.

A control signal injected into SOA1 is a sum of the constant $\bar{P}_{CTR,o}$ and variation $\Delta P_{CTR,o}$ powers as illustrated in Figure 2.6. The phase shifter φ_o is placed after SOA1 in the upper arm which can be biased to provide a phase optimization for both output ports. The optical output power at the SOA-MZI output (P_s) can be changed from zero to a maximum value depending on the optical control signal.

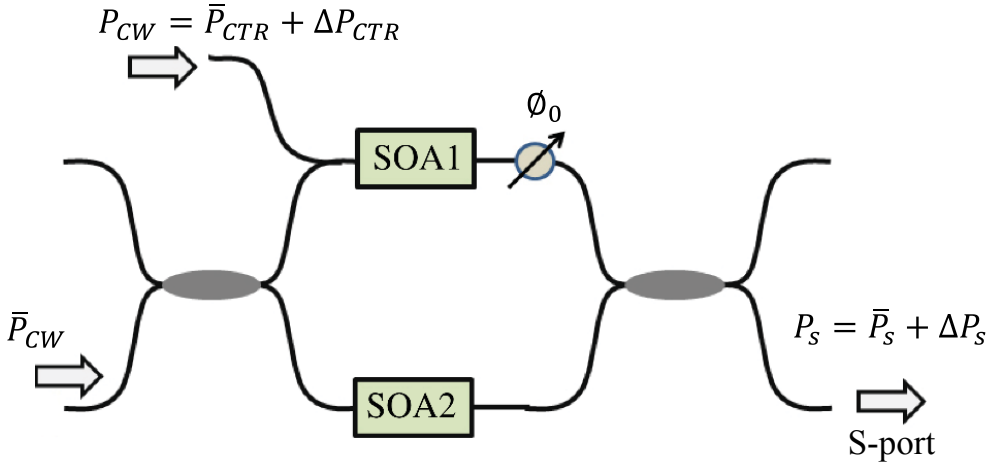

Figure 2.6: SOA-MZI configuration used to identify its frequency response [84].

Interference result in an optical power at the output S-port depending on cosine of the phase difference between the signals from both SOAs is provided by the following expression [132] [133]:

$$P_s = \frac{1}{4}\left(P_{CW,x} + P_{CW,y} - 2\sqrt{P_{CW,x}P_{CW,y}}.cos\left(\varphi_o + \phi_{CW,x} - \phi_{CW,y}\right)\right) \qquad (2.5)$$

Where $P_{CW,x}$ and $P_{CW,y}$ are respectively the optical power at the output of SOA1 and SOA2 and $\phi_{CW,x}$ and $\phi_{CW,y}$ are respectively the respective phase values along SOA1 and SOA2 obtained at the output of the x and y arms.

2.3.1 Static Characteristic of a SOA-MZI

In static regime, a CW optical signal is only injected at the SOA-MZI input. The operating point of the SOA-MZI is adjusted to obtain the minimum optical power at the SOA-MZI output. This case is called the OFF state. When a DC optical control signal is injected at the SOA-MZI input after adjusting the operating point, the output power is maximized. This situation is called the

ON state. The optical output powers are calculated in both cases to indicate the extinction ratio (ER). In OFF state, φ_o is equal to zero and the phase difference of SOAs is null. Thus, the optical output power is expressed in the equation below:

$$P_{s,OFF} = \frac{1}{4}\left(P_{CW,x,OFF} + P_{CW,y} - 2\sqrt{P_{CW,x,OFF}P_{CW,y}}\right) \quad (2.6)$$

When the optical control signal is injected at its input, $\phi_{CW,x}$ is changed and $\varphi_o + \phi_{CW,x} - \phi_{CW,y}$ is equal to π. Hence, the optical power at the output S-port in the case of ON state is given in the equation below:

$$P_{s,ON} = \frac{1}{4}\left(P_{CW,x,ON} + P_{CW,y} + 2\sqrt{P_{CW,x,ON}P_{CW,y}}\right) \quad (2.7)$$

The output power at the output of the x arm is denoted $P_{CW,x,ON}$ when the control signal is injected at the SOA-MZI input and $P_{CW,x,OFF}$ when there is no control signal at the SOA-MZI input.

The ER between the ON state and the OFF state is defined as the ratio between the maximum and the minimum optical power at the SOA-MZI output as given in the equation below:

$$ER = \frac{P_{s,ON}}{P_{s,OFF}} = \frac{P_{CW,x,ON} + P_{CW,y} + 2\sqrt{P_{CW,x,ON}P_{CW,y}}}{P_{CW,x,OFF} + P_{CW,y} - 2\sqrt{P_{CW,x,OFF}P_{CW,y}}} \quad (2.8)$$

The phase delay in each arm depends on the carrier density and the length of the SOA, so the interferometric response can be mapped out by altering the bias current to one SOA while keeping the bias current to the other fixed. We have adjusted the phase shifters and bias currents to minimize the optical power at the SOA-MZI output. This operating point leads to maximize the ER at the SOA-MZI output.

2.3.2 Dynamic Characteristic of a SOA-MZI

In this paragraph, the small signal study is based on the model developed in [84]. This permits us to evaluate the contribution of the amplitudes and phases of cross phase modulation (XPM) and cross gain modulation (XGM) effects at the SOA-MZI output.

For dynamic characteristic, an optical modulated signal is injected into SOA1. This signal modulates the carrier density of SOA1. The power and the phase characteristics of the optical signal evaluated through each SOA can be derived as presented in [84].

It is important to note that the SOA-MZI frequency response based on a frequency conversion function does not take into account any noise of the related signal degradation effects while noise is considered in the functional performance of the device. So, the ASE noise is not taken into account in the small signal equations. However, the effect of gain recovery acceleration induced by increasing ASE power levels can be incorporated by considering the ASE signal as an additional optical signal.

The conversion efficiency (η_s) at the output S-port of a SOA-MZI is defined as a ratio between the output power variation ΔP_s and input control power one ΔP_{CTR} as given in Equation (2.9).

$$\eta_s = \frac{\Delta P_s}{\Delta P_{CTR}} = \frac{1}{4}(1-\cos(\varphi_o)).$$
$$\left[\left(e^{\left(\frac{-g\mathrm{L}}{\tau_s.\left(\frac{1}{\tau_{eff}}+j\omega\right)}\right)}-1\right)-\gamma.\frac{-g}{\tau_s.\left(\frac{1}{\tau_{eff}}+j\omega\right)}\right].$$
$$\left[\left((g-\alpha_{\mathrm{int}})+\frac{-g}{\tau_s.\left(\frac{1}{\tau_{eff}}+j\omega\right)}\right)^{-1}.e^{\left(\frac{-g\mathrm{L}}{\tau_s.\left(\frac{1}{\tau_{eff}}+j\omega\right)}\right)}\right] \quad (2.9)$$

Where $\gamma = \alpha_H.\sin(\varphi_o)/(1-\cos(\varphi_o))$ is the bandwidth enhancement factor [84], α_H is Henry's factor, τ_s is the stimulated carrier recombination time, τ_{eff} is the effective carrier lifetime, and ω is an angular frequency. SOA1 and SOA2 are identical having the same parameters such as g, τ_{eff}, and L [84].

The transfer function results of a SOA-MZI are theoretically obtained based on the small signal analytical expression defined in Equation (2.9). Figure 2.7 clarifies the normalized efficiency as a function of the frequency for different total gain factors (gL) and effective carrier lifetimes (τ_{eff}). Figure 2.7(a) depicts the normalized frequency response of the SOA-MZI for $\tau_{eff} = 25$ ps. The transmission response is observed to be flat only for frequencies below 1 GHz. After that, it starts increase to reach a maximum value of 20 dB around 25 GHz when $g\mathrm{L} = 9$ that corresponds to the maximum optical gain of around 38 dB. The normalized efficiency around 25 GHz increases with gL. The SOA-MZI transfer function has the characteristic transmission of a bandpass behavior at the higher total gain factor values while it exhibits a low pass behavior at the lower gL values.

The normalized efficiency η_s of the SOA-MZI reduces towards lower frequencies when higher effective carrier lifetimes are used. This reduces the capabilities of the frequency conversion

speed. This can be emphasized by Figure 2.7(b) that illustrates the transfer function of the SOA-MZI configuration for $\tau_{eff} = 100$ ps. The frequency response also has a maximum value at the frequency lower than 10 GHz. The normalized efficiency variation between the maximum and the flat spectral region below 1 GHz is now smaller than in the case of $\tau_{eff} = 25$ ps but still approaches 10 dB when gL is equal to 9.

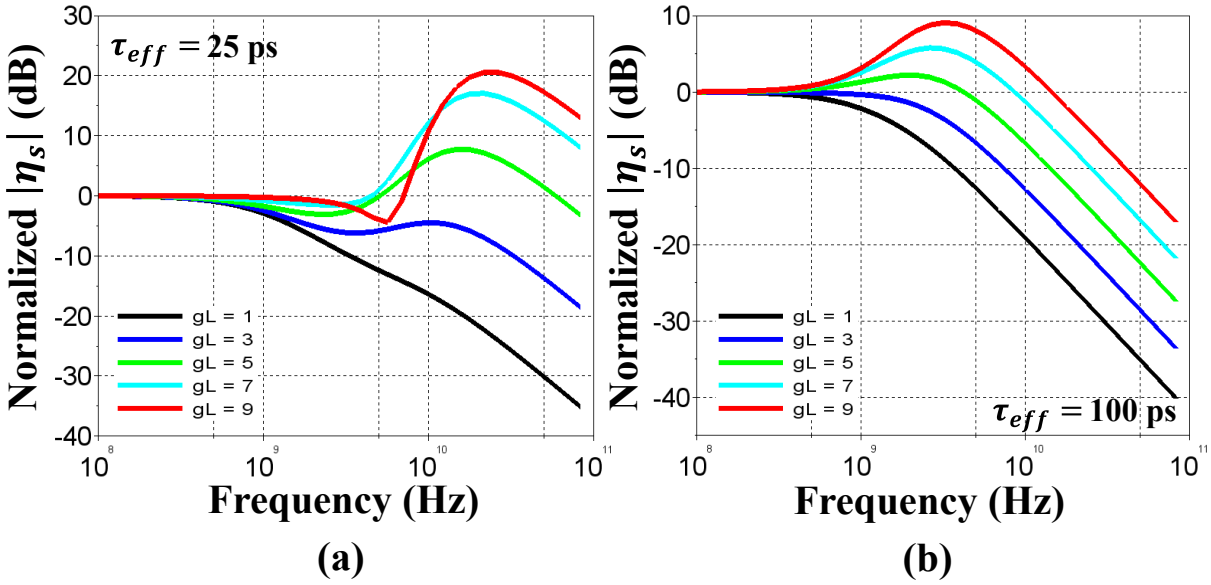

Figure 2.7: Normalized frequency response of the SOA-MZI for different effective carrier lifetimes $\tau_{eff} = 25$ ps (a) and $\tau_{eff} = 100$ ps (b) with different total gain factors.

In order to study the performance of frequency conversion based on a SOA-MZI, it is useful to define the transfer function of a SOA-MZI given in Equation (2.9) as a sum of the two terms which are the XPM and XGM terms calculated at the SOA-MZI output. This leads to investigate their individual contributions to the overall frequency response of frequency conversion. The XPM and XGM are respectively defined in Equations (2.10) and (2.11).

$$XPM = -\alpha_H . \sin(\varphi_o) . \left(\frac{-g}{\tau_s . \left(\frac{1}{\tau_{eff}} + j\omega \right)} \right) . \left((g - \alpha_{\text{int}}) + \frac{-g}{\tau_s . \left(\frac{1}{\tau_{eff}} + j\omega \right)} \right)^{-1} . e^{\left(\frac{-g\text{L}}{\tau_s . \left(\frac{1}{\tau_{eff}} + j\omega \right)} \right)} \quad (2.10)$$

$$XGM = (1 - \cos(\varphi_o)).\left(e^{\left(\frac{-gL}{\tau_S.\left(\frac{1}{\tau_{eff}} + j\omega \right)} \right)} - 1 \right) \qquad (2.11)$$

Figure 2.8 shows the XGM and XPM magnitudes and phases as a function of the frequency for different total gain factors with $\tau_{eff} = 25$ ps. The frequency conversion scheme corresponds to the SOA-MZI for a standard configuration. The transfer function has a bandpass frequency response with resonant overshooting that is mainly dictated by the contribution of the XPM term when $gL = 9$.

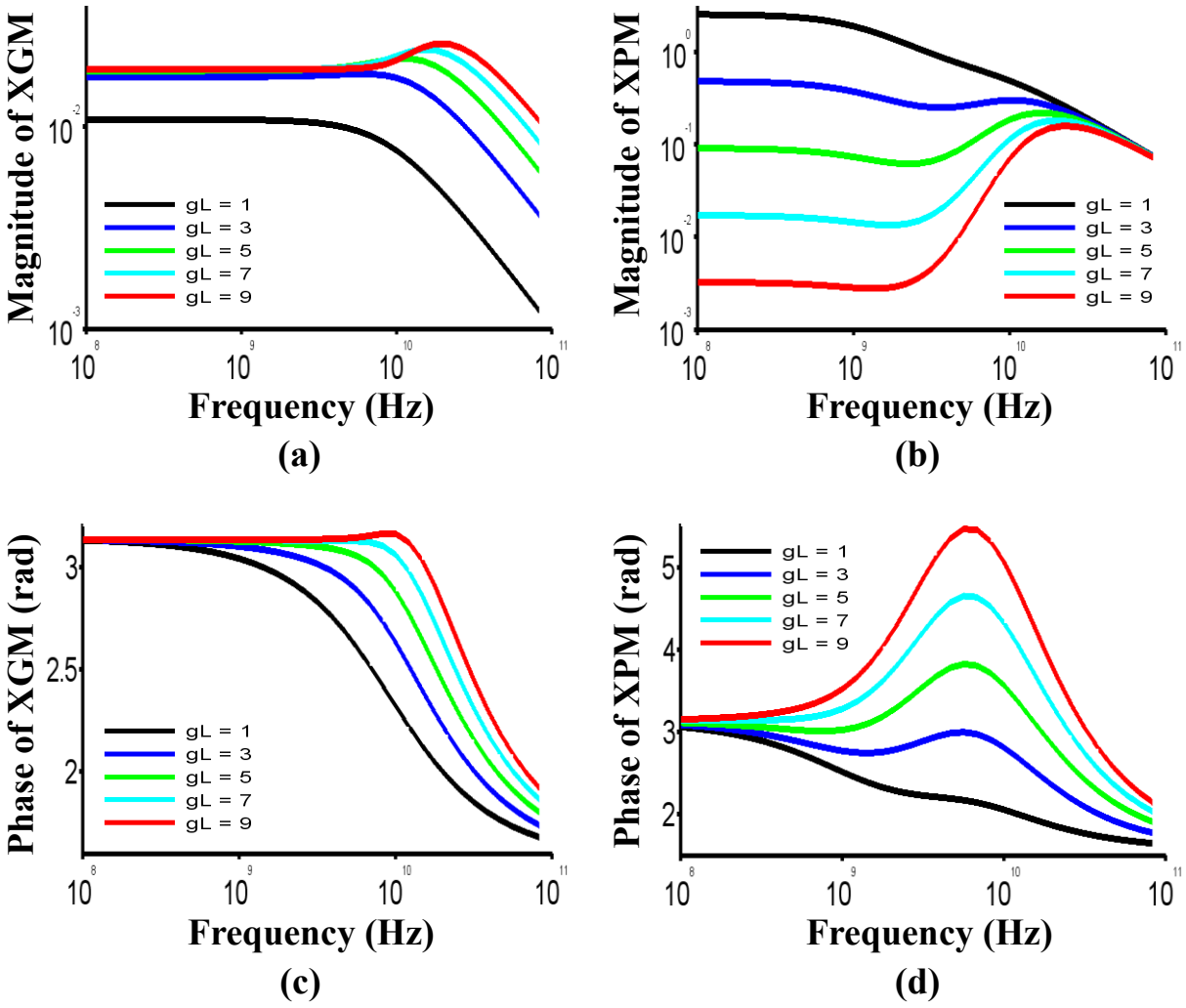

Figure 2.8: Amplitude (a) and phase (c) of the XGM and amplitude (b) and phase (d) XPM for various total gain factors with the SOA effective carrier lifetime of 25 ps.

The XPM amplitude shown in Figure 2.8(b) has the same behavior of the SOA-MZI transfer function. The resonant peak of 20 dB is around 25 GHz when $gL = 9$. This peak value decreases when gL decreases. The XPM phase has a maximum value of 5.5 rad around 5 GHz when gL is equal to 9 as observed in Figure 2.8(d). It increases with gL around 5 GHz. The value of the phase around 25 GHz is half the one around 5 GHz for all total gain factors. This adds more effect on the XPM amplitude around 25 GHz.

The effect of the XPM amplitude decreases when the total gain factor increases for frequencies below 1 GHz as displayed in Figure 2.8(b) while the effect of the XGM increases with gL as shown in Figure 2.8(a) in the same range of frequencies. The XGM and XPM phases are constant around 3 rad below 1 GHz. The phases seem to be in phase because there is no change with the total gain factor. Below 10 GHz, the magnitude of XGM is 10 dB when $gL = 9$. As a result, the XGM magnitude appears clearly when gL increases at the low frequencies and cannot be avoided. This influences on the frequency conversion based on a SOA-MZI by using XPM for a standard configuration.

The comparison between the XGM and XPM amplitudes is clearer in Figure 2.9 that shows the ratio of amplitude between the XPM and XGM versus frequency. The ratio increases with the frequency at the higher total gain factors. It has a maximum value around 25 GHz when $gL = 9$. At low frequencies, the ratio decreases with gL due to increasing the XGM amplitude effect.

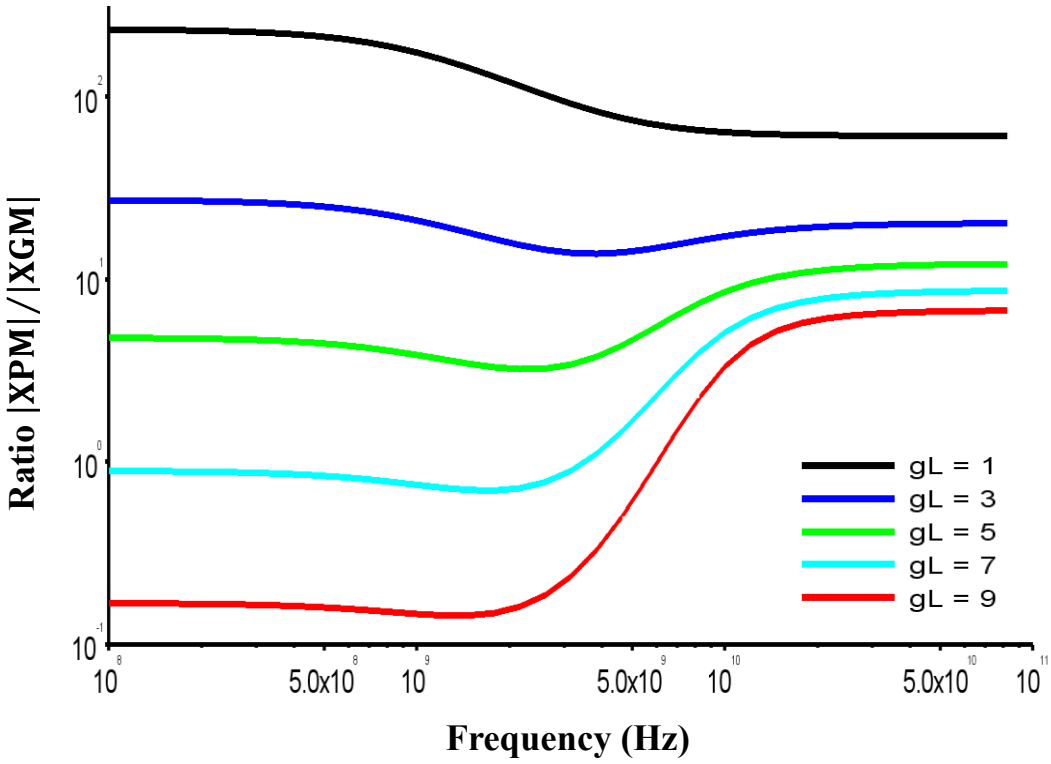

Figure 2.9: Ratio of XPM and XGM amplitudes for a number of total gain factors.

Hence, the ratio has the same behavior of the XPM amplitude with higher values due to the XGM amplitude effect. As a result, the XGM effect is very low compared to the XPM one at the frequencies higher than 5 GHz.

2.4 Experimental Characterizations of the Used SOA-MZI

The optical module used in our laboratory is an integrated hybrid device. It includes two SOA-MZIs made by the Center for Integrated Photonics (CIP) Technologies as seen in Figure 2.10. In our work, the upper SOA-MZI is used in the measurements. This SOA-MZI performs a variety of optical logic functions and can be used in optical processing applications.

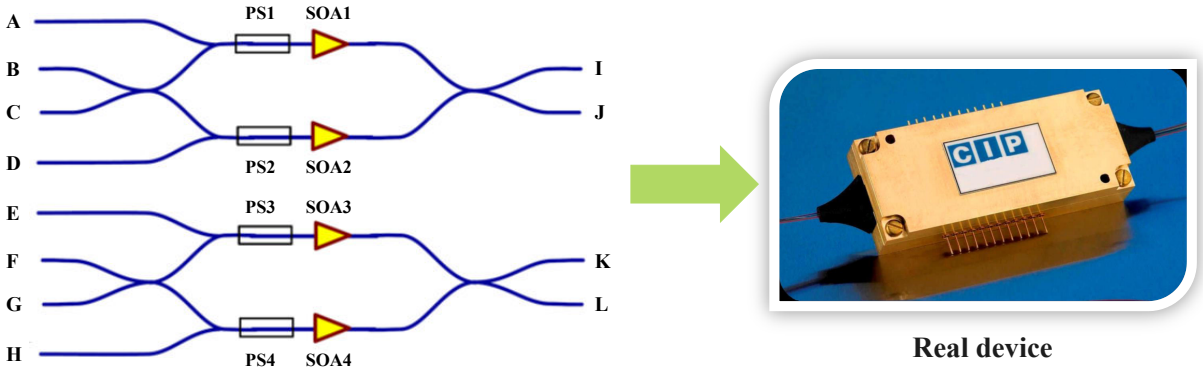

Figure 2.10: The real device defined in [134], it is used in experimental measurements includes two SOA-MZIs. PS is the phase shifter.

The module includes a Peltier cooler and a thermistor for a necessary temperature control due to the high rise in temperature during operation. The SOA-MZI contains electrical pins for SOA bias currents and phase shifters. Independent thermo-optic phase shifters are incorporated to allow precise phase control of the interferometers. The resistance of all phase shifters is approximately 100 ohms (Ω). The phase shifters are resistive heaters and should be powered from a voltage source. For stable performance, the operating temperature of the SOA-MZI must be constant.

The upper SOA-MZI is used to obtain frequency conversion to higher or lower frequencies by all-optical sampling while its static and dynamic characteristics are studied in the section below in order to choose the best operating point used in the frequency conversion techniques.

2.4.1 Static Characteristic

We have firstly studied the static characteristic for the two SOAs used in the upper SOA-MZI of the schematic seen in Figure 2.10. A continuous optical signal is injected into the SOA input, then the optical gain is measured as the input optical power is varied. The increase in the input

optical power after saturation leads to decrease the optical gain of the SOA for each wavelength injected into the SOA input as shown in Figure 2.11.

Figure 2.11 depicts the evolution of optical gain versus the optical input power (P_{in}) for different wavelengths injected into SOA1 and SOA2 inputs. The range of wavelengths is limited to the C-band. The bias current for both SOAs is 0.35 A. The optical gain of SOA1 and SOA2 is respectively 20 dB and 21 dB at the wavelength of 1560 nm. The input saturation power $P_{sat,in}$ of SOA1 and SOA2 is respectively −16.6 dBm and −17.1 dBm. The optical gain at two higher wavelengths is very close for SOA1 as seen in Figure 2.11(a).

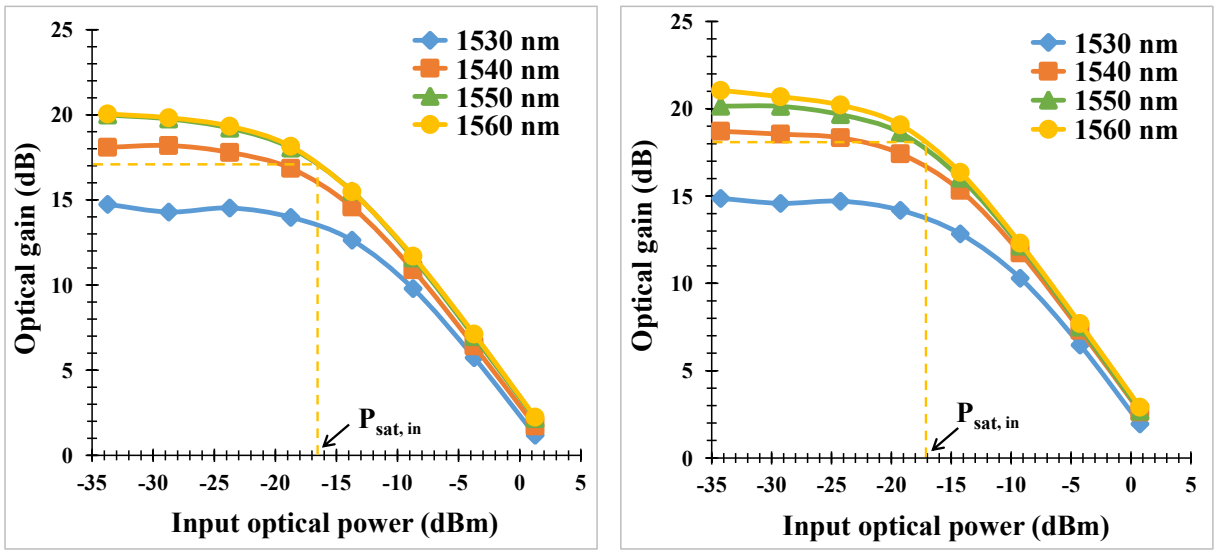

Figure 2.11: Static characteristic of SOA1 (a) and SOA2 (b) at $I_{SOA1} = 350$ mA for different wavelengths injected at their input.

Figure 2.12 shows the evolution of the optical gain as a function of the wavelength for different optical input powers. The optical gain decreases when the optical input power increases. At high input powers, the optical gain has no real effect with the wavelength.

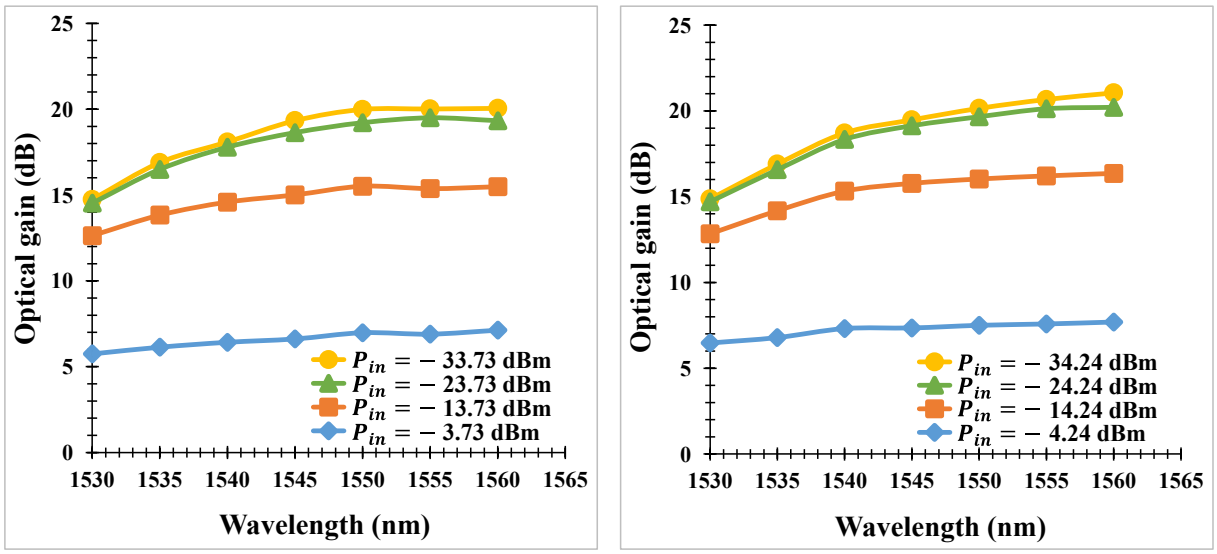

Figure 2.12: Static characteristic of SOA1 (a) and SOA2 (a) for different input optical powers applied at their input at the bias current of 350 mA for both SOAs.

The noise figure (NF) of SOA1 and SOA2 is measured as a function of the input optical power at the wavelength of 1545 nm and with the bias current $I_b = 350$ mA as seen in Figure 2.13.

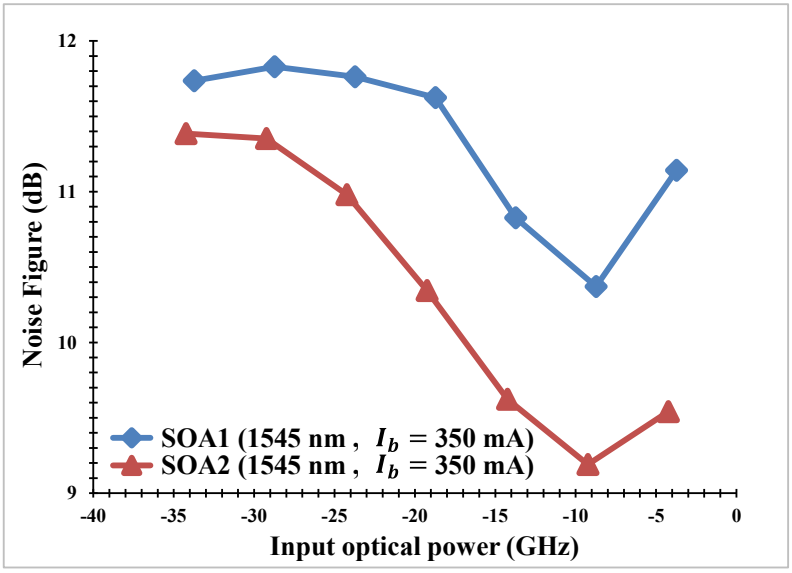

Figure 2.13: Noise figure of SOA1 and SOA2 versus the input optical power at $I_b = 350$ mA with the wavelength of 1545 nm.

The efficiency of the switching function provided by the SOA-MZI is given by the ratio of the power between the ON and OFF states. They correspond respectively to a high and a low

transmission of the injected optical power at the input port (C) to the output port (J) according to the optical power injected at the input port (A). The experimental setup used to measure the static characteristic of the SOA-MZI is shown in Figure 2.14.

The nominal operating point is chosen to obtain an OFF state which is as follow: the bias currents of SOA1 and SOA2 I_{SOA1} and I_{SOA2} are respectively biased at 350 mA and 280 mA and the phase shifters φ_1 and φ_2 are tuned in order to obtain the minimum optical power at the output port (J) when the command signal at the input port (A) is null. I_{SOA1} is chosen at 350 mA while I_{SOA2} is changed to obtain the minimum optical power at the SOA-MZI output. Moreover, the phase shifters φ_1 and φ_2 are adjusted at the same time with I_{SOA2}. At $I_{SOA2} =$ 280 mA, the lowest minimum power at the output port (J) is achieved. The operating point has been chosen to maximize the ER on the output port (J).

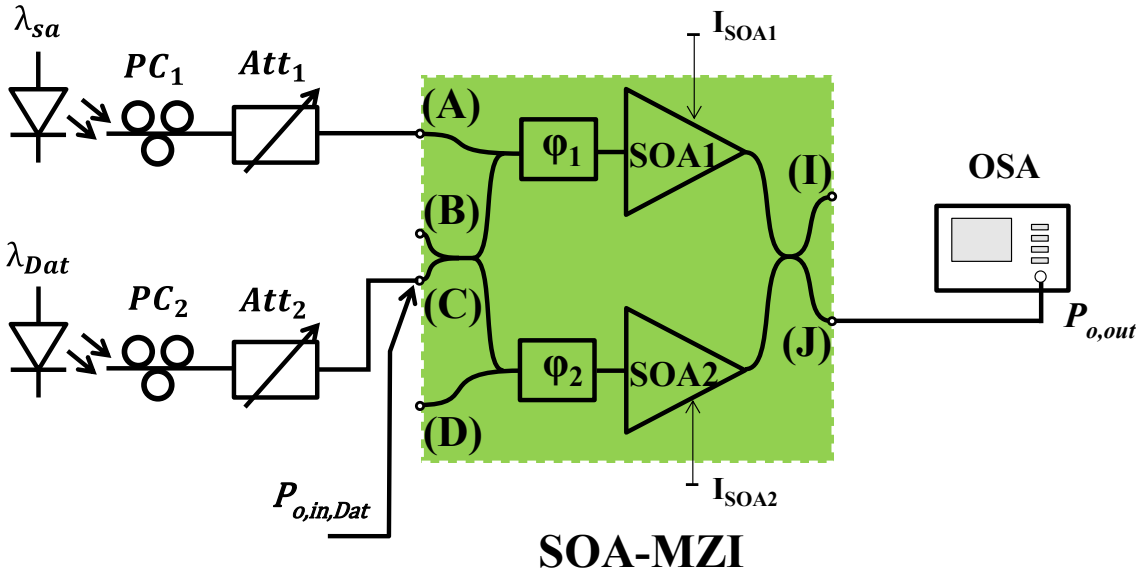

Figure 2.14: Static experimental setup of the used SOA-MZI. SOA: Semiconductor Optical Amplifier, PC: Polarization Controller, Att: Attenuator, φ: Phase Shifter, and OSA: Optical Spectrum Analyzer.

The CW probe signal which is the data signal having a mean optical power of $P_{o,in,Dat} = -10$ dBm at the wavelength $\lambda_{Dat} = 1545$ nm is injected into the input port (C). The transmitted power at the output port (J) depends on the optical power of the pump signal which is the sampling signal applied to the input port (A). The wavelength of the pump signal called the sampling wavelength λ_{sa} is 1550 nm. Figure 2.15 shows the static characteristic of the SOA-MZI with a maximum ER = 23 dB. The maximum transmitted power of the data signal at the SOA-MZI output is achieved at the optical power at the input port (A) equal to -5 dBm.

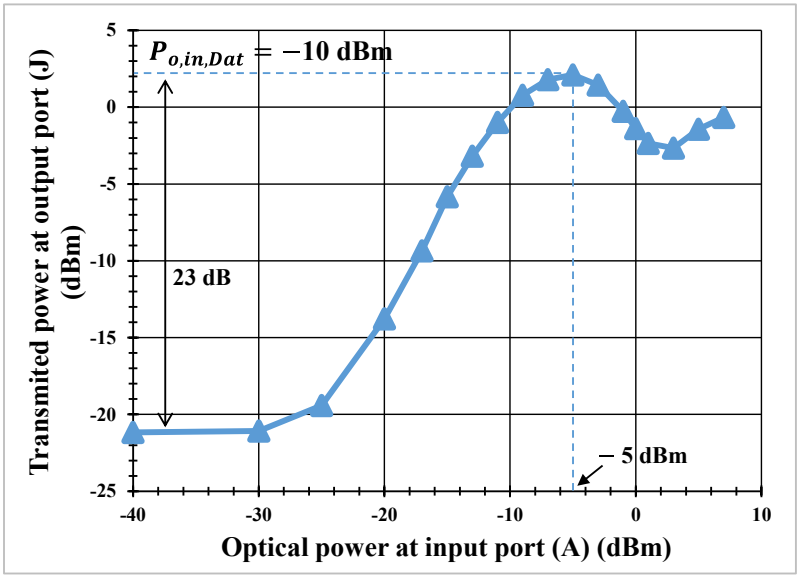

Figure 2.15: Static characteristic of the SOA-MZI used as an optical sampling device at the output port (J) with ER = 23 dB. The wavelength of data $\lambda_{Dat} = 1545$ nm.

Figure 2.16 displays the transmitted power and the ER at the output port (J) as a function of the optical power at the input port (A) for several optical powers injected at the input port (C). The increase in powers at the input port (C) from −20 dBm to −5 dBm leads to increase the maximum transmitted power at the output port (J) as shown in Figure 2.16(a).

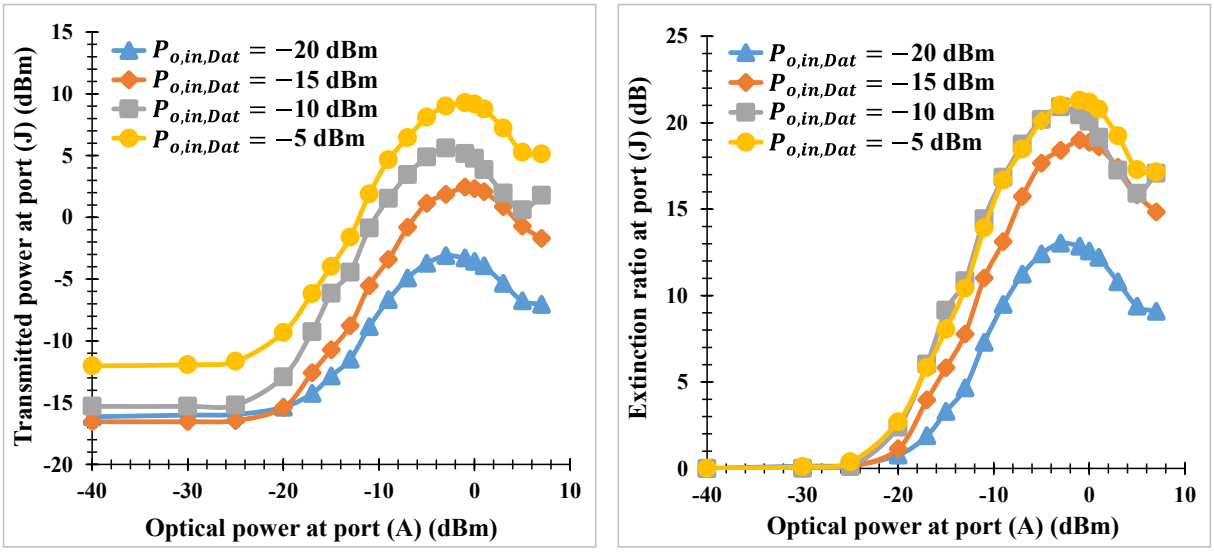

Figure 2.16: Static characteristic (a) and extinction ratio (b) on the output port (J) for different optical powers.

We have adjusted the operating point of the SOA-MZI at each data optical power injected at the input port (C) with a null control optical power injected at the input port (A). The increase in the optical data powers also leads to maximize the ER on the output port (J) as shown in Figure 2.16(b). The highest maximum of the ER at the output port (J) is 21.3 dB at the optical power of −1 dBm at the input port (A) with the optical power of −5 dBm at the input port (C). The tuning of phase shifters of the SOA-MZI is not in the same condition in Figure 2.15 and Figure 2.16 because they have not been measured at the same time.

Figure 2.17 represents the transmitted power (a) and the ER (b) at the output port (J) as a function of the optical input power and different wavelengths at the input port (A). The change in the sampling wavelengths from $\lambda_{sa} = 1560$ nm to $\lambda_{sa} = 1530$ nm leads to shift and increase the maximum transmitted power at the output port (J) as observed in Figure 2.17(a).

The alteration in the sampling wavelengths at the input port (A) also leads to maximize the ER at the output port (J) as shown in Figure 2.17(b). The highest maximum of ER at the output port (J) is 23.9 dB at the optical power of 5 dBm at the input port (A) with the wavelength equal to 1530 nm injected into the input port (A). As a result, the ER is maximized when the wavelength decreases.

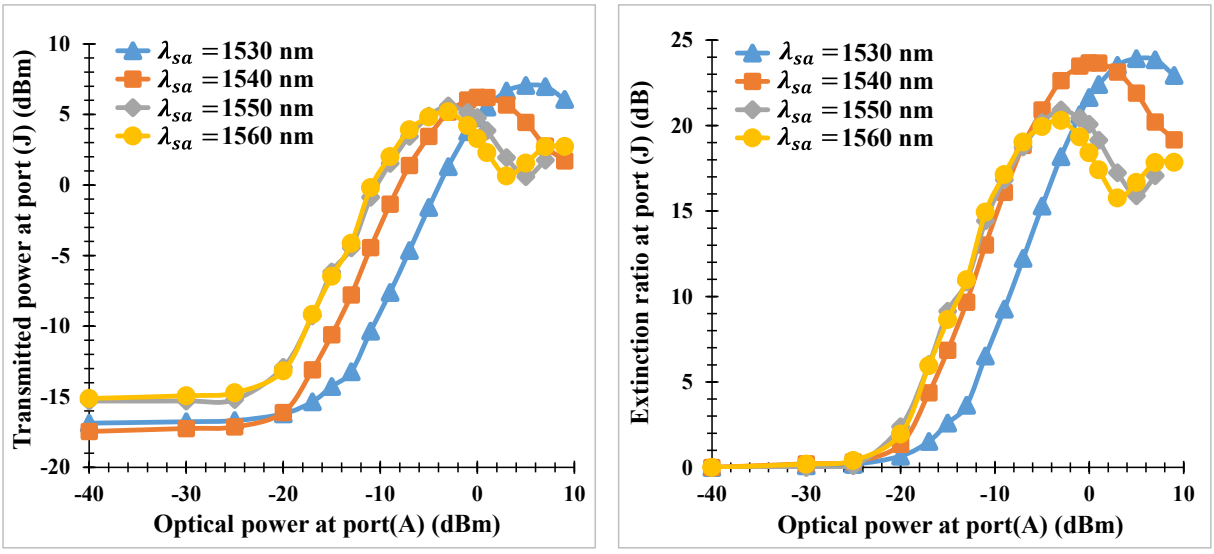

Figure 2.17: Static characteristic (a) and extinction ratio (b) on the output port (J) for different wavelengths.

We have measured the maximum ER, the transmitted power, and the minimum power at the output port (J) as a function of a data power introduced at the input port (C) as depicted in Figure 2.18. The operating point of the SOA-MZI have been adjusted one time at the data power

of −10 dBm at the input port (C) with a null control power at the input port (A) to obtain the minimum power at the output port (J).

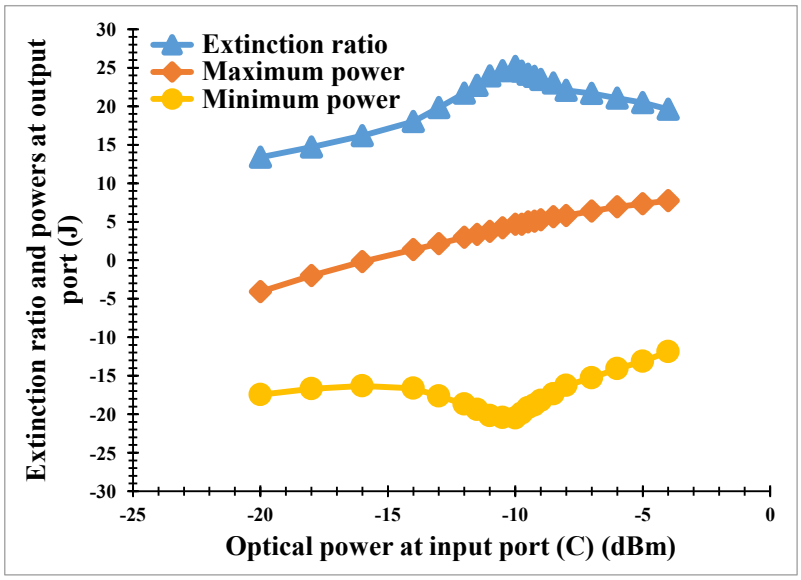

Figure 2.18: Maximum extinction ratio, maximum power, and minimum power at the output port (J).

The change of the data power leads to a change the operating point, which, in turns, leads to increase the minimum power at the output port (J), particularly at high data powers. The maximum transmitted power at the input port (J) increases with the data power at the input port (C). The maximum ER corresponds to the data power equal to −10 dBm, as shown in Figure 2.18, for which the operating point of the SOA-MZI has been adjusted.

The ER degrades for the other data powers due to increasing the maximum transmitted power and the minimum power at the output port (J). The degradation of ER at the high data powers between −10 dBm and −4 dBm is 5.5 dB because the SOA gain saturates, this degradation is lower the one of 11.8 dB at the low data powers between −20 dBm and −10 dBm. This explains the different shapes of degradation of ER at high and low input powers.

2.4.2 Dynamic Characteristic

The dynamic characteristic of the SOA-MZI have been measured by using the experimental setup shown in Figure 2.19. The optical mean power at the input port (C) $P_{o,in,Dat}$ is −10 dBm with the wavelength $\lambda_{Dat} = 1545$ nm. The modulated control signal is injected to the input port (A) with the wavelength $\lambda_{sa} = 1550$ nm. The optical attenuator Att_1 is adjusted in order that the SOA-MZI works in the linear region of its transmission shown in Figure 2.15. The optical

filter tuned at $\lambda_{Dat} = 1545$ nm at the SOA-MZI output is used to remove the control signal and the amplified spontaneous emission (ASE).

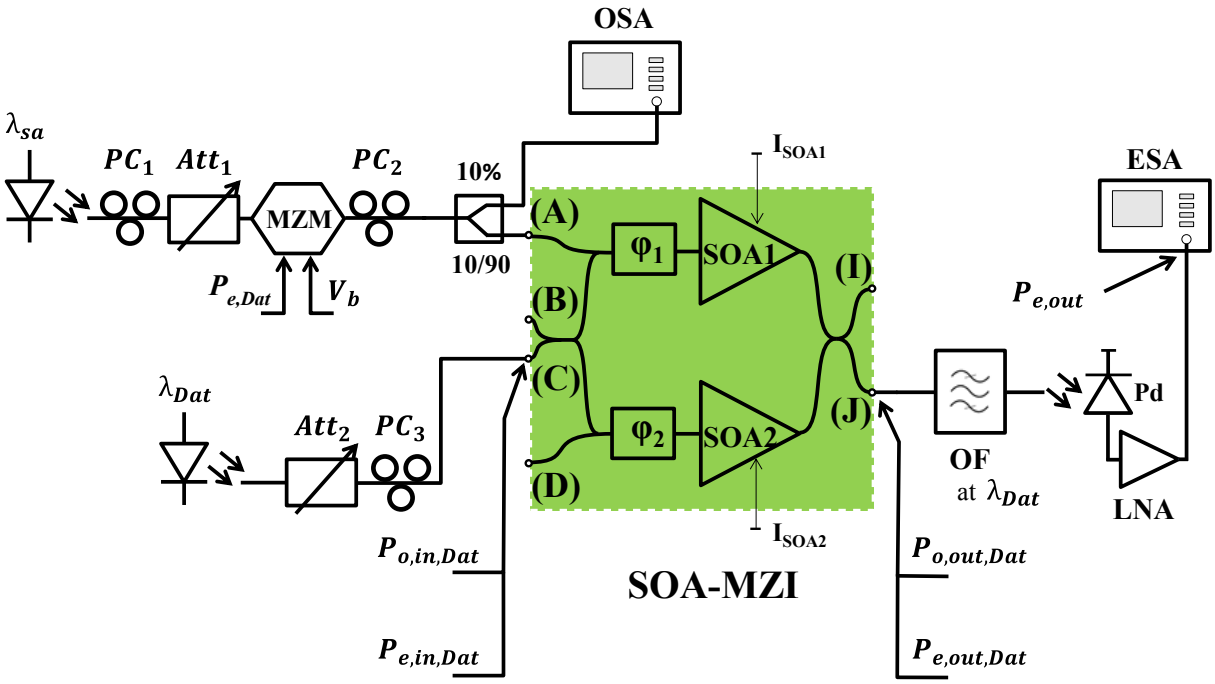

Figure 2.19: Dynamic experimental setup of the SOA-MZI. Att: Attenuator, PC: Polarization Controller, MZM: Mach-Zehnder Modulator, Pd: Photodiode, LNA: Low-Noise Amplifier, OF: Optical Filter, ESA: Electrical Spectrum Analyzer, OSA: Optical Spectrum Analyzer, φ: Phase Shifter, and V_b: Bias Voltage.

The SOA-MZI acts as an optical modulator leading to a modulated optical signal at the output port (J). The dynamic behavior of the SOA-MZI depends on the carrier lifetime (τ_c) and the stimulated carrier recombination time (τ_s). According to the used SOAs, the corresponding effective carrier lifetime ($1/\tau_{eff} = 1/\tau_s + 1/\tau_c$) ranges from few tens ps to few hundreds ps [84]. In order to improve its dynamic behavior, a SOA must be biased with a high bias current and high optical powers must be injected at its input. It is mainly true for SOA1 which gain is periodically saturated by the optical control signal. In this measurement, the bias current of SOA1 $I_{SOA1} = 350$ mA is close to the maximum allowed bias current of 400 mA.

The dynamic characteristic of the used SOA-MZI is displayed in Figure 2.20 that represents the normalized frequency response of the electrical output power.

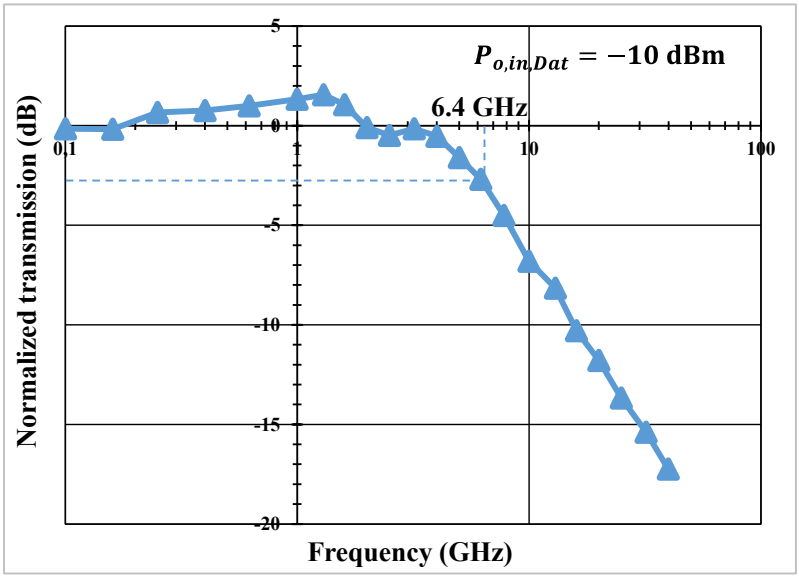

Figure 2.20: Dynamic characteristic of the SOA-MZI with the bandwidth of 6.4 GHz.

The frequency response presents a low pass behavior due to the dynamics of the carrier density of the SOA with a 6.4 GHz bandwidth at -3 dB from the maximum value of the normalized transmission.

2.5 Conclusion

The architecture of a SOA-MZI used as an optical switch and its function were presented. We have studied the characteristics of a SOA and its nonlinearities. The theoretical performance analysis of the static and dynamic behavior for the architectural standard configuration SOA-MZI scheme is presented. Despite of the frequency conversion is based on XPM effects, the XGM always exists particularly at low frequencies. Static and dynamic characteristics of the used SOA-MZI are experimentally measured. We show that the measured extinction ratio (ER) can attain 23 dB when the SOA-MZI is used an optical switch. The measured frequency response of SOA-MZI shows a low-pass behavior with a 6.4 GHz cutoff frequency. Due to the frequency response of the interferometer structure, this bandwidth is higher than the one of a single SOA.

Chapter Three

All-Optical Sampling Mixing Based on a SOA-MZI

3.1 Principle of All-Optical Mixing Based on a SOA-MZI

This chapter concerns the experimental framework to achieve frequency conversion by all optical sampling methods by using a SOA-MZI. We present in this chapter a comprehensive analysis of a SOA-MZI standard configuration.

The principle of the SOA-MZI standard configuration is shown in Figure 3.1. A data signal is injected into the two arms of the SOA-MZI, while a clock signal from an optical pulse source is injected in the SOA-MZI upper arm. In absence of this pulse signal, the SOA-MZI is configured to be in the OFF state for the data signal at the SOA-MZI output. It will be switched to the ON state due to the modification of the phase condition consequently to the presence of the clock pulse in the upper arm of the SOA-MZI. Thereby, the data signal will be sampled at the SOA-MZI output and a replica of its spectrum will be obtained which permits to have frequency up-conversion or frequency down-conversion.

In our work, the used clock pulse repetition rate is fixed, as a function of the number of the data spectrum replica in order to achieve up-conversion and down-conversion for IF/RF signals in the maximum range of 40 GHz. This chosen frequency is fixed by the measurements facilities. It corresponds to the bandwidth of the electrical spectrum analyzer (ESA) and the maximum frequency of the wave signal generator used in the laboratory.

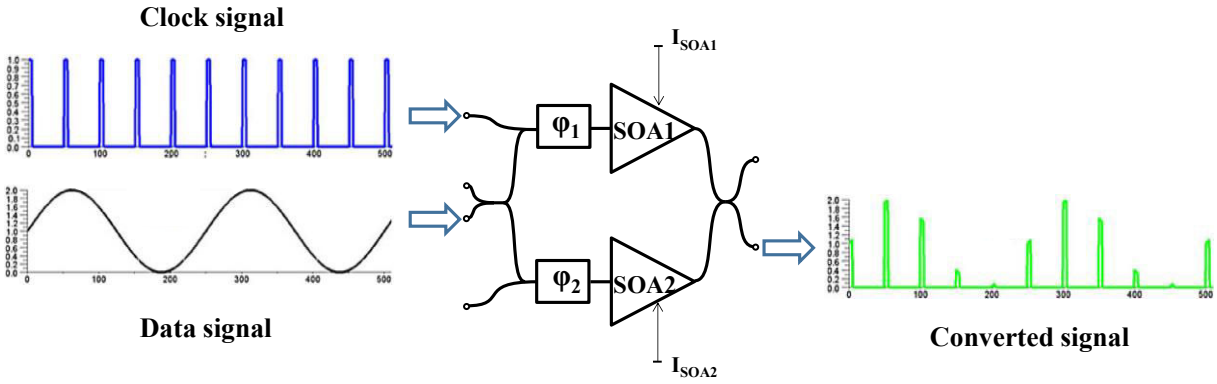

Figure 3.1: Principle of the SOA-MZI standard configuration scheme based on sampling.

The up-conversion and down-conversion are performed respectively at a frequency up to 39.5 GHz and down to 0.5 GHz by fixing the repetition frequency rate f_{sa} of the optical pulse source (OPS) to 7.8 GHz to be able to make measurements up to the fifth harmonic which corresponds to the harmonic rank equal to 5. Other repetition frequencies of the OPS are also used at 9.75 GHz, 13 GHz, and 19.5 GHz. The harmonic rank decreases from 5 at 7.8 GHz to 2 at 19.5 GHz.

In this chapter, we will present first the experimental setup. The efficiency of the frequency conversion is then evaluated through the conversion gain, the third input intercept point, and isolation for up-conversion and down-conversion.

Finally, up-converted and down-converted QPSK and QPSK-OFDM signals are realized. The quality of frequency conversion is evaluated for these two signals through the error vector magnitude (EVM) and the signal to noise ratio (SNR) for different bit rates and frequency shifts.

3.2 Mixer Characteristics

3.2.1 Experimental Setup of the All-Optical Mixer Characterization

The experimental setup of the all-optical sampling mixer based on the SOA-MZI standard configuration used for frequency up-conversion and frequency down-conversion techniques is shown in Figure 3.2. A continuous wave (CW) signal at the wavelength $\lambda_{Dat} = 1545$ nm is intensity-modulated by an optical Mach-Zehnder modulator (MZM) driven by an electrical subcarrier that can carry data at a frequency f_{Dat}. This electrical subcarrier is at an intermediate frequency (IF) for up-conversion and a radiofrequency (RF) for down-conversion. The MZM is biased in its linear region. The electrical bandwidth of this MZM is 6 GHz and it must have low modulation index (M_I) to avoid its nonlinearities, see Appendix A. The first polarization controller (PC_1) is used to adjust the operating point of the optical MZM. The power of the CW signal can be changed by the second optical attenuator Att_2 before being applied through the second polarization controller (PC_2) at the output of the MZM to the common inputs of the upper and lower arms of the SOA-MZI (port (C)).

The optical pulse source from Pritel is called the ultrafast optical clock (UOC). It plays the role of a sampling or clock signal. It generates optical pulses at the wavelength $\lambda_{sa} = 1550$ nm with a repetition frequency rate f_{sa} and with a pulse width of 10 ps. This sampling signal is applied via the optical attenuator Att_1 to control its power before being injected into the upper arm of the SOA-MZI (input port (A)) where it is used to sample the IF/RF signal. The stability of the clock signal is monitored on an optical spectrum analyzer (OSA).

The output port (J) of the SOA-MZI is used as an output of the mixer. At this output, the optical signal at λ_{Dat} is filtered by an optical filter (OF) that has 3 dB losses. The OF not only rejects the sampling signal but also reduces the amplified spontaneous emission (ASE) from both SOAs. The filtered signal is photo-detected by a 70 GHz photodiode (Pd) having a responsively of 0.68 A/W and amplified by a 33 dB low noise amplifier (LNA) before being displayed on an electrical spectrum analyzer (ESA) to measure its electrical powers at different frequencies. The electrical power of the output signal denoted $P_{e,out,Dat}$ at the output of the SOA-MZI is calculated from the corresponding electrical power of the same signal measured on an ESA by taking into account the losses of the optical filter.

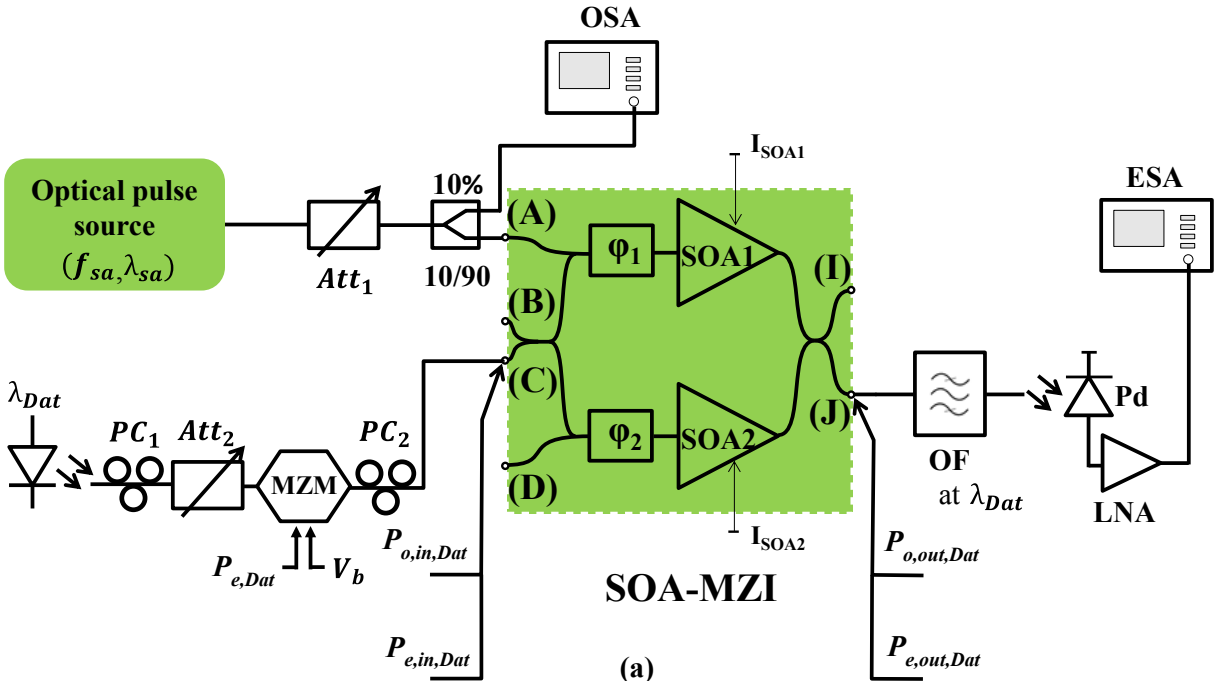

(b)

Figure 3.2: Experimental setup of the frequency conversion technique (a) and a photo of the experimental bench of the frequency conversion technique (b). PC: Polarization Controller, MZM: Mach-Zehnder Modulator, Att: Attenuator, Pd: Photodiode, LNA: Low-Noise Amplifier, OF: Optical Filter, ESA: Electrical Spectrum Analyzer, OPS: Optical Pulse Source, OC: Optical Coupler, OSA: Optical Spectrum Analyzer, φ: Phase shifter, and V_b: Bias Voltage.

3.2.2 Optical Pulse Source Characteristics and Its Influence on the Data Signal at the SOA-MZI Output

The optical pulse source contains a mode locked fiber laser [135] [136]. It requires an external RF generator that operates from 1 GHz to 20 GHz with RF output powers up to a maximum of 0 dBm. The experimental setup and the function of the used optical pulse source are explained

in [136]. 10 ps width optical pulses can be obtained [136] with a power of the central mode of −4.4 dBm at the sampling wavelength $\lambda_{sa} = 1550$ nm as shown in Figure 3.3.

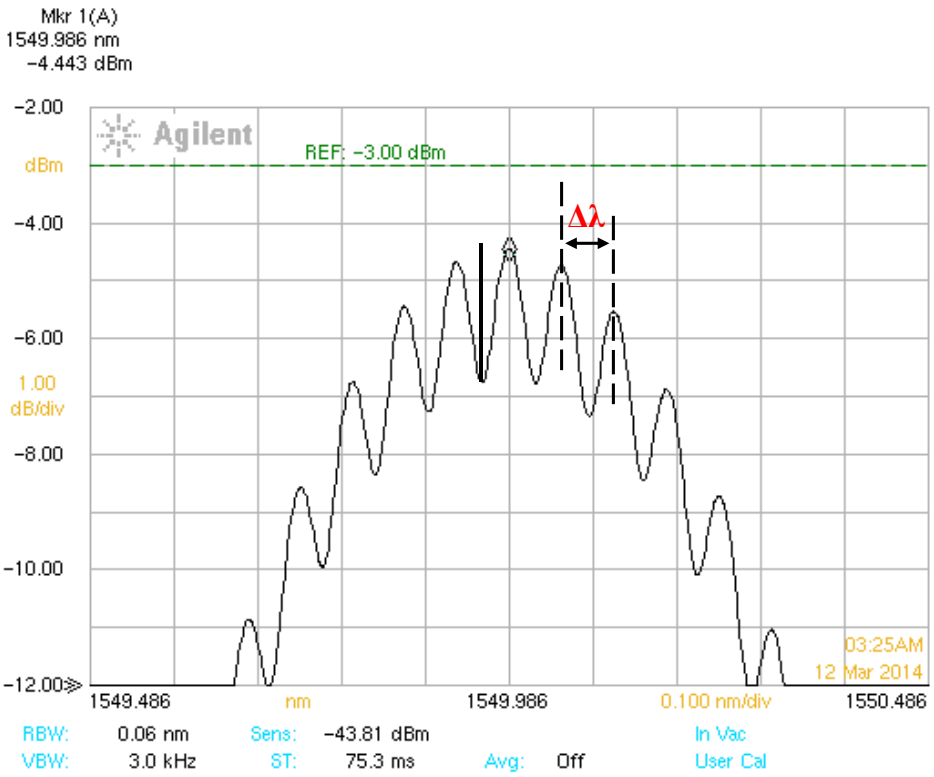

Figure 3.3: Optical spectrum of the optical pulse source with a repetition rate of 7.8 GHz.

In Figure 3.3, the difference between two modes is called delta wavelength (Δλ) equal to 62.5 pm corresponds to the repetition frequency $f_{sa} = 7.8$ GHz as defined in the equation below:

$$f_{sa} = \frac{c}{\lambda_{sa}^2}.\Delta\lambda \tag{3.1}$$

Where c is the speed of light which is approximately equal to 3×10^8 m/s.

The electrical spectrum of the optical pulse source after photo-detection is shown in Figure 3.4. The repetition rate f_{sa} and the duty cycle (α) of optical pulses are respectively 7.8 GHz and 7.8 %. The harmonics at frequencies nf_{sa} are denoted H_n, where n is an integer. The α is calculated in Equation (1.21).

The electrical power of the harmonics of the sampling signal measured on an ESA decreases with the frequency as displayed in Figure 3.4. Both the pulse shape and the duty cycle of the sampling signal and the bandwidth of the photodiode and low noise amplifier have an impact on its harmonics that have different power levels. The difference between the power of the fifth

harmonic H_5 of the sampling signal at the frequency of 39 GHz and the power of first one H_1 at 7.8 GHz of the used optical pulse source is about 6.1 dB.

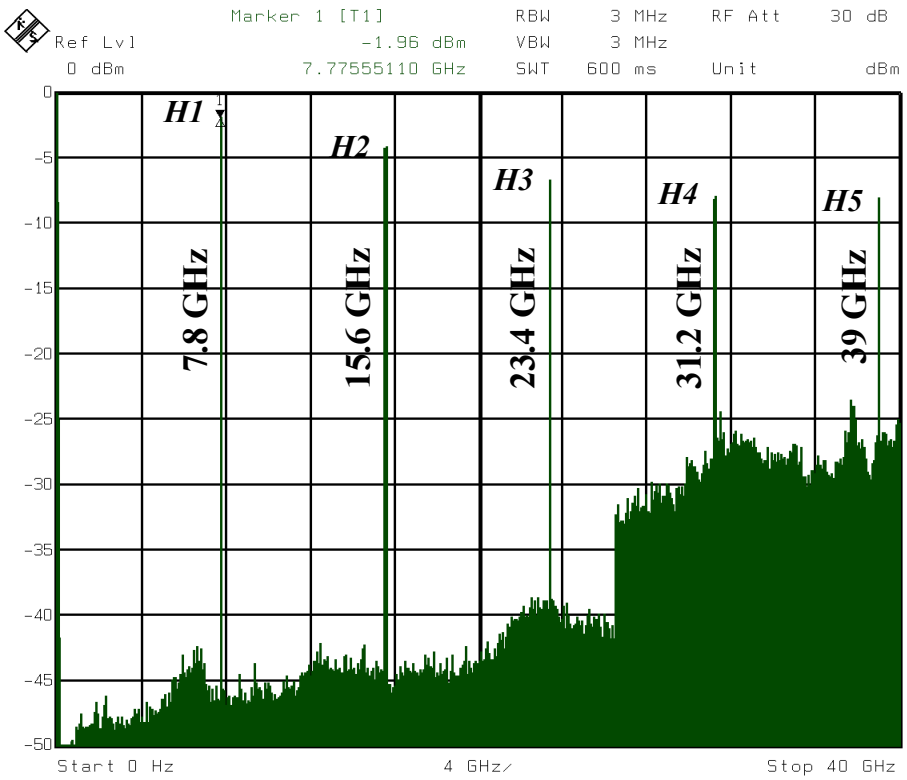

Figure 3.4: First five harmonics of the electrical spectrum of the optical pulse source at a repetition rate of 7.8 GHz measured on an ESA.

In the time domain, the peak power of the optical pulses is estimated from their average power and duty cycle as defined in Equation (3.2) which is about 6.7 dBm. Equation (3.2) represents the peak power of the pulse width modulation (PWM) pulses.

$$P_{peak} = \frac{P_{av}}{\alpha} \tag{3.2}$$

Where P_{av} is the average optical power and α is the duty cycle defined in Equation (1.21).

The characteristics of different repetition rates of 9.75 GHz, 13 GHz, and 19.5 GHz that are used in this work are presented in Table 2. The difference between the harmonic at a frequency of 39 GHz and the one at f_{sa} of the optical pulse source decreases when the sampling frequency increases with 10 ps pulse width. The power of the harmonic at 39 GHz is improved by increasing the sampling frequency as shown in Table 2.

In fact, increasing f_{sa} in the range from 7.8 GHz to 19.5 GHz leads to increase the duty cycle from 7.8 % to 19.5 %. Therefore, the power level of high order harmonics P_{H_n} at the frequency of 39 GHz will be more attenuated than the fundamental one P_{H_1} at f_{sa} but by decreasing the rank of harmonics at 39 GHz which is H_5 for $f_{sa} = 7.8$ GHz, H_4 for $f_{sa} = 9.75$ GHz, H_3 for $f_{sa} = 13$ GHz, and H_2 for $f_{sa} = 19.5$ GHz the difference $P_{H_1} - P_{H_n}$ remains improved.

Table 2: Difference between the first harmonic at f_{sa} and the one at 39 GHz at the port (A).

f_{sa} (GHz)	Peak power (dBm)	Electrical power at 39 GHz (P_{H_n}(dBm))	P_{H_1} (dBm) at $f_{sa} - P_{H_n}$ (dBm) at 39 GHz
7.8	6.7	-8.1 ($H_n = H_5$)	6.1 dB
9.75	5.7	-6.7 ($H_n = H_4$)	4.9 dB
13	4.8	-5.7 ($H_n = H_3$)	3.8 dB
19.5	3.6	-3.5 ($H_n = H_2$)	1.5 dB

3.2.2.1 Optical Pulse Signal Response at the SOA-MZI Output

We use a continuous wave (CW) power of -10 dBm for the data signal injected at the common input port of the two arms of the SOA-MZI. The wavelength of the OF tuned at $\lambda_{sa} = 1550$ nm corresponds to the wavelength of the optical pulse source. Figure 3.5 represents the electrical spectrum of optical amplification of the clock signal in the upper arm of the SOA-MZI. The harmonics of the pulse signal are amplified compared its harmonics at the input port (A). The difference between the harmonics is close at high frequencies as shown in Table 3.

Table 3: Amplification of the OPS harmonics at the SOA-MZI output at λ_{sa}.

	Amplification in dB of the optical pulse source harmonics at the SOA-MZI output after filtering
H_n (GHz)	$\lambda_{sa} = 1550$ nm
7.8	5
15.6	2.5
23.4	2.1
31.2	1.9
39	1.7

The gain at f_{sa} = 7.8 GHz is the higher one due to its frequency which is close to the limited frequency of the used SOA-MZI as seen in Table 3.

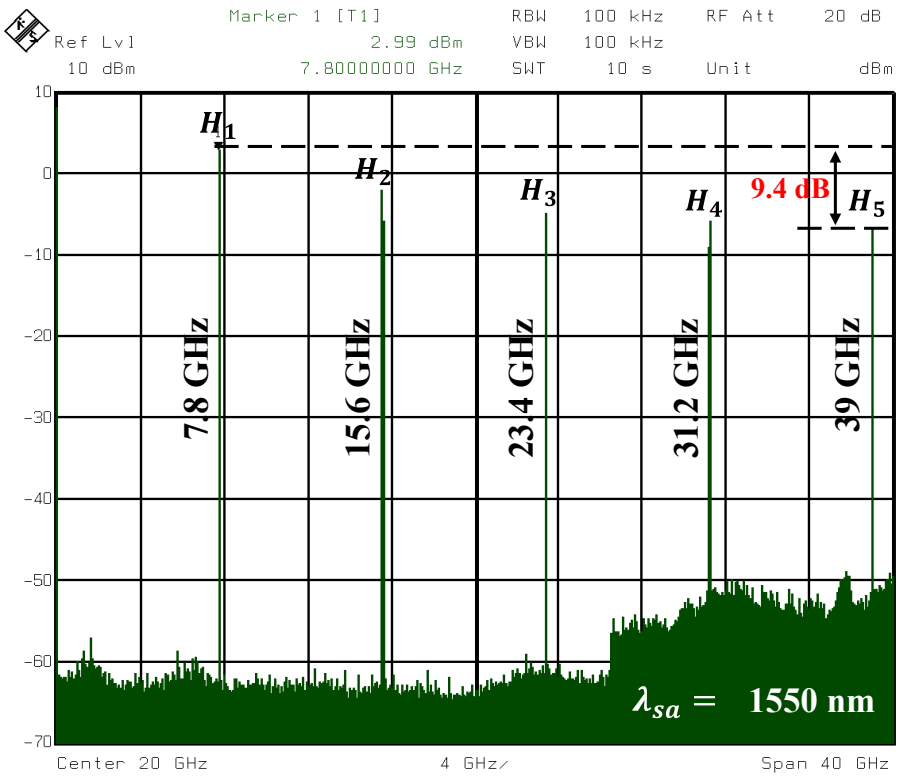

Figure 3.5: Sampling signal at the output port (J) of the SOA-MZI after being filtered at 1550 nm, photo-detected, amplified, and displayed on an ESA.

The pulse signal is studied for different repetition rates from 7.8 GHz to 19.5 GHz. The harmonic at 39 GHz at the SOA-MZI output increases with the repetition rate as well as the one at the SOA-MZI input (port (A)). The leads to increase the gain as shown in Table 4.

Table 4: Electrical power of the harmonic of the pulse signal at 39 GHz measured on an ESA for different repetition rates at the SOA-MZI output after filtering at 1550 nm.

	Electrical powers of the harmonic at 39 GHz (dBm)		
	Input port (A)	Output port (J) after filtering	Gain (dB)
f_{sa}(GHz)	λ_{sa} = 1550 nm	λ_{sa} = 1550 nm	
7.8	-8.1	-6.4	1.7
9.75	-6.7	-3.4	3.3
13	-5.7	0.2	5.9
19.5	-3.5	3.4	6.9

3.2.2.2 Optical Data Signal at the Output Port of the SOA-MZI

The data signal is injected at the common input of the SOA-MZI. It average power is −10 dBm. The optical filter (OF) is tuned at λ_{Dat} =1545 nm. The optical mean power of the sampled signal at the output port (J) is −2.9 dBm after filtering. The clock signal transposed at λ_{Dat} as depicted in Figure 3.6 shows that the transposition efficiency is lower for the harmonics at the high frequencies.

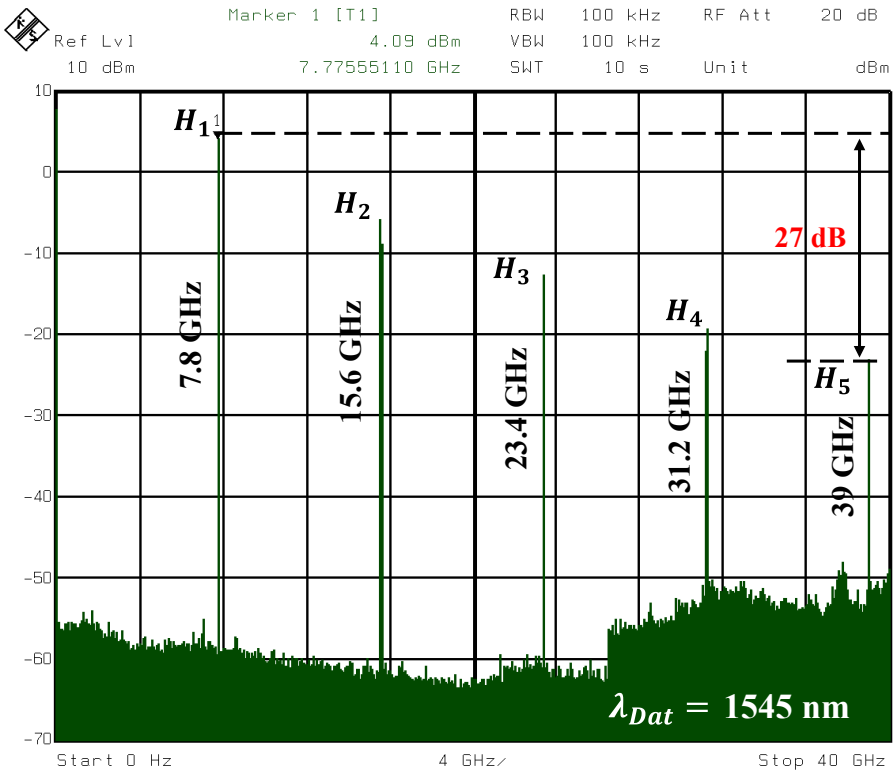

Figure 3.6: Sampled signal at the output port (J) of the SOA-MZI after being filtered at the wavelength of data of 1545 nm, photo-detected, amplified, and displayed on an ESA.

The difference between the power of fifth harmonic H_5 P_{H_5} and the power of first one H_1 P_{H_1} at the output port (J) after filtering is 27 dB. This result is due to the low pass behavior of the SOA-MZI in the XPM effect that was shown in Figure 2.20.

By increasing the repetition frequencies rate of the optical pulse source, the gain increases as dissected in Table 5. The difference of the harmonic at 39 GHz between the high and the low repetition frequencies is 11.1 dB at λ_{dat}.

Table 5: Electrical powers of the harmonic at 39 GHz and its gain at the SOA-MZI output.

	Electrical powers of the harmonic at 39 GHz (dBm)		
	Input port (A)	Output port (J) after filtering	Gain (dB)
f_{sa}(GHz)	$\lambda_{sa} = 1550$ nm	$\lambda_{Dat} = 1545$ nm	
7.8	-8.1	-24.8	-16.7
9.75	-6.7	-21.9	-15.2
13	-5.7	-17.5	-11.8
19.5	-3.5	-13.7	-10.2

3.2.3 Frequency Up and Down-Conversion Experimental Spectrums with an IF/RF Sinusoidal Signal

In order to show the frequency up-conversion signal spectrum, we have modulated an optical carrier at the wavelength $\lambda_{Dat} = 1545$ nm by a sinewave data signal at the frequency $f_{Dat} = 0.5$ GHz. The average optical power $P_{o,in,Dat}$ at the common input of the two arms of the SOA-MZI (input port (C)) is -10 dBm and the electrical modulation power $P_{e,in,Dat}$ carried by the optical signal is -32.4 dBm as displayed in Figure 3.7.

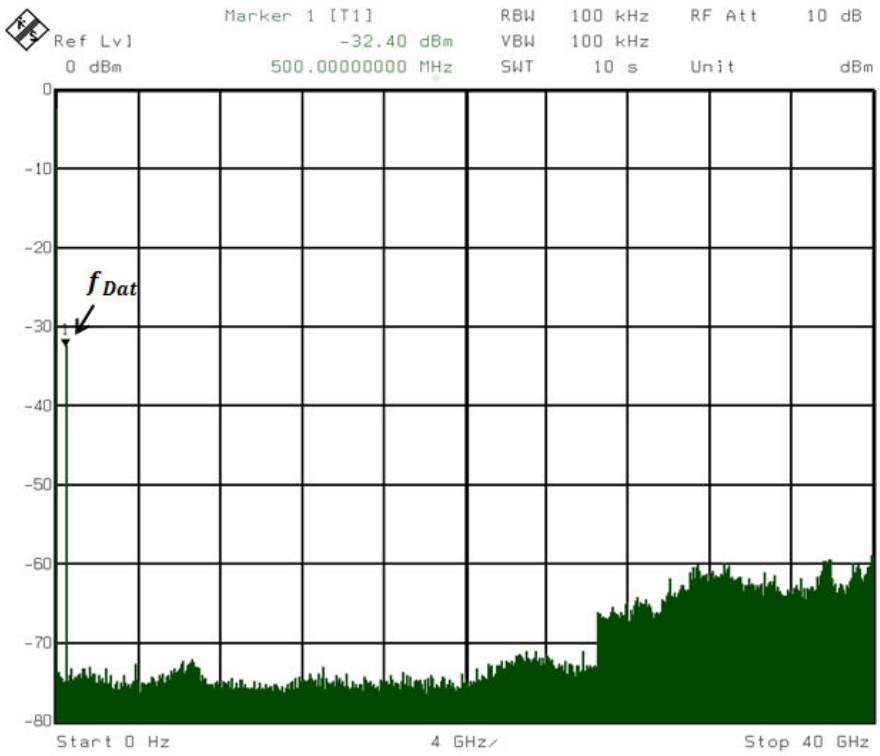

Figure 3.7: Electrical spectrum of the optical signal driven by an electrical subcarrier at $f_{Dat} = 0.5$ GHz at the common input of the two arms of the SOA-MZI.

The optical pulse source used as an optical sampling signal generates, at the sampling wavelength $\lambda_{sa} = 1550$ nm, a 10 ps width pulse at the repetition rate $f_{sa} = 7.8$ GHz with a peak power of -5 dBm. This peak power is adjusted by the first optical attenuator (Att_1) to correspond to the power that places the SOA-MZI at the ON state.

At $\lambda_{Dat} = 1545$ nm, the photo-detected sampled signal spectrum at the SOA-MZI output is observed at different frequencies showing that the input signal has been replicated at the frequencies $nf_{sa} \pm f_{Dat}$ around each harmonic of the sampling signal at the SOA-MZI output as shown in Figure 3.8. As a result, the original optical signal at f_{Dat} has been frequency up-converted at $nf_{sa} \pm f_{Dat}$.

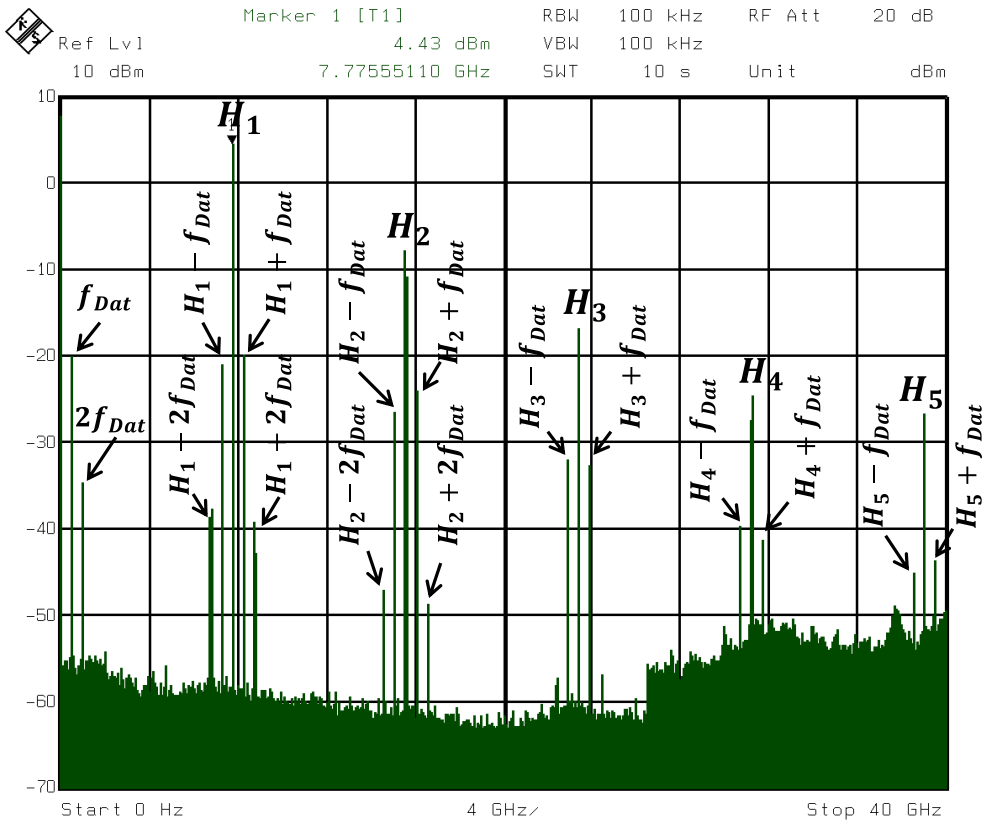

Figure 3.8: Electrical spectrum of the sampled signal (up-converted) at the SOA-MZI output after filtering. Replicas of the optical IF signal modulated at $f_{Dat} = 0.5$ GHz around each harmonic of the sampling signal at $nf_{sa} \pm f_{Dat}$.

It is also worth noting that the electrical spectrum of the optical signal at the input port (C) has only the fundamental harmonic at $f_{Dat} = 0.5$ GHz. The second harmonic at the input port (C) is lower than the noise floor due to biasing the optical MZM in its linear region. This harmonic is generated at the output port (J) as displayed in Figure 3.8 due to nonlinearities of the SOAs. The difference in powers between the first harmonic at $f_{Dat} = 0.5$ GHz and the second one at $2f_{Dat} = 1$ GHz is 14 dB at the SOA-MZI output. Figure 3.8 shows also replicas of the original

signal at frequencies $nf_{sa} \pm nf_{Dat}$ around each harmonic of the sampling signal which appear clearly around the first two harmonics due to their sufficient power. The replicas at $nf_{sa} \pm f_{Dat}$ represents the real up-converted signals we have used.

For frequency down-conversion, we use a sinewave signal at the frequency $f_{Dat} = 39.5$ GHz as shown in Figure 3.9. The optical mean power of the optical signal $P_{o,in,Dat}$ injected at the common input of the two arms of the SOA-MZI (port (C)) is -10 dBm with the wavelength $\lambda_{Dat} = 1545$ nm. The electrical power of this signal $P_{e,in,Dat}$ is -36.8 dBm. It is important to notice that we have used the same experimental setup of an all-optical mixer and the same optical pulse source with the same operating point for frequency up-conversion and frequency down-conversion techniques.

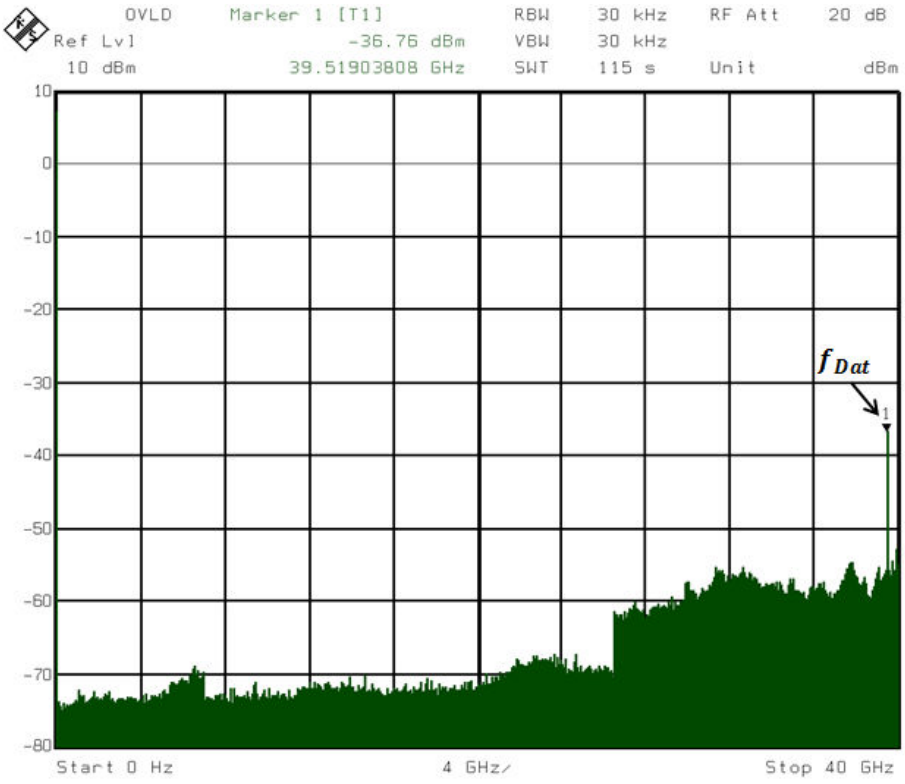

Figure 3.9: Electrical spectrum of the optical signal at the input port (C) at f_{Dat} = 39.5 GHz.

Figure 3.10 shows the electrical spectrum of the down-converted signal at the SOA-MZI output that represents the harmonics H_n and replicas of the original RF carrier at f_{Dat}. These replicas are found at different frequencies $|f_{Dat} - nf_{sa}|$ on either side of harmonics as explained in the frequency down-conversion technique in the chapter one. The frequency of harmonics nf_{sa} of the sampling signal is given in Table 6, where n is altered from 1 to 9. We can observe in Figure 3.10 that the down-converted signals at the output port (J) at $|f_{Dat} - nf_{sa}|$ involve up to the ninth harmonic H_9 of the sampling signal.

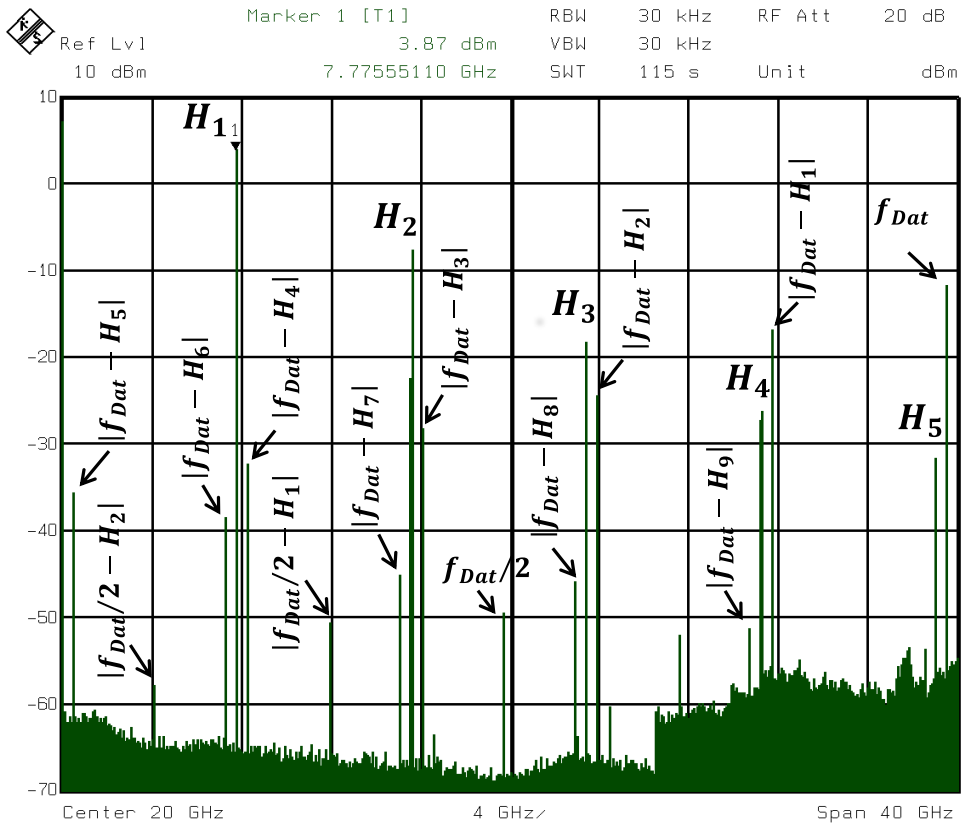

Figure 3.10: Electrical spectrum of the sampled RF signal at the output port (J). The frequency of the RF signal is f_{Dat} = 39.5 GHz, the sampling frequency is f_{sa} = 7.8 GHz.

Table 6: Frequency of the harmonics H_n of the optical pulse source.

Harmonic	Frequency (GHz)	Harmonic	Frequency (GHz)
H1	7.8	H6	46.8
H2	15.6	H7	54.6
H3	23.4	H8	62.4
H4	31.2	H9	70.2
H5	39		

The parasitic signal at the frequency $f_{Dat}/2$ at the common SOA-MZI input (port (C)) is delivered by the RF generator used to generate the signal at f_{Dat}. This unwanted signal is amplified at the SOA-MZI output and it is frequency down-converted at frequencies $|(f_{Dat}/2) - nf_{sa}|$. The RF generator has the limited frequency of 40 GHz.

3.2.4 Experimental Results of Up and Down-Conversion Gains

The efficiency of the frequency conversion at the SOA-MZI output can be evaluated through the conversion gain G_c. Conversion efficiency is measured in the electrical domain after converting the optical signal at the output port (J) through the photodiode (Pd). G_c is studied in terms of the target frequencies of the up-converted and the down-converted signals.

The conversion gain is defined by the ratio of the electrical power of converted signals at different target frequencies at the SOA-MZI output to the electrical power of the sinewave input signal at the frequency f_{Dat}. The corresponding conversion gains are $G_{c,up}$ and $G_{c,down}$ as given by Equations (3.3) and (3.4), respectively.

$$G_{c,up}\big|_{nf_{sa}\pm f_{Dat}} = \frac{P_{e,out,Dat}\big|_{nf_{sa}\pm f_{Dat}}}{P_{e,in,Dat}\big|_{f_{Dat}}} \tag{3.3}$$

$$G_{c,down}\big|_{|f_{Dat}-nf_{sa}|} = \frac{P_{e,out,Dat}\big|_{|f_{Dat}-nf_{sa}|}}{P_{e,in,Dat}\big|_{f_{Dat}}} \tag{3.4}$$

The up-conversion gain $G_{c,up}$ is measured at different target frequencies $nf_{sa} + f_{Dat}$ where n is varied from 1 to 5 as plotted in Figure 3.11. These target frequencies range from $f_{sa} + f_{Dat} =$ 8.3 GHz to $5f_{sa} + f_{Dat} = 39.5$ GHz. The $G_{c,up}$ has a maximum value of 15.5 dB at $f_{sa} + f_{Dat}$ related to the first harmonic H_1 of the sampling signal. This value decreases to -13.4 dB at $5f_{sa} + f_{Dat}$ related to the fifth harmonic H_5.

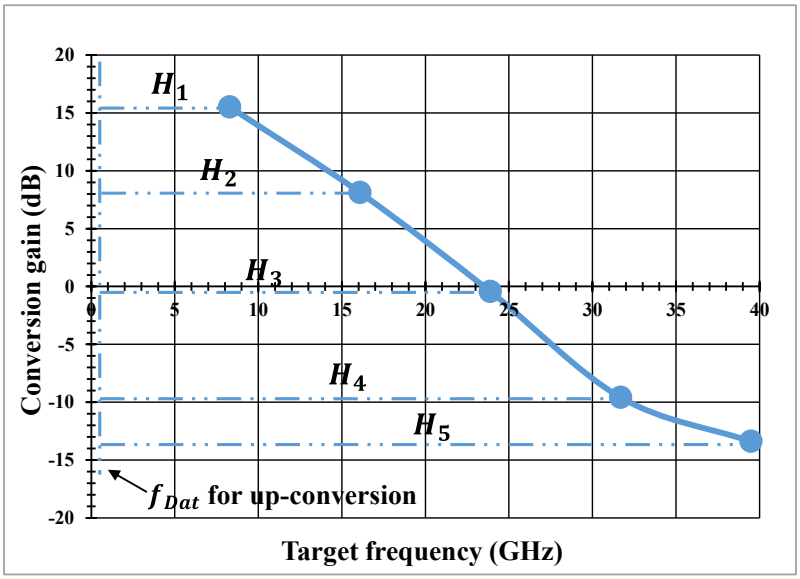

Figure 3.11: Frequency up-conversion gain at different target frequencies $nf_{sa} + f_{Dat}$.

The difference between the first and the fifth up-conversion gains is 28.9 dB. The conversion gains are influenced by the low pass behavior of the SOA-MZI and by the attenuation of the harmonics H_n of the sampling signal.

In Figure 3.12, the down-conversion gain $G_{c,down}$ is measured as a function of target frequencies $|f_{Dat} - nf_{sa}|$. There are five target frequencies ranged from $f_{Dat} - f_{sa} = 31.7$ GHz to $f_{Dat} - 5f_{sa} = 0.5$ GHz. $G_{c,down}$ has a positive slope because of the lower target frequencies involve the higher harmonics of the sampling signal. $G_{c,down}$ decreases with the target frequency due to the limited bandwidth of the SOA-MZI and the power of harmonics of the sampling signal. The difference between the first down-conversion gain at the frequency of 31.7 GHz and the fifth one at 0.5 GHz is 20.4 dB which is lower than the one of 28.9 dB for up-conversion gain. This differences will be discussed in the paragraph 3.2.6.

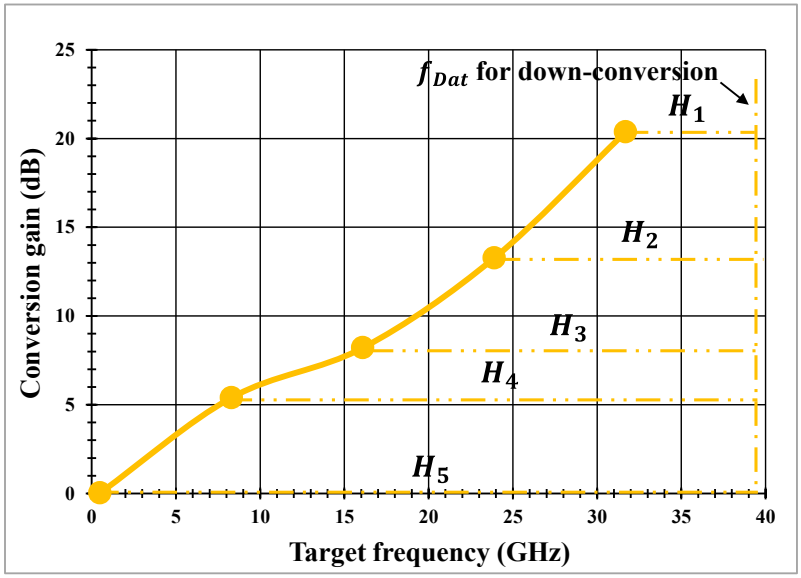

Figure 3.12: Frequency down-conversion gain at different target frequencies $|f_{Dat} - nf_{sa}|$.

The up-conversion and down-conversion gains are also studied for different repetition frequency rates of the optical pulse source. These frequencies are 9.75 GHz, 13 GHz, and 19.5 GHz in addition to the main one of 7.8 GHz. The operating point of the SOA-MZI is the same for the one used in the up-conversion and down-conversion results at $f_{sa} = 7.8$ GHz. The conversion gains are measured at the target frequency of 39.5 GHz for up-conversion and 0.5 GHz for down-conversion for different sampling frequencies as displayed in Figure 3.13.

The increase of the sampling frequency at the input port (A) leads to enhancing the power of the harmonic at 39 GHz as shown in Table 2 due to reducing the harmonic order. The improvement of the power of the harmonic at 39 GHz at the output port (J) is obtained with the sampling frequency. The electrical powers of up-converted signal at 39.5 GHz and the down-

converted signal at 0.5 GHz are increased with the sampling frequency due to increasing the power of the harmonic at 39 GHz at the SOA-MZI output and reducing the harmonic order.

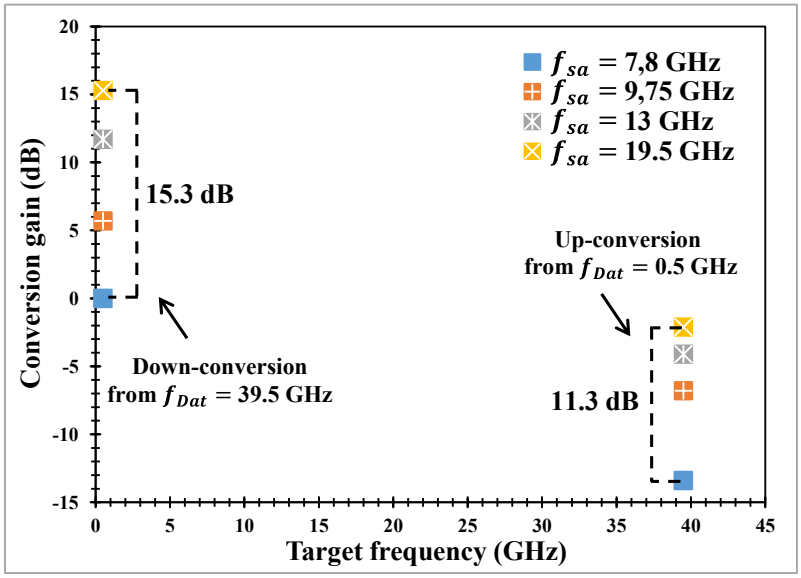

Figure 3.13: Conversion gain for different repetition rates of the optical pulse source.

The up-conversion gains $G_{c,up}$ increases from -13.4 dB at the target frequency of 39.5 GHz related to the fifth harmonic H_5 for $f_{sa} = 7.8$ GHz to -2.1 dB at the same target frequency related to the second harmonic H_2 for $f_{sa} = 19.5$ GHz. $G_{c,up}$ is still negative even the sampling frequency is increased. The down-conversion gains $G_{c,down}$ at the target frequency of 0.5 GHz related to the common harmonic at 39 GHz increases with the sampling frequency as shown in Figure 3.13. At $f_{sa} = 19.5$ GHz, $G_{c,down}$ is 15.3 dB at 0.5 GHz related to H_2 at 39 GHz. This value is higher than the one of 0 dB at the same target frequency related to H_5 at 39 GHz for $f_{sa} = 7.8$ GHz.

3.2.5 Frequency Up and Down-Conversion Theoretical Responses by Small Signal Analysis

The frequency up and down-conversion theoretical responses are calculated by small signal analysis in order to highlight the origin of the differences between up and down-conversion responses as it was shown in the above paragraph. In order to proceed a small signal analysis, the following assumptions are done:

- The optical data input power $P_{dat,i}$ is injected into each SOA_k, where $k = x$ for SOA_x and $k = y$ for SOA_y, at the wavelength λ_{Dat} as plotted in Figure 3.11. It is worth noting that SOA_x and SOA_y respectively correspond to SOA1 and SOA2 in the architecture of the used SOA-MZI in the experimental results.

- $P_{dat,i}$ is constituted by a sum of a constant power $\overline{P}_{dat,i}$ and a sinusoidal variation power $\Delta P_{dat,i}$ at an angular frequency ω_{dat} where:

$$P_{dat,i} = \bar{P}_{dat,i} + \Delta P_{dat,i} = \bar{P}_{dat,i} + \frac{p_{dat,i}}{2} e^{j\omega_{dat}t} + \frac{p^*_{dat,i}}{2} e^{-j\omega_{dat}t} \quad (3.5)$$

Where $p_{dat,i}$ is the amplitude of sinusoidal modulation of the data signal.

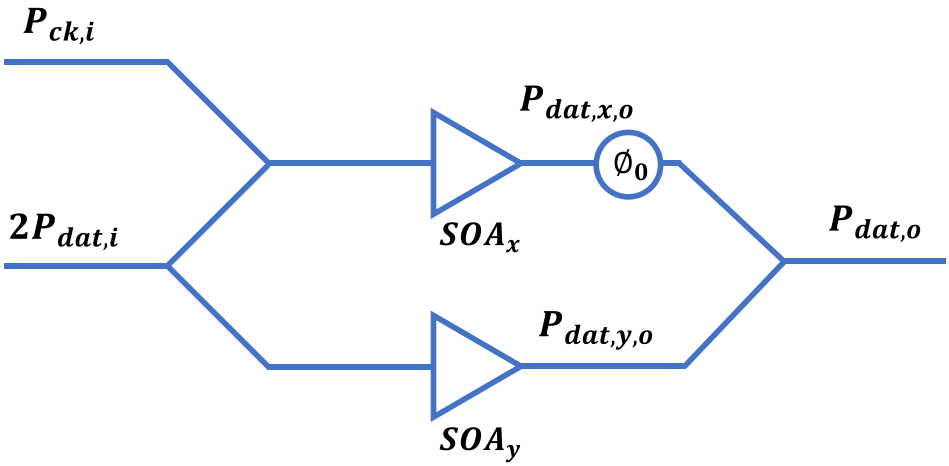

Figure 3.14: SOA-MZI configuration used for the theoretical study.

- The optical clock input power is constituted of the sum of n harmonics. The i[th] harmonic power is noted $P_{ck,i}$ modulated as a sum of a constant power $\bar{P}_{ck,i}$ and a sinusoidal variation power $\Delta P_{ck,i}$ at an angular frequency ω_{ck} where:

$$P_{ck,i} = \bar{P}_{ck,i} + \Delta P_{ck,i} = \bar{P}_{ck,i} + \frac{p_{ck,i}}{2} e^{j\omega_{ck}t} + \frac{p^*_{ck,i}}{2} e^{-j\omega_{ck}t} \quad (3.6)$$

Where $p_{ck,i}$ is the amplitude of the sinusoidal modulation of the clock signal.

- The carrier density of SOA_y is modulated by the data signal. Its variation Δn_y around its operating point $\overline{N}_y$ has only terms at ω_{dat} by injecting only $P_{dat,i}$ as shown in Figure 3.14. The carrier density of SOAy is given by

$$N_y = \overline{N}_y + \Delta n_y = \overline{N}_y + \frac{n_{dat,y}}{2} e^{j\omega_{dat}t} + \frac{n^*_{dat,y}}{2} e^{-j\omega_{dat}t} \quad (3.7)$$

Where $n_{dat,y}$ is the carrier density modulation of SOA_y.

- At λ_{Dat}, the modulated gain $G_{dat,y}$ and the amplified output power of SOAy $P_{dat,y,o}$ can be developed by:

$$G_{dat,y} = \bar{G}_{dat,y} + \frac{\partial G_{dat,y}}{\partial N_y} \Delta n_y \tag{3.8}$$

Leading to:

$$P_{dat,y,o} = G_{dat,y}\, P_{dat,i} = \bar{P}_{dat,y,o} + \Delta P_{dat,y,o} \tag{3.9}$$

Where $\bar{P}_{dat,y,o}$ and $\Delta P_{dat,y,o}$ are respectively the constant and the sinusoidal variation powers at the output arm y of the interferometer.

- As $P_{dat,i}$ and $P_{ck,i}$ are injected into SOA_x, they will induce, in a first approximation, a carrier density variation that has terms at ω_{ck}, ω_{dat}, and intermodulation terms at $\omega_{ck} \pm \omega_{dat}$.

- In order to take into account the generation and the amplification of the second order terms, the small signal equations are written for a section x_l of SOA_x. Modeling SOAs with several sections are consistent with a long device into which the carrier density varies along the SOA_x active region. Furthermore, the amplification of intermodulation terms that appears on the optical signal at λ_{Dat} can be taken into account. The input and output powers of a section are shown in Figure 3.15.

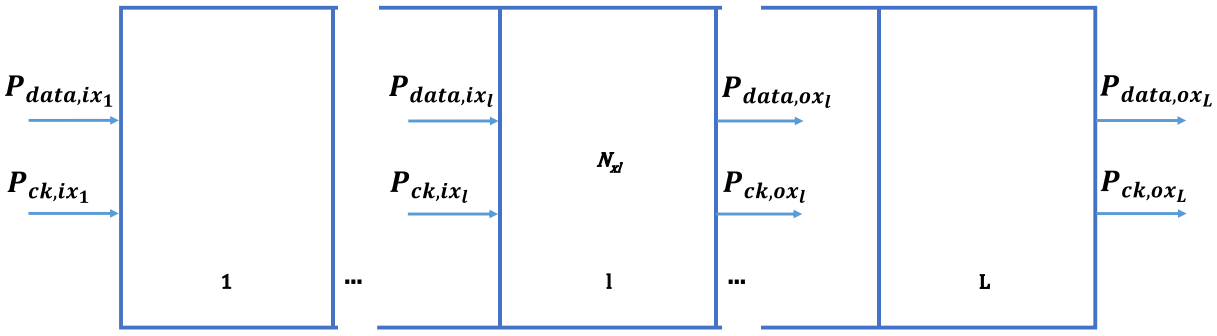

Figure 3.15: Input and output powers of a section l of SOA_x.

The powers at the input and output of SOA_x are:

$$P_{dat,ix_1} = P_{dat,i} \qquad P_{dat,ox_L} = P_{dat,x,o} \tag{3.10}$$

$$P_{ck,ix_1} = P_{ck,i} \qquad P_{ck,ox_L} = P_{ck,x,o} \tag{3.11}$$

The input powers P_{dat,ix_l} and P_{ck,ix_l} of a section l, except at the first section, have intermodulation terms. They are constituted by a power variation around a mean power as given below. The whole variation is the sum of sinusoidal variations at angular frequencies ω_{ck}, ω_{dat}, and $\omega_{ck} \pm \omega_{dat}$:

$$\begin{aligned} P_{dat,ix_l} &= \overline{P}_{dat,ix_l} + \Delta P_{dat,ix_l} = \overline{P}_{dat,ix_l} + \sum_{\substack{r=dat,ck,\\ ck+dat,\\ ck-dat}} \Delta P_{dat,r,ix_l} \\ &= \overline{P}_{dat,ix_l} + \sum_{\substack{r=dat,ck,\\ ck+dat,\\ ck-dat}} \left(\frac{p_{dat,r,ix_l}}{2} e^{j\omega_r t} + \frac{p^*_{dat,r,ix_l}}{2} e^{-j\omega_r t} \right) \end{aligned} \tag{3.12}$$

Where p_{dat,r,ix_l} is the amplitude of the sinusoidal modulation of the data signal at ω_r at the input of the section l along the SOA_x active region.

$$\begin{aligned} P_{ck,ix_l} &= \overline{P}_{ck,ix_l} + \Delta P_{ck,ix_l} = \overline{P}_{ck,ix_l} + \sum_{\substack{s=dat,ck,\\ ck+dat,\\ ck-dat}} \Delta P_{ck,s,ix_l} \\ &= \overline{P}_{ck,ix_l} + \sum_{\substack{s=dat,ck,\\ ck+dat,\\ ck-dat}} \left(\frac{p_{ck,s,ix_l}}{2} e^{j\omega_s t} + \frac{p^*_{ck,s,ix_l}}{2} e^{-j\omega_s t} \right) \end{aligned} \tag{3.13}$$

Where p_{ck,s,ix_l} is the amplitude of the sinusoidal modulation of the clock signal at ω_s at the input of the section l during the SOA_x active region.

In a section x_l, the carrier density variation Δn_{x_l} around its operating point $\overline{N}_{x_l}$ can be written as:

$$N_{x_l} = \overline{N}_{x_l} + \Delta n_{x_l} = \overline{N}_{x_l} + \sum_{\substack{m\,=\,dat,ck,\\ ck+dat,\\ ck-dat}} \left(\frac{n_{m,x_l}}{2} e^{j\omega_m t} + \frac{n^*_{m,x_l}}{2} e^{-j\omega_m t} \right) \tag{3.14}$$

At λ_{dat}, the modulated gain G_{dat,x_l} and the amplified output power of SOA_x, $P_{dat,x,o}$, can be developed by:

$$G_{dat,x_l} = \bar{G}_{dat,x_l} + \left. \frac{\partial G_{dat,x_l}}{\partial N_{x_l}} \right|_{N = \bar{N}_{x_l}} \Delta n_{x_l} \tag{3.15}$$

Leading to:

$$P_{dat,ox_l} = G_{dat,x_l}\, P_{dat,ix_l} = \bar{P}_{dat,ox_l} + \sum_{\substack{r=dat,ck,\\ ck+dat,\\ ck-dat}} \Delta P_{dat,r,ox_l}$$

$$= \overline{P}_{dat,ox_l} + \sum_{\substack{r=dat,ck,\\ ck+dat,\\ ck-dat}} \left(\frac{p_{dat,r,ox_l}}{2} e^{j\omega_r t} + \frac{p^*_{dat,r,ox_l}}{2} e^{-j\omega_r t} \right) \quad (3.16)$$

Where $\Delta P_{dat,r,ox_l}$ is the variation power of the data signal at λ_{Dat} at the output of the section l within the SOA_x active region. p_{dat,r,ox_l} is the amplitude of the sinusoidal modulation of the data signal at ω_r at the output of the section l within SOA_x active region. The equations of the constant and the variation powers of SOA_x and SOA_y are shown in Appendix B.1.

At the SOA_k output, the variation of the phase $\Phi_{dat,k,o}$ of $P_{dat,k,o}$ at λ_{dat} around its mean value $\overline{\Phi}_{dat,k,o}$ can be written by:

$$\Delta\Phi_{dat,k,o} = -\frac{\alpha_H}{2\bar{G}_{dat,k}} \frac{\partial G_{dat,k}}{\partial N_k} \Delta n_k \quad (3.17)$$

Where α_H is the Henry′s factor.

For SOA_x, N_x and Δn_x are mean values inside the active region calculated from the carrier density N_{x_l} and the variation Δn_{x_l} of the carrier density of each section. The carrier densities at the output of the upper arm x at ω_{dat}, ω_{ck}, ω_{ck+dat}, and ω_{ck+dat} are derived as seen in Appendix B.2.

At the SOA-MZI output, the power of the optical signal at the wavelength λ_{Dat} is given by:

$$P_{dat,o} = \frac{1}{4}\Big(P_{dat,x,o} + P_{dat,y,o} - 2\sqrt{P_{dat,x,o} P_{dat,y,o}}\, cos\big(\Phi_{dat,x,o} - \Phi_{dat,y,o} + \emptyset_0\big)\Big) \quad (3.18)$$

The output power $P_{dat,o}$ is written as the sum of the constant and variation powers of $P_{dat,x,o}$ and $P_{dat,y,o}$ and the constant and variation phases of $\Phi_{dat,x,o}$ and $\Phi_{dat,y,o}$ as observed in Appendix B.3.

The different up and down frequency components of the output power, limited to the first order terms, are:

$$p_{dat,ck+dat,o} = \frac{1}{4}\left(\frac{p_{dat,ck+dat,ox_L}}{2} - \sqrt{\bar{P}_{dat,ox_L}\bar{P}_{dat,y,o}}\cdot\left[\frac{\alpha_H}{\bar{G}_{dat,x}}\frac{\partial G_{dat,x}}{\partial N_x}\frac{n_{ck+dat,x}}{2}\sin(\Psi_0) + \frac{p_{dat,ck+dat,ox_L}}{2\bar{P}_{dat,ox_L}}\cos(\Psi_0)\right]\right) \quad (3.19)$$

$$p_{dat,ck-dat,o} = \frac{1}{4}\left(\frac{p_{dat,ck-dat,ox_L}}{2} - \sqrt{\bar{P}_{dat,ox_L}\bar{P}_{dat,y,o}}\cdot\left[\frac{\alpha_H}{\bar{G}_{dat,x}}\frac{\partial G_{dat,x}}{\partial N_x}\frac{n_{ck-dat,x}}{2}sin(\Psi_0) + \frac{p_{dat,ck-dat,ox_L}}{2\bar{P}_{dat,ox_L}}\cos(\Psi_0)\right]\right) \quad (3.20)$$

Where Ψ_0 is given as:

$$\Psi_0 = \bar{\Phi}_{dat,x,o} - \bar{\Phi}_{dat,y,o} + \Phi_0 \quad (3.21)$$

The analysis of the above equations will be conducted for four different uses of the mixer: frequency up- and down-conversions, corresponding respectively to an angular frequency output ω_{ck+dat} and ω_{ck-dat}, and an optical clock at low/medium and high frequencies, respectively $ck1$ and $ck5$. These clocks correspond to the harmonics of a pulse train at the repetition rate f_{ck1}. Each harmonic of the clock signal corresponds to frequencies f_{ck1}, $2f_{ck1}$, $3f_{ck1}$,…, respectively noted $ck1$, $ck2$, $ck3$, …

In addition, we assume, on one hand, that, for up-conversion $\omega_{dat} = \omega_d \ll (\omega_{ck1}, \omega_{ck5})$ and for down-conversion $\omega_{dat} = \omega_D \gg \omega_{ck1}$ and $\omega_{dat} = \omega_D \sim \omega_{ck5}$; on the other hand, that $\omega_{ck1} \sim 2\pi BW_{\mathrm{SOA-MZI}}$ and $\omega_{ck5} \gg 2\pi BW_{\mathrm{SOA-MZI}}$ where $BW_{\mathrm{SOA-MZI}}$ is the SOA-MZI frequency bandwidth. D and d represent the data for down-conversion at the high frequency and up-conversion at the low frequency, respectively. $ck1$ and $ck5$ represent respectively the clock at the low frequency f_{ck1} and the high one f_{ck5}.

The amplitude of the up-converted and down-converted powers related to $ck1$ and $ck5$, respectively, derived from Equations (B.20) and (B.17), see Appendix B.4, are given in the equations below when $\bar{P}_{dat,ox_L} \cong \bar{P}_{dat,y,o}$ are supposed to be $\bar{P}_{dat,o}$ for up-conversion and down-conversion.

a) Down-conversion, $ck1$ and $ck5$:

$$p_{dat,z_D,o} = \frac{p_{dat,z_D,ox_L}}{8}\left(1 - cos(\Psi_0)\right) + Kn_{z_D,x}\, sin(\Psi_0) \tag{3.22}$$

Where z_D that is the target frequency related to $ck1$ or $ck5$ and K are defined as:

$$z_D = \ ck1 - D \text{ or } \ ck5 - D \tag{3.23}$$

$$K = -\frac{\alpha_H}{\bar{G}_{dat,x}} \frac{\partial G_{dat,x}}{\partial N_x} \frac{\overline{P}_{dat,o}}{8} \tag{3.24}$$

b) Up-conversion, $ck1$ and $ck5$:

$$p_{dat,z_d,o} = \frac{p_{dat,z_d,ox_L}}{8}\left(1 - cos(\Psi_0)\right) + Kn_{z_d,x}\, sin(\Psi_0) \tag{3.25}$$

Where z_d is the target frequency related to $ck1$ or $ck5$ as given in the equation below:

$$z_d = ck1 + d \ \text{ or } ck5 + d \tag{3.26}$$

3.2.6 Qualitative Analysis of Frequency Up and Down-Conversion Theoretical Responses

In this section, we present the main points of the qualitative analysis which is developed in Appendix B.5. The down-converted powers at $z_D = ck1 - D$ or $ck5 - D$ and up-converted ones at $z_d = ck1 + d$ or $ck5 + d$ after adding the simplified equations of carrier densities $n_{Z_D,x}$ and $n_{Z_d,x}$ seen in Appendix B.4 in Equations (3.22) and (3.25) are respectively given as:

$$\begin{aligned} p_{dat,z_D,o} = \frac{p_{dat,z_D,ox_L}}{8}\left(1 - cos(\Psi_0)\right) + \\ K\left(\frac{1}{L}\sum_{l=1}^{L} f_w \left[\bar{G}_{dat,\boldsymbol{x_{l-1}}}\, p_{dat,z_D,i\boldsymbol{x_{l-1}}} + \frac{\partial G_{dat,\boldsymbol{x_{l-1}}}}{\partial N_{\boldsymbol{x_{l-1}}}}\left[n_{z_D,x_{l-1}}\bar{P}_{dat,i\boldsymbol{x_{l-1}}} + \right.\right.\right. \\ \left.\left.\left.\frac{1}{2} n_{ck1/5,\boldsymbol{x_{l-1}}} p^{*}_{dat,D,i\boldsymbol{x_{l-1}}}\right]\frac{\partial R_{dat,x_l}}{\partial P_{dat,ix_l}} + \bar{G}_{ck,\boldsymbol{x_{l-1}}}\, p_{ck,z_D,i\boldsymbol{x_{l-1}}} + \right. \\ \left.\left.\frac{\partial G_{ck,\boldsymbol{x_{l-1}}}}{\partial N_{\boldsymbol{x_{l-1}}}}\left[n_{z_D,\boldsymbol{x_{l-1}}}\bar{P}_{ck,i\boldsymbol{x_{l-1}}}\right]\frac{\partial R_{ck,x_l}}{\partial P_{ck,ix_l}}\right]\right)\right) sin(\Psi_0) \end{aligned} \tag{3.27}$$

$$p_{dat,z_d,o} = \frac{p_{dat,z_d,ox_L}}{8}\left(1 - cos(\Psi_0)\right) +$$

$$K\left(\frac{1}{L}\sum_{l=1}^{L} f_w \left[\bar{G}_{dat,\boldsymbol{x_{l-1}}}\, p_{dat,z_d,i\boldsymbol{x_{l-1}}} + \frac{\partial G_{dat,\boldsymbol{x_{l-1}}}}{\partial N_{\boldsymbol{x_{l-1}}}}\left[n_{z_d,x_{l-1}}\bar{P}_{dat,i\boldsymbol{x_{l-1}}} + \right.\right.\right.$$

$$\left.\frac{1}{2} n_{ck1/5,\boldsymbol{x_{l-1}}} p^{*}_{dat,d,i\boldsymbol{x_{l-1}}}\right]\frac{\partial R_{dat,x_l}}{\partial P_{dat,ix_l}} + \bar{G}_{ck,\boldsymbol{x_{l-1}}}\, p_{ck,z_d,i\boldsymbol{x_{l-1}}} + \tag{3.28}$$

$$\left.\left.\left.\frac{\partial G_{ck,\boldsymbol{x_{l-1}}}}{\partial N_{\boldsymbol{x_{l-1}}}}\left[n_{z_d,\boldsymbol{x_{l-1}}}\bar{P}_{ck,i\boldsymbol{x_{l-1}}}\right]\frac{\partial R_{ck,x_l}}{\partial P_{ck,ix_l}}\right]\right)\right) sin(\Psi_0)$$

Where f_w is defined as:

$$f_w = -\frac{\tau_{d,x_l}}{\left(1 + j\omega_{z_d,z_D}\tau_{d,x_l}\right)} \tag{3.29}$$

The generated intermodulation and filtering terms of powers given by Equations (3.27) and (3.28) for up-conversion and down-conversion, respectively, are observed in Table 11 in Appendix B.5 by taking into account the following points:

- The power of the clock $ck1$ is higher than the one of the clock $ck5$. In the real system, these clocks correspond to the harmonics of a pulse train at the repetition rate f_{ck1}. Each harmonic corresponds to a clock at frequencies f_{ck1}, $2f_{ck1}$, $3f_{ck1}$,…, respectively noted $ck1$, $ck2$, $ck3$, … The power of harmonics decreases with their rank. In the following, we are interested by the first and the fifth harmonics which are respectively $ck1$ and $ck5$.

- The frequency response of the carrier density is a low pass one with a cutoff frequency equal to $f_{LP} = 1/(2\pi\tau_d)$, see Figure 3.16(a). This characteristic implies that all phenomenon involving the carrier density is low pass filtered. For example, the transposition of a clock signal from a clock wavelength λ_{ck} to an optical carrier wavelength λ_{Dat} is more efficient at the frequency f_{ck1} than at the frequency f_{ck5}.

- The optical gain of a saturated SOA depends on the input signal frequency. At low frequencies, less than f_{sat} (see Figure 3.16(b) that corresponds to Figure 2.5), the input signal modulates the carrier density of the active region and, in turns, saturates the optical gain. At high frequencies, higher than f_{unsat}, the carrier density is no longer modulated due to its frequency response resulting in an unsaturated optical

dynamic gain. Then, the intensity-modulated optical input signal at the wavelength λ_{Dat} is better amplified at the high angular frequency ω_D than at the low one ω_d.

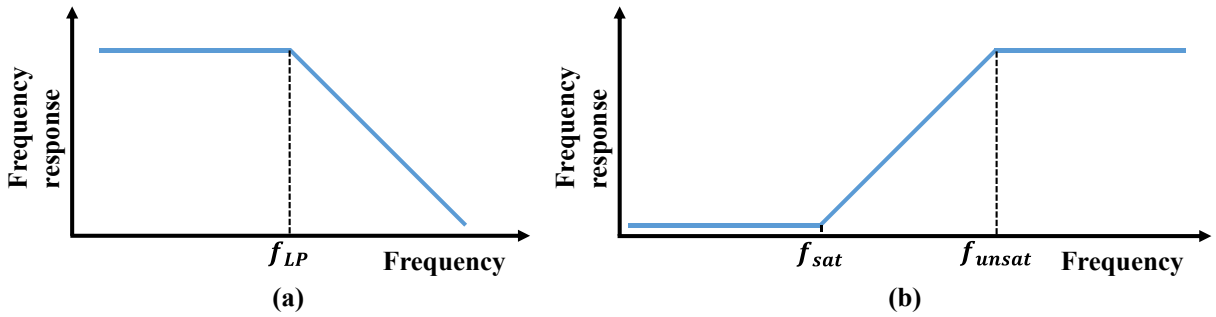

Figure 3.16: Frequency response of carrier density (a) and SOA (b) that represents the amplification at its output.

- The mean optical gain at λ_{Dat} is close to the one at λ_{ck}.

- When developed in Equations (3.22) and (3.25), the first term p_{dat,z_d,z_D,ox_L} and the second one $n_{z_d,z_D,x}$ are constituted by terms having the same frequency behavior. The analysis is then the same in both cases.

- For Equations (3.27) and (3.28), they exist amplified intermodulation terms and generated intermodulation terms. The amplified ones are due to generation of intermodulation terms into previous sections of the SOA. They do not add asymmetry between frequency components of optical carriers. On the contrary, the generated intermodulation terms in a section of the SOA can make appear asymmetry due to the points cited above. Then, only these terms are analyzed to bring out the different values of conversion gains.

With these considerations and by comparing the terms of $p_{dat,ck1-D,o}$ at $ck1-D$ and $p_{dat,ck5-D,o}$ at $ck5-D$ for down-conversion and the ones of $p_{dat,ck1+d,o}$ at $ck1+d$ and $p_{dat,ck5+d,o}$ at $ck5+d$ for up-conversion , we can conclude (see Appendix B.5) that the difference between the conversion gain for the down-converted signal involving $ck1$ and $ck5$ is smaller than the one between the conversion gain for the up-converted signal involving $ck1$ and $ck5$. This corresponds to $(G_{c,down,1}-G_{c,down,5}) < (G_{c,up,1}-G_{c,up,5})$ and $G_{c,down,5} > G_{c,up,5}$, see Figure 3.17 that represents the measured conversion gains at first and the fifth target frequencies for up-conversion and down-conversion.

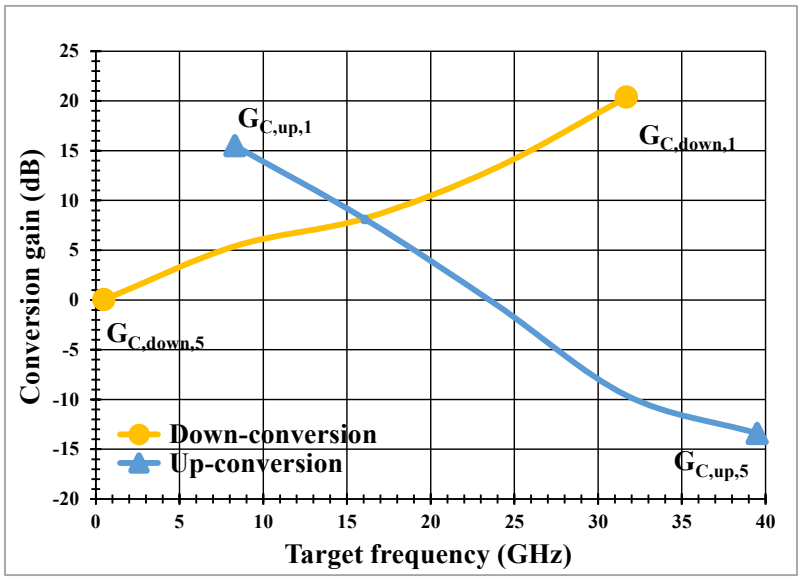

Figure 3.17: Measured conversion gain related to $H_1 = ck1$ and $H_5 = ck5$ for frequency up-conversion and frequency down-conversion.

3.2.7 Isolation

Isolation (Iso) is defined as a ratio of powers between the sampling signal or data signal and the converted signal at the SOA-MZI output for up-conversion and down-conversion as defined in the equations below:

$$Iso_{up,\ LO-RF} = \frac{P_{H_n}|_{nf_{sa}}}{P_{e,out,Dat}|_{nf_{sa}+f_{Dat}}} \tag{3.30}$$

$$Iso_{up,\ IF-RF} = \frac{P_{e,out,Dat}|_{f_{Dat}}}{P_{e,out,Dat}|_{nf_{sa}+f_{Dat}}} \tag{3.31}$$

$$Iso_{down,\ LO-IF} = \frac{P_{H_n}|_{nf_{sa}}}{P_{e,out,Dat}|_{|f_{Dat}-nf_{sa}|}} \tag{3.32}$$

$$Iso_{down,\ RF-IF} = \frac{P_{e,out,Dat}|_{f_{Dat}}}{P_{e,out,Dat}|_{|f_{Dat}-nf_{sa}|}} \tag{3.33}$$

Two types of isolations called LO-RF and IF-RF are measured at the SOA-MZI output for up-conversion as presented in Figure 3.18. The LO-RF isolation decreases slightly with the target frequency while the IF-RF isolation increases. The LO-RF isolation is constant at the high target frequencies due to degradation of the harmonic powers of the sampling signal and the replicas.

The IF-RF isolation is the relation between the optical signal at f_{Dat} and its replicas at $nf_{sa} + f_{Dat}$ at the SOA-MZI output. This isolation augments from -2.1 dB at $f_{sa} + f_{Dat} = 8.3$ GHz to 26.8 dB at $f_{sa} + f_{Dat} = 39.5$ GHz due to attenuation of the power of the replicas with the target frequency.

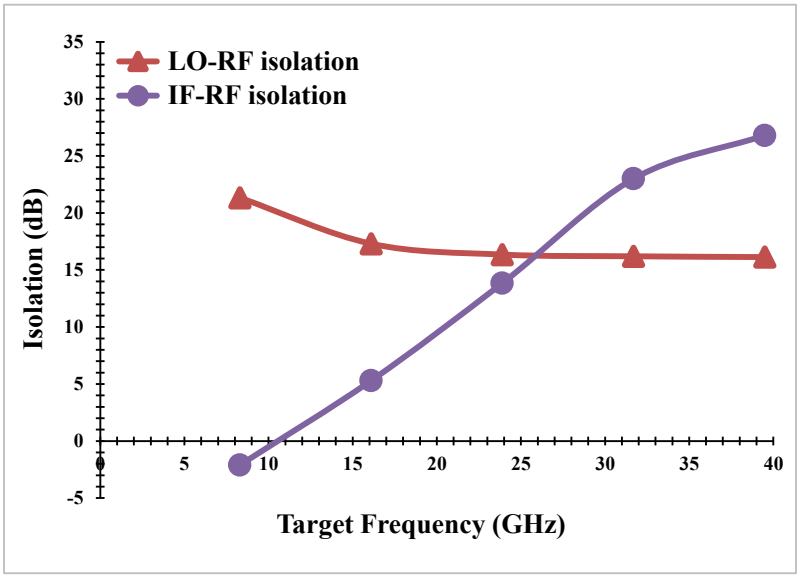

Figure 3.18: LO-RF and IF-RF isolations at the SOA-MZI output for up-conversion.

In Figure 3.19, LO-IF and RF-IF isolations are measured at the SOA-MZI output for down-conversion.

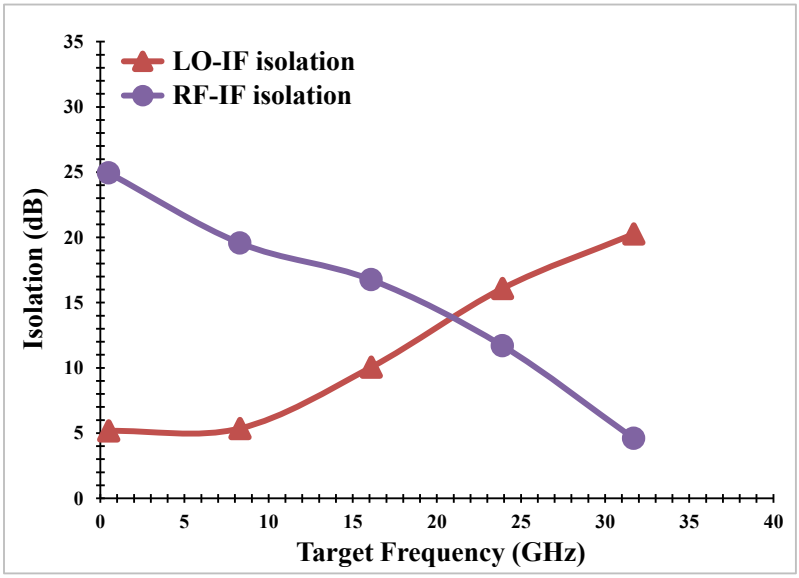

Figure 3.19: LO-IF and RF-IF isolations at the SOA-MZI output for down-conversion.

The LO-IF isolation decreases with the target frequency while the RF-IF isolation increases. This different behavior is due to the LO-IF isolation relying on the harmonic power of the sampling signal at nf_{sa} while the RF-IF isolation relies on an optical RF signal at f_{Dat}. The LO-IF isolation at the higher target frequencies for down-conversion has the lower values compared to the LO-RF isolation for up-conversion due to improving the signal power of the replicas at the higher frequencies. The RF-IF isolation at all target frequencies for down-conversion is higher than the IF-RF isolation for up-conversion due to improving the optical RF power at f_{Dat} at the SOA-MZI output.

3.2.8 Third Order Input Intercept Point

Two tone third order input intercept point (IIP3) [137] [138] [139] is obtained by measuring the third order terms generated in presence of two incident equal amplitude optical signals at the common input port (C) of the SOA-MZI. The experimental setup shown in Figure 3.20 is used to measure the IIP3. Two tone signals at frequencies f_1 and f_2 are generated by an arbitrary waveform generator (AWG) after filtering by a low pass filter (LPF) and attenuated by a variable electrical attenuator (EAtt).

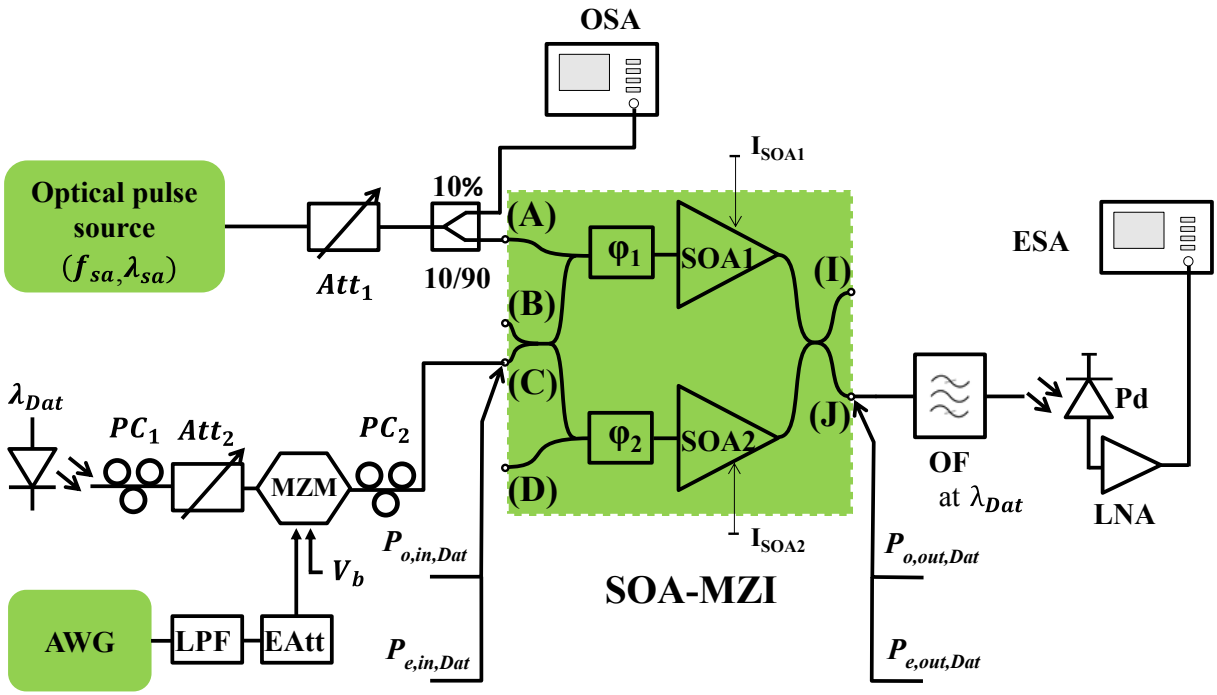

Figure 3.20: Experimental setup of the two-tone measurement. AWG: Arbitrary Waveform Generator, LNA: Low-Noise Amplifier, MZM: Mach-Zehnder Modulator, OF: Optical Filter, PC: Polarization Controller, Pd: Photodiode, φ: Phase shifter, V_b: Bias Voltage, LPF: Low Pass Filter, ESA: Electrical Spectrum Analyzer, OSA: Optical Spectrum Analyzer, and EAtt: Electrical Attenuator.

The IIP3 is measured only around the first harmonic H_1 where the fifth harmonic H_5 is 31 dB lower than H_1, the measurement of IIP3 for H_5 is not reliable due to the lower electrical power of the first order and third order terms compared to the ones related to H_1.

The frequencies f_1 and f_2 of the two optical signals are respectively 100 MHz and 110 MHz. The SOA-MZI generates intermodulation products at its output due to inherent nonlinearity. These intermodulation products have been evaluated through IIP3 at frequencies in the form shown in the equation below:

$$nf_{sa} \pm mf_1 \pm kf_2 \tag{3.34}$$

Here, n, m, and k are positive integers. The value of m and k is in the range between 1 and 2 in our measurement.

The third order nonlinearities by definition are shown in Figure 3.21 that gives rise to the output signals close to up-converted signals. The products $nf_{sa} - f_1$ and $nf_{sa} - f_2$ are called first order products and $nf_{sa} - 2f_2 + f_1$ and $nf_{sa} - 2f_1 + f_2$ are called third order products as they are generated when two-tone signals are applied simultaneously at the input port (C).

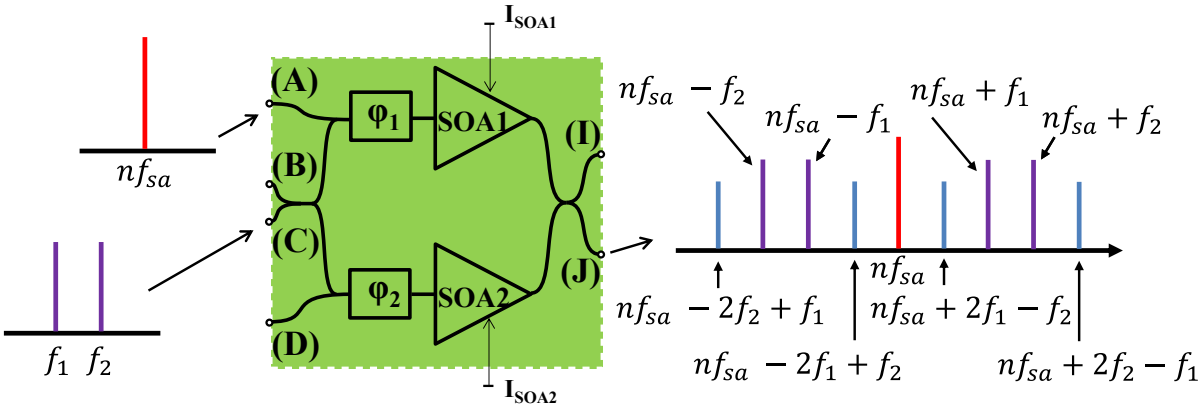

Figure 3.21: Conceptual diagram of two tone method based on a SOA-MZI to measure the IIP3.

The evolution of the electrical spectrum of the first order and the third order terms of the electrical output modulation power at the SOA-MZI output as a function of the electrical input modulation power at the input port (C) is given in Figure 3.22. The first and the third order frequencies are respectively 7.69 GHz and 7.68 GHz related to H_1. The value of the IIP3 exists around H_1 at the frequency of 7.8 GHz of the sampling signal as shown in Figure 3.22. This value is equal to −14.5 dBm. The third order terms fall on a straight line with a slope of 3 while the desired signal power falls on a straight line with a slope of 1.

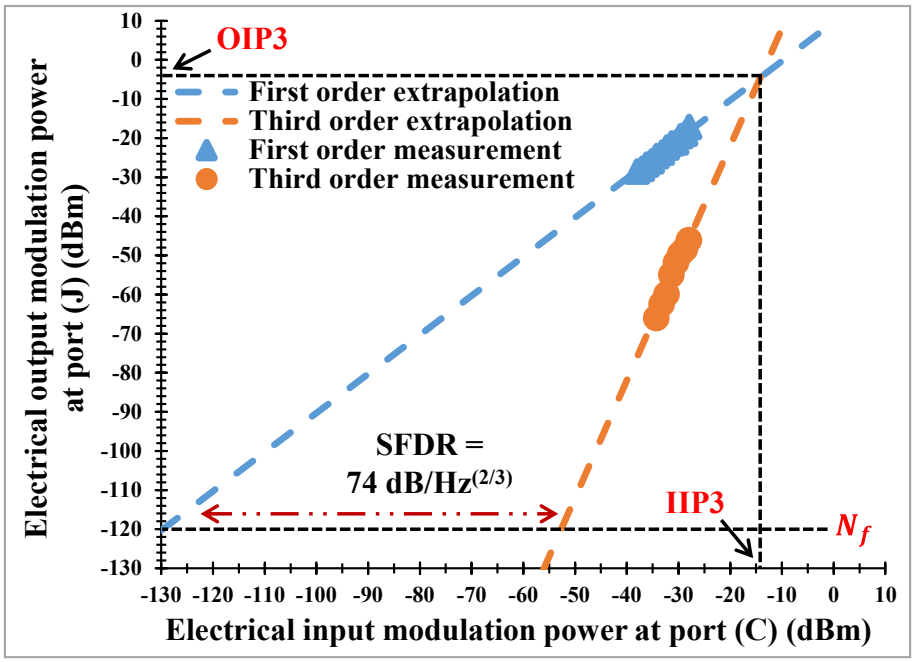

Figure 3.22: Electrical output modulation power of the first and third order measured experimentally around the first harmonic at 7.8 GHz.

The spurious free dynamic range (SFDR) [140] [141] calculated in Figure 3.22 is defined as a difference between the first order and the third order terms when they have the same noise floor (N_f). The SFDR value related for H_1 in a 1 Hz resolution bandwidth (RBW) is 74 dB/Hz$^{2/3}$ at the SOA-MZI output. This value is calculated from the extrapolation which corresponds to the fitting points displayed in Figure 3.22. The measured PSD of the noise floor in a 1 Hz RBW is -120 dBm at $f_{sa} = 7.8$ GHz.

3.3 Frequency Conversion of Complex Modulated Data Based on the SOA-MZI

QPSK (quadratic phase shift keying) and OFDM (orthogonal frequency division multiplexing) format modulations are used to evaluate the quality of the optical transmission system for frequency up-conversion and frequency down-conversion through the error vector magnitude (EVM).

A 2 GSa/s AWG board (Arbitrary Waveform Generator) is used to generate QPSK or OFDM data at the carrier frequency $f_c = 0.512$ GHz for different symbol rates. This I-Q signal is filtered by a root raised cosine (RRC) filter with a roll-off coefficient a $= 0.18$. The error vector amplitude (EVM) is used to measure the quality of the transmission given by the vector signal analyzer (VSA) software facility. This VSA software is connected to a real time digital sampling oscilloscope (DSO) which has limited frequency of 1.5 GHz used to digitalize the received signals.

3.3.1 QPSK and OFDM Modulation Formats

3.3.1.1 Quadrature Phase Shift Keying

Quadrature phase shift keying (QPSK) or 4-QAM (Quadrature Amplitude Modulation) is considered as a type of phase modulation. QPSK signal can be written by:

$$\begin{aligned} s_i(t) &= A\cos(2\pi f_c t + \varphi_i) \\ &= A\cos\varphi_i \cos(2\pi f_c t) - A\sin\varphi_i \sin(2\pi f_c t) \end{aligned} \tag{3.35}$$

Where the carrier frequency f_c is selected as an integer multiple of the symbol rate (SR) and $\varphi_i = (2i-1)\pi/4$ is the symbol phase. It can be implemented by an AWG or by the use of an I & Q modulator. In presence of a root raised cosine filter (RRC), the bandwidth of the QPSK signal is defined with respect to the symbol rate (SR) as:

$$BW = (1 + \mathrm{a}).SR \tag{3.36}$$

Where a is roll-off coefficient and SR is half of the bit rate (BR).

The signal constellation for QPSK modulation in Figure 3.23 uses the gray coding. There are four possible dibits 00, 01, 10, and 11. Each dibit consists of two bits. We can represent in the complex plane four signals, each one corresponding to one dibit, by four points or vectors s_i where *i* is equal to 1, 2, 3, and 4.

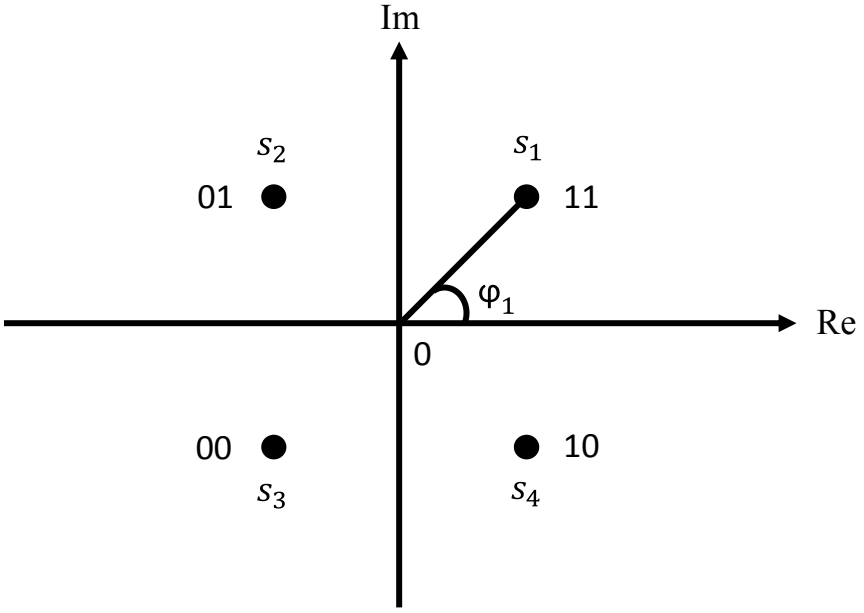

Figure 3.23: QPSK signal constellation.

3.3.1.2 Orthogonal Frequency Division Multiplexing

An orthogonal frequency division multiplexing (OFDM) has become the most popular technique of multicarrier transmission due to overlapping subcarriers in frequency and therefore bandwidth utilization increases. Overlapping subcarriers are allowed because in OFDM modulation subcarriers are orthogonal to each other. Each subcarrier that has specific frequency carries data independently modulated by binary phase shifted keying (BPSK), QPSK, M-QAM [142], or another modulation technique. The overall OFDM signal is then used to modulate a main radio frequency (RF) carrier [143].

Figure 3.24 shows the spectra for WDM (or FDM) and OFDM signals where FDM is frequency division multiplexing and WDM is wavelength division multiplexing. In FDM, there are frequency guard bands between subcarriers, so at the receiver, individual subcarriers are recovered using analog filtering techniques [143]. Each OFDM subcarrier has significant side lobes over a frequency range which includes many other subcarriers as shown in Figure 3.24. The spectrum of an OFDM subcarrier with a QAM modulation has a $|sinc(x)|^2$ form. The orthogonally requires the subcarrier frequency spacing f_{sp}. Therefore, with the number of subcarriers N_{sc}, the system bandwidth (BW_s) is defined in Equation (3.37).

$$BW_s = N_{sc}.f_{sp} \tag{3.37}$$

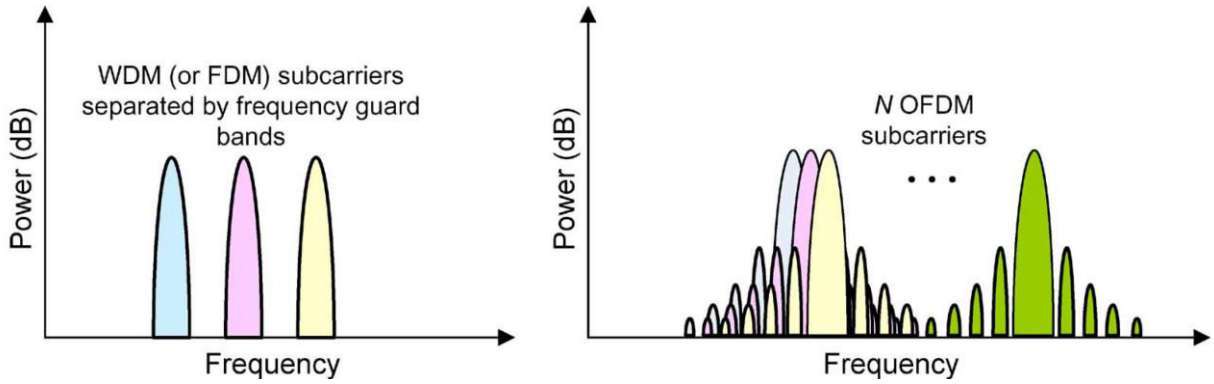

Figure 3.24: Spectrum of WDM or FDM signal (a) and OFDM signal (b) [143].

A real electrical spectrum of the OFDM signal generated at the AWG output is shown in Figure 3.25. The number of subcarriers N_{sc} of the OFDM signal is divided into data subcarriers N_d carrying QPSK, pilot subcarriers N_p, guard lower subcarriers N_{GL}, and guard upper subcarriers N_{GU} as displayed in Figure 3.25. This is in addition to the centered null subcarrier. The structure of an OFDM symbol for 64 subcarriers is illustrated in Figure 3.26.

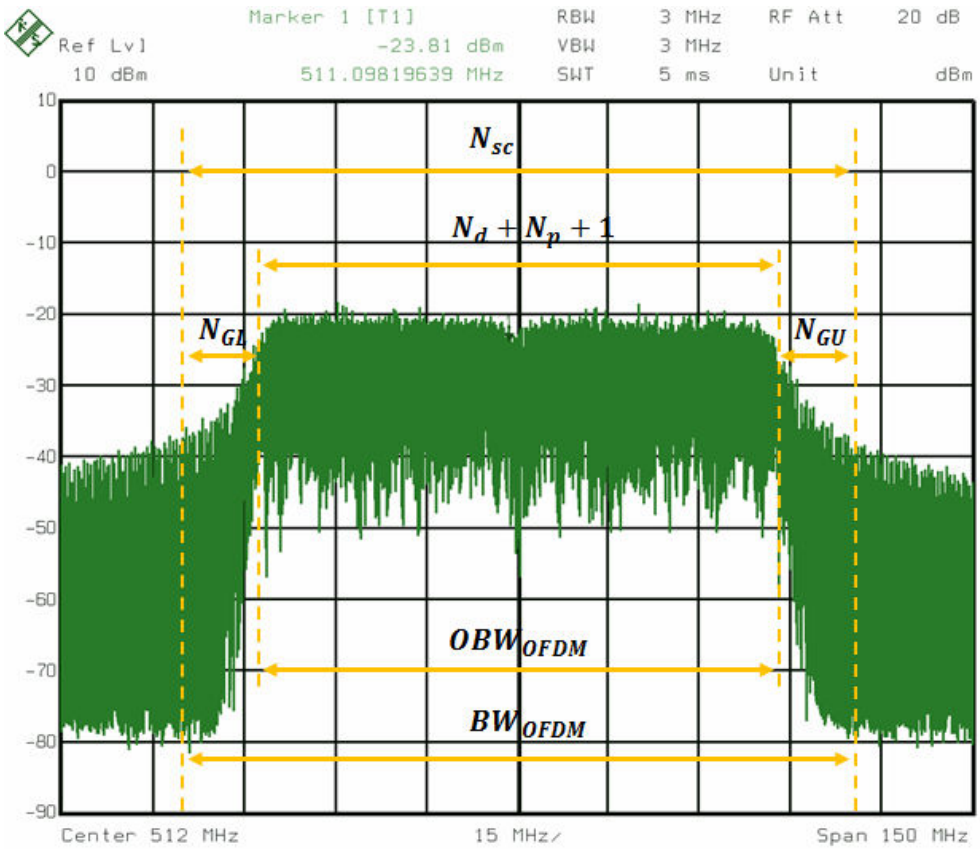

Figure 3.25: Electrical spectrum of an OFDM signal with a number of subcarriers N_{sc}.

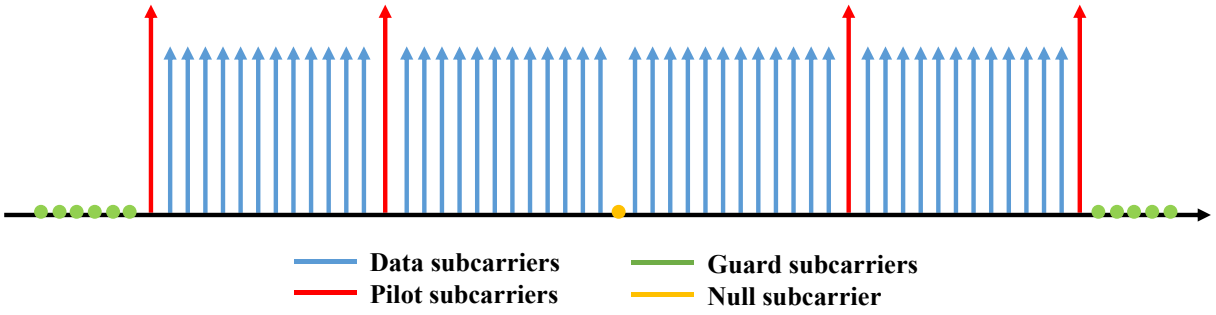

Figure 3.26: OFDM symbol structure for 64 subcarriers including data, pilot, and guard subcarriers.

The bandwidth of the OFDM signal BW_{OFDM} is calculated in Equation (3.38) while the occupied bandwidth of the OFDM signal (OBW_{OFDM}) is the BW_{OFDM} without guard subcarriers as defined in Equation (3.39).

$$BW_{OFDM} = \frac{BW}{N_{sc}}\left(\frac{2}{1+CP} + N_{sc} - 1\right) \quad (3.38)$$

$$OBW_{OFDM} = BW_{OFDM} - \frac{BW}{N_{sc}} N_G = \frac{BW}{N_{sc}} \left(\frac{2}{1+CP} + N_{sc} - N_G - 1 \right) \quad (3.39)$$

Where $N_G = N_{GL} + N_{GU}$ is guard subcarriers and CP is the cyclic prefix.

The CP is transmitted during the guard interval as illustrated in Figure 3.27. It consists of the end of the OFDM symbol copied into the guard interval that is existed between the OFDM symbols. The addition of the CP adds robustness to the OFDM signal. The guard interval introduced by the CP enables the effects of ISI (inter symbol interference) to be reduced.

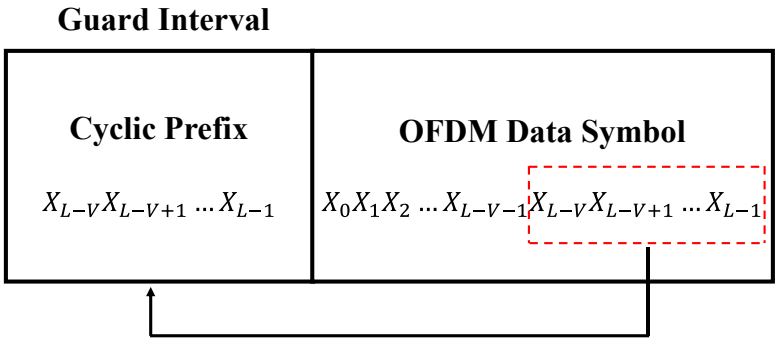

Figure 3.27: Cyclic prefix insertion consists of the end of the OFDM data symbol.

The symbol rate (SR) of the OFDM signal is related to the BW_s and CP as defined in Equation (3.40) while the bit rate (BR) is directly related to the SR and N_{sc} as given in Equation (3.41).

$$SR = \frac{BW_s}{1+CP} \quad (3.40)$$

$$BR = \frac{n.SR.N_d}{N_{sc}} \quad (3.41)$$

Where n is the number of bits of the QPSK signal which is equal to 2 due to subcarriers carrying QPSK data. The increase of the system bandwidth (BW_s) of the OFDM signal leads to increasing the symbol rate (SR). Consequently, this leads to increasing the bit rate (BR).

In our work, $N_{sc} = 64$ subcarriers are utilized to simultaneously transmit OFDM data at the carrier frequency $f_c = 0.512$ GHz by using an arbitrary waveform generator (AWG). The cyclic prefix (CP) is 25 % which is fixed in this measurement. Finally, the electrical OFDM signal is ready to drive directly the optical MZM to modulate the injected continuous wave (CW) signal at the wavelength of data $\lambda_{Dat} = 1545$ nm. $N_{sc} = 64$ subcarriers of the OFDM signal is divided to $N_d = 48$ data subcarriers carrying QPSK, $N_p = 4$ pilot subcarriers, $N_{GL} = 6$ guard lower subcarriers, $N_{GU} = 5$ guard upper subcarriers, and a centered null subcarrier as seen in Table 7.

Table 7: Several numbers of subcarriers including data, pilot, and guard subcarriers.

Subcarriers	8	16	32	64	128
Data	4	10	24	48	98
Pilot	2	2	2	4	8
Guard	1	3	5	11	21

The OFDM signal is studied for different system bandwidths (BW_s) as well as different SRs. The BRs of the 64 subcarriers of OFDM signal calculated in Equation (3.41) is shown Table 8. The increase of BW_s leads to increasing the BR of this signal as given in Table 8.

Table 8: Symbol rates and bit rates of 64 subcarriers OFDM signals.

64 subcarriers OFDM signals		
BW_s (MHz)	SR (MSymb/s)	BR (Mb/s)
8	6.4	9.6
12.8	10.24	15.36
25.6	20.48	30.72
51.2	40.96	61.44
102.4	81.92	122.88
204.8	163.84	245.76

The OFDM signal is also studied for different numbers of the subcarriers to evaluate the quality of the multicarrier transmission system. The BR of the OFDM signals for different numbers of subcarriers at $BW_s = 102.4$ MHz is shown in Table 9.

Table 9: Bit rate of the OFDM signals for different numbers of subcarriers at the system bandwidth $BW_s = 102.4$ MHz.

N_{sc} subcarriers	BR (Mb/s)
8	81.92
16	102.4
32	122.88
64	122.88
128	125.44

3.3.2 Error Vector Magnitude (EVM)

Error vector magnitude (EVM) is a measure of transmission quality. It is normally used with multi-symbol modulation methods. It provides a method to evaluate the performance of a transmission system and is widely used as an alternative to bit error rate (BER) measurements to determine impairments that affect signal reliability. It is the vector difference between ideal and actual transmitted signals as presented in Figure 3.28. Informally, EVM is a measure of how far the points are from the ideal locations. EVM measurements can provide a great deal of insight into the performance of digitally modulated signals.

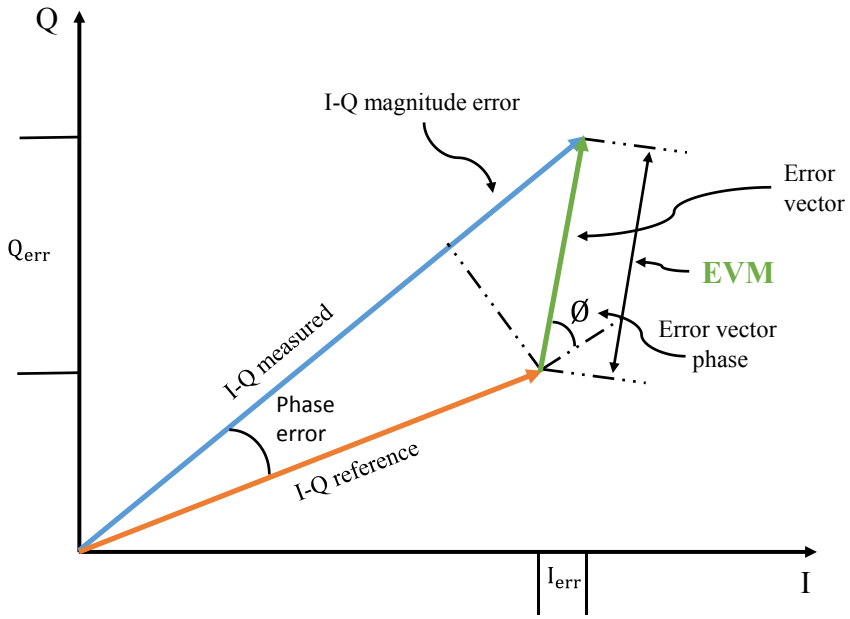

Figure 3.28: Definition of EVM. I_{err} and Q_{err} are respectively in phase and quadratic error.

As depicted in Figure 3.28, the relation between I-Q reference symbol and I-Q measured symbol is observed. The vector between the ideal symbol and the received symbol location is the error vector and the magnitude of that is the error vector magnitude [144]. The magnitude error and the phase error are also observed in Figure 3.28. Mathematically, EVM can be defined as [145]:

$$EVM = \sqrt{\frac{\frac{1}{M}\sum_{t=1}^{M}(|n_{I,t}|^2 + |n_{Q,t}|^2)}{P_0}} \qquad (3.42)$$

Where M is the number of received points, $n_{I,t}$ and $n_{Q,t}$ are the in phase and quadrature error amplitudes of the complex noise being considered that correspond to I_{err} and Q_{err}, respectively, as shown in Figure 3.28, and P_0 is the power of the normalized ideal constellation or the transmitted constellation.

EVM and Signal to noise ratio (SNR) are related to each other as given in the equation below:

$$EVM \approx \frac{1}{k\sqrt{SNR}} \tag{3.43}$$

Where k is the modulation format-dependent factor [144].

The bit error rate (BER) expressed as a percentage is the ultimate criterion used to evaluate the quality of an optical transmission system. The BER is the number of bit errors divided by the total number of conveyed bits during a time interval. It depicts the error probability in terms of number of erroneous bits per bits transmitted. The error probability is defined as the probability of incorrect identification of a bit. BER is directly related to EVM as follows [145]:

$$BER = \frac{2(1-\frac{1}{\sqrt{M}})}{log_2\sqrt{M}} Q\left[\sqrt{\left[\frac{3log_2\sqrt{M}}{M-1}\right] \times \left[\frac{2}{k^2 EVM^2 log_2 M}\right]}\right] \tag{3.44}$$

Where M is the number of states and $Q[.]$ is the Gaussian co-error function. As the signal degrades, the received symbols are located further from their ideal locations and the measured EVM value will increase. Ultimately the symbols will be incorrectly interpreted, and the BER will rise.

3.3.3 Frequency Up-Converted Modulated Data Results

3.3.3.1 Experimental Setup and Back to Back EVM Measurements

The experimental setup used for frequency up-conversion is shown in Figure 3.29. The QPSK and OFDM data generated by the AWG at the carrier frequency $f_c = 0.512$ GHz is applied to the RF input of the optical MZM after being filtered by a low pass filter (LPF) of 1 GHz bandwidth and attenuated by the first electrical attenuator $EAtt_1$. The optical signal is injected at the common input of the two arms of the SOA-MZI (port (C)), its optical mean power is -10 dBm with the wavelength $\lambda_{Dat} = 1545$ nm. The electrical power $P_{e,in,Dat}$ of the QPSK and OFDM signal at the input port (C) is -20.3 dBm at $f_{Dat} = 0.512$ GHz.

The optical pulse source at a repetition rate $f_{sa} = 7.8$ GHz is injected at the upper input of the SOA-MZI (port (A)) at $\lambda_{sa} = 1550$ nm. The optical signal at the SOA-MZI output is photo-detected by a 70 GHz Pd and amplified by a 33 dB LNA after filtering by an optical filter (OF) tuned at λ_{Dat}. The demodulation is performed by using a DSO provided with a sampling rate of 5 Gsa/s and has a 1.5 GHz bandwidth.

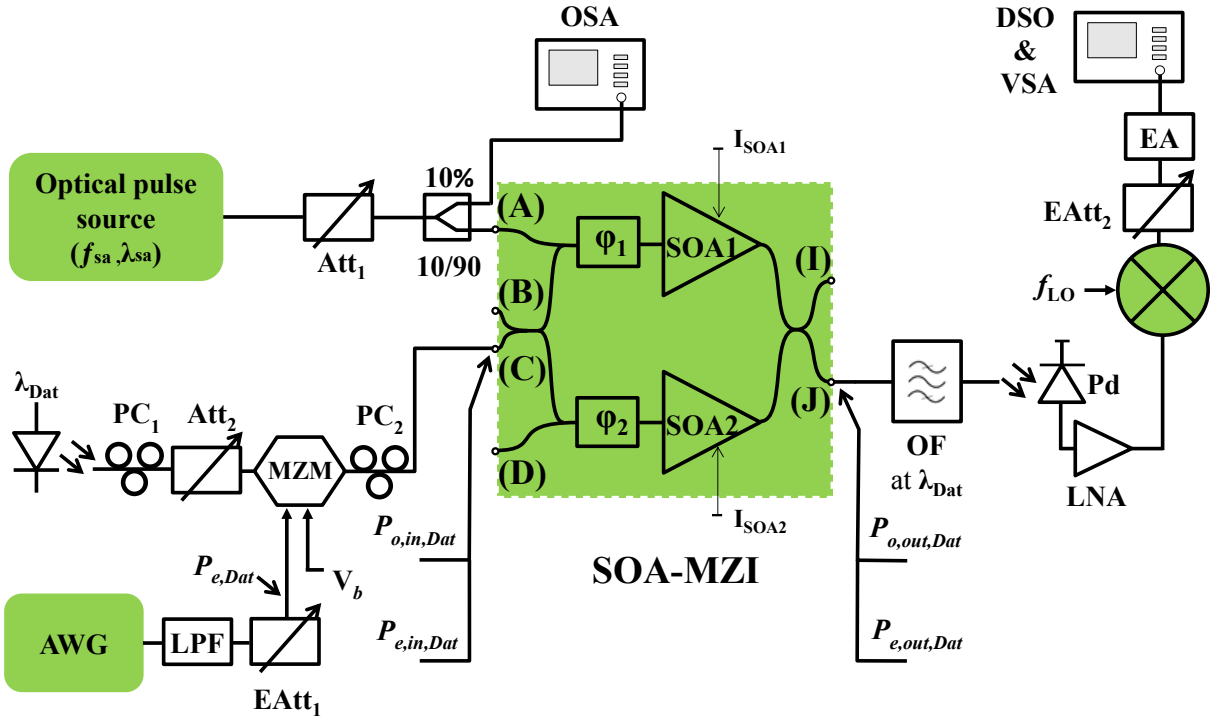

Figure 3.29: Experimental setup of the all-optical sampling mixer for up-converted QPSK and OFDM data. AWG: Arbitrary Waveform Generator, DSO: Digital Sampling Oscilloscope, LNA: Low-Noise Amplifier, MZM: Mach-Zehnder Modulator, OF: Optical Filter, PC: Polarization Controller, Pd: Photodiode, φ: Phase shifter, V_b: Bias Voltage, OSA: Optical Spectrum Analyzer, VSA: Vector Signal Analyzer, LPF: Low Pass Filter, EA: Electrical Amplifier, and EAtt: Electrical Attenuator.

For analyzing the up-conversion by using DSO, the received signal is frequency down-shifted by an electrical mixer to the low frequency at 0.768 GHz with respect to the electrical bandwidth of the real time DSO. The electrical power of the local oscillator (LO) signal at f_{LO} of the electrical mixer is 10 dBm. Before the DSO, the down-converted signal is amplified by using an electrical amplifier (EA) after attenuation by a second electrical attenuator ($EAtt_2$) as shown in Figure 3.29 to avoid the saturation of the EA. The gain and the bandwidth of the EA are respectively 40 dB and 2 GHz.

a) Electrical Back to Back EVM of the QPSK Signal

The electrical back to back EVM of the QPSK data is measured at the AWG board output directly for different symbol rates of 32 MSymb/s, 128 MSymb/s, and 512 MSymb/s that are respectively 0.53 %, 1.68 %, and 1.83 % with fluctuations of approximately $\pm$ 0.25 %.

b) Optical Back to Back EVM of the QPSK Signal

The optical back to back EVM of the optical signal carrying QPSK data, without the SOA-MZI shown in Figure 3.30, is studied for different optical average powers at the Pd input at SR = 32 MSymb/s. The optical back to back EVM of the QPSK and OFDM data is measured at the output of the second polarization controller (PC_2) as shown in Figure 3.29 after being detected by a photodiode (Pd), amplified by a low noise amplifier (LNA), and digitized by a real time digital sampling oscilloscope (DSO). Figure 3.30 shows that the minimum EVMs are in the range of the attenuation of $EAtt_1$ from 12 dB to 21 dB for different optical mean powers.

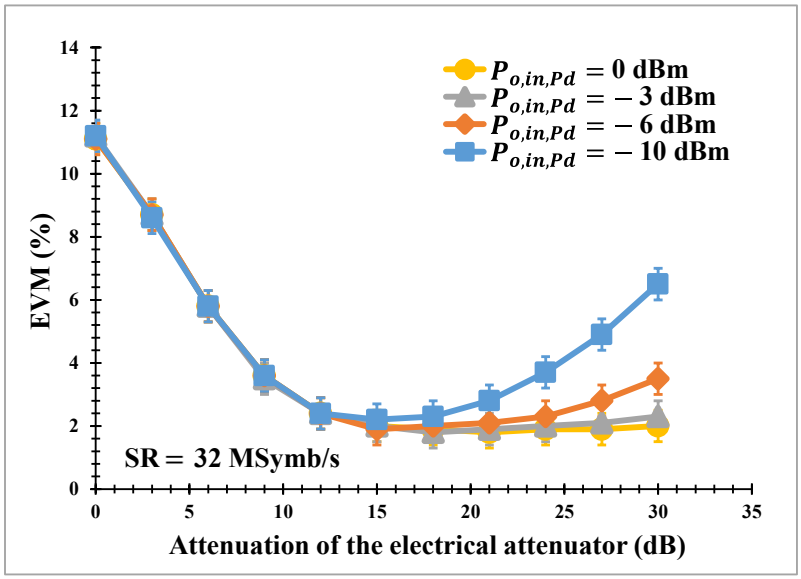

Figure 3.30: Optical back to back EVM of the optical signal carrying QPSK data, without the SOA-MZI, versus the attenuation of $EAtt_1$ at SR = 32 MSymb/s.

The EVM is also measured versus the attenuation of $EAtt_1$ at $P_{o,in,Pd} = -10$ dBm as seen in Figure 3.31. It is measured for three SRs which are 32 MSymb/s, 128 MSymb/s, and 512 MSymb/s. It degrades at high attenuations and with the symbol rate. At SR = 32 MSymb/s, the EVM increases from 2.2 % at 12 dB to 6.5 % at 30 dB. At low attenuation from 0 dB to 12 dB, the EVM decreases for all SRs. The best one is at the attenuation of 13 dB that is 2.1 % at 32 MSymb/s, 4 % at 128 MSymb/s, and 5.3 % at 512 MSymb/s.

We have also measured the optical back to back EVM of the QPSK signal as a function of the optical average power for several symbol rates as seen in Figure 3.32. The $EAtt_1$ attenuation is 13 dB. The EVM decreases as the optical mean power increases for the all symbol rates as observed in Figure 3.32. The minimum EVMs are obtained for the optical powers in the range from −10 dBm to 0 dBm.

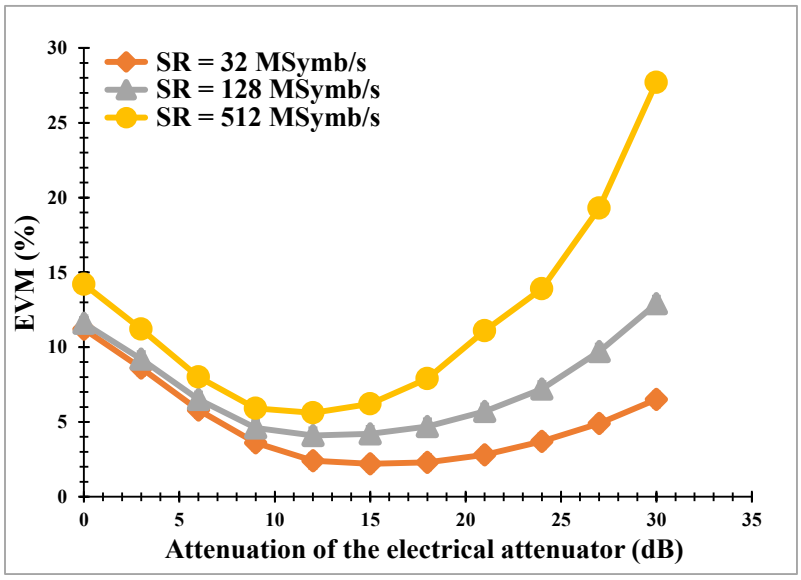

Figure 3.31: EVM versus the attenuation of $EAtt_1$ for different SRs at $P_{o,in,Pd} = -10$ dBm.

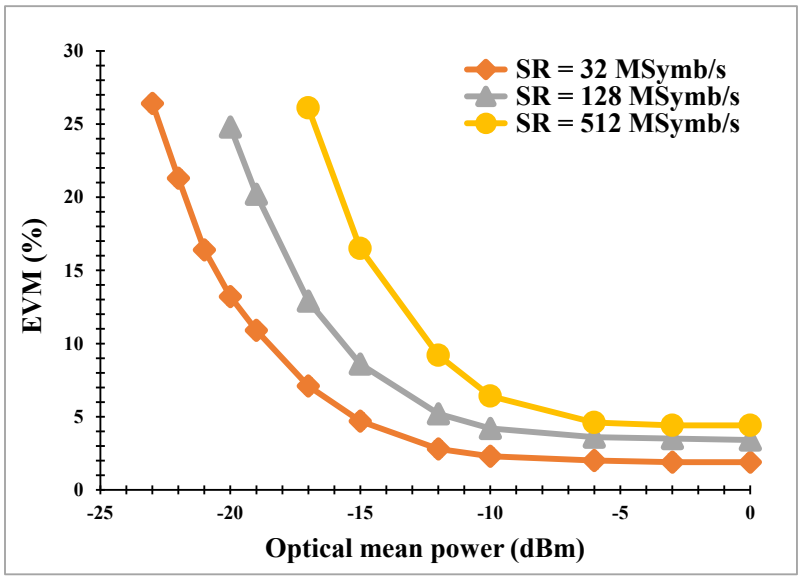

Figure 3.32: Optical back to back EVM versus the optical mean power for different SRs.

Back to back EVM of the QPSK signal versus the symbol rate at $P_{o,in,Pd} = -10$ dBm is shown in Figure 3.33. The attenuation of $EAtt_1$ is 13 dB. The EVM increases as the SR increases. It ranges from 1.5 % at the minimum symbol rate $SR_{min} = 8$ MSymb/s to 5.6 % at the maximum one $SR_{max} = 512$ MSymb/s. The increase of the SR leads to increase the BW of the QPSK signal. This also leads to increase the noise power while the total signal power is not changed.

The ratio of the EVM between two symbol rates x and y is related to the ratio of symbol rates SR_x/SR_y by:

$$\frac{EVM_x}{EVM_y} = \frac{\sqrt{SNR_y}}{\sqrt{SNR_x}} = \frac{\sqrt{P_{noise,x}}}{\sqrt{P_{noise,y}}} = \frac{\sqrt{(1+a)SR_x}}{\sqrt{(1+a)SR_y}} = \frac{\sqrt{n.SR_y}}{\sqrt{SR_y}} = \sqrt{n} \qquad (3.45)$$

Where n is an integer defined as $n = SR_x/SR_y$. It is observed that the SNR decreases by the factor n while the EVM increases by the factor of $\sqrt{n}$ as defined in Equation (3.45) when the symbol rate increases. Due to fluctuations in the measured values of the back to back EVM at the common port of the SOA-MZI (port (C)), a fitting $\sqrt{n}$ equation has been plotted for QPSK modulation.

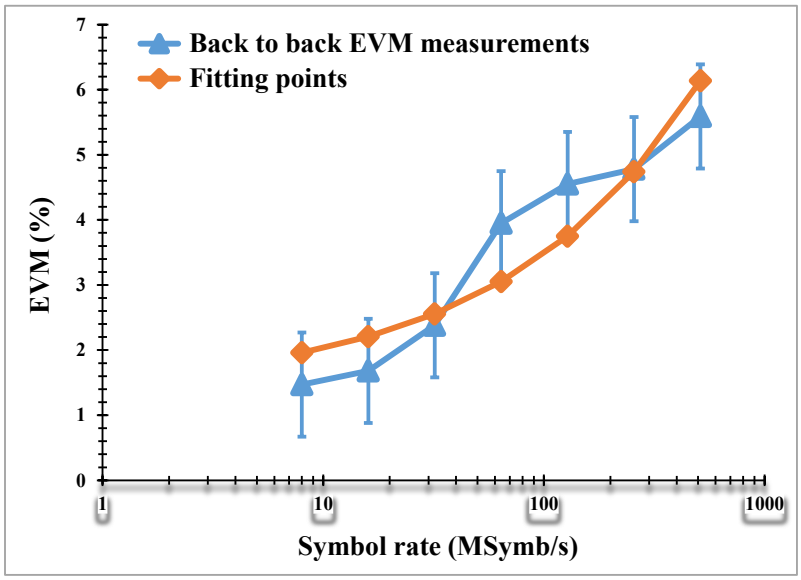

Figure 3.33: Optical back to back EVM for different SRs and the fitting points.

We can observe in Figure 3.33 the different fluctuations of the EVM with the symbol rate. It is worth noting that the measured EVM fluctuates around $\pm$ 0.8 %, as a maximum, at the symbol rates of 64 MSymb/s and 128 MSymb/s.

c) Optical Back to Back EVM of the OFDM Signal

The AWG board generates an OFDM signal driven by 64 subcarriers at f_c = 0.512 GHz for different system bandwidth BW_s. The optical back to back EVM of the OFDM signal versus the attenuation of $EAtt_1$ is measured for different optical mean powers at BW_s = 102.4 MHz as shown in Figure 3.34. It shows that the best EVMs are in the range of the attenuation from 9 dB to 15 dB for different optical mean powers. The EVMs degrade slightly at -6 dBm, -3 dBm, and 0 dBm at high attenuations while the EVM degrades considerably at -10 dBm at high ones. Hence, the best EVM is at the attenuation of 10 dB for all optical powers that is used in the frequency up-conversion technique of an optical signal carrying OFDM data.

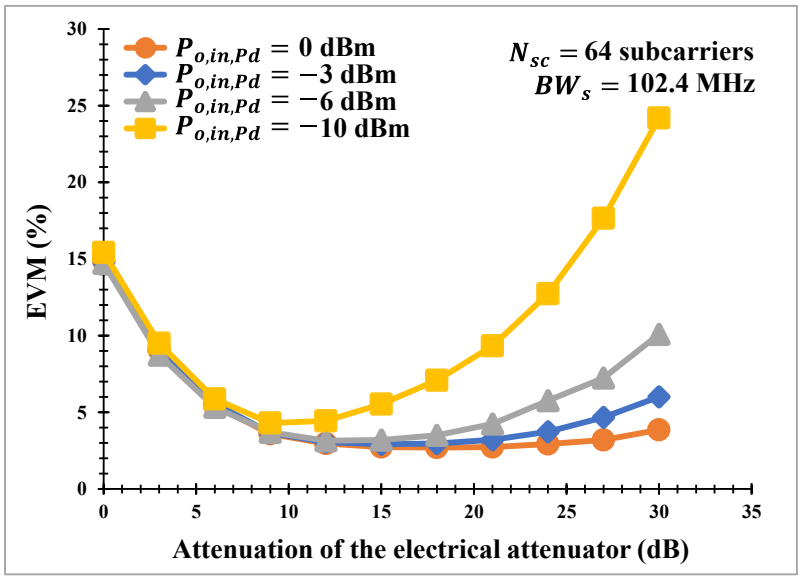

Figure 3.34: Optical back to back EVM of the OFDM signals as a function of the attenuation of $EAtt_1$ for different optical powers at $BW_s = 102.4$ MHz.

The EVM is also measured versus the optical average power $P_{o,in,Pd}$ of the OFDM signal for different system bandwidths as shown in Figure 3.35. The attenuation of $EAtt_1$ is 10 dB. The EVM decreases as $P_{o,in,Pd}$ increases while it degrades with the system bandwidth. It decreases from 24.2 % at $P_{o,in,Pd} = -24$ dBm to 2.8 % at −2 dBm for $BW_s = 25.6$ MHz. As a result, the best EVMs are in the range of $P_{o,in,Pd}$ from −10 dBm to −2 dBm.

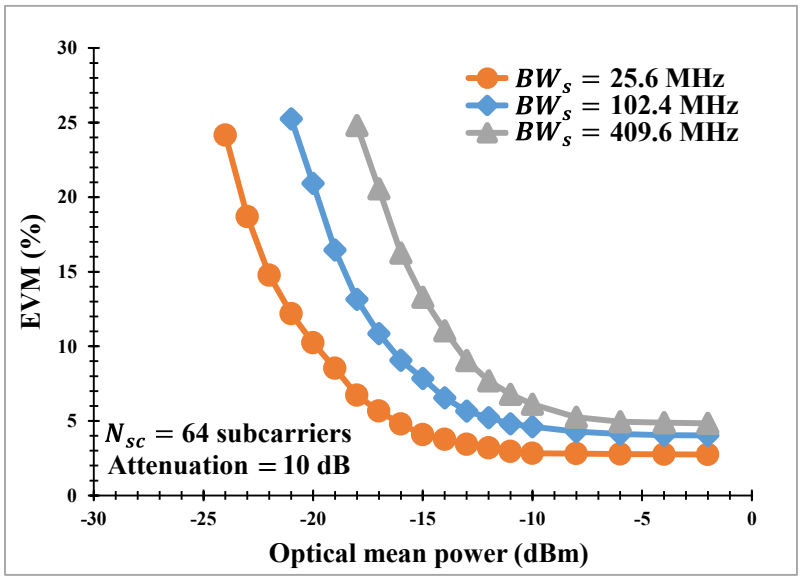

Figure 3.35: Optical back to back EVM as a function of the optical average power at the attenuation of 10 dB.

The OFDM signals are generated for different numbers of subcarriers to evaluate the EVM. Figure 3.36 shows the EVM versus $P_{o,in,Pd}$ at BW_s = 102.4 MHz for different numbers of subcarriers. There is slight effect when N_{sc} increases as observed in Figure 3.36. The EVM improves 1 % at 128 subcarriers at the average power higher than −10 dBm while it degrades 1 % at the one lower than −18 dBm. As a result, the EVM is the same for all numbers of subcarriers while this variation is due to fluctuation of the OFDM signal at all average powers.

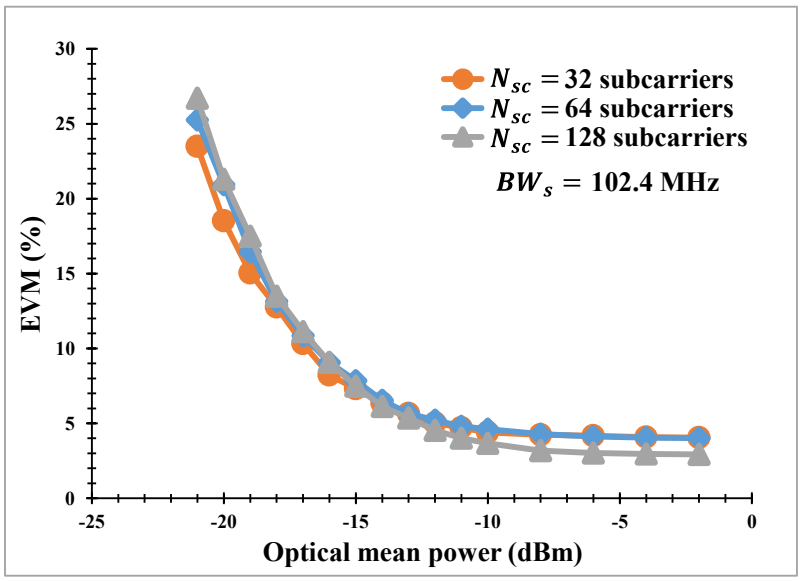

Figure 3.36: Optical back to back EVM for several numbers of subcarriers at BW_s = 102.4 MHz.

The optical back to back EVM of the OFDM signal is also measured as a function of the symbol rate (SR) at $P_{o,in,Pd} = -10$ dBm as shown in Figure 3.37. The electrical power $P_{e,Dat}$ is attenuated by 10 dB of $EAtt_1$ before being injected into the RF input of the optical MZM. The back to back EVM degrades as the symbol rate increases. It increases from 2.6 % at SR = 6.4 MSymb/s to 5.6 % at SR = 163.84 MSymb/s.

Fitting points are plotted in Figure 3.37 to indicate the fluctuations of the measured EVM for the OFDM modulation at different symbol rates. As observed in Figure 3.37, the measured EVM is close to its fitting point at all the symbol rates except at the higher ones. It fluctuates around ± 0.8 % at the symbol rate of 163.84 MSymb/s.

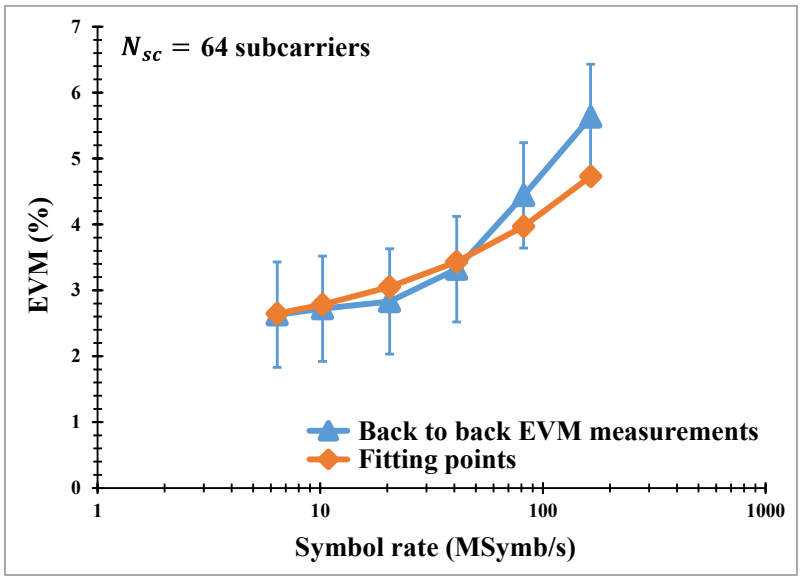

Figure 3.37: Optical Back to back EVM of the OFDM signal at the common port of the SOA-MZI (port (C)).

Comparing the results in Figure 3.37 and Figure 3.33, one can conclude that the back to back EVMs of OFDM and QPSK signals are close.

3.3.3.2 QPSK and QPSK-OFDM Frequency Up-Conversion Experimental Results

The EVM of up-converted symbols at the SOA-MZI output is measured for different SRs and for the first five target frequencies $nf_{sa} - f_{Dat}$ where f_{sa} is set at 7.8 GHz as shown in Figure 3.38. The EVM degrades when the target frequency increases. It also degrades with the SR.

For up-converted QPSK data, the EVM ranges from 8 % at the lower target frequency $f_{sa} - f_{Dat}$ at the minimum symbol rate $SR_{min} = 8$ MSymb/s to 14 % at the higher target frequency $5f_{sa} - f_{Dat}$. It reaches 27.4 % which is below the forward error correction (FEC) limit for BER $= 3.8\times10^{-3}$ [146] at the maximum symbol rate $SR_{max} = 128$ MSymb/s at $5f_{sa} - f_{Dat}$ as displayed in Figure 3.38(a).

For up-converted OFDM signal, the EVM ranges from 5.5 % at $f_{sa} - f_{Dat} = 7.288$ GHz at $SR_{min} = 6.4$ MSymb/s to 15.8 % at $5f_{sa} - f_{Dat} = 38.488$ GHz. It reaches 33 % which is below the FEC limit for BER $= 3.8\times10^{-3}$ at $SR_{max} = 163.84$ MSymb/s at $5f_{sa} - f_{Dat} = 38.488$ GHz as observed in Figure 3.38 (b).

As a result, the bit rate (BR) can attain 256 Mb/s for QPSK signals and 245.76 Mb/s for OFDM signals.

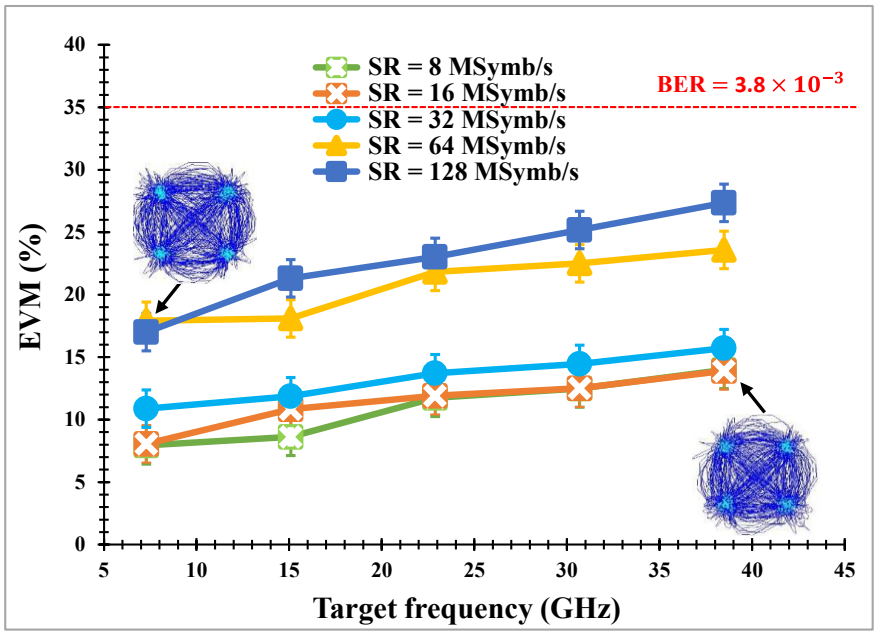

(a)

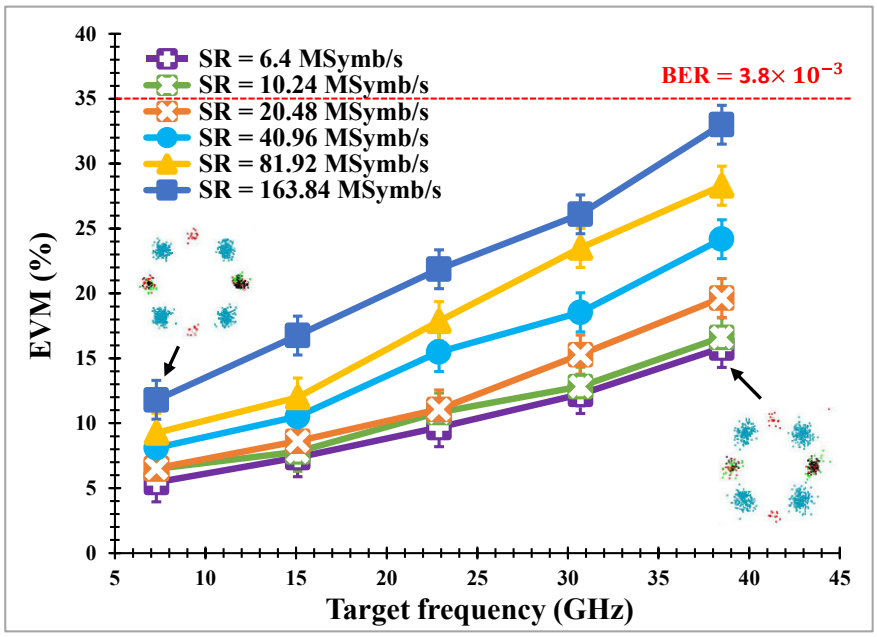

(b)

Figure 3.38: EVM of a frequency up-converted QPSK signal (a) and a frequency up-converted OFDM signal (b) from f_{Dat} to target frequencies $nf_{sa} - f_{Dat}$.

The OFDM signals are generated for different numbers of subcarriers at SR = 81.92 MSymb/s at the input port (C), these signals are up-converted at the SOA-MZI output at $nf_{sa} - f_{Dat}$. The demodulation of EVM for different numbers of subcarriers is shown in Figure 3.39. It is

observed that the EVM has a tendency to slightly degrade as the number of subcarriers increases. It increases about 1.5 % at 128 subcarriers compared to the one at 8 subcarriers for all target frequencies.

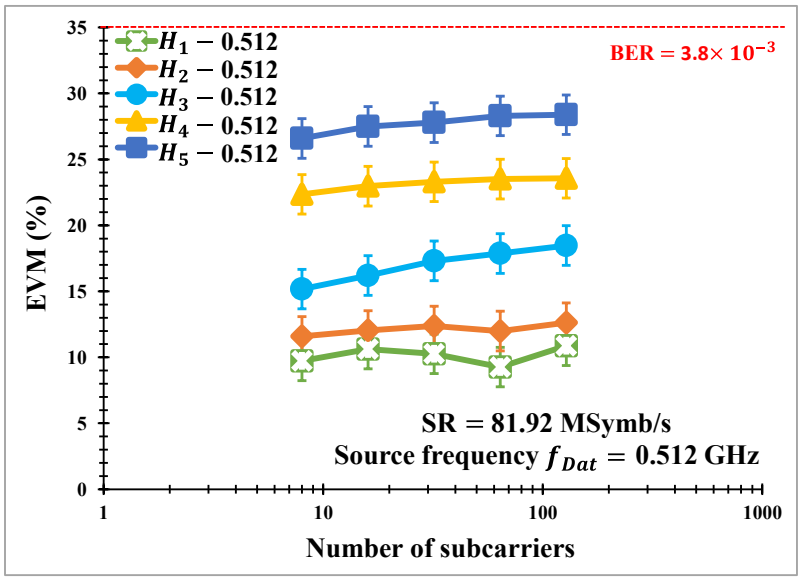

Figure 3.39: Demodulation of the up-converted OFDM signals for different numbers of subcarriers.

The frequency conversion of up-converted QPSK data is also evaluated through EVM for different sampling frequencies of the optical pulse source, see Figure 3.40.

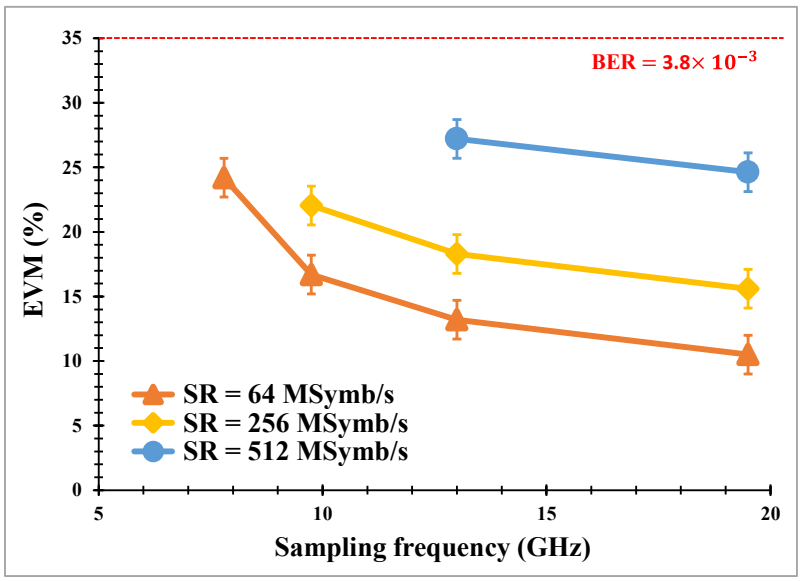

Figure 3.40: EVM of a frequency up-converted QPSK signal from $f_{Dat} = 0.512$ GHz to target frequency of 38.488 GHz for three different symbol rates.

The EVM of the up-converted QPSK data is measured versus the repetition frequency for three different symbol rates as shown in Figure 3.40. The EVM is only measured at the target frequency $5f_{sa} - f_{Dat} = 38.488$ GHz related to the common harmonic at the frequency of 39 GHz for all repetition frequencies. It decreases as the repetition frequency increases. The improvement of the EVM for the common harmonic at 39 GHz is mainly due to increasing the harmonic power and reducing the harmonic order. The obtained results show that a bit rate of 1024 Mb/s can be attained at H_2 and H_3 for $f_{sa} = 13$ GHz and 19.5 GHz, respectively.

3.3.4 Frequency Down-Converted Modulated Data Results

3.3.4.1 Experimental Setup

The experimental setup of the all-optical sampling mixer to obtain the down-converted signal at the SOA-MZI output is shown in Figure 3.41. The sampling signal at the repetition rate $f_{sa} = 7.8$ GHz is used at the input port (A) of the SOA-MZI with the wavelength $\lambda_{sa} = 1550$ nm.

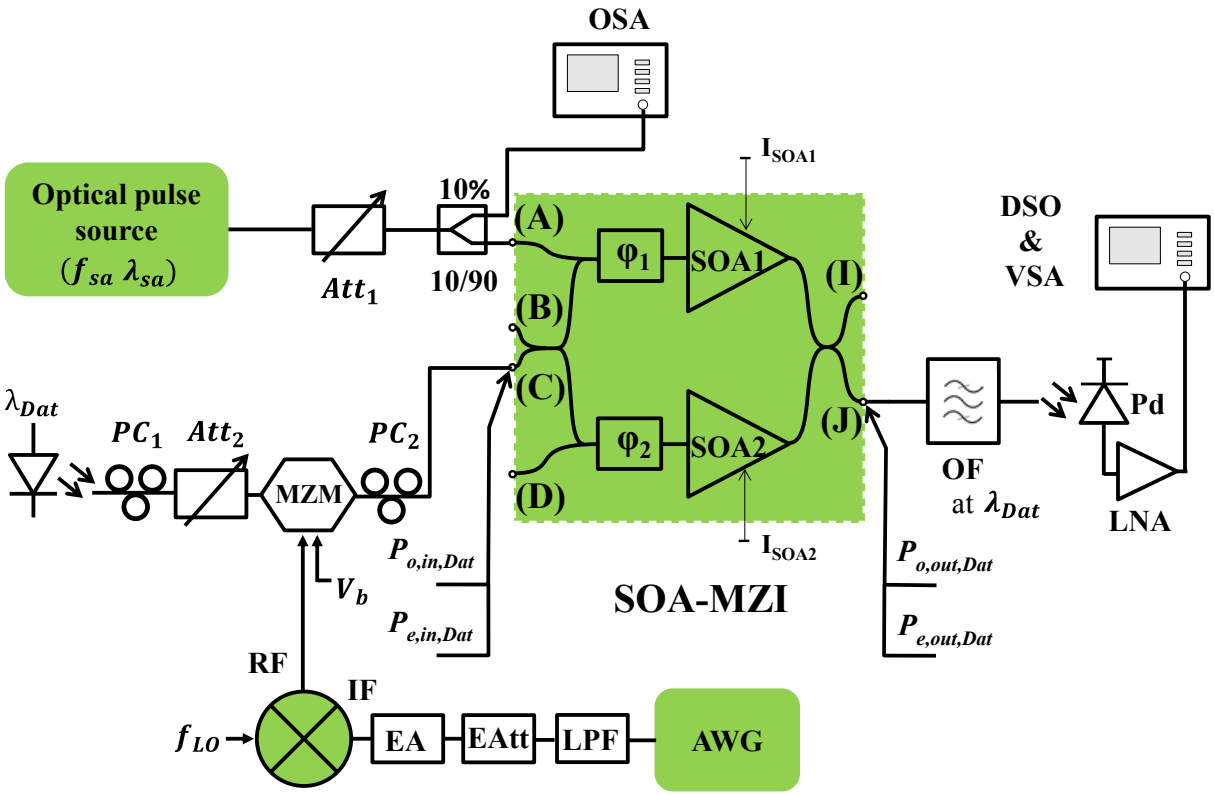

Figure 3.41: Experimental setup of the all-optical sampling mixer for down-conversion. AWG: Arbitrary Waveform Generator, DSO: Digital Sampling Oscilloscope, LNA: Low-Noise Amplifier, OF: Optical Filter, PC: Polarization Controller, Pd: Photodiode, φ: Phase shifter, V_b: Bias Voltage, VSA: Vector Signal Analyzer, LPF: Low Pass Filter, EA: Electrical Amplifier, LO: Local Oscillator, RF: Radio Frequency, IF: Intermediate Frequency, and EAtt: Electrical Attenuator.

The QPSK and OFDM signals are generated by the AWG board at the carrier frequency $f_c =$ 0.512 GHz. The QPSK and OFDM signals at the mixer IF input are at $f_c = 0.512$ GHz. These signals are frequency up-converted at the source frequencies $H_n - 0.312$ at the input port (C) of the SOA-MZI as shown in Figure 3.41. The optical mean power $P_{o,in\,Dat}$ at the input port (C) is -10 dBm with the wavelength of data $\lambda_{Dat} = 1545$ nm. The range of the QPSK symbol rates is changed from 8 MSymb/s to 128 MSymb/s and the one of OFDM symbol rates was shown in Table 8.

The experimental setup, shown in Figure 3.41, is used to achieve the frequency down-conversion technique. The maximum electrical power of the QPSK and OFDM signal at the IF input of the electrical mixer is 5 dBm after being attenuated by 26 or 14 dB of the electrical attenuator (EAtt) at 0.512 GHz, respectively. The electrical power at the local oscillator (LO) input of the electrical mixer is 10 dBm at the frequencies $H_n - 0.824$. The output RF signal of the mixer is at $H_n - 0.312$. This signal is applied to the RF input of the MZM. The electrical power of the QPSK and OFDM signal at the input port (C) $P_{e,in,Dat}$ is -27.8 dBm at $H_n -$ 0.312.

The optical signals at the input port (C) at the source frequencies $H_n - 0.312$ are frequency down-converted at the target frequency of 0.312 GHz at the SOA-MZI output. These down-converted signals at 0.312 GHz are photo-detected by a 70 GHz photodiode (Pd) and amplified by a 33 dB low noise amplifier (LNA). Then, the real time digital sampling oscilloscope (DSO) is used to digitize the received signals and the VSA software demodulates them.

3.3.4.2 QPSK and QPSK-OFDM Frequency Down-Conversion Experimental Results

The EVM of the down-converted QPSK and OFDM signals increases as the source frequency increases at the SOA-MZI output as seen in Figure 3.42. It also increases with the symbol rate.

The EVM ranges, for QPSK signal as observed in Figure 3.42(a), from 3.5 % from the lower source frequency $H_1 - 0.312$ at $SR_{min} = 8$ MSymb/s to 14.4 % from the higher source frequency $H_5 - 0.312$. It reaches 31.8 % which is below the FEC limit for BER = 3.8×10^{-3} at the maximum symbol rate $SR_{max} = 128$ MSymb/s from the source frequency $H_4 - 0.312$ as observed in Figure 3.42. The EVM degrades highly and it is not possible to be measured at the symbol rate higher than 128 MSymb/s from $H_5 - 0.312$ at $f_{sa} = 7.8$ GHz.

The EVM degrades, for OFDM data as seen in Figure 3.42(b), from 7.6 % from the source frequency $H_1 - 0.312$ at $SR_{min} = 6.4$ MSymb/s to 17.8 % from $H_5 - 0.312$. The EVM reaches 31.6 % which is below the FEC limit for BER = 3.8×10^{-3} at $SR_{max} = 163.84$ MSymb/s from $H_5 - 0.312$. The SR_{max} of the down-converted QPSK and OFDM signals from $H_5 - 0.312$ reaches up to 64 MSymb/s and 163.84 MSymb/s, respectively. This corresponds to the maximum bit rate (BR) of 128 Mb/s and 245.76 Mb/s, respectively.

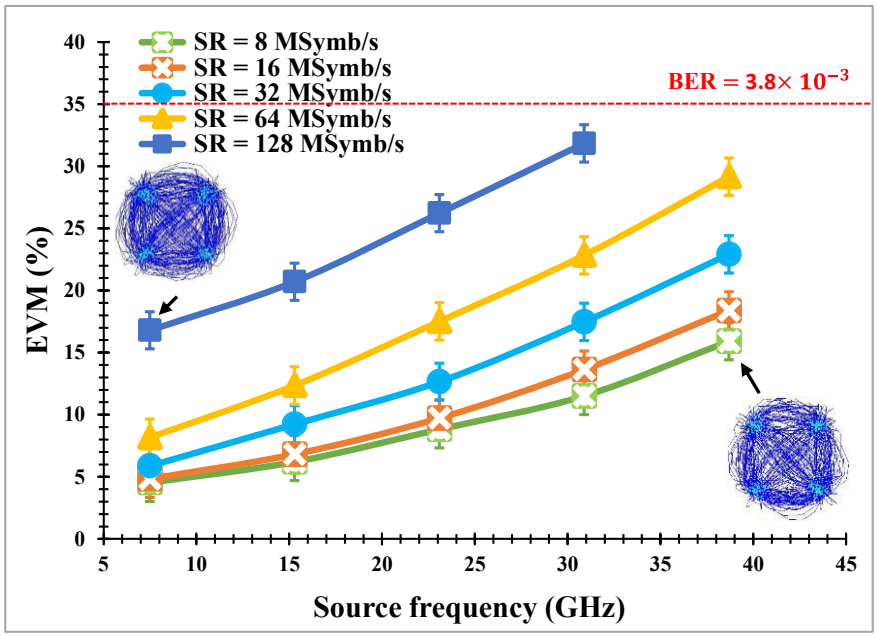

(a)

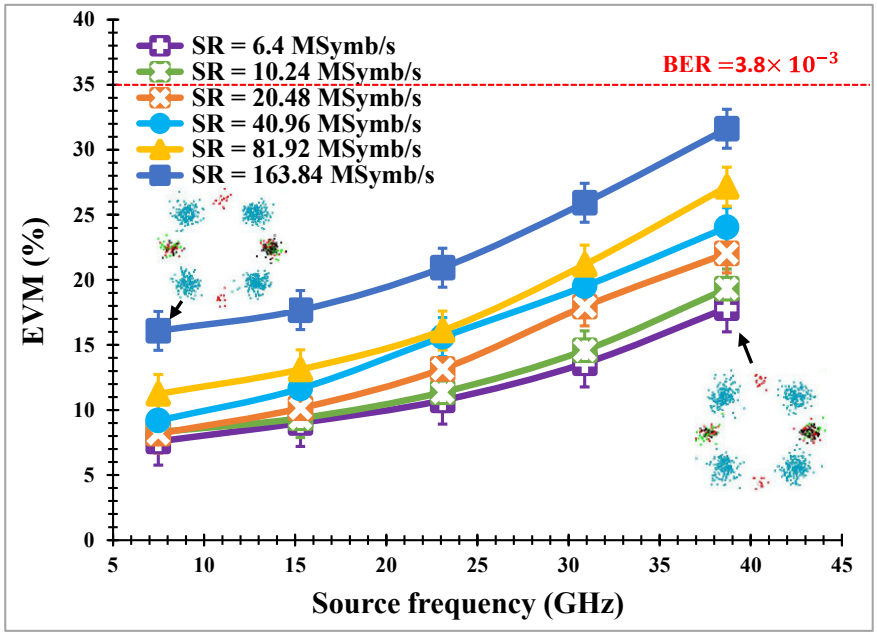

(b)

Figure 3.42: EVM of a frequency down-converted QPSK signal (a) and a frequency down-converted OFDM signal (b) from source frequencies $H_n - 0.312$ to 0.312 GHz.

The comparison of EVM in results in Figure 3.38(a) and Figure 3.42 shows that the EVM is better for the frequency down-conversion case from the first three source frequencies for all symbol rates except the maximum one. The reverse situation applies for the two higher

frequencies due to quadratic degradation of the EVM as the frequency increases. The maximum symbol rate of the QPSK signals reaches up to 128 MSymb/s for up-conversion at $H_5 - 0.512$ related to the fifth harmonic H_5 of the sampling signal and 64 MSymb/s for down-conversion from $H_5 - 0.312$ related to H_5.

The comparison in results between the up-converted OFDM signals shown in Figure 3.38(b) and the down-converted OFDM signals shown in Figure 3.42(b) shows that the EVM is better for the frequency up-conversion case for the all target frequencies at the first four symbol rates with an average value of 1.6 %. The maximum symbol rate of the OFDM signals reaches up to 163.84 MSymb/s for frequency up-conversion at the maximum target frequency related to H_5 and frequency down-conversion from the maximum source frequency related to H_5. As a result, the EVM of the up-converted and down-converted OFDM signals is very close to each other for all symbol rates.

The down-converted OFDM signals are studied for different numbers of subcarriers at SR = 81.92 MSymb/s at the SOA-MZI output. The EVM increases with the source frequency for all numbers of subcarriers as shown in Figure 3.43. The EVM slightly increases with the number of subcarriers. The difference between the EVM at 128 subcarriers and the one at 8 subcarriers is less than 1 % for all target frequencies. This result has the same behavior of the EVM of the up-converted OFDM signals shown in Figure 3.39.

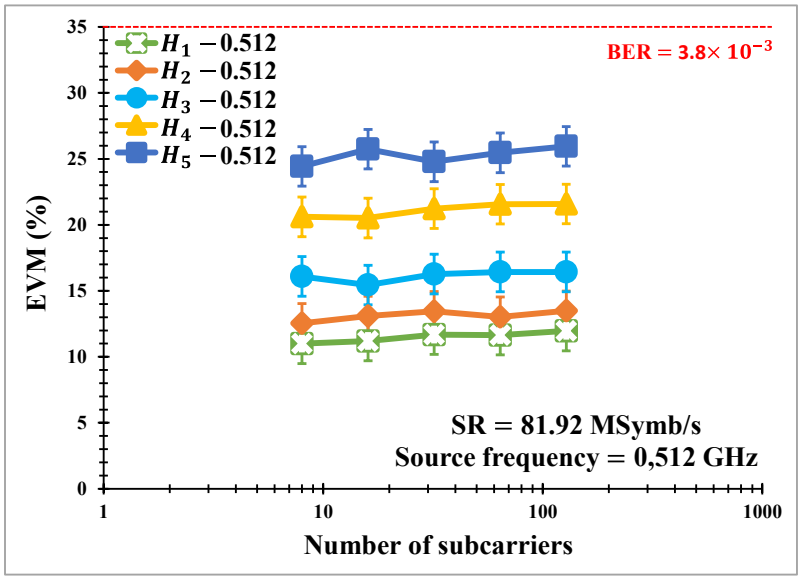

Figure 3.43: Demodulation of the down-converted OFDM signals for different numbers of subcarriers at SR = 81.92 MSymb/s.

The comparison in EVMs between up-converted and down-converted signals shows that the EVM is better for down-conversion which improves about 1.5 % with the source frequency for

each number of subcarriers. As a result, the benefit of increasing the number of subcarriers is approximately the same for up-conversion and down-conversion.

The EVM of the down-converted QPSK signals is measured versus the sampling frequency for different symbol rates as shown in Figure 3.44. The EVM is only measured from the source frequency $H_5 - 0.312 = 38.688$ GHz related to the common harmonic of the sampling signal at the frequency of 39 GHz for all sampling frequencies of the optical pulse source.

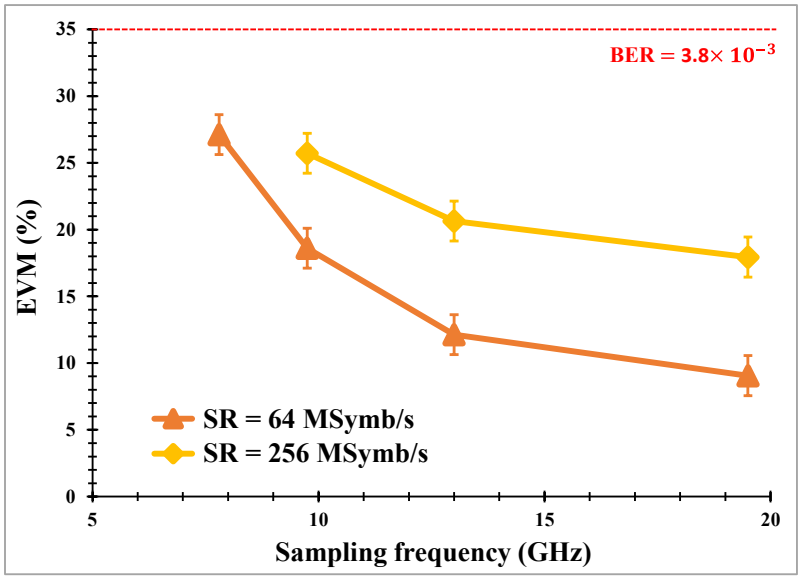

Figure 3.44: EVM of a down-converted QPSK signal from the source frequency of 38.688 GHz to target frequency of 0.312 GHz for two different symbol rates.

The EVM decreases as the sampling frequency increases for all the symbol rates. It ranges from 27.2 % at $f_{sa} = 7.8$ GHz to 10.1 % at $f_{sa} = 19.5$ GHz at SR = 64 MSymb/s. This improvement is due to increasing the harmonic power with the sampling frequency and decreasing the harmonic order. The EVM at $f_{sa} = 19.5$ GHz at SR = 256 MSymb/s reaches 17.9 % which is 7.8 % higher than the one at SR = 64 MSymb/s at the same sampling frequency. The symbol rate at $f_{sa} > 9.75$ GHz can attain 256 MSymb/s with more improvement in comparison to the symbol rate obtained at $f_{sa} = 7.8$ GHz (64 MSymb/s).

The comparison of the EVM between the up-converted QPSK signal shown in Figure 3.40 and the down-converted QPSK signal shown in Figure 3.44 shows that the EVM decreases with the sampling frequency for all symbol rates. The EVM at SR = 256 MSymb/s at $f_{sa} = 19.5$ GHz is 17.9 % for down-conversion while it is 24.6 % at SR = 512 MSymb/s at the same sampling frequency for up-conversion. As a result, the increase of the sampling frequency from 7.8 GHz to 19.5 GHz leads to improving the bit rate from 256 Mb/s to 1024 Mb/s for up-conversion and from 128 Mb/s to 512 Mb/s for down-conversion.

3.4 Conclusion

The experimental results of an all-optical radiofrequency sampling mixer based on a SOA-MZI controlled by a 10 ps pulse width of an optical pulse source are presented. By using up to the fifth harmonic of the sampling signal, all-optical frequency up-conversion and frequency down-conversion can be performed in the range 0.5-39.5 GHz. The frequency characteristics of the sampled signals are exploited to frequency shift with the same configuration, to lower or higher frequencies, QPSK and QPSK-OFDM data. The efficiency of this mixer has been evaluated through conversion gain, isolation, and third order intercept point.

The theoretical study of the SOA-MZI is developed to obtain the conversion gain for up-conversion and down-conversion by using a small signal modal. A qualitative analysis that explains the difference between up and down-conversion gains is achieved. This quantitative analysis could be completed in future work.

Frequency conversion in presence of QPSK and OFDM data shows exploitable EVM for bit rates up to 256 Mb/s and 245.76 Mb/s for frequency up-conversion and frequency down-conversion, respectively at the sampling frequency of 7.8 GHz of the optical pulse source. We show also that the conversion gains are improved by increasing the sampling frequency related to the common harmonic at the frequency of 39 GHz about 11.3 dB for up-conversion and 15.3 dB for down-conversion. Thanks to this, the frequency conversion of QPSK data shows that transmission up to 1024 Mb/s for up-conversion and 512 Mb/s for down-conversion can be obtained.

Chapter Four

Frequency Conversion by Using the SOA-MZI Differential Configuration

4.1 Principle of All-Optical Mixing Based on the SOA-MZI Differential Configuration

Wavelength conversion based on the SOA-MZI [147] [148] [149] [150] [151] [152] [153] [154] [155] where the high bit rate can be obtained thanks to the differential configuration. Working on the differential scheme with the SOA-MZI can deploy to operate beyond the speed limitation of the SOAs.

In our work, the standard configuration where one input is only used to control the optical switch state has tuning the switch ON time faster than turning the switch OFF due to the gain recovery time of SOA1. One solution to speed up this operation is to use a SOA-MZI differential configuration. Both input ports at the upper and the lower arms of the SOA-MZI are driven by the clock signal, each one is sent to an arm of the SOA-MZI, but the control at the input port of the lower arm is slightly delayed by a differential delay time $\Delta\tau$ compared to the one applied at the input port of the upper arm as exhibited in Figure 4.1.

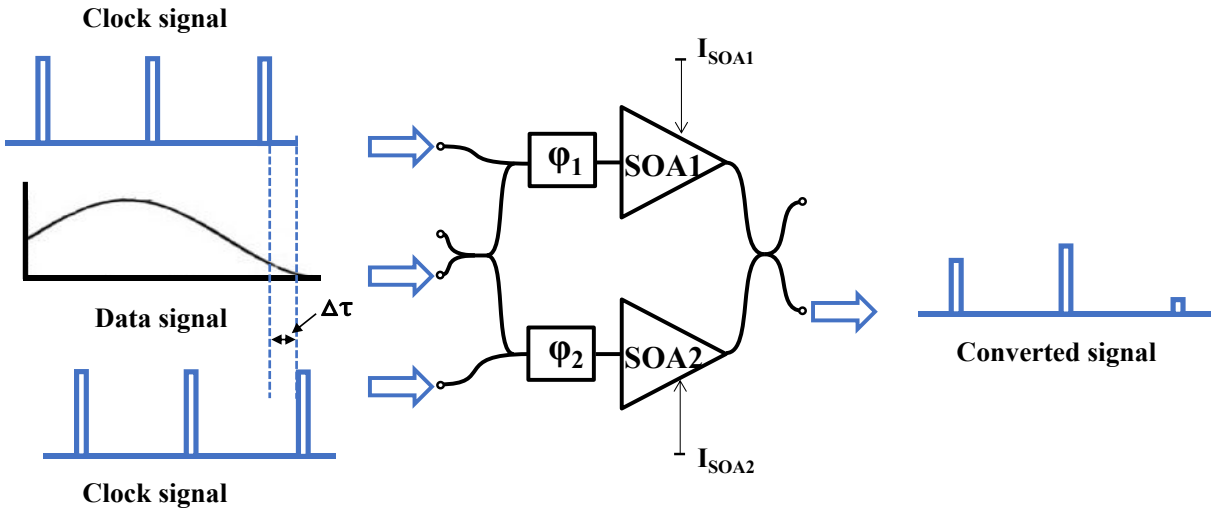

Figure 4.1: Description of the principle of the SOA-MZI differential configuration scheme based on sampling.

The carrier densities of both SOAs are affected by inserting two clock signals. The first clock signal modulates the phase of the data at the upper arms and the second one at the lower arm is responsible to produce also a phase modulation. The delayed signal at the input port after attenuation traveling in the lower arm is used to cancel the broadened converted pulse due to the slow SOA recovery time. This configuration which actively turns off the optical switch [156] leads to create a transmission window as illustrated in Figure 4.2 and also leads to reduce the switching speed of the SOA-MZI for an optimum value of a differential delay time $\Delta\tau$ where

the performances of the frequency mixing by the sampling technique can be enhanced in a SOA-MZI differential configuration.

Figure 4.2 shows the operation principle for generating the transmission window based on the SOA-MZI differential configuration. Figure 4.2(a) and (b) illustrate the input pulse at the upper and lower arms respectively. The time evolution of the acquired gain and phase of the upper and lower arm in the presence of a control clock signal is shown in Figure 4.2(c) and (d), respectively. Figure 4.2(e) shows the resulting transmission window at the SOA-MZI output.

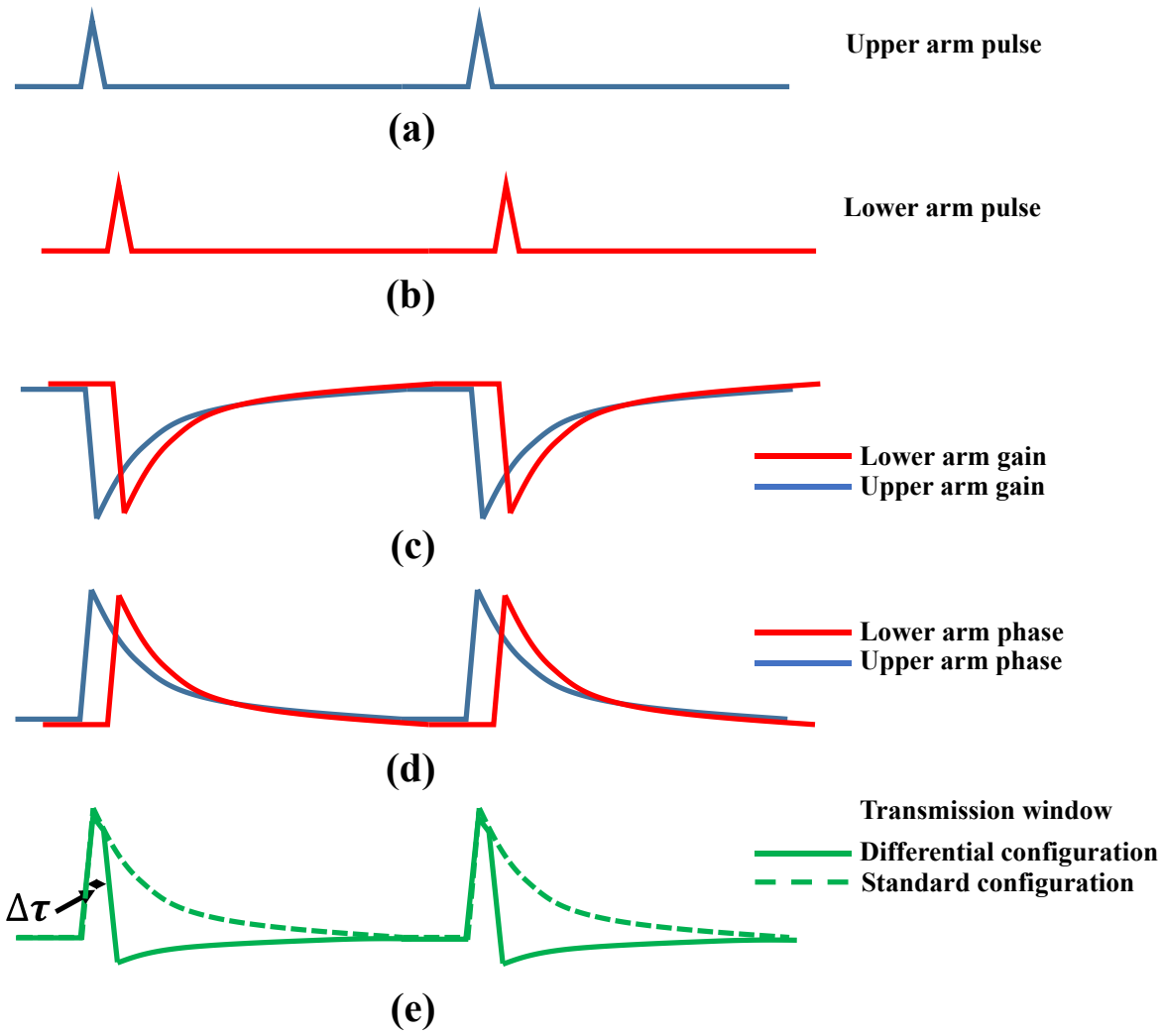

Figure 4.2: Principle of generation the transmission window at the SOA-MZI output. The pulse at the SOA1 input (a) and SOA2 input (b), the gain at the SOA1 and SOA2 output (c), the phase at the SOA1 and SOA2 output (d), and the generation of the transmission window (e). $\Delta\tau$ is a differential delay time.

When the two clock signals are injected into the SOA-MZI inputs, the gain of each SOA is saturated at different times separated by $\Delta\tau$, while the optical power of the clock signals induces

in this way a differential phase shift $\Delta\Phi$ for the time fraction $\Delta\tau$. This differential drive of the SOA-MZI improves the dynamic characteristics of the optical switch compared to the standard configuration.

In this chapter, the differential experimental setup is first presented. The conversion gain and the EVM of the up-converted and down-converted QPSK and QPSK-OFDM signals are given and compared with the SOA-MZI standard configuration.

4.2 Frequency Conversion Based on the SOA-MZI Differential Configuration

4.2.1 Experimental Setup Description

In order to improve the efficiency of the frequency conversion technique through the conversion gain G_c and the quality of the transmission system through EVM of the frequency up-converted signal at the target frequency $H_5 - 0.512 = 38.488$ GHz and the frequency down-converted signal from the source frequency $H_5 - 0.312 = 38.688$ GHz, we have used the differential configuration of the SOA-MZI.

The experimental setup includes now a variable optical delay line (VODL) used to adjust the relative delay time $\Delta\tau$ of the control pulses between the input ports (A) and (D), as shown in Figure 4.3. The relative average optical power between the input ports (A) and (D) is controlled by the first optical attenuator (Att_1) and the third optical attenuator (Att_3), respectively. The optical pulse source at the sampling wavelength $\lambda_{sa} = 1550$ nm is applied at the input port (A) after being attenuated by Att_1 with the repetition rate $f_{sa} = 7.8$ GHz. This signal is also injected at the input port (D) of the SOA-MZI after being delayed by VODL and attenuated by Att_3. The optical signal carrying OFDM and QPSK data generated by an AWG is injected at the input port (C) at the wavelength $\lambda_{Dat} = 1545$ nm with the optical mean power $P_{o,in\,Dat} = -10$ dBm. The optical power of the up-converted and down-converted signals at the output port (J) is filtered by an optical filter (OF) tuned at λ_{Dat}, detected by a photodiode (Pd), amplified by a low noise amplifier (LNA), and digitized by a digital sampling oscilloscope (DSO) for up-conversion and down-conversion.

For up-conversion, the QPSK and OFDM data generated by the AWG board at the carrier frequency $f_c = 0.512$ GHz is applied to the RF input of the MZM after being filtered by a LPF and attenuated by 13 dB $EAtt_1$ for QPSK data and 10 dB $EAtt_1$ for OFDM data. The electrical power of the QPSK and OFDM signal at the input port (C) is -20.3 dBm at $f_{Dat} = 0.512$ GHz. The received signal at the output port (J) is frequency down-converted by an electrical mixer (2) at the frequency of 0.768 GHz due to limited electrical bandwidth of 1.5 GHz of the real time DSO as displayed in Figure 4.3. Hence, the EVM of the up-converted QPSK and OFDM signals is measured at the target frequency $5f_{sa} - f_{Dat} = 38.488$ GHz at the output port (J) after being down-converted at 0.768 GHz.

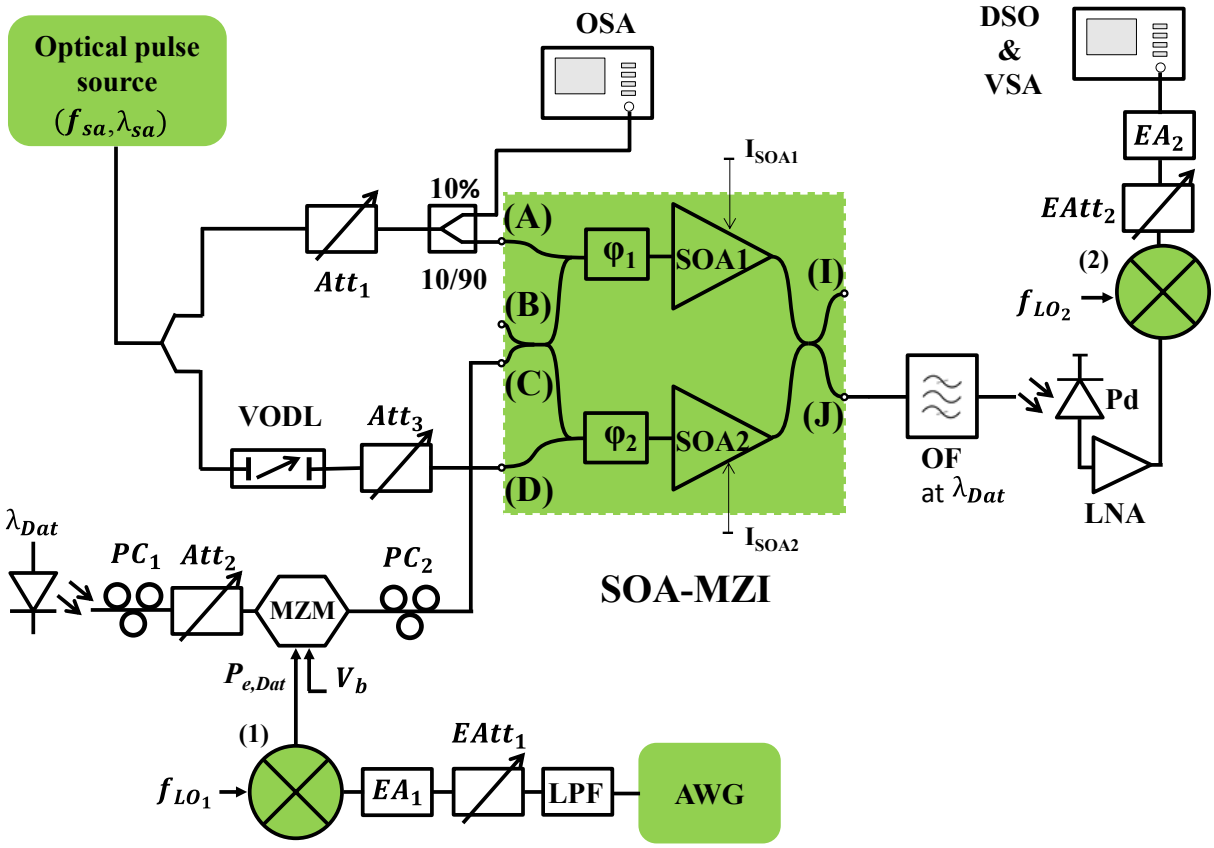

Figure 4.3: Differential configuration setup of the all-optical sampling mixer. VODL: Variable Optical Delay Line. Mixer (1) is used for frequency down-conversion from RF signal to IF signal. Mixer (2) is used for frequency up-conversion from IF signal to RF signal.

For down-conversion, an AWG board is used to generate the QPSK and OFDM signal at different bit rates at $f_c = 0.512$ GHz. This signal is frequency up-converted at the source frequency $H_5 - 0.312 = 38.688$ GHz at the input port (C) by using the electrical mixer (1) in the experimental setup shown in Figure 4.3. The electrical power of the QPSK and OFDM signals at the input port (C) is -27.8 dBm at 38.688 GHz. The optical signal at the input port (C) from the source frequency 38.644 GHz is frequency down-converted at the target frequency of 0.312 GHz at the output port (J). This down-converted signal is injected to the real time DSO after photo-detection and amplification to measure the EVM. The EVM is used to measure the quality of the transmission system by using the SOA-MZI differential configuration.

The static characteristic of the SOA-MZI with the differential configuration, see Figure 4.4, is studied to measure the peak power of the sampling signal at the input ports (A) and (D). The interferometer is set for low transmission of the continuous wave (CW) signal which is injected into the input port (C). The maximum transmitted power at the output port (J) corresponds to the optical power at the input port (A) equal to -3 dBm with extinction ratio $ER = 23.8$ dB

when canceling the optical power at the input port (D) as displayed in Figure 4.4. This transmitted power also corresponds to the optical power of −1 dBm at the input port (D) with ER = 23.2 dB when there is no optical power introduced at the input port (A).

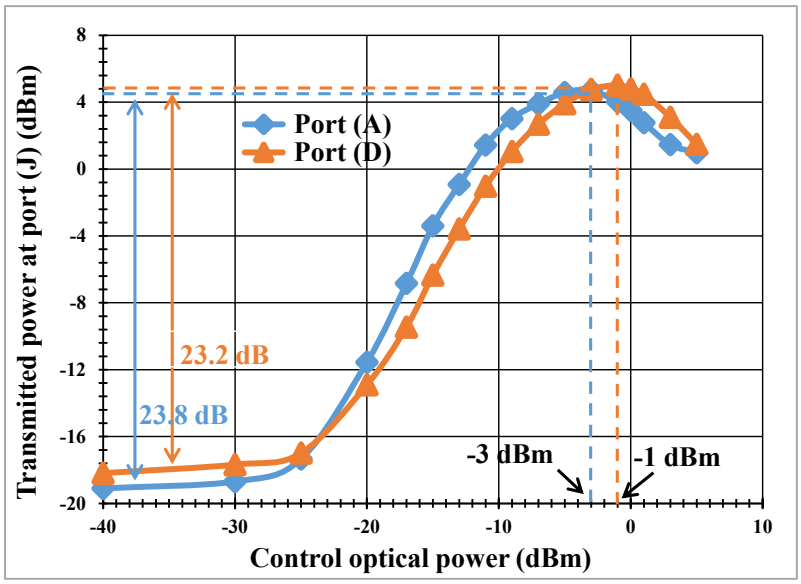

Figure 4.4: Static characteristic of the SOA-MZI using a differential configuration.

As a result, the static switching characteristics of the SOA-MZI indicate that the value of the attenuation of Att_3 must be 2 dB lower than the one of Att_1. Then, the EVM of a frequency up and down-converted QPSK signals at the output port (J) as shown in Figure 4.5.

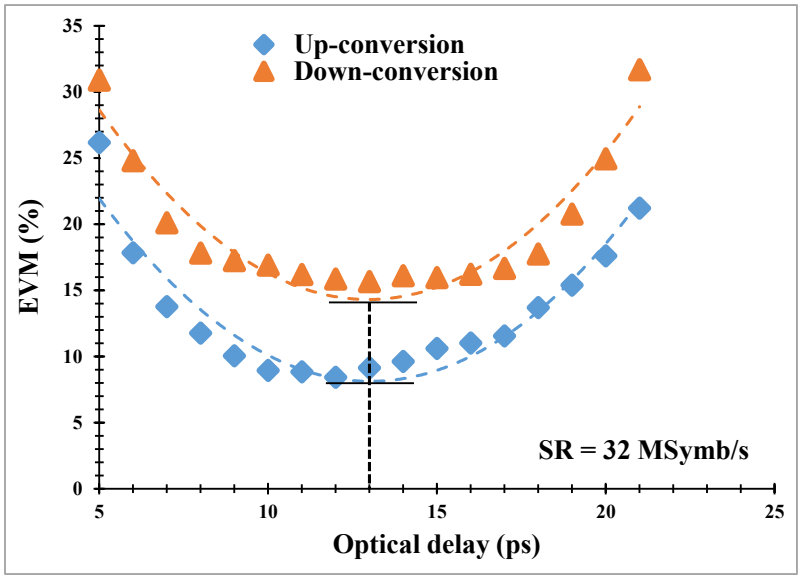

Figure 4.5: EVM of a QPSK signal as a function of the optical delay time $\Delta\tau$ between the control input ports (A) and (D) for up-conversion and down-conversion.

The EVM has been measured as a function of the relative delay time $\Delta\tau$ as shown in Figure 4.5 in order to find the best tuning of the VODL. In both cases, for frequency up-conversion at the target frequency of 38.488 GHz and frequency down-conversion from the source frequency of 38.688 GHz of QPSK data at a symbol rate of 32 MSymb/s, the minimum value of the EVM shown in Figure 4.5 is obtained at the relative delay $\Delta\tau = 13$ ps. The EVM of the QPSK signal decreases in the range of $\Delta\tau$ from 5 ps to 13 ps. It degrades as the relative delay time continues increasing in both cases. It is worth observing that the EVM fluctuates about $\pm$ 1.5 %.

Due to the finite width of the sampling pulses, a shorter relative delay time $\Delta\tau$ does not allow the SOA-MZI to reach the maximum phase difference between SOA1 and SOA2 that is necessary to obtain the best ON state. In that case, SOA2 is driven by the pulse to turn the switch OFF while SOA1 is not fully saturated. On the contrary, a very long relative delay reduces the efficiency of the differential technique because the switching window width increases, this leads to lower the speed of the optical switch [157]. It is worth noting that the delayed pulse helps to turn off the optical switch but does not reduce the time needed by both SOAs to recover their original steady state before a new switching window can exist.

4.2.2 Conversion Gain

For frequency conversion, the sampling signal at $f_{sa} = 7.8$ GHz is applied at the input port (A) and (D), its peak powers at the input ports (A) and (D) are respectively -3 dBm and -1 dBm. The optical carrier injected at the input port (C) is intensity modulated by a sinewave signal at f_{Dat}. The chosen frequency is 0.5 GHz for up-conversion measurements and 39.5 GHz for down-conversion ones. The electrical power at the input port (C) for up-conversion and down-conversion is respectively -32.4 dBm and -36.8 dBm after filtering, photo-detection, and amplification. The filtering of the optical signal at the input port (C) is used to take into account the losses of the optical filter (OF) used to measure the up and down-converted signals at the SOA-MZI output.

The conversion gain (G_c) is measured both for an optical IF signal at 0.5 GHz up-converted at the target frequency of 39.5 GHz and for an optical RF signal at 39.5 GHz down-converted at 0.5 GHz. The conversion gain measured at the output port (J) is respectively -4.8 dB at 39.5 GHz for frequency up-conversion and 9.1 dB at 0.5 GHz for frequency down-conversion as displayed in Figure 4.6.

As a result, the differential configuration improves the obtained conversion gains for up-conversion and down-conversion respectively 8.6 dB and 9 dB higher than the conversion gains obtained with the standard configuration.

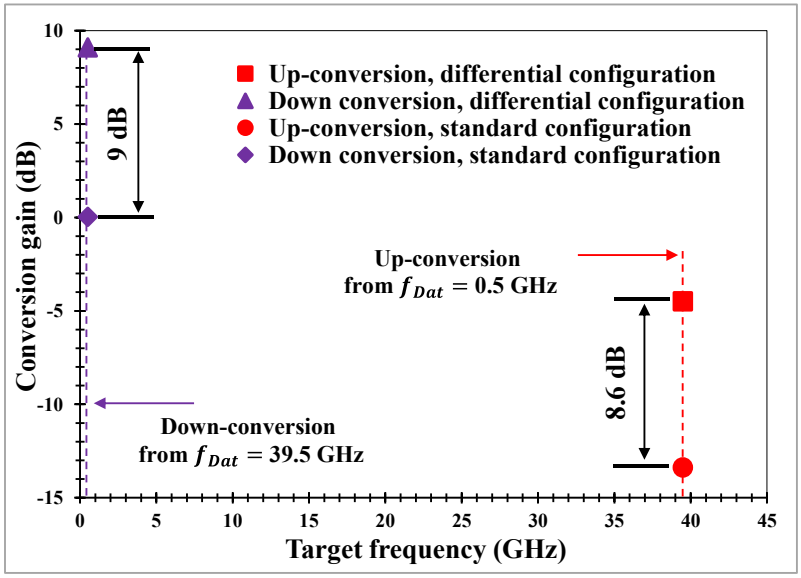

Figure 4.6: Frequency up and down-conversion gains obtained with the SOA-MZI standard configuration and the SOA-MZI differential configuration at f_{sa} = 7.8 GHz.

Conversion gains of the up-converted signal at 39.5 GHz and the down-converted signal at 0.5 GHz are also measured for different sampling frequencies of the optical pulse source by using the SOA-MZI differential configuration scheme as observed in Figure 4.7. They are respectively 5.4 dB and 20.3 dB at the sampling frequency f_{sa} = 19.5 GHz related to the second harmonic of the sampling signal.

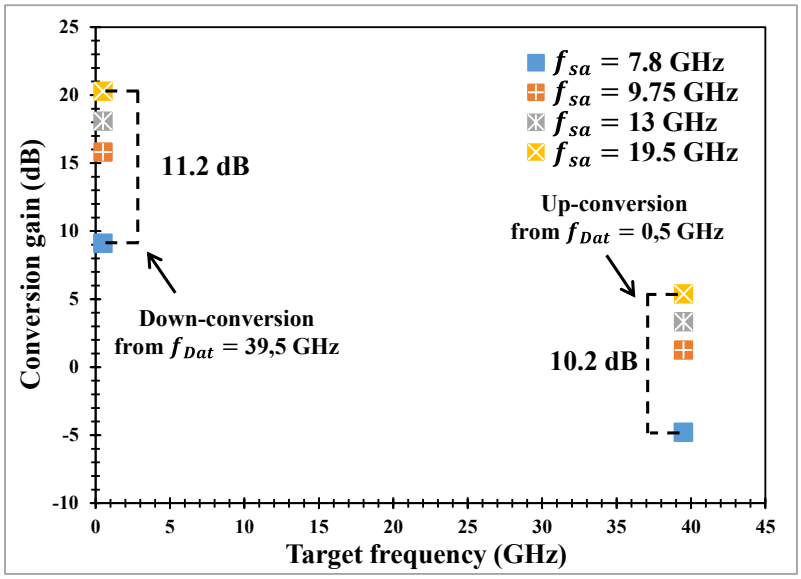

Figure 4.7: Conversion gain versus the target frequency for different sampling frequencies of the optical pulse source by using the SOA-MZI differential configuration for up-conversion and down-conversion.

Conversion gains are improved with the sampling frequency for only the harmonic at the frequency of 39 GHz due to increasing the electrical harmonic power and decreasing the harmonic order. This improvement is 10.2 dB for up-conversion and 11.2 dB for down-conversion which are higher than the conversion gains obtained for $f_{sa} = 7.8$ GHz by using the SOA-MZI differential configuration.

The augmentation of the conversion gain with the sampling frequency by using the SOA-MZI standard configuration was 11.3 dB for up-conversion and 15.3 dB for down-conversion as observed in Figure 3.13. The comparison of the conversion gains for $f_{sa} = 19.5$ GHz by using the standard configuration and the differential configuration shows that the conversion gain is enhanced 7.5 dB for up-conversion and 5 dB for down-conversion with the differential one.

4.2.3 Frequency Conversion of a QPSK Signal

The frequency conversion of QPSK signals as a function of the bit rate is shown in Figure 4.8 for up-conversion and down-conversion by using the SOA-MZI standard configuration and the SOA-MZI differential configuration. It is only achieved for the frequency involving the fifth harmonic H_5 of the sampling signal to obtain the maximum frequency shift. Figure 4.8 shows the evolution of the EVM of the up-converted QPSK signal at 38.488 GHz at the output port (J) versus the bit rate for the standard and differential configurations.

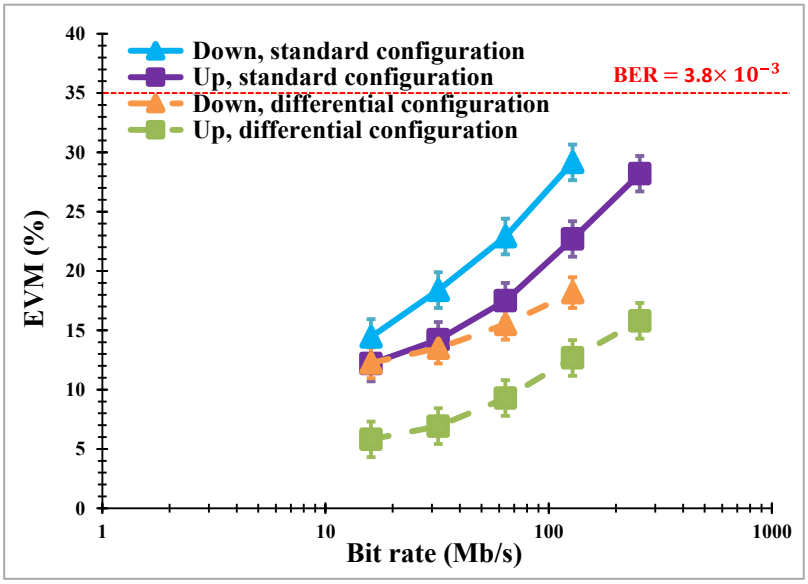

Figure 4.8: EVM of an up-converted QPSK signal and a down-converted signal QPSK signal, with and without a differential configuration, as a function of the BR.

The EVM is measured at different BRs in the range from 16 Mb/s to 256 Mb/s. It degrades as the bit rate increases for both cases. It ranges for differential configuration from 5.8 % at the minimum BR of 16 Mb/s to 15.8 % at the maximum one of 256 Mb/s. For the standard

configuration, the EVM is 14 % at 16 Mb/s instead of 5.8 % for the differential one. The benefit provided by the differential configuration is nearly constant all over the bit rate range with an average value of 8.9 %. As a result, the demodulation of EVM for up-conversion at 38.488 GHz is enhanced by using the differential configuration for all BRs compared to the standard one. For the QPSK modulation, the worst bit error rate (BER) of 10^{-3} corresponding to the EVM obtained at the higher frequency related to the fifth harmonic of the sampling signal and at the higher bit rates. Such a BER remains acceptable by applying a forward error correction (FEC) code on the received QPSK data.

Figure 4.8 also shows the demodulation of the down-converted QPSK signal at 38.688 GHz through EVM with and without the differential configuration. When the bit rate increases form 16 Mb/s to 128 Mb/s, the EVM increases for the differential configuration that ranges from 12.3 % at 16 Mb/s to 18.2 % at 256 Mb/s. The degradation is higher for the standard configuration. In that case, the benefit provided by the differential configuration is higher for the high bit rates. The EVM is 29.2 % for the standard configuration at 128 Mb/s that is higher than the one of 18.2 % for the differential one at the same bit rate.

The comparison in results between the EVM of up-converted and down-converted QPSK signals shown in Figure 4.8 for the differential configuration shows that the EVM is greatly improved for up-conversion at 38.488 GHz for the all range of the bit rates.

Increasing the sampling frequency of the OPS from 7.8 GHz to 19.5 GHz leads to upgrade the righteousness of the optical transmission system through EVM for up-conversion and down-conversion as shown respectively in Figure 4.9 and Figure 4.10 for different SRs.

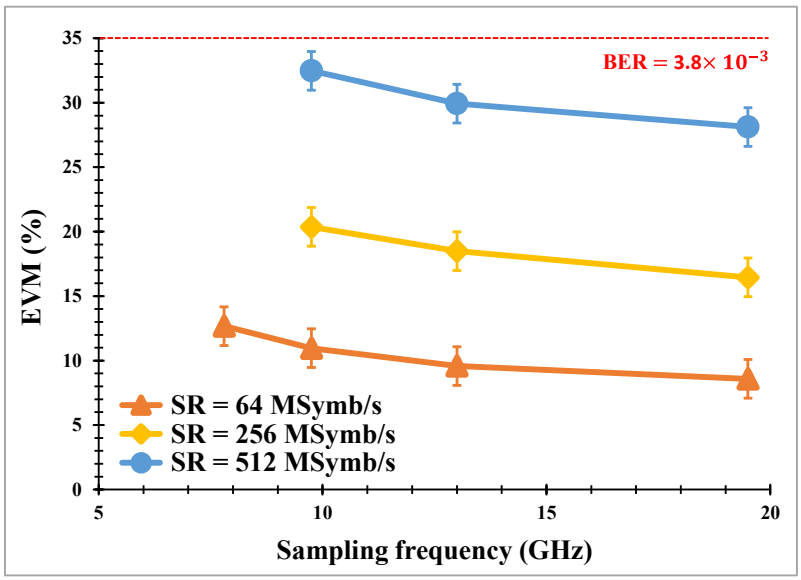

Figure 4.9: Up-converted QPSK signals for different sampling frequencies by using the SOA-MZI differential configuration.

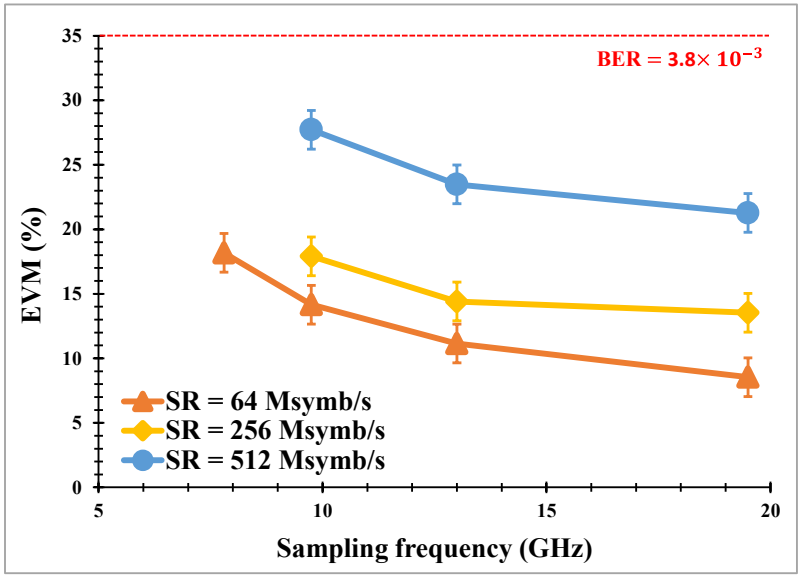

Figure 4.10: Down-converted QPSK signals for different sampling frequencies by using the SOA-MZI differential configuration.

The EVM diminishes with the sampling frequency while it degrades with the symbol rate. The improvement of the EVM with the sampling frequency is higher for down-conversion for the all symbol rates. For $f_{sa} > 9.75$ GHz the measurements show that it is possible to demodulate the up-converted and down-converted QPSK signals at the higher bit rate up to 1024 Mb/s for both cases.

4.2.4 Frequency Conversion of an OFDM Signal

The up-converted OFDM signal at 38.688 GHz and the down-converted OFDM signal at 38.688 GHz are obtained by using the same experimental setup for the differential configuration shown in Figure 4.3. The EVM of the OFDM signal as a function of the bit rate by using a standard configuration and a differential configuration for up-conversion and down-conversion is shown in Figure 4.11.

For up-conversion, the EVM increases as the bit rate increases for both cases. It ranges from 5.8 % for the differential configuration instead of 15.2 % for the standard one at the minimum bit rate of 9.6 Mb/s to 21.2 % for the differential configuration instead of 33 % for the standard one at the maximum bit rate of 245.76 Mb/s. When it comes to down-conversion, increasing the bit rate from 9.6 Mb/s to 245.76 Mb/s leads to degrading the EVM from 8.2 % to 20 % for the differential configuration and from 17.8 % to 31.6 % for the standard one.

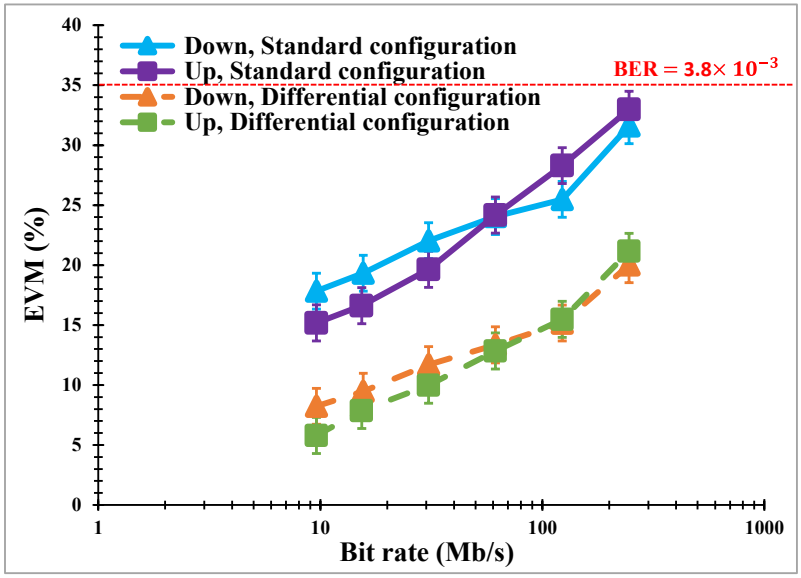

Figure 4.11: Demodulation of an up-converted OFDM signal from 0.512 GHz to 38.488 GHz and a down-converted OFDM signal from 38.688 GHz to 0.312 GHz, with and without a differential configuration, as a function of the bit rate.

The experimental results in Figure 4.11 show the benefit provided by the differential configuration. It is nearly constant all over the bit rate range with an average value of 10.6 % and 10.4 % for up- and down-conversion, respectively.

4.3 Conclusion

The differential configuration of the SOA-MZI for frequency up-conversion and frequency down-conversion utilizing an all-optical sampling method is presented. Conversion gains are improved by 8.6 dB at 39.5 GHz for up-conversion and 9.1 dB at 0.5 GHz for down-conversion. The improvement of the EVM of the up-converted and the down-converted QPSK signals is respectively achieved for the bit rates up to 256 Mb/s and 128 Mb/s. The EVM decreases from 23.6 % to 12.7 %, for up-conversion and from 29.2 % to 18.2 %, for down-conversion, at BR = 128 Mb/s for f_{sa} = 7.8 GHz. The improvement of the EVM of the up-converted and down-converted OFDM signals is fulfilled for bit rates up to 245.76 Mb/s. The benefit provided by the differential configuration is nearly constant all over the bit rate range with an average value of 10.6 % for up-conversion and 10.4 % for down-conversion. Finally, by combining the increase of the sampling frequency of the optical pulse source and the differential configuration, a maximum bit rate of 1024 Mb/s for both cases can be reached.

Conclusion and Perspectives

We have presented all along this manuscript a new architecture for an all-optical mixer based on a sampling technique. The same setup allows both up and down frequency conversions. Two different configurations of the all-optical mixer have been evaluated: a standard configuration and a differential one improving the dynamic characteristics of the SOA-MZI. The frequency of signals used in the experimental work ranges from 0 to 40 GHz. The frequency conversion of complex-modulated data, such as QPSK and OFDM, has been successfully realized for bit rates up to 1 Gb/s in both up and down-conversions.

The thesis began with a comprehensive review of the high speed photonic networks demands and the study of the frequency mixing technique based on optical mixers as presented in the chapter one. The sampling methods are also studied, such as bandpass sampling which is used in the frequency down-conversion technique. The effect of the duty cycle, the pulse shape, and the harmonic order on the amplitude of harmonics of the sampling signal which influences on the sampled signal at the mixer output is studied and analyzed. The main sources of noise are also investigated.

The chapter two presented the main study of the SOA-MZI. This study concerns the static and dynamic behavior of the SOA-MZI analyzed through simulations based on a small-signal model. The main function of the SOA-MZI is sampling the optical data signal between ON and OFF states according to the command pulsed signal injected into its control port. The best operating point of the used SOA-MZI we have found is measured to be used in the frequency conversion techniques. Accordingly, a comprehensive study of the SOA fundamental characteristics and its major nonlinear effects that are useful for high speed optical communication networks are presented in the chapter two. The principles of operation of the SOA including different processes that occur when input optical signals propagate along its active region are explained.

We have experimentally presented frequency conversion techniques by all-optical sampling based on a SOA-MZI as shown in the chapter three. An incoming signal at the frequency f_{Dat} has been sampled by the sampling signal at a repetition rate of 7.8 GHz. The experimental setup of the all-optical mixer is studied and analyzed to obtain the frequency conversion. The frequency conversion techniques are achieved based on a SOA-MZI by all-optical sampling, the data carried by the electrical subcarrier at the low frequency of 0.5 GHz have been up-converted at the different target frequencies from 8.3 GHz to 39.5 GHz. The data carried by the electrical subcarrier at the high frequency of 39.5 GHz have been down-converted at the different target frequencies from 31.7 GHz to 0.5 GHz. Some parameters at the SOA-MZI output are measured such as conversion gain and third order input intercept point to evaluate the efficiency of frequency conversion. Positive conversion gains are reached over the full range of frequencies for down-conversion and for the three first target frequencies for up-conversion.

The different performance obtained for the up-conversion gain and the down-conversion gain are analyzed through the development of small-signal equations.

In the second part of the chapter three, we present frequency conversion of QPSK and OFDM data by using the SOA-MZI standard configuration. The demodulation of the up-converted and down-converted QPSK and OFDM signals through EVM is measured at the SOA-MZI output after filtering, photo-detection, amplification, and digitalization. The comparison of the EVM between the up-converted and down-converted QPSK signals shows that the EVM is better for the frequency down-conversion case for the three lowest source frequencies except at the maximum symbol rate. For OFDM data, we have obtained approximately the same effect of demodulation for up-conversion and down-conversion. The increase of the sampling frequency of the optical pulse source from 7.8 GHz to 19.5 GHz improves the efficiency as well as the quality of the optical transmission system at the frequency related to the common harmonic of the sampling signal at 39 GHz. This leads to demodulate the up-converted and down-converted QPSK signals at high bit rates up to 1024 Mb/s and 512 Mb/s, respectively.

In the chapter four, frequency conversion by using the SOA-MZI differential configuration scheme is studied for up-conversion and down-conversion. It is shown that differential configuration technique improved the performance of the frequency conversion. The EVM value is highly reduced as well as the conversion gain compared to the technique based on the SOA-MZI standard configuration. The maximum bit rate of 1.024 Gb/s is reached for the frequency up-converted and frequency down-converted QPSK signals related to the harmonic at 39 GHz of the sampling signal at a repetition rate of 19.5 GHz with more improvement in EVMs compared to the SOA-MZI standard configuration.

Although, frequency conversion by all-optical sampling based on the SOA-MZI standard and differential configurations to be applied on RoF networks at frequencies up to 39.5 GHz is demonstrated and achieved interesting results in this work, we propose some points to be addressed that would be a possible extension of this Ph.D work:

- Frequency conversion of the RoF system at higher frequencies and at higher bit rates.

- Simultaneous frequency conversion to high or low frequencies of different optical carriers at different wavelengths.

- Numerical results of the theoretical study of the SOA-MZI as used in the chapter three can be extended to the differential configuration case and implemented by using a numerical calculation software for simulation purposes.

- The SOA-MZI can be used as a switch to implement high speed all-optical sampling of wideband analog signals.

Bibliography

[1] N. J. Gomes, P. P. Monteiro, and A. Gameiro, Next Generation Wireless Communications Using Radio Over Fiber, Wiley, 2012.

[2] A. M. Gutiérrez, J. V. Galan, J. Herrera, A. Brimont, M. Aamer, J. Martí, D. Marris-Morini, L. Vivien, J-M. Fédéli, D. J. Thomson, F. Y. Gardes, G. T. Reed, and P. Sanchis, "Silicon-Based Electro-Optic Modulators for Linear and Nonlinear Radio-over-Fiber Applications," *IEEE Conf. Microw. Photon.,* pp. 168-171, 2012.

[3] G. H. Nguyen, J. Poette, and B. Cabon, "Importance of chirp effect in millimeter wave optical upconversion systems," *IEEE J. Lightw. Technol.,* vol. 29, no. 12, pp. 1753-1758, 2011.

[4] F. Paresys, T. Shao, G. Maury, Y. Le Guennec, and B. Cabon, "Bidirectional Millimeter-Wave Radio-Over-Fiber System Based on Photodiode Mixing and Optical Heterodyning," *IEEE J. Optical Communications and Networking,* vol. 5, no. 1, pp. 74-80, 2013.

[5] C. S. Park, C. K. Oh, C. G. Lee, D. H. Kim, and C. S.Park, "A Photonic Up-Converter for a WDM Radio-over-Fiber System Using Cross-Absorption Modulation in an EAM," *IEEE Photon. Technol. Lett.,* vol. 17, no. 9, pp. 1950-1952, 2005.

[6] H. J. Kim, and J. I. Song, "Simultaneous WDM RoF Signal Generation Utilizing an All Optical Frequency Upconverter Based on FWM in a SOA," *IEEE Photon. Technol. Lett.,* vol. 23, no. 12, pp. 828-830, 2011.

[7] J. S. Lee, H. J. Song, W. B. Kim, M. Fujise, Y. H. Kim, and J. I. Song, "All-Optical Harmonic Frequency Up-Conversion of Radio over Fibre Signal Using Cross-Phase Modulation in Semiconductor Optical Amplifier," *Electron. Lett.,* vol., 40, no. 19, pp. 1211-1213, 2004.

[8] J. Kim and J-I. Song, "Full-Duplex WDM-Based RoF System Using All-Optical SSB Frequency Upconversion and Wavelength Re-use Techniques," *IEEE Trans. Microwave Theory and Techniques,* vol. 58, no. 11, pp. 3175-3180, 2010.

[9] T. Durhuus, B. Mikkelsen, C. Joergensen, S. Lykke Danielsen, and K. E.Stubkjaer, "All-Optical Wavelength Conversion by Semiconductor Optical Amplifiers," *IEEE J. Lightw. Technol.,* vol. 14, no. 6, pp. 942-954, 1996.

[10] G. Contestabile, F. Martelli, A. Mecozzi, L. Graziani, A. D'Ottavi, P. Spano, R. Dall'Ara, and J. Ecker, "Efficiency Flattening and Equalization of Frequency Up- and Down Conversion Using Four-Wave Mixing in Semiconductor Optical Amplifiers," *IEEE Photon. Technol. Lett.,* vol. 10, no. 10, pp. 1398-1400, 1998.

[11] C. Bohemond, T. Rampone, and A. Sharaiha, "Performances of a Photonic Microwave Mixer Based on Cross-Gain Modulation in a Semiconductor Optical Amplifier," *IEEE J. Lightw. Technol.,* vol. 29, no. 16, pp. 2402-2409, 2011.

[12] C. Bohémond, P. Morel, A. Sharaiha, T. Rampone, and B. Pucel, "Experimental and simulation analysis of the third-order input interception point in an all-optical RF mixer based on a semiconductor optical amplifier," *IEEE J. Lightw. Technol.,* vol. 29, no. 1, pp. 91-96, 2011.

[13] K. Morito, J. Leuthold, and H. Melchior, "Dynamic Analysis of MZI-SOA All Optical Switches for Balanced Switching," *IEEE Conf. Optics and Optical Fibre Communications,* vol. 2, no. 448, pp. 81-84, 1997.

[14] N. Pleros, C. Bintjas, G. T. Kanellos, K. Vlachos, H. Avramopoulos, and G. Guekos, "Recipe for Intensity Modulation Reduction in SOA-based Interferometric Switches," *IEEE J. Lightw. Technol.,* vol. 22, no. 12, pp. 2834-2841, 2004.

[15] A. Maziotis, B. Schrenk, M. Bougioukos, and H. Avramopoulos , "Cognitive Routing in Converged Access-Metro Environment via Selective SOA-MZI Switch," *IEEE Photon. Technol. Lett.,* vol. 23, no. 23, pp. 1820-1822, 2011.

[16] L. Xu, B. C. Wang, V. Baby, I. Glesk and P. R. Prucnal, "All-Optical Data Format Conversion Between RZ and NRZ Based on a Mach-Zehnder Interferometric Wavelength Converter," *IEEE Photon. Technol. Let.,* vol. 15, no. 2 pp. 308-310 2003.

[17] J. Kurumida, Y. Tatara, H. Uenohara, and K. Kobayashi, "All-Optical Header Recognition Sub-system Based on SOA-MZI Switches," *IEEE Conf. Lasers and Electro-Optics society,* pp. 1790-1791, 2005.

[18] H. J. Song, J. S. Lee, and J. I. Song, "Error-Free Simultaneous All-Optical Upconversion of WDM Radio over Fiber Signals," *IEEE Photon. Technol. Lett.,* vol. 17, no. 8, pp. 1731-1733, 2005.

[19] Rohde and Schwarze, "Upconverting Modulated Signals to Microwave with an External Mixer and the R&S SMF100A Microwave Signal Generator," *Application Note.*

[20] Mini Circuits, "Understanding Mixers Terms Defined and Measuring Performance," *Application Note.*

[21] SAGE Millimeter, "D-Band Balanced Mixers," *Data sheet SFB-06-N1*.

[22] M. Tsuchiya and T. Hoshida, "Nonlinear Photodetection Scheme and Its System Applications to Fiber-Optic Millimeter-Wave Wireless Down-links," *IEEE Trans. Microw. Theory Tech.,* vol. 47, no. 7, pp. 1342-1350, 1999.

[23] S. Malyshev, B. Galwas, A. Chizh, J. Dawidczyk, and V. Andrievski, "Frequency Conversion of Optical Signals in p-i-n Photodiodes," *IEEE Trans. Microw. Theory Tech.,* vol. 53, no. 2, pp. 439-443, 2005.

[24] R. Gary, Y. Le Guennec, and B. Cabon, "60 GHz UWB over Ber System Using Photodiode Based Frequency Up-Conversion," *Microwave and Optical Technology Letters,* vol. 51, no.2, pp. 421-423, 2009.

[25] G. Maury, A. Hilt, T. Berceli, B. Cabon, and A. Vilcot, "Microwave-frequency conversion methods by optical interferometer and photodiode," *IEEE Trans. Microwave Theory and Techniques,* vol. 45, no.8, pp. 1481-1485, 1997.

[26] B. Cabon, "Microwave Photonic Mixing," *Trans. Computer Science and Engineering and electrical Engineering,* vol. 17, no. 2, pp. 149-162, 2010.

[27] E. Rouvalis, M. J. Fice, C. C. Renaud, and A. J. Seeds, "Millimeter-Wave Optoelectronic Mixers Based on Uni-Traveling Carrier Photodiodes," *IEEE Trans. Microwave Theory and Techniques,* vol. 60, no. 3, pp. 686-691, 2012.

[28] T. Nagatsuma, H. Ito, and T. Ishibashi, "High-power RF photodiodes and their applications," *Wiley Laser and Photonics Reviews,* vol. 3, pp. 123-137, 2009.

[29] K. S. Giboney, M. J. W. Rodwell and J. E. Bowers, "Traveling-Wave Photodetector Theory," *IEEE Trans. Microwave Theory and Techniques,,* vol. 45, no. 8, pp. 1310-1319, 1997.

[30] 60G-R-EAM-1550, " 60 GHz Reflective Electroabsorption Modulator," *Preliminary Datasheet.*

[31] J. H. Seo, C. S. Choi, W. Y. Choi, Y. S. Kang, Y. D. Chung, and J. Kim, "Remote Optoelectronic Frequency Down-Conversion Using 60 GHz Optical Heterodyne Signals and Electroabsorption Modulator," *IEEE Photon. Technol. Lett.,* vol. 17, no. 5, pp. 1073-1075, 2005.

[32] D. S. Shin, G. L. Li, C. K. Sun, S. A. Pappert, K. K. Loi,W. S. C. Chang, and P. K. L. Yu, "Optoelectronic RF Signal Mixing Using an Electroabsorption Waveguide As an Integrated Photodetector/Mixer," *IEEE Photon. Technol. Lett.,* vol. 12, no. 2, pp. 193-195, 2000.

[33] J. Thouras, B. Benazet, L. Herve, C. A. Berthelemot, "Photonic radio frequency down-converter based on parallel electro-absorption modulators in Ku/Ku band for space applications," *IEEE Conf. OptoElectronics and Communications/ photonics in switching,* 2016.

[34] J. H. Seo, C. S. Choi, Y. S. Kang, Y. D. Chung, J. Kim, and W. Y. Choi, "SOA-EAM Frequency Up/Down-Converters for 60 GHz Bi-Directional Radio-on-Fber Systems," *IEEE Trans. Microw. Theory Tech.,* vol. 54, no. 2, pp. 959-966, 2006.

[35] B. Cabon, Y. L. Guennec, M. Lourdiane, and G. Maury, "Photonic Mixing in RF Modulated Optical Links," *IEEE Conf. Laser and Electro-Optics Society,* pp. 408-409, 2006.

[36] J. L. Corral, J. Marti, and J. M. Fuster, "General Expressions for IM/DD Dispersive Analog Optical Links with External Modulation or Optical Up-Conversion in a Mach-Zehnder Electrooptical Modulator," *IEEE Trans. Microw. Theory Tech.,* vol. 49, no. 10, pp. 1968-1976, 2001.

[37] Y. Le Guennec, G. Maury, J. Yao, and B. Cabon, "New Optical Microwave Up-Conversion Solution in Radio-Over-Fiber Networks for 60-GHz Wireless Applications," *IEEE J. Lightw Technol.,* vol. 24, no.3, pp. 1277-1282, 2006.

[38] Y. Zhang, K. Xu, R. Zhu, J. Li, J. Wu, X. Hong, and J. Lin, "Photonic Generation of M-QAM/M-ASK Signals at Microwave/Millimeter- Wave Band Using Dual-Drive Mach-Zehnder Modulators With Unequal Amplitudes," *IEEE J. Light. Technol.,* vol. 26, no.15, pp. 2604-2610, 2008.

[39] M. Weiß, A. Stöhr, M. Huchard, S. Fedderwitz, B. Charbonnier, V. Rymanov, S. Babiel, and D. Jäger, "60 GHz radio-over-fibre wireless system for bridging 10 Gb/s Ethernet links," *34th Eur. Conf. Opt. Commun.,* pp. 1-2, 2008.

[40] G. H. Nguyen, B. Cabon, and Y. L. Guennec., "Generation of 60-GHz MB-OFDM Signal-Over-Fiber by Up- Conversion Using Cascaded External Modulators," *IEEE J. Lightw. Technol.,* vol. 27, no.11, pp.1496-1502, 2009.

[41] J. Lamperski, "Cross Gain Modulation Techniques for All Optical Wavelength Conversion," *Poznań Telecommunication Workshop, Poland, 2010.*

[42] H. J. Song, M. Park, H. J. Kim, J. S. Lee, and J. I. Song, "All-Optical Frequency Down-Conversion For Full-Duplex WDM RoF Systems Utilizing an SOA-MZI," *IEEE Conf. Microw. Photon.,* pp. 321-324, 2005.

[43] H. D. Jung, C. Okonkwo, E. Tangdiongga, and T. Koonen, "All-optical multicasting of millimetre-wave signals using optical frequency multiplication technique for in-building networks," *35th Eur. Conf. Opt. Commun.,* pp. 1-2, 2009.

[44] G. Contestabile, M. Presi, and E. Ciaramella, "Multiple Wavelength Conversion for WDM Multicasting by FWM in an SOA," *IEEE Photon. Technol. Lett.,* vol. 16, no. 7, pp. 1775-1777, 2004.

[45] C. Bohémond, A. Sharaiha, T. Rampone, and H. Khaleghi, "Electro-Optical Radiofrequency Mixer Based on Semiconductor Optical Amplifier," *Electron. Lett.,* vol. 47, no. 5, pp. 331-333, 2011.

[46] T. Rampone, R. Zulma, and A. Sharaiha , "Electro-Optical Radiofrequency Up-Converter Based on a Semiconductor Optical Amplifier," *IEEE Conf. Microw. Photon.,* pp. 145-148, 2011.

[47] H. J. Song, J. S. Lee, and J. I. Song, "Linearity Performance of a Signal Up-Conversion by Using Cross-Phase Modulation in All Optical SOA-MZI Wavelength Converter," *Conf. Lasers and Electro-Optics Society,* vol. 2, pp. 1007-1008, 2003.

[48] H. J. Song, J. S. Lee, and J. I. Song, "Signal Up-Conversion by Using a Cross-Phase Modulation in All-Optical SOA-MZI Wavelength Converter," *IEEE Photon. Technol. Lett.,* vol. 16, no. 2, pp.593-595, 2004.

[49] H. J. Song, and J. I. Song, "Simultaneous All-Optical Frequency Downconversion Technique Utilizing an SOA-MZI for WDM Radio Over Fiber (RoF) Applications," *IEEE J. Lightw. Technol.,* vol. 24, no. 8, pp. 3028-3034, 2006.

[50] J. I. Song, and H. J. Song, "Simultaneous Frequency Conversion Technique Utilizing an SOA-MZI For Full-Duplex WDM Radio over Fiber Applications," *IEICE Trans. Electron.,* vol.E90–C, no. 2, pp. 351-358, 2007.

[51] Y. K. Seo, C. S. Choi, and W. Y. Choi, "All-Optical Signal Up-Conversion for Radio-on-Fiber Applications Using Cross-Gain Modulation in Semiconductor Optical Amplifiers," *IEEE Photon. Technol. Lett.,* vol. 14, no. 10, pp. 1489-1550, 2002.

[52] H. J. Song, J. S. Lee, and J. I. Song, "All-Optical Harmonic Frequency Up-Conversion for a WDM Radio over Fiber System," *IEEE Conf. Microwave Symposium Digest,* vol. 1, pp.405-407, 2004.

[53] A. J. Jerri, "The Shannon Sampling Theorem - Its Various Extensions and Applications: a tutorial review," *Proceedings IEEE,* vol. 65, no. 11, pp. 1565-1596, 1977.

[54] D. L. Jagerman and L. Fogel,, "Some General Aspects of the Sampling Theorem," *IRE Trans. Inform. Theory,,* vol. 2, no. 4, pp. 139-146, 1956.

[55] L. Fogel, "A Note on the Sampling Theorem," *IRE Trans. Information Theory,* vol. 1, no. 1, pp. 47-48, 1955.

[56] N. Wong and T. S. Ng, "An Efficient Algorithm for Downconverting Multiple Bandpass Signals Using Bandpass Sampling," *IEEE Conf. Communications,* vol. 3, pp. 910-914, 2001.

[57] P. W. Juodawlkis, J. J. Hargreaves, R. D. Younger, G. W. Titi, and J. C. Twichell, "Optical down-sampling of wide-band microwave signals," *IEEE J. Lightw. Technol.,* vol. 21, no. 12, pp. 3116–3124, 2003.

[58] D. M. Akos, M. Stockmaster, J. B. Y. Tsui, and J. Caschera, "Direct bandpass sampling of multiple distinct RF signals," *IEEE Trans. on Communications,* vol. 47, no. 7, pp. 983-988, 1999.

[59] C. H. Tseng and S. C. Chou, "Direct Downconversion of Multiband RF Signals Using Bandpass Sampling," *IEEE Trans. Wireless Communications,* vol. 5, no. 1, pp.72-76, 2006.

[60] A. J. Coulson, "A generalization of nonuniform bandpass sampling," *IEEE Trans. on Signal processing,* vol. 43, no. 3, pp. 694-704, 1995.

[61] R. G. Vaughan, N. L. Scott, and D. R. White, "The Theory of Bandpass Sampling," *IEEE Trans. on Signal Process.,* vol. 39, no. 9, pp. 1973-1984, 1991.

[62] P. A. Gamage, A. Nirmalathas, C. Lim, D. Novak, and R. Waterhouse, "Design and Analysis of Digitized RF-Over-Fiber Links," *IEEE J. Lightw. Technol.,* vol. 27, no. 12, pp. 2052-2061, 2009.

[63] Y. R. Sun and S. Signell, "Effects of Noise and Jitter on Algorithms for Bandpass Sampling in Radio Receiver," *IEEE Conf. Circuits and Systems,* vol. 1, pp. 761-764, 2004.

[64] Y. R. Sun and S. Signell, "Generalized Quadrature Bandpass Sampling with FIR Filtering," *IEEE Conf. Circuits and Systems,* vol. 5, pp. 4429-4432, 2005.

[65] B. Almeroth and G. Fettweis, "The Impact of Jitter on the Signal-to-Noise Ratio in Uniform Bandpass Sampling Receivers," *IEEE Conf. Vehicular Technology,* pp. 1-5, 2014.

[66] M. L ohning and G. Fettweis, "The Effects of Aperture Jitter and Clock Jitter in Wideband ADCs," *International Workshop on ADC Modelling and Testing,* pp. 187-191, 2003.

[67] N. Da Dalt, M. Harteneck, C. Sandner, and A. Wiesbauer, "On the Jitter Requirements of the Sampling Clock for Analog-to-Digital Converters," *IEEE Trans. Circuits and Systems,* vol. 49, no. 9, pp. 1354-1360, 2002.

[68] H. Kobayashi, M. Morimura, K. Kobayashi, and Y. A. O. Oanya, "Aperture jitter effects in wideband ADC systems," *IEEE Conf. ICECS,* pp. 1705-1708, 1999.

[69] A. V. Balakrishnan, "On the Problem of Time Jitter in Sampling," *IRE Trans. Information Theory,* vol. 8, no. 3, pp. 226-236, 1962 .

[70] R. Rutten, L. J. Breems, and R. H. M. van Veldhoven, "Digital Jitter-Cancellation for Narrowband Signals," *IEEE Conf. Circuits and Systems,* pp. 1444-1447, 2008.

[71] V. Syrjälä and M. Valkama, "Sampling Jitter Cancellation in Direct-Sampling Radio," *IEEE Conf. Wireless Communications and Networking,* pp. 1-6, 2010.

[72] J. Leuthold, P. A. Besse, J. Eckner, E. Gamper, M. Dulk, and H. Melchior, "All-Optical Space Switches With Gain and Principally Ideal Extinction Ratios," *IEEE J. Quantum Electron.,* vol. 34, no. 4, pp. 622-633, 1998.

[73] W. Idler, M. Schilling, K. Daub, D. Baums, U. Korner, E. Lach, E. Laube, K. Wünstel, "Signal quality and BER performance improvement by wavelength conversion with an integrated three-port Mach-Zehnder interferom¬eter," *Electron. Lett.,* vol. 31, no. 6, pp. 454-455, 1995.

[74] B. Mikkelsen, S.L. Danielsen, C. Joergensen, R.J.S. Pedersen, H.N. Poulsen, K.E. Stubkjaer, "All-optical noise reduction capability of interferometric wavelength converters," *Electron. Lett.,* vol. 32, no. 6, pp. 566-567, 1996.

[75] T. Rampone, A. Lagrost, A. Sharaiha, and A. Kabalan, "Optical Radiofrequency Signal Mixing by All-Optical Sampling Based on a Semiconductor Optical Amplifier Mach-Zehnder Interferometer," *IEEE J. Lightw. Technol.,* vol. 31, no. 23, pp. 3597-3602, 2013.

[76] T. Rampone, A. Hallal, H. Khaleghi, and A. Sharaiha, "Down-Conversion Gain of an All-Optical SOA-MZI-Based Mixer Using Bandpass Sampling," *IEEE Photon. Technol. Lett.,* vol. 26, no. 4, pp. 411-413, 2014.

[77] A. Rostami, H. Nejad, R. M. Qartavol, and H. R. Saghai, "Tb/s Optical Logic Gates Based on Quantum-Dot Semiconductor Optical Amplifiers," *IEEE J. Quantum Electron.,* vol. 46, no. 3, pp. 354-360, 2010.

[78] J. de Merlier, G. Morthier, P. Van Daele, I. Moerman and R. Baets, "All-optical 2R regeneration based on integrated asymmetric Mach-Zehnder interferometer incorporating MMI-SOA," *Electron. Lett.,* vol. 38, no. 5, pp. 238-239, 2002.

[79] D. Wolfson, T. Fjelde, A. Kloch, C. Janz, F. Poingt, I. Guillemot, F. Gaborit, A. Coquelin, and M. Renaud , "All-optical wavelength conversion scheme in SOA-based interferometric devices," *Electron. Lett.,* vol. 36, no. 21, pp. 1794-1795, 2000.

[80] S. J. B. Yoo, "Wavelength Conversion Technologies for WDM Network Applications," *IEEE J. Lightw. Technol.,* vol.14, no.6, pp. 955-966, 1996.

[81] D. Wolfson, A. Kloch, T. Fjelde, C. Janz, B. Dagens, and M. Renaud, "40-Gb/s All-optical Wavelength Conversion, Regeneration, and Demultiplexing in an SOA-based All-Active Mach–Zehnder Interferometer," *IEEE Photon. Technol. Lett.,* vol. 12, no. 3, pp. 332-334, 2000.

[82] A. P. Pardo, T. T. Ng, P. Petropoulos, S. Sales, and D. J. Richardson, "Analysis of the Dynamic Responses of SOA Wavelength Converters Using Linear Frequency Resolved Gating Technique," *IEEE Photon. Technol. Lett.,* vol. 20, no.13, pp. 1079-1081, 2008.

[83] J. Wang, G. Berrettini, G. Meloni, L. Potì, A. Bogoni, "All-Optical Clocked D Type Flip-Flop Exploiting SOA-Based Optical SR Latch and Logic Gates," *IEEE Conf. Photonic in Switching,* pp. 1-2, 2009.

[84] M. Spyropoulou, N. Pleros, and A. Miliou, "SOA-MZI-Based Nonlinear Optical Signal Processing: A Frequency Domain Transfer Function for Wavelength Conversion, Clock Recovery, and Packet Envelope Detection," *IEEE J. of Quantum Electron.,* vol. 47, no. 1, pp. 40-49, 2011.

[85] M. Connelly, Semiconductor Optical Amplifiers, NewYork: Springer-Verlag, 2002.

[86] E. Desurvire, Erbium Doped Fiber Amplifier, New Jersey: John Wiley, 2002.

[87] D. R. Zimmerman and L. H. Spiekman, "Amplifiers for the Masses: EDFA, EDWA, and SOA Amplets for Metro and Access Applications," *IEEE J. Lightw. Technol.,* vol. 22, no. 1, pp. 63-70, 2004.

[88] A. K. Srivastava, Y. Sun, J. L. Zyskind, and J. W. Sulhoff, "EDFA transient response to channel loss in WDM transmission system," *IEEE Photon. Technol. Lett.,* vol. 9, no.3, pp. 386-388, 1997.

[89] E. Desurvire, "Analysis of transient gain saturation and recovery in erbium-doped fiber amplifiers," *IEEE Photon. Technol. Lett.,* vol. 1, no. 8, pp. 196-199, 1989.

[90] R. J. Mears, "The EDFA: Past, Present and Future," *IEEE Conf. Communications,* vol.2, p. 1332, 1999.

[91] J. Yu, Y. Yeo, O. Akanbi, and G. Chang, "Bi-Directional Transmission of 8 X 10Gb/s DPSK Signals Over 80 km of SMF-28 Fiber Using In-line Semiconductor Optical Amplifier," *IEEE Conf. Lasers and Electro-Optics Society,* vol. 2, pp. 782-783, 2004.

[92] O. Qasaimeh, "Optical Gain and Saturation Characteristics of Quantum-Dot Semiconductor Optical Amplifiers," *IEEE J. Quantum Electron.,* vol. 39, no. 6, pp. 793-798, 2003.

[93] E. Kehayas, J. Seoane, Y. Liu, J. M. Martinez, J. Herrera, P. V. HolmNielsen, S. Zhang, R. McDougall, G. Maxwell, F. Ramos, J. Marti, H. J. S. Dorren, P. Jeppesen, and H. Avramopoulos, "All-Optical Network Subsystems Using Integrated SOA-Based Optical Gates and Flip-flops for Label-Swapped Networks," *IEEE Photon. Technol. Lett.,* vol. 18, no. 16, pp. 1750-1752, 2006.

[94] L. Gong-Ru, Y. Kun-Chieh, P. Ci-Ling, and L. Yu-Sheng, "All-Optical Decision Gating of 10-Gb/s RZ Data in a Semiconductor Optical Amplifier Temporally Gain-Shaped With Dark-Optical-Comb," *IEEE J. Lightw. Technol.,* vol. 25, no.7, pp. 1651-1658, 2007.

[95] W. Yaping, W. Chongqing, W. Yongjun, W. Zhi, and S. Xinzhi, "Optical Packet Replicator Using Cascaded SOA-Based Active Fiber Ring," *IEEE Photon. Technol. Lett., ,* vol. 21, no. 18, pp. 1320-1322, 2009.

[96] A. Sharaiha and A. Hamie, "Comprehensive Analysis of Two Cascaded Semiconductor Optical Amplifiers for All-Optical Switching Operation," *IEEE J. Lightw. Technol.,* vol. 22, no. 3, pp. 850-858, 2004.

[97] K. E. Stubkjaer, "Semiconductor Optical Amplifier-Based All-Optical Gates for High-Speed Optical Processing," *IEEE J. Quantum Electron.,* vol. 6, no.6, pp. 1428-1435, 2000.

[98] Y. Boucher and A. Sharaiha, "Spectral Properties of Amplified Spontaneous Emission in Semiconductor Optical Amplifiers," *IEEE J. Quantum Electron.,* vol. 36, no. 6, pp. 708-720, 2001.

[99] N. A. Olsson, "Lightwave systems with optical amplifiers," *IEEE J. Lightw. Technol.,* vol. 7, no.7, pp. 1071-1082, 1989.

[100] M. Eiselt, W. Pieper, and H. G. Weber, "SLALOM: Semiconductor Laser Amplifier in a Loop Mirror," *IEEE J. Lightw. Technol.,* vol. 13, no.10, pp. 2099-2112, 1995.

[101] G. P. Agrawal and N. K. Dutta, "Semiconductor Lasers 2nd edition," *International Thomson Publishing,* Scarborough, Ontario, Canada, 1993.

[102] G. Toptchiyski, S. Kindt, K. Petermann, E. Hilliger, S. Diez and H. G. Weber, "Time-domain modeling of semiconductor optical amplifiers for OTDM applications," *IEEE J. Lightw. Technol.,* vol. 17, no. 12, pp. 2577-2583, 1999.

[103] Mines Rd., "The Enhanced Functionalities of Semiconductor Optical Amplifiers and Their Role in Advanced Optical Networking," *InPhenix, Inc. ,* USA, 2011.

[104] R. Gutiérrez-Castrejón, L. Schares, L. Occhi, and G. Guekos, "Modeling and Measurement of Longitudinal Gain Dynamics in Saturated Semiconductor Optical Amplifiers of Different Length," *IEEE J. Quantum Electron.,* vol. 36, no. 12, pp. 1476-1484, 2000.

[105] G. Walker, R. Steele, and N. Walker, "Optical amplifier noise figure in a coherent optical transmission system," *IEEE J. Lightw. Technol.,* vol. 8, pp. 1409-1413, 2002.

[106] A. Crottini, F. Salleras, P. Moreno, M. A. Dupertuis, B. Deveaud, and R. Brenot, "Noise Figure Improvement in Semiconductor Optical Amplifiers by Holding Beam at Transparency Scheme," *IEEE Photon. Technol. Let.,* vol. 17, no. 5, pp. 977-979, 2005.

[107] G. P. Agrawal, Fiber-Optic Communications Systems, Wiley, New York, 1997.

[108] R. B. Picard, M. Alouini, J. Lopez, N. Vodjdani, and J-C. Simon, "Impact of the Gain Saturation Dynamics in Semiconductor Optical Amplifiers on the Characteristics of an Analog Optical Link," *IEEE J. Lightw. Technol.,* vol. 23, no. 8, pp. 2420-2426, 2005.

[109] P. Eriksson and H. Tenhunen, "The noise figure of a sampling mixer: Theory and measurement," *IEEE Conf. Electronics, Circuits, and Systems,* vol. 2, pp. 899-902, 1999.

[110] M. Movassaghi, M. K. Jackson, V. M. Smith, J. F. Young, and W. J. Hallam, "Noise figure of saturated erbium-doped fiber amplifiers," *Conf. Optical Fiber Communications Conference,* vol. 6, pp. 104-105, 1997.

[111] D. M. Baney and R. L. Jungerman, "Optical noise standard for the electrical method of opticalamplifier noise figure measurement," *in Optical Amplifiers and Their Applications, Optical Society of America, Washington,* 1997.

[112] J. L. Pleumeekers, M. Kauer, K. Dreyer, C. Burrus, A. G. Dentai, S. Shunk, J. Leuthold, and C. H. Joyner, "Acceleration of Gain Recovery in Semiconductor Optical Amplifiers by Optical Injection Near Transparency Wavelength," *IEEE Photon. Technol. Lett.,* vol. 14, no.1, pp. 12-14, 2002.

[113] C. Cheng, X. Zhang, Y. Zhang, L. Liu, and D. Huang,, "Measurement of the Carrier Recovery Time in SOA Based on Dual Pump FWM," *IEEE Conf. Asia Communications and Photonics ,* pp. 1-2, 2009.

[114] L. H. Spiekman, J. M. Wiesenfeld, U. Koren, B. I. Miller, and M. D. Chien, "All-optical Mach-Zehnder wavelength converter with monolithically integrated preamplifiers," *IEEE Photonics Technol. Lett.,* vol. 10, pp. 1115-1117, 1998.

[115] B. Mikkelsen, T. Durhuus, C. Joergensen, R. J. S. Pedersen, C. Braagaard, and K. E. Stubkjaer, "Polarisation insensitive wavelength conversion of 10 Gbit/s signals with SOAs in a Michelson interferometer," *Electron. Lett.,* vol. 30, pp. 260-261, 1994.

[116] G. Contestabile, A. Maruta, S. Sekiguchi, K. Morito, M. Sugawara, and K. Kitayama, "80 Gb/s Multicast Wavelength Conversion by XGM in a QDSOA," *36th Eur. Conf. Opt. Commun.,* pp. 1-3, 2010.

[117] T. Hung Nguyen, M. Matsuura, and N. Kishi, "Reduction of FWM and XGM for Dynamic Range Improvement in SOA-Based Multiwavelength Amplification Using Holding Beam," *IEEE Conf. OptoElectronics and Communications,* pp. 192-193, 2010.

[118] T. T. Ng, A. Perez, S. Sales, D. J. Richardson, and P. Petropoulos, "Characterization of XGM and XPM in a SOA-MZI Using a Linear Frequency Resolved Gating Technique," *IEEE Conf. Lasers and Electro-Optics Society,* pp. 656-657, 2007.

[119] J. M. Wiesenfeld, B. Glance, J. S. Perino, and A. H. Gnauck, "Wavelength Conversion at 10 GBit/s using a semiconductor optical amplifier," *IEEE Photon Technol. Lett.,* vol. 5, no. 11, pp. 1300-1303, 1993.

[120] J. S. Perino, J. M. Wiesenfeld, and G. Glance, "Fibre transmission of 10 GBit/s signals following wavelength conversion using a travelling-wave semiconductor optical amplifier," *Electron. Lett.,* vol. 30, no. 3, pp. 256-258, 1994.

[121] G. P. Agrawal and N. A. Olsson, "Self-Phase Modulation and Spectral Broadening of Optical Pulses in Semiconductor Laser Amplifiers," *IEEE J. Quantum Electron. ,* vol. 25, no. 11, pp. 2297-2306, 1989.

[122] M. V. Drummond, L. N. Costa, R. N. Nogueira, P.Monteiro, and A. Teixeira, "GVD and PMD Monitoring by Means of SPM and XPM Effects in a SOA," *IEEE Conf. Transparent Optical Networks,* vol.1, pp. 106-108, 2008.

[123] H. Zhaoyang, M. Davanco, and D. J. Blumenthal, "Extinction Ratio Improvement by Strong External Light Injection and SPM in an SOA for OTDM Pulse Source Using a DBR Laser Diode," *IEEE Photon. Technol. Lett.,* vol. 15, no.10, pp. 1419-1421, 2003.

[124] L. K. Oxenlowe, D. Zibar, M. Galili, A. T. Clausen, L. J. Christiansen, and P. Jeppesen, "Clock Recovery for 320 Gb/s OTDM Data Using Filtering-Assisted XPM in an SOA," *IEEE Conf. Lasers and Electro-Optics Europe,* p. 486, 2005.

[125] A. M. Clarke, G. Girault, P. Anandarajah, C. Guignard, L. Bramerie, L. P. Barry, J. C. Simon, and J. Harvey, "FROG Characterisation of SOA-Based Wavelength Conversion Using XPM in Conjunction with Shifted Filtering Up to Line Rates of 80 GHz," *IEEE Conf. Lasers and Electro-Optics Society,* pp. 152-153, 2006.

[126] H-J. Kim, H-J. Song, and J-I. Song, "All-optical Frequency Up-conversion Technique using Four-wave Mixing in Semiconductor Optical Amplifiers for Radio-over-fiber Applications," *IEEE Conf. Microwave Symposium,* pp. 67-70, 2007.

[127] M. Matsuura and N. Kishi, "High-Speed Wavelength Conversion of RZDPSK Signal Using FWM in a Quantum-Dot SOA," *IEEE Photon. Technol. Lett.,* vol. 23, no.10, pp. 615-617, 2011.

[128] S. Watanabe, S. Takeda, and T. Chikama, "Interband wavelength conversion of 320 Gb/s (32x10 Gb/s) WDM signal using a polarization-insensitive fiber four-wave mixer," *Conf. Optical Communication,* vol. 3, pp. 85-86, 1998.

[129] T. Durhuus, B. Mikkelsen, and K. E. Stubkjaer, "Detailed Dynamic model for semiconductor optical amplifiers and their crosstalk and intermodulation distortion," *IEEE J. Lightw. Technol.,* vol. 10, no. 8, pp. 1056-1064, 1992.

[130] T. Saitoh and T. Mukay, "Gain Saturation Characteristics of Travelling Wave Semiconductor Laser Amplifiers in Short Optical Pulse Amplification," *IEEE J. Quantum Electron.,* vol. 26, no. 12, pp. 2086-2094, 1990.

[131] L. Zhang, and P. Ye, "Theory of Direct Frequency Modulation of Semiconductor Lasers With Integrated External Cavity," *IEEE J. Quantum Electron.,* vol. 8, no. 1, pp. 66-70, 1990.

[132] A. M. de Melo, S. Randel, and K. Petermann, "Mach–Zehnder Interferometer-Based High-Speed OTDM Add-Drop Multiplexing," *IEEE J. Lightw. Technol.,* vol. 25, no. 4, pp. 1017-1026, 2007.

[133] D. A. O. Davies, "Small-Signal Analysis of Wavelength Conversion in Semiconductor Laser Amplifier via Gain Saturation," *IEEE Photon. Technol. Lett.,,* vol. 7, no. 6, pp. 617-619, 1995.

[134] Preliminary datasheet 40G-2R2-ORP, "Twin 40G/s 2R Optical Regenerator," www .ciphotonics.com.

[135] A. Fernandez, L. Chao, and J. W. D. Chi, "All-optical clock recovery and pulse reshaping using semiconductor optical amplifier and dispersion compensating fiber in a ring cavity," *IEEE Photon. Technol. Lett.,* vol. 20, no. 13, pp. 1148-1150, 2008.

[136] Valaddmir Stasyuk, "Test Data and Operation Manual of Ultrafast Optical Clock," *Pritel, Inc., www.pritel.com.*

[137] J-D. Chen and Z-M. Lin, "2.4 GHz high IIP3 and low-noise downconversion mixer," *IEEE Conf. Circuits and Systems,* pp. 37-40, 2006.

[138] G. Niu, Q. Liang, J. D. Cressler, C. S.Webster, and D. L. Harame, "RF Linearity Characteristics of SiGe HBTs," *IEEE Trans. Microw. Theory Tech.,* vol. 49, no. 9, pp. 1558-1565, 2001.

[139] X. Wang, A. Dengi, and S. Kiaei, "A high IIP3 X-band BICMOS mixer for radar applications," *IEEE Conf. Circuits and Systems,* vol. 1, pp. 113-116, 2004.

[140] Y-Y. Won, H-C. Kwon, and S-K. Han, "1.25-Gb/s Wavelength-Division Multiplexed Single-Wavelength Colorless Radio-on-Fiber Systems Using Reflective Semiconductor Optical Amplifier," *IEEE J. Lightw. Technol.,* vol. 25, no. 11, pp. 3472-3478, 2007.

[141] J-H Seo, Y-K Seo, and W-Y Choi, "Spurious-Free Dynamic Range Characteristics of the Photonic Up-Converter Based on a Semiconductor Optical Amplifier," *IEEE Photon. Technol. Lett.,* vol. 15, no. 11, pp. 1591-1593, 2003.

[142] B. Hirosaki, "An Orthogonally Multiplexed QAM System Using the Discrete Fourier Transform," *IEEE Trans. Communications,* vol. 29, no.7, pp. 982-989, 1981.

[143] J. Armstrong, "OFDM for Optical Communications," *IEEE J. Lightw. Technol.,* vol. 27, no. 3, pp. 189-204, 2009.

[144] R. Schmogrow, B. Nebendahl, M. Winter, A. Josten, D. Hillerkuss,S. Koenig, J. Meyer, M. Dreschmann, M. Huebner, C. Koos, J. Becker,W. Freude, and J. Leuthold, "Error Vector Magnitude as a Performance Measure for Advanced Modulation Formats," *IEEE Photon. Technol. Lett.,* vol. 24, no. 1, pp. 61-63, 2012.

[145] R. A. Shafik, S. Rahman, and A. R. Islam, "On the Extended Relationships among EVM, BER and SNR as Performance Metrics," *IEEE Conf. Electrical and Computer Engineering,* pp. 408-411, 2006.

[146] M. A. Mestre, H. Mardoyan, C. Caillaud, R. R. Muller, J. Renaudier, P. Jenneve, F. Blache, F. Pommereau, J. Decobert, F. Jorge, P. Charbonnier, A. Konczykowska, J-Y. Dupuy, K. Mekhazni, J-F. Paret, M. Faugeron, F. Mallecot, M. Achouche, and S. Bigo,

"Compact InP-Based DFB-EAM Enabling PAM-4 112 Gb/s Transmission Over 2 km," *IEEE J. Lightw. Technol.,* vol. 34, no. 7, pp. 1572-1578, 2016.

[147] N. Yan, J. del Val Puente, T. G. Silveira, A. Teixeira, A. P. S. Ferreira, E. Tangdiongga, P. Monteiro, and A. M. J. Koonen, "Simulation and Experimental Characterization of SOA-MZI-Based Multi-Wavelength Conversion," *IEEE J. Lightw. Technol.,* vol. 27, no. 2, pp. 117-127, 2009.

[148] M. Spyropoulou, N. Pleros, K. Vyrsokinos, D. Apostolopoulos, M. Bougioukos, D. Petrantonakis, A. Miliou, and H. Avramopoulos, "40 Gb/s NRZ Wavelength Conversion Using a Differentially-Biased SOA-MZI: Theory and Experiment," *IEEE J. Lightw. Technol.,* vol. 29, no. 10, pp. 1489-1499, 2011.

[149] K. E. Stubkjaer, "Semiconductor Optical Amplifier-Based All-Optical Gates for High-Speed Optical Processing," *IEEE J. Quantum Electron.,* vol. 6, no. 6, pp. 1458-1435, 2000.

[150] N. Yan, T. Silveira, A. Teixeira, A. Ferreira, E. Tangdiongga, P. Monteiro, and A. M. J. Koonen, “40 Gb/s Wavelength Multicast Via SOA-MZI and Applications,” *IET Electron. Lett.,* vol. 43, no. 23, 2007.

[151] D. Reading-Picopoulos, F. Wang, Y. J. Chai, R. V. Penty, and I. H. White, “10 Gb/s and 40 Gb/s WDM Multi-casting Using a Hybrid Integrated Mach–Zehnder Interferometer,” *IEEE Conf. Optical Fiber Communication and National Fiber Optic Engineers,* 2006.

[152] W. Hong, M. Li, X. Zhang, J. Sun, and D. Huang, “Dynamic Analysis of All-Optical Wavelength Conversion of Differential Phase-Shift Keyed Signals Based on Semiconductor Optical Amplifier Mach–Zehnder Interferometer,” *IEEE J. Lightw. Technol.,* vol. 27, no. 24, pp. 5580-5589, 2009.

[153] D. Apostolopoulos, D. Klonidis, P. Zakynthinos, K. Vyrsokinos, N. Pleros, I. Tomkos, "Cascadability Performance Evaluation of a new NRZ SOA-MZI Wavelength Converter," *IEEE Photon. Technol. Lett.,* vol. 21, no. 18, pp. 1341-1343, 2009.

[154] X. Yi, R. Yu, J. Kurumida, and S. J. B. Yoo, "A Theoretical and Experimental Study on Modulation-Format-Independent Wavelength Conversion," *J. Lightw Technol.,* vol. 28, no. 4, pp. 587-595, 2010.

[155] D. Petrantonakis, D. Apostolopoulos, M. Spyropoulou, N. Pleros, K. Vyrsokinos, and H. Avramopoulos, "40 Gb/s NRZ Wavelength Conversion With Enhanced 2R Regeneration Characteristics Using a Differentially-Biased SOA-MZI Switch," *IEEE Conf. Lasers and Electro-Optics scociety,* pp. 781-782, 2009.

[156] R. P. Schreieck, M. H. Kwakernaak, H. Jackel, and H. Melchior, "All Optical Switching at Multi-100-Gb/s Data Rates With Mach-Zehnder Interferometer Switches," *IEEE J. Quantum Electron.,* vol. 38, no. 8, pp.1053-1061, 2002.

[157] C. Schubert, J. Berger, S. Diez, H. J. Ehrke, R. Ludwig, U. Feiste, C. Schmidt, H. G. Weber, G. Toptchiyski, S. Randel, and K. Petermann, "Comparison of Interferometric All-Optical Switches for Demultiplexing Applications in High-Speed OTDM Systems," *IEEE J. Lightw. Technol.,* vol. 20, no. 4, pp. 618-624, 2002.

Publications

International Journal Paper

[1] **H. Termos**, T. Rampone, A. Sharaiha, A. Hamié, A. Alaeddine "All-Optical Radiofrequency Sampling Mixer Based on a Semiconductor Optical Amplifier Mach-Zehnder Interferometer Using a Standard and a Differential Configuration", IEEE J. Lightw. Technol., vol. 34, no. 20, pp. 4688-4695, October 2016.

International Conference Paper

[2] **H. Termos**, T. Rampone, A. Sharaiha, A. Hamié, and A. Alaeddine, "Up and Down Frequency Conversion of a QPSK Signal by an All-Optical Radiofrequency Sampling Mixer Based on a Semiconductor Optical Amplifier Mach-Zehnder Interferometer", Microwave Photonic (MWP), Paphos, Cyprus, October 2015.

National Conference Papers

[3] **H. Termos**, T. Rampone, A. Sharaiha, A. Hamié, and A. Alaeddine, "Performances d'un mélangeur tout-optique pour des applications radiofréquences dans la bande 0,5 – 39,5 GHz à base de SOA-MZI", Journées Nationales Microondes (JNM), Saint-Malo, France, May, 2017.

[4] **H. Termos**, T. Rampone, A. Sharaiha, A. Hamié, and A. Alaeddine, "Transposition de signaux QPSK vers les hautes et basses fréquences (0,5-39 GHz) par échantillonnage tout-optique", Journée Club Optique et Microondes de la Société Française d'Optique (JCOM), Nantes, France, June 2015.

[5] T. Rampone, **H. Termos**, A. Sharaiha, A. Hamié, and A. Alaeddine, "Transposition de fréquence de signaux radiofréquences par échantillonnage tout-optique", Journée Club Optique et Microondes de la Société Française d'Optique (JCOM), Lannion, France, June 2014.

Seminars

[1] **H. Termos**, "Up and Down Frequency Conversion of a QPSK Signal by an All-Optical Radiofrequency Sampling Mixer Based on a Semiconductor Optical Amplifier Mach-Zehnder Interferometer", Journée des Doctorants de l'Ecole Doctorale (SICMA), Brest, France, 2015.

[2] **H. Termos**, "Frequency Conversion Techniques by All-Optical Sampling Methods Based on A SOA-MZI", Université de Bretagne Occidentale (UBO), Brest, France, 2015.

[3] **H. Termos**, "Transposition de fréquence de signaux radiofréquences par échantillonnage tout-optique", Télécom Bretagne, Brest, France, 2014.

[4] **H. Termos**, "Techniques of Frequency Conversion by All-Optical Sampling Methods for Applications in Data Transmission Based on A SOA-MZI", École Nationale d'ingénieurs de Brest (ENIB), Brest, France, 2014.

Technical Reports

[1] **H. Termos**, "Technique of Frequency Conversion by All-Optical Sampling for Applications in Data Transmission Based on a SOA-MZI", (34 pages), Université de Bretagne Occidentale (UBO), Brest, France, 2015.

[2] **H. Termos**, "Frequency Conversion Techniques by All-Optical Sampling Methods Based on A SOA-MZI", (10 pages), Bretagne Region, France, 2015.

Appendix A

Mach-Zehnder Modulator Characteristics

The Mach-Zehnder modulator (MZM) is used to modulate the optical carrier carrying data at the input port (C). The wavelength of data λ_{Dat} is 1545 nm. The experimental setup used to measure the static and dynamic characteristics of the optical MZM is displayed in Figure A.1. Figure A.2 shows its static characteristic. The extinction ration ER of the optical MZM is equal to 32.3 dB. The voltage V_π observed in Figure A.2 between the maximum transmission point and the minimum transmission point is 6.7 V.

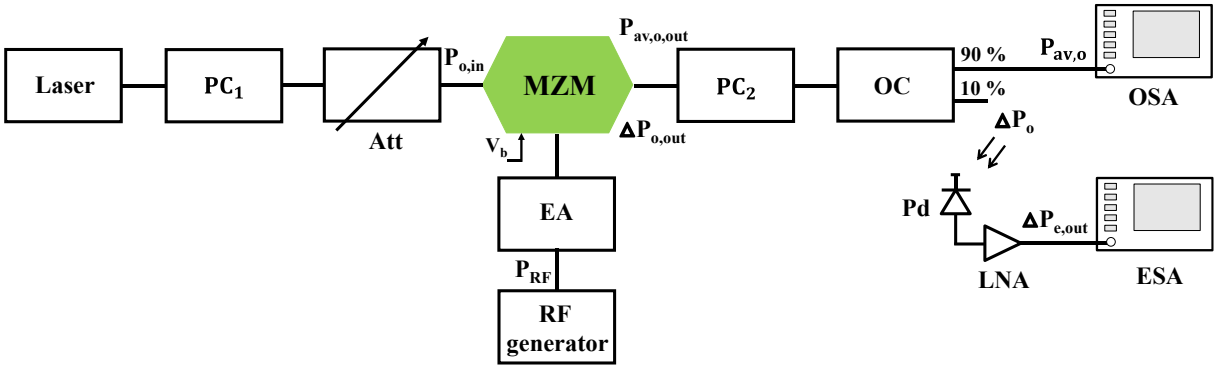

Figure A.1: Static and dynamic experimental setup of the used MZM. PC: Polarization Controller, Att: Attenuator, OSA: Optical Spectrum Analyzer, EA: Electrical Amplifier, ESA: Electrical Spectrum Analyzer, LNA: Low Noise Amplifier, Pd: Photodiode, V_b: Bias voltage, and MZM: Mach-Zehnder Modulator.

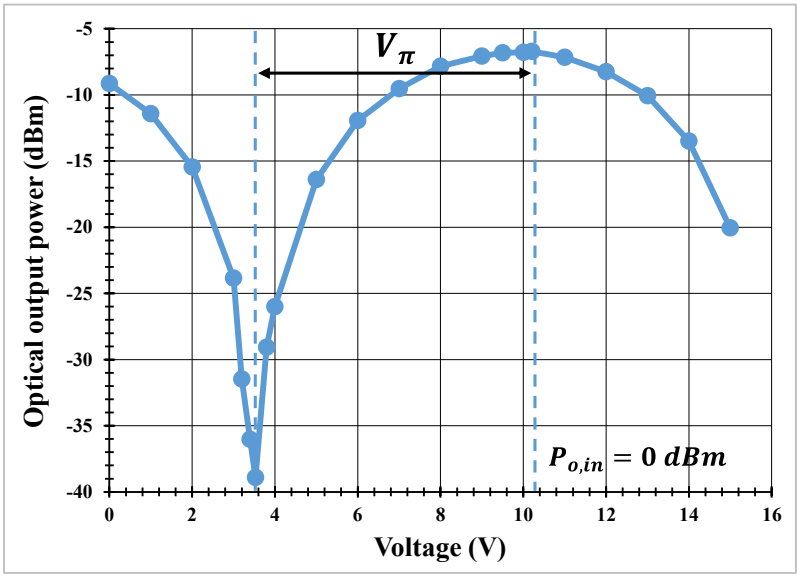

Figure A.2: Static characteristic of the MZM. V_π is a voltage between the maximum transmission point and the minimum transmission point.

In dynamic regime, Figure A.3 shows the −3 dB bandwidth of the used MZM which is 6 GHz by using an extrapolation of the measured points. The electrical power P_{RF} injected into the RF input of the MZM is −10 dBm which decreases with the frequency of the generator.

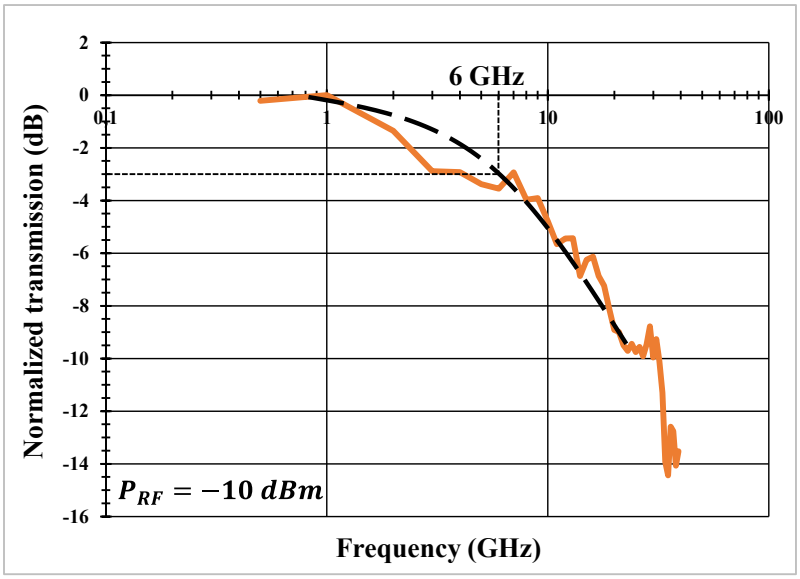

Figure A.3: Dynamic characteristic of the MZM. Its electrical bandwidth is 6GHz.

The modulation index (M_I) of the optical MZM is measured as a function of the power level of the RF generator for different frequencies as shown in Figure A.4, where the modulation index can be defined as the measure of extent of amplitude variation about an unmodulated carrier. It indicates the amount by which the modulated carrier varies around its static unmodulated level.

The experimental setup used to obtain M_I was shown in Figure A.1. The electrical power $\Delta P_{e,out}$ is measured on the electrical spectrum analyzer (ESA). The optical power ΔP_o at the input of a photodiode (Pd) is calculated from the measured $\Delta P_{e,out}$. The optical power $\Delta P_{o,out}$ at the output of the MZM is calculated from ΔP_o by taking into account the losses of PC_2 and the optical coupler (OC) 10 %. The optical average power $P_{av,o}$ measured on the optical spectrum analyzer (OSA) is directly related to the average optical power $P_{av,o,out}$ at the output of the MZM by taking into account the losses of PC_2 and OC 90 %. After measuring these two powers, the MI is calculated as defined in Equation (A.1). The MI increases when the power level of the RF generator increases while it is decreased with the frequency (f). The M_I of the MZM at the power level of −10 dBm is 19.5 % at the low frequency of 1 GHz which is higher than the M_I at high one of 10 GHz as displayed in Figure A.4.

For quantifying the degree of modulation, M_I is calculated through the equation below:

$$MI = \frac{\Delta P_{o,out}}{P_{av,o,out}} = \frac{\frac{1}{L_{o1}}\sqrt{\frac{2\Delta P_{e,out}}{L_e G_p R r^2}}}{\frac{P_{o,out}}{L_{o2}}} \qquad \text{(A.1)}$$

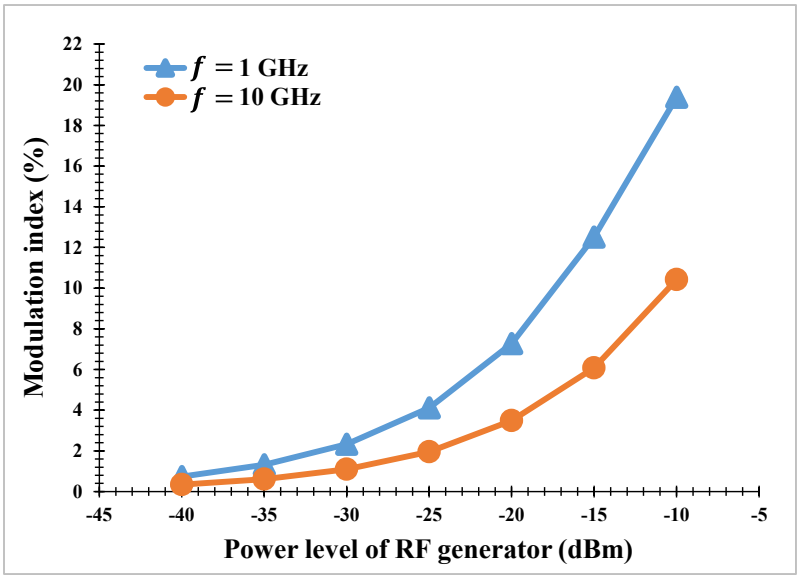

Figure A.4: Modulation index (M_I) of the optical MZM for different frequencies.

ΔP_o is the optical power at the output OC 10 %, it is calculated from the measured electrical power $\Delta P_{e,out}$ as shown in the equation below:

$$\Delta P_o = \sqrt{\frac{2\Delta P_{e,out}}{L_e G_p R r^2}} \qquad \text{(A.2)}$$

Where G_P is the power gain of the low noise amplifier (LNA), r is the responsivity of the photodiode (Pd), R is a resistor and L_e is the electrical losses between the LNA and the ESA. These constant parameters are given in Table 10.

Table 10: Parameters to calculate M_I of the MZM.

G_P	33 dB	L_e	-1 dB
L_{o1}	-1.04 dB	r	0.68 A/W
L_{o2}	-10.84 dB	R	50 Ω

$\Delta P_{o,out}$ is the optical power of the MZM directly at its output, it can be defined as

$$\Delta P_{o,out} = \frac{\Delta P_o}{L_{o1}} \quad \text{(A.3)}$$

Where L_{o1} stands for losses denoted in dB between the MZM output and OC 10 %.

$P_{av,o,out}$ is directly the average output power of the optical MZM calculated at its output that is defined by:

$$P_{av,o,out} = \frac{P_{av,o}}{L_{o2}} \quad \text{(A.4)}$$

Where $P_{av,o}$ is the optical average power at OC 90 % measured on the OSA, and L_{o2} stands for losses between the output of the MZM and OC 90 %.

Appendix B

Small Signal Analysis of Up and Down-Conversions

Appendix B.1

Constant and Variation Powers of SOA_x and SOA_y

The different frequency components of the output powers, limited to the first order terms only for w_{dat} and w_{ck}, are:

For SOA_y:

$$\bar{P}_{dat,y,o} = \bar{G}_{dat,y}\,\bar{P}_{dat,i} \tag{B.1}$$

$$\begin{aligned}\Delta P_{dat,y,o} &= \frac{1}{2}\left(p_{dat,y,o}e^{j\omega_{dat}t} + cc\right)\\ &= \frac{1}{2}\left(\bar{G}_{dat,y}\,p_{dat,i} + \bar{P}_{dat,i}\frac{\partial G_{dat,y}}{\partial N_y}n_{dat,y}\right)e^{j\omega_{dat}t} + cc\end{aligned} \tag{B.2}$$

For SOA_x:

$$\bar{P}_{dat,ox_l} = \bar{G}_{dat,x_l}\,\bar{P}_{dat,ix_l} \tag{B.3}$$

$$\begin{aligned}\Delta P_{dat,dat,ox_l} &= \frac{1}{2}\left(p_{dat,dat,ox_l}e^{j\omega_{dat}t} + cc\right)\\ &= \frac{1}{2}\left(\bar{G}_{dat,x_l}\,p_{dat,dat,ix_l} + \frac{\partial G_{dat,x_l}}{\partial N_{x_l}}\left(n_{dat,x_l}\bar{P}_{dat,ix_l}\right)\right)e^{j\omega_{dat}t} + cc\end{aligned} \tag{B.4}$$

$$\begin{aligned}\Delta P_{dat,ck,ox_l} &= \frac{1}{2}\left(p_{dat,ck,ox_l}e^{j\omega_{ck}t} + cc\right)\\ &= \frac{1}{2}\left(\bar{G}_{dat,x_l}\,p_{dat,ck,ix_l} + \frac{\partial G_{dat,x_l}}{\partial N_{x_l}}\left(n_{ck,x_l}\bar{P}_{dat,ix_l}\right)\right)e^{j\omega_{ck}t} + cc\end{aligned} \tag{B.5}$$

$$\begin{aligned}\Delta P_{dat,ck+dat,ox_l} &= \frac{1}{2}\left(p_{dat,ck+dat,ox_l}e^{j\omega_{ck+dat}t} + cc\right)\\ &= \frac{1}{2}\left(\bar{G}_{dat,x_l}\,p_{dat,ck+dat,ix_l} + \frac{\partial G_{dat,x_l}}{\partial N_{x_l}}\left[n_{ck+dat,x_l}\bar{P}_{dat,ix_l} + \right.\right.\\ &\quad \left.\left.\frac{1}{2}n_{ck,x_l}p_{dat,dat,ix_l}\right]\right)e^{j\omega_{ck+dat}t} + cc\end{aligned} \tag{B.6}$$

$$\Delta P_{dat,ck-dat,ox_l} = \frac{1}{2}\left(p_{dat,ck-dat,ox_l} e^{j\omega_{ck-dat}t} + cc\right)$$

$$= \frac{1}{2}\Big(\bar{G}_{dat,x_l}\, p_{dat,ck-dat,ix_l} + \frac{\partial G_{dat,x_l}}{\partial N_{x_l}}\Big[n_{ck-dat,x_l}\bar{P}_{dat,ix_l} + \frac{1}{2} n_{ck,x_l} p^*_{dat,dat,ix_l}\Big]\Big) e^{j\omega_{ck-dat}t} + cc \tag{B.7}$$

Appendix B.2

Carrier Density Modulation for Different Angular Frequencies

The rate equation for the carrier density is developed around the mean values of the recombination terms:

$$\frac{d\left(\bar{N}_{x_l}+\Delta n_{x_l}\right)}{dt} =$$

$$-\left[\frac{dR_{x_l}\left(\bar{N}_{x_l}+\Delta n_{x_l}\right)}{dt} + \frac{dR_{dat,x_l}\left(\bar{N}_{x_l}+\Delta n_{x_l},\bar{P}_{dat,ix_l}+\Delta P_{dat,ix_l}\right)}{dt} + \frac{dR_{ck,x_l}\left(\bar{N}_{x_l}+\Delta n_{x_l},\bar{P}_{ck,ix_l}+\Delta P_{ck,ix_l}\right)}{dt}\right] \tag{B.8}$$

By using Taylor formula, the carrier density rate equation becomes:

$$\frac{d\left(\bar{N}_{x_l}+\Delta n_{x_l}\right)}{dt} = -\Big[\bar{R}_{x_l} + \Delta n_{x_l}\frac{\partial R_{x_l}}{\partial N_{x_l}} + \frac{\Delta n_{x_l}^2}{2}\frac{\partial^2 R_{x_l}}{\partial {N_{x_l}}^2} + \bar{R}_{dat,x_l} + \Delta n_{x_l}\frac{\partial R_{dat,x_l}}{\partial N_{x_l}} + \Delta P_{dat,ix_l}\frac{\partial R_{dat,x_l}}{\partial P_{dat,ix_l}} + \frac{1}{2}\Big(\Delta n_{x_l}^2\frac{\partial^2 R_{dat,x_l}}{\partial {N_{x_l}}^2} + \Delta P_{dat,ix_l}^2\frac{\partial^2 R_{dat,x_l}}{\partial {P_{dat,ix_l}}^2} + 2\Delta n_{x_l}\Delta P_{dat,ix_l}\frac{\partial^2 R_{dat,x_l}}{\partial N \partial P_{dat,ix_l}}\Big) + \bar{R}_{ck,x_l} + \Delta n_{x_l}\frac{\partial R_{ck,x_l}}{\partial N_{x_l}} + \Delta P_{ck,ix_l}\frac{\partial R_{ck,x_l}}{\partial P_{ck,ix_l}} + \frac{1}{2}\Big(\Delta n_{x_l}^2\frac{\partial^2 R_{ck,x_l}}{\partial {N_{x_l}}^2} + \Delta P_{ck,ix_l}^2\frac{\partial^2 R_{ck,x_l}}{\partial {P_{ck,ix_l}}^2} + 2\Delta n_{x_l}\Delta P_{ck,ix_l}\frac{\partial^2 R_{ck,x_l}}{\partial N \partial P_{ck,ix_l}}\Big)\Big] \tag{B.9}$$

From (B.9) one can write the expression of the carrier density at a specific angular frequency. Only the first order terms are taken into account at ω_{dat} and ω_{ck}.

$$n_{dat,x_l} = -\frac{\tau_{d,x_l}}{\left(1+j\omega_{dat}\tau_{d,x_l}\right)}\left(\frac{\partial R_{dat,x_l}}{\partial P_{dat,ix_l}}p_{dat,dat,ix_l} + \frac{\partial R_{ck,x_l}}{\partial P_{ck,ix_l}}p_{ck,dat,ix_l}\right) \tag{B.10}$$

$$n_{ck,x_l} = -\frac{\tau_{d,x_l}}{\left(1+j\omega_{ck}\tau_{d,x_l}\right)}\left(\frac{\partial R_{dat,x_l}}{\partial P_{dat,ix_l}}p_{dat,ck,ix_l} + \frac{\partial R_{ck,x_l}}{\partial P_{ck,ix_l}}p_{ck,ck,ix_l}\right) \tag{B.11}$$

$$\begin{aligned} n_{ck+dat,x_l} = &-\frac{\tau_{d,x_l}}{\left(1+j\omega_{ck+dat}\tau_{d,x_l}\right)}\left[p_{dat,ck+dat,ix_l}\frac{\partial R_{dat,x_l}}{\partial P_{dat,ix_l}} + \right. \\ &p_{ck,ck+dat,ix_l}\frac{\partial R_{ck,x_l}}{\partial P_{ck,ix_l}} + \frac{n_{dat,x_l}\,n_{ck,x_l}}{2}\frac{\partial \tau_{d,x_l}^{-1}}{\partial N_{x_l}} + \frac{p_{dat,dat,ix_l}p_{dat,ck,ix_l}}{2}\frac{\partial^2 R_{dat,x_l}}{\partial P_{dat,ix_l}^{\,2}} + \\ &\frac{p_{ck,dat,ix_l}p_{ck,ck,ix_l}}{2}\frac{\partial^2 R_{ck,x_l}}{\partial P_{ck,ix_l}^{\,2}} + \frac{\left(n_{dat,x_l}p_{dat,ck,ix_l} + n_{ck,x_l}p_{dat,dat,ix_l}\right)}{2}\frac{\partial^2 R_{dat,x_l}}{\partial N_{x_l}\partial P_{dat,ix_l}} + \\ &\left.\frac{\left(n_{dat,x_l}p_{ck,ck,ix_l} + n_{ck,x_l}p_{ck,dat,ix_l}\right)}{2}\frac{\partial^2 R_{ck,x_l}}{\partial N_{x_l}\partial P_{ck,ix_l}}\right] \end{aligned} \tag{B.12}$$

$$\begin{aligned} n_{ck-dat,x_l} = &-\frac{\tau_{d,x_l}}{\left(1+j\omega_{ck-dat}\tau_{d,x_l}\right)}\left[p_{dat,ck-dat,ix_l}\frac{\partial R_{dat,x_l}}{\partial P_{dat,ix_l}} + \right. \\ &p_{ck,ck-dat,ix_l}\frac{\partial R_{ck,x_l}}{\partial P_{ck,ix_l}} + \frac{n_{ck,x_l}n^*_{dat,x_l}}{2}\frac{\partial \tau_{d,x_l}^{-1}}{\partial N_{x_l}} + \frac{p_{dat,ck,ix_l}p^*_{dat,dat,ix_l}}{2}\frac{\partial^2 R_{dat,x_l}}{\partial P_{dat,ix_l}^{\,2}} + \\ &\frac{p_{ck,ck,ix_l}p^*_{ck,dat,ix_l}}{2}\frac{\partial^2 R_{ck,x_l}}{\partial P_{ck,ix_l}^{\,2}} + \frac{\left(n_{ck,x_l}p^*_{dat,dat,ix_l} + n^*_{dat,x_l}p_{dat,ck,ix_l}\right)}{2}\frac{\partial^2 R_{dat,x_l}}{\partial N_{x_l}\partial P_{dat,ix_l}} + \\ &\left.\frac{\left(n_{ck,x_l}p^*_{ck,dat,ix_l} + n^*_{dat,x_l}p_{ck,ck,ix_l}\right)}{2}\frac{\partial^2 R_{ck,x_l}}{\partial N_{x_l}\partial P_{ck,ix_l}}\right] \end{aligned} \tag{B.13}$$

Where τ_{d,x_l} is the recombination time which is defined in the equation below:

$$\tau_{d,x_l} = \frac{1}{\frac{\partial R_{x_l}}{\partial N_{x_l}} + \frac{\partial R_{dat,x_l}}{\partial N_{x_l}} + \frac{\partial R_{ck,x_l}}{\partial N_{x_l}}} \tag{B.14}$$

We note that the highlighted yellow color terms are cancelled for simplification in this section and the following ones.

Appendix B.3

Optical Power at the SOA-MZI Output

$$P_{dat,o} = \frac{1}{4}\left(\bar{P}_{dat,ox_L} + \sum_{\substack{r=dat,ck,\\ ck+dat,\\ ck-dat}} \Delta P_{dat,r,ox_L} + \bar{P}_{dat,y,o} + \Delta P_{dat,y,o} - \right.$$

$$\left. 2\sqrt{\left(\bar{P}_{dat,ox_L} + \sum_{\substack{r=dat,ck,\\ ck+dat,\\ ck-dat}} \Delta P_{dat,r,ox_L} \right)\left(\bar{P}_{dat,y,o} + \Delta P_{dat,y,o}\right)}.cos\left(\bar{\Phi}_{dat,x,o}\right. \right. \quad \text{(B.15)}$$

$$\left. \left. + \Delta\Phi_{dat,x,o} - \bar{\Phi}_{dat,y,o} - \Delta\Phi_{dat,y,o} + \Phi_0\right) \right)$$

By setting $\Psi_0 = \bar{\Phi}_{dat,x,o} - \bar{\Phi}_{dat,y,o} + \Phi_0$ and limiting the expression of $P_{dat,o}$ to the first order terms, it comes:

$$P_{dat,o} \cong \frac{1}{4}\left(\bar{P}_{dat,ox_L} + \sum_{\substack{r=dat,ck,\\ ck+dat,\\ ck-dat}} \Delta P_{dat,r,ox_L} + \bar{P}_{dat,y,o} + \right.$$

$$\Delta P_{dat,y,o} - 2\sqrt{\bar{P}_{dat,ox_L}\bar{P}_{dat,y,o}}\, cos(\Psi_0)\left(1 - \left(\Delta\Phi_{dat,x,o} - \right.\right. \quad \text{(B.16)}$$

$$\left.\left. \Delta\Phi_{dat,y,o}\right) tg(\Psi_0) + \frac{\sum_{\substack{r=dat,ck,\\ ck+dat,\\ ck-dat}} \Delta P_{dat,r,ox_L}}{2\bar{P}_{dat,ox_L}} + \frac{\Delta P_{dat,y,o}}{2\bar{P}_{dat,y,o}} \right) \right)$$

Appendix B.4

Up-Converted and Down-Converted Powers at the SOA-MZI Output

➢ ***Up-conversion, ck1 and ck5***

The optical output power related to $ck1$ and $ck5$ is derived from Equation (3.19).

$$p_{dat,z_d,o} = \frac{1}{4}\left(\frac{p_{dat,z_d,ox_L}}{2} - \sqrt{\bar{P}_{dat,ox_L}\bar{P}_{dat,y,o}}\cdot\left[\frac{\alpha_H}{\bar{G}_{dat,x}}\frac{\partial G_{dat,x}}{\partial N_x}\frac{n_{z_d,x}}{2}sin(\Psi_0) + \frac{p_{dat,z_d,ox_L}}{2\bar{P}_{dat,ox_L}}cos(\Psi_0)\right]\right) \quad \text{(B.17)}$$

Where p_{dat,z_d,ox_L} and $n_{z_d,x}$ are derived in the equations below:

$$p_{dat,z_d,ox_L} = \bar{G}_{dat,x_L}\,p_{dat,z_d,ix_L} + \frac{\partial G_{dat,x_L}}{\partial N_{x_L}}\left[n_{z_d,x_L}\bar{P}_{dat,ix_L} + \frac{1}{2}n_{ck1/5,x_L}p_{dat,d,ix_L}\right] \quad \text{(B.18)}$$

$$n_{z_d,x} = \frac{1}{L}\sum_{l=1}^{L}\left(f_w\left[p_{dat,z_d,ix_l}\frac{\partial R_{dat,x_l}}{\partial P_{dat,ix_l}} + p_{ck,z_d,ix_l}\frac{\partial R_{ck,x_l}}{\partial P_{ck,ix_l}} + \frac{n_{d,x_l}\,n_{ck1/5,x_l}}{2}\frac{\partial \tau_{d,x_l}^{-1}}{\partial N_{x_l}} + \frac{n_{ck1/5,x_l}p_{dat,d,ix_l}}{2}\frac{\partial^2 R_{dat,x_l}}{\partial N_{x_l}\partial P_{dat,ix_l}} + \frac{n_{d,x_l}p_{ck,ck1/5,ix_l}}{2}\frac{\partial^2 R_{ck,x_l}}{\partial N_{x_l}\partial P_{ck,ix_l}}\right]\right) \quad \text{(B.19)}$$

➢ ***Down-conversion, ck1 and ck5***

The optical output power related to $ck1$ and $ck5$ is derived from Equation (3.20) as given in the equation below:

$$p_{dat,z_D,o} = \frac{1}{4}\left(\frac{p_{dat,z_D,ox_L}}{2} - \sqrt{\bar{P}_{dat,ox_L}\bar{P}_{dat,y,o}}\cdot\left[\frac{\alpha_H}{\bar{G}_{dat,x}}\frac{\partial G_{dat,x}}{\partial N_x}\frac{n_{z_D,x}}{2}sin(\Psi_0) + \frac{p_{dat,z_D,ox_L}}{2\bar{P}_{dat,ox_L}}cos(\Psi_0)\right]\right) \quad \text{(B.20)}$$

Where p_{dat,z_D,ox_L} and $n_{z_D,x}$ are derived in the equations below:

$$p_{dat,z_D,ox_L} = \bar{G}_{dat,x_L}\, p_{dat,z_D,ix_L} + \frac{\partial G_{dat,x_L}}{\partial N_{x_L}}\left[n_{z_D,x_L}\bar{P}_{dat,ix_L} + \frac{1}{2}n_{ck1/5,x_L}p^*_{dat,D,ix_L}\right] \quad \text{(B.21)}$$

$$n_{z_D,x} = \frac{1}{L}\sum_{l=1}^{L}\left(f_w\left[p_{dat,z_D,ix_l}\frac{\partial R_{dat,x_l}}{\partial P_{dat,ix_l}} + p_{ck,z_D,ix_l}\frac{\partial R_{ck,x_l}}{\partial P_{ck,ix_l}} + \frac{n^*_{D,x_l}\, n_{ck1/5,x_l}}{2}\frac{\partial \tau^{-1}_{d,x_l}}{\partial N_{x_l}} + \frac{n_{ck1/5,x_l}p^*_{dat,D,ix_l}}{2}\frac{\partial^2 R_{dat,x_l}}{\partial N_{x_l}\partial P_{dat,ix_l}} + \frac{n^*_{D,x_l}p_{ck,ck1/5,ix_l}}{2}\frac{\partial^2 R_{ck,x_l}}{\partial N_{x_l}\partial P_{ck,ix_l}}\right]\right) \quad \text{(B.22)}$$

The simplified expressions, limited to the first order, of terms involved in Equations (3.22) and (3.25) are:

A: Down-conversion with clock ck1 (D1)

$p_{dat,ck1-D,o}$ defined in Equation (3.22) at the frequency $ck1 - D$ is simplified to:

$$n_{ck1-D,x} = \frac{1}{L}\sum_{l=1}^{L}\left(f_w\left[p_{dat,ck1-D,ix_l}\frac{\partial R_{dat,x_l}}{\partial P_{dat,ix_l}} + p_{ck,ck1-D,ix_l}\frac{\partial R_{ck,x_l}}{\partial P_{ck,ix_l}}\right]\right)$$

$(n_{ck1-D,x})$ is simplified from Equation (B.22).

$$p_{dat,ck1-D,ix_l} = p_{dat,ck1-D,ox_{l-1}} = \bar{G}_{dat,x_{l-1}}\, p_{dat,ck1-D,ix_{l-1}} + \frac{\partial G_{dat,x_{l-1}}}{\partial N_{x_{l-1}}}\left[n_{ck1-D,x_{l-1}}\bar{P}_{dat,ix_{l-1}} + \frac{1}{2}n_{ck1,x_{l-1}}p^*_{dat,D,ix_{l-1}}\right]$$

$$p_{ck,ck1-D,ix_l} = p_{ck,ck1-D,ox_{l-1}} = \bar{G}_{ck,\boldsymbol{x_{l-1}}}\, p_{ck,ck1-D,\boldsymbol{ix_{l-1}}} + \frac{\partial G_{ck,\boldsymbol{x_{l-1}}}}{\partial N_{\boldsymbol{x_{l-1}}}}\left[n_{ck1-D,\boldsymbol{x_{l-1}}}\bar{P}_{ck,\boldsymbol{ix_{l-1}}} + \frac{1}{2}n_{ck1,\boldsymbol{x_{l-1}}}p^*_{ck,D,\boldsymbol{ix_{l-1}}}\right]$$

$$p_{dat,ck1-D,ox_L} = \bar{G}_{dat,x_L}\, p_{dat,ck1-D,ix_L} + \frac{\partial G_{dat,x_L}}{\partial N_{x_L}}\left[n_{ck1-D,x_L}\bar{P}_{dat,ix_L} + \frac{1}{2}n_{ck1,x_L}p^*_{dat,D,ix_L}\right]$$

$p_{dat,ck5-D,ox_L}$ is simplified from Equation (B.21)

B: Down-conversion with clock ck5 (D5)

$p_{dat,ck5-D,o}$ defined in Equation (3.22) at the frequency $ck5 - D$ is simplified to:

$$n_{ck5-D,x} = \frac{1}{L}\sum_{l=1}^{L} f_w \left[p_{dat,ck5-D,ix_l} \frac{\partial R_{dat,x_l}}{\partial P_{dat,ix_l}} + p_{ck,ck5-D,ix_l} \frac{\partial R_{ck,x_l}}{\partial P_{ck,ix_l}} \right]$$

$(n_{ck5-D,x})$ is simplified from Equation (B.22).

$$p_{dat,ck5-D,ix_l} = p_{dat,ck5-D,ox_{l-1}} = \bar{G}_{dat,x_{l-1}}\, p_{dat,ck5-D,ix_{l-1}} + \frac{\partial G_{dat,x_{l-1}}}{\partial N_{x_{l-1}}} \left[n_{ck5-D,x_{l-1}} \bar{P}_{dat,ix_{l-1}} + \frac{1}{2} n_{ck5,x_{l-1}} p^*_{dat,D,ix_{l-1}} \right]$$

$$p_{ck,ck5-D,ix_l} = p_{ck,ck5-D,ox_{l-1}} = \bar{G}_{ck,\boldsymbol{x_{l-1}}}\, p_{ck,ck5-D,i\boldsymbol{x_{l-1}}} + \frac{\partial G_{ck,\boldsymbol{x_{l-1}}}}{\partial N_{\boldsymbol{x_{l-1}}}} \left[n_{ck5-D,\boldsymbol{x_{l-1}}} \bar{P}_{ck,i\boldsymbol{x_{l-1}}} + \frac{1}{2} \boldsymbol{n_{ck5,x_{l-1}} p^*_{ck,D,ix_{l-1}}} \right]$$

$$p_{dat,ck5-D,ox_L} = \bar{G}_{dat,x_L}\, p_{dat,ck5-D,ix_L} + \frac{\partial G_{dat,x_L}}{\partial N_{x_L}} n_{ck5-D,x_L} \bar{P}_{dat,ix_L}$$

$p_{dat,ck5-D,ox_L}$ is simplified from Equation (B.21).

C: Up-conversion with clock ck1 (U1)

$p_{dat,ck1+d,o}$ defined in Equation (3.25) at the frequency $ck1 + d$ is simplified to:

$$n_{ck5-D,x} = \frac{1}{L}\sum_{l=1}^{L} f_w \left[p_{dat,ck1+d,ix_l} \frac{\partial R_{dat,x_l}}{\partial P_{dat,ix_l}} + p_{ck,ck1+d,ix_l} \frac{\partial R_{ck,x_l}}{\partial P_{ck,ix_l}} \right]$$

$n_{ck1+d,x}$ is simplified from Equation (B.19).

$$p_{dat,ck1+d,ix_l} = p_{dat,ck1+d,ox_{l-1}} = \bar{G}_{dat,\boldsymbol{x_{l-1}}}\, p_{dat,ck1+d,i\boldsymbol{x_{l-1}}} + \frac{\partial G_{dat,\boldsymbol{x_{l-1}}}}{\partial N_{\boldsymbol{x_{l-1}}}} \left[n_{ck1+d,\boldsymbol{x_{l-1}}} \bar{P}_{dat,i\boldsymbol{x_{l-1}}} + \frac{1}{2} n_{ck1,\boldsymbol{x_{l-1}}} p_{dat,d,i\boldsymbol{x_{l-1}}} \right]$$

$$p_{ck,ck1+d,ix_l} = p_{ck,ck1+d,ox_{l-1}} = \bar{G}_{ck,\boldsymbol{x_{l-1}}}\, p_{ck,ck1+d,i\boldsymbol{x_{l-1}}} + \frac{\partial G_{ck,\boldsymbol{x_{l-1}}}}{\partial N_{\boldsymbol{x_{l-1}}}} \left[n_{ck1+d,\boldsymbol{x_{l-1}}} \bar{P}_{ck,i\boldsymbol{x_{l-1}}} + \frac{1}{2} n_{ck1,x_{l-1}} \boldsymbol{p_{ck,d,ix_{l-1}}} \right]$$

$$p_{dat,ck1+d,ox_L} = \bar{G}_{dat,x_L}\, p_{dat,ck1+d,ix_L} + \frac{\partial G_{dat,x_L}}{\partial N_{x_L}} n_{ck1+d,x_L} \bar{P}_{dat,ix_L}$$

$p_{dat,ck1+d,ox_L}$ is simplified from Equation (B.18).

D: Up-conversion with clock ck5 (U5)

$p_{dat,ck5+d,o}$ defined in Equation (3.25) at the frequency $ck5 + d$ is simplified to:

$$n_{ck5+d,x} = \frac{1}{L}\sum_{l=1}^{L} f_w \left[p_{dat,ck5+d,ix_l} \frac{\partial R_{dat,x_l}}{\partial P_{dat,ix_l}} + p_{ck,ck5+d,ix_l} \frac{\partial R_{ck,x_l}}{\partial P_{ck,ix_l}} \right]$$

$n_{ck5+d,x}$ is simplified from Equation (B.19).

$$p_{dat,ck5+d,ix_l} = p_{dat,ck5+d,ox_{l-1}} = \bar{G}_{dat,\boldsymbol{x_{l-1}}}\, p_{dat,ck5+d,i\boldsymbol{x_{l-1}}} + \frac{\partial G_{dat,\boldsymbol{x_{l-1}}}}{\partial N_{\boldsymbol{x_{l-1}}}} \left[n_{ck5+d,\boldsymbol{x_{l-1}}} \bar{P}_{dat,i\boldsymbol{x_{l-1}}} + \frac{1}{2} n_{ck5,x_{l-1}} p_{dat,d,i\boldsymbol{x_{l-1}}} \right]$$

$$p_{ck,ck5+d,ix_l} = p_{ck,ck5+d,ox_{l-1}} = \bar{G}_{ck,\boldsymbol{x_{l-1}}}\, p_{ck,ck5+d,i\boldsymbol{x_{l-1}}} + \frac{\partial G_{ck,\boldsymbol{x_{l-1}}}}{\partial N_{\boldsymbol{x_{l-1}}}} \left[n_{ck5+d,\boldsymbol{x_{l-1}}} \bar{P}_{ck,i\boldsymbol{x_{l-1}}} + \frac{1}{2} n_{ck5,\boldsymbol{x_{l-1}}} p_{ck,d,i\boldsymbol{x_{l-1}}} \right]$$

$$p_{dat,ck5+d,ox_L} = \bar{G}_{dat,x_L}\, p_{dat,ck5+d,ix_L} + \frac{\partial G_{dat,x_L}}{\partial N_{x_L}} n_{ck5+d,x_l} \bar{P}_{dat,ix_L}$$

$p_{dat,ck5+d,ox_L}$ is simplified from Equation (B.18).

Appendix B.5

Generated Intermodulation Terms for Up-Conversion and Down-Conversion

The generated intermodulation and filtering terms shown in Table 11 for down-converted signals at $z_D = ch1 - D$ or $ck5 - D$ and up-converted signals at $z_d = ch1 + d$ or $ck5 + d$ are obtained by (3.27) and (3.28). These intermodulation terms are compared to analysis the different behaviors of the conversion gain related to $ck1$ and $ck5$.

Table 11: Generated intermodulation and filtering terms of the down-converted powers (D1 and D5) and up-converted powers (U1 and U5) that influence on the conversion gain.

Down-converted power $p_{dat,ck1-D,o}$ (D1) from Equation (3.27) at $z_D = ck1 - D$
Generated intermodulation terms:

D1.1: $n_{ck1-D,x_{l-1}}\bar{P}_{dat,ix_{l-1}}$

D1.2: $n_{ck1-D,x_{l-1}}\bar{P}_{ck,ix_{l-1}}$

D1.3: $n_{ck1,x_{l-1}}p^{*}_{dat,D,ix_{l-1}}$

Filtering term of f_w by taking into account that $\omega_{ck1-D}\tau_{d,x_l} \gg 1$:

D1.4: $\frac{1}{j\omega_{ck1-D}}$

Comparison between the terms of the down-converted signal (D1) at $ck1-D$ from Equation (3.27):

- D1.1 and D1.2 are identical due to the assumptions made on optical mean powers.
- D1.1 and D1.2 correspond to weak carrier density modulations due to the high frequency $ck1-D$.
- D1.3 beating term involves the carrier density modulation at a frequency close to the SOA-MZI bandwidth and a high frequency data modulation amplified with an unsaturated gain.
- D1.4 corresponds to the attenuation due to the low pass filtering behavior of the carrier density.

Down-converted power $p_{dat,ck5-D,o}$ (D5) from Equation (3.27) at $z_D = ck5-D$

Generated intermodulation terms:

D5.1: $n_{ck5-D,x_{l-1}}\bar{P}_{dat,ix_{l-1}}$

D5.2: $n_{ck5-D,x_{l-1}}\bar{P}_{ck,ix_{l-1}}$

D5.3: $n_{ck5,x_{l-1}}p^{*}_{dat,D,ix_{l-1}}$

Filtering term of f_w by taking into account that $\omega_{ck5-D}\tau_{d,x_l} \ll 1$:

D5.4: τ_{d,x_l}

Comparison between the terms the down-converted signal (D5) at $ck5-D$ from Equation (3.27):

- D5.1 and D5.2 are identical due to the assumptions made on optical mean powers.
- D5.1 and D5.2 correspond to efficient carrier density modulations due to the low frequency $ck5-D$.
- D5.3 beating term involves a weak carrier density modulation due to the high frequency $ck5$ and a high frequency data modulation amplified with an unsaturated gain.
- D5.4 corresponds to the transmission of a low frequency signal.

Up-converted power $p_{dat,ck1-d,o}$ (U1) from Equation (3.28) at $z_d = ck1 + d$

Generated intermodulation terms:

U1.1: $n_{ck1+d,x_{l-1}}\bar{P}_{dat,ix_{l-1}}$

U1.2: $n_{ck1+d,x_{l-1}}\bar{P}_{ck,ix_{l-1}}$

U1.3: $n_{ck1,x_{l-1}}p_{dat,d,ix_{l-1}}$

Filtering term of f_w:

U1.4: $\frac{\tau_{d,x_l}}{\left(1+j\omega_{ck1+d}\tau_{d,x_l}\right)}$

Comparison between the terms of the up-converted signal (U1) at $ck1 + d$ from Equation (3.28):

- U1.1 and U1.2 are identical due to the assumptions made on optical mean powers.
- U1.1 and U1.2 correspond to carrier density modulations close to the SOA-MZI bandwidth.
- U1.3 beating term involves the carrier density modulation at a frequency close to the SOA-MZI bandwidth and a low frequency data modulation amplified with a saturated gain.
- U1.4 corresponds to the transfer function of the low-pass filter close to its cutoff frequency.

Up-converted power $p_{dat,ck5-d,o}$ (U5) from Equation (3.28) at $z_d = ck5 + d$

Generated intermodulation terms:

U5.1: $n_{ck5+d,x_{l-1}}\bar{P}_{dat,ix_{l-1}}$

U5.2: $n_{ck5+d,x_{l-1}}\bar{P}_{ck,ix_{l-1}}$

U5.3: $n_{ck5,x_{l-1}}p_{dat,d,ix_{l-1}}$

Filtering term of f_w by taking into account that $\omega_{ck5+d}\tau_{d,x_l} \gg 1$:

U5.4: $\frac{1}{j\omega_{ck5+d}}$

Comparison between the terms of the up-converted signal (U5) at $ck5 + d$ from Equation (3.28):

- U5.1 and U5.2 are identical due to the assumptions made on optical mean powers.
- U5.1 and U5.2 correspond to weak carrier density modulations due to the high frequency $ck5 + d$.

- U5.3 beating term involves a weak carrier density modulation due to the high frequency $ck5$ and a low frequency data modulation amplified with a saturated gain.
- U5.4 corresponds to the attenuation due to the low pass filtering behavior of the carrier density.

The comparison between the terms of $p_{dat,ck1-D,o}$ at the angular frequency $ck1-D$ and $p_{dat,ck5-D,o}$ at $ck5-D$ proves that the two beating terms D1.3 and D5.3 differ in the frequency of the carrier density modulation. D5.3 is lower than D1.3 because both the input power and the frequency of $ck5$ are compared to the ones of $ck1$. These terms, in turn, modulate the carrier density respectively at low $(ck5-D)$ and high $(ck1-D)$ frequencies. These induce modulations favor terms linked to $ck5$ (D5.1, D5.2) compared to the ones linked to $ck1$ (D1.1, D1.2). Finally, the filtering term has the same effect and favor terms generated at $ck5-D$. As a conclusion, the ratio at the SOA-MZI output between $p_{dat,ck5-D,o}$ and $p_{dat,ck1-D,o}$ powers indicated from Equation (3.27) is less than the one of generated beating terms D5.3 and D1.3.

The comparison between the terms of $p_{dat,ck1+d,o}$ at $ck1+d$ and $p_{dat,ck5+d,o}$ at $ck5+d$ clarifies that the two beating terms U1.3 and U5.3 differ in the frequency of the carrier density modulation. U5.3 is lower than U1.3 because both the input power and the frequency of $ck5$ are compared to the ones of $ck1$. These terms, in turn, modulate the carrier density respectively at high $(ck5+d)$ and medium $(ck1+d)$ frequencies. These induced modulations favor terms linked to $ck1$ (U1.1, U1.2) compared to the ones linked to $ck5$ (U5.1, U5.2). Finally the filtering term has the same effect and favor terms generated at $ck1+d$. As a result, the ratio at the SOA-MZI output between $p_{dat,ck5+d,o}$ and $p_{dat,ck1+d,o}$ powers indicated from Equation (3.28) is higher than the one of the generated beating terms U5.3 and U1.3.

From the above analysis, we can conclude that the difference between the conversion gain for the down-converted signal involving $ck1$ and $ck5$ is smaller than the one between the conversion gain for the up-converted signal involving $ck1$ and $ck5$.

The down-converted power (D5) $p_{dat,ck5-D,o}$ at $ck5-D$ and the up-converted power (U5) $p_{dat,ck5+d,o}$ at $ck5+d$ are compared to prove that the two beating terms D5.3 and U5.3 differ in the gain, respectively unsaturated and saturated gain, leading to D5.3 being higher than U5.3. These terms, in turn, modulate the carrier density respectively at low $(ck5-D)$ and high $(ck5+d)$ frequencies leading to high efficiency in carrier modulation for down conversion terms and weak efficiency in carrier modulation for up conversion ones. Moreover, the filtering term has the same effect and favor down conversion terms are generated at $ck5-D$.

Glossary of Acronyms

ASE:	Amplified Spontaneous Emission
Att:	Attenuator
AWG:	Arbitrary Waveform Generator
BER:	Bit Error Rate
BR:	Bit Rate
BPF:	Band Pass Filter
BPSK:	Binary Phase Shift Keying
BW:	Bandwidth
CB:	Conduction Band
CDM:	Carrier Density Modulation
CH:	Carrier Heating
CIP:	Centre of Integrated Photonics
CT:	Continuous Time
CP:	Cyclic Prefix
CW:	Continuous Wave
DFT:	Discrete Fourier Transform
DT:	Discrete Time
DSB:	Double Side Band
DSO:	Digital Sampling Oscilloscope
EA:	Electrical Amplifier
EAM:	Electro Absorption Modulator
EAtt:	Electrical Attenuator
EDFA:	Erbium Doped Fiber Amplifier
EOM:	Electro-Optic Modulator
ER:	Extinction Ratio
ESA:	Electrical Spectrum Analyzer
EVM:	Error Vector Magnitude
FEC	Forward Error Correction
FR:	Frequency Response
FWHM:	Full Width at Half Maximum
FWM:	Four Wave Mixing
IEEE:	Institute of Electrical and Electronics Engineers
IF:	Intermediate Frequency
IIP3:	Third-order Input Intercept Point
Im:	Imaginary
I-Q	In phase-Quadrature

ISI:	Inter-Symbol Interference
IP3:	Third-order Intercept Point
LD:	Laser Diode
LNA:	Low Noise Amplifier
LO:	Local Oscillator
LSB:	Lower Side Band
LPF:	Low Pass Filter
MI:	Michelson Interferometer
MZI:	Mach-Zehnder Interferometer
MZM:	Mach-Zehnder Modulator
NF:	Noise Figure
OC:	Optical Coupler
O/E	Optic/ Electric
OF:	Optical Filter
OFDM:	Orthogonal Frequency Division Multiplexing
OIP3:	Output Third-order Intercept Point
OPS:	Optical Pulse Source
OSA:	Optical Spectrum Analyzer
PC:	Polarization Controller
Pd:	Photodiode
PIN-Pd:	P type Intrinsic N type-Photodiode
PS:	Phase Shifter
PSD:	Power Spectral Density
PWM:	Pulse Width Modulation
QAM:	Quadrature Amplitude Modulation
QPSK:	Quadrature Phase Shift Keying
RBW:	Resolution Bandwidth
Re	Real
RF:	Radio Frequency
RIN:	Relative Intensity Noise
RoF:	Radio over Fiber
RRC:	Root Raised Cosine
SFDR:	Spurious Free Dynamic Range
SGM:	Self-Gain Modulation
SHB:	Spectral Hole Burning
SMF:	Single Mode Fiber
SNR:	Signal to Noise Ratio
SOA:	Semiconductor Optical Amplifier
SOA-MZI:	Semiconductor Optical Amplifier Mach-Zehnder Interferometer
SPM:	Self-Phase Modulation
SR:	Symbol Rate

SSB:	Single Side Band
TE:	Transverse Electric
TF	Transfer Function
TM:	Transverse Magnetic
USB:	Upper Side Band
UTC-Pd:	Uni-Traveling Carrier Photodiode
VB:	Valence Band
VODL:	Variable Optical Delay Line
VSA:	Vector Signal Analyzer
WDM:	Wavelength Division Multiplexing
XAM:	Cross Absorption Modulation
XGM:	Cross Gain Modulation
XPM:	Cross Phase Modulation

List of Symbols

Symbols	Description	Value and SI units
a	roll-off coefficient	-
B_o	optical bandwidth	m
BW_s	System bandwidth	Hz
BW_{OFDM}	bandwidth of the OFDM signal	Hz
c	speed of light	3×10^8 m/s
E_J	electric Field at port J	V/m
f	frequency	Hz
f_c	carrier frequency	Hz
f_{Dat}	data frequency	Hz
f_{IF}	intermediate frequency	Hz
f_{LO}	local frequency	Hz
f_{LP}	cutoff frequency	Hz
f_{max}	maximum frequency	Hz
f_{min}	minimum frequency	Hz
f_{sa}	sampling frequency	Hz
f_{sat}	saturated gain at a frequency	Hz
f_{sp}	frequency spacing	Hz
f_{RF}	radio frequency	Hz
f_w	filtering term	s/rad
f_{unsat}	unsaturated gain at a frequency	Hz
$g_m(\lambda, N)$	material gain at the wavelength λ and the carrier density N	1/m
g_n	net gain	1/m
G	gain	dB
G_c	conversion gain	dB
$G_{c,up}$	up-conversion gain	dB
$G_{c,down}$	down-conversion gain	dB
$G_{dat,x}$	modulated gain of SOAx	dB
$G_{dat,y}$	modulated gain of SOAy	dB
G_{opt}	optical mean gain	dB
h	Planck′s constant	6.63×10^{-34} m^2 kg /s

H_n	harmonic rank	Hz
I_b	bias current	A
I_{err}	in-phase error amplitude	-
I_p	photo-current	A
Iso	isolation	dB
$I_{SOA1,2}$	bias current of SOA1 and SOA2	A
L	length of the active region	m
L_e	Electric loss	dB
L_o	optical loss	dB
M_I	modulation index	%
$n_{data,x}$	carrier density of SOAx	$1/m^3$
$n_{data,y}$	carrier density of SOAy	$1/m^3$
N	carrier density	$1/m^3$
N_d	data subcarriers	-
N_f	noise floor	dB
N_G	guard subcarriers	-
N_{GL}	lower guard subcarriers	-
N_{GU}	upper guard subcarriers	-
N_o	carrier density at transparency	$1/m^3$
N_P	pilot subcarriers	-
N_{sc}	number of subcarriers	-
OBW_{OFDM}	occupied bandwidth of the OFDM signal	Hz
P_{ASE}	ASE noise power	W
P_{av}	average power	W
$P_{av,o,out}$	average output power of MZM	W
P_{CTR}	control power	W
P_{cki}	clock input power	W
$P_{dat,i}$	data input power	W
$P_{dat,x,i}$	data input power of SOAx	W
$P_{dat,x,o}$	data output power of SOAx	W
$P_{dat,y,i}$	data input power of SOAy	W
$P_{dat,y,o}$	data output power of SOAy	W
$P_{e,Dat}$	electrical power at the RF input of the MZM	W
$P_{e,in,Dat}$	electrical input power of the data signal	W
$P_{e,out,Dat}$	electrical output power of the sampled data signal	W
$P_{first,out}$	first order output power	W
P_{H_n}	harmonic power	W
P_{in}	input power	W

P_{noise}	noise power	W
$P_{o,in}$	optical input power of MZM	W
$P_{o,in,Dat}$	optical input power	W
$P_{o,in,Pd}$	optical input power of the photodiode	W
$P_{o,out,Dat}$	optical output power	W
P_{out}	output power	W
P_{peak}	peak power	W
P_{RF}	power level of the RF generator	W
P_s	output power at s-port	W
$P_{sat,in}$	saturated input power	W
$P_{sat,out}$	saturated output power	W
P_{signal}	signal power	W
$P_{third,out}$	third order output power	W
q	electric charge	1.6×10^{-19} C
Q_{err}	quadratic error amplitude	-
r	responsivity	A/W
R	resistor	ohms
R_{sp}	spontaneous recombination rate	$1/m^3S$
R_s	stimulated recombination rate	$1/m^3S$
SNR_{in}	input signal to noise ratio	dB
SNR_{out}	output signal to noise ratio	dB
SR_{max}	maximum symbol rate	MSymb/s
SR_{min}	minimum symbol rate	MSymb/s
t	time	S
T_s	period	S
V	volume of the active region	m^3
V_b	bias voltage	V
v_g	group velocity	m/s
V_π	driving voltage	V
w_{ck}	clock angular frequency	rad/s
w_d	lower data angular frequency	rad/s
w_D	higher data angular frequency	rad/s
w_{dat}	data angular frequency	rad/s
$X_{IF/RF}$	amplitude of IF/RF signal	W
X_{LO}	amplitude of LO signal	W
α	duty cycle	%
α_H	Henry′s factor	6
α_{int}	internal loss coefficient	0 1/m

Γ	confinement factor	-
η_i	current injection efficiency	dB
η_s	conversion efficiency at s-port	dB
λ_{dat}	wavelength of data	m
λ_{sa}	sampling wavelength	m
λ	wavelength	m
$\Delta\lambda$	delta wavelength	m
$\Delta\tau$	differential delay time	S
τ_c	carrier lifetime	S
τ_{d,x_l}	recombination time	S
τ_{eff}	effective carrier lifetime	S
τ_s	stimulated carrier recombination time	S
τ_{sp}	spontaneous lifetime	S
γ	bandwidth enhancement factor	-
δ_t	Pulse width	S
φ	Phase shifter	rad
Ψ_0	constant factor	rad

List of Figures

List of Tables

(Study of up and down conversion technique by all optical sampling based on a SOA-MZI)

Abstract : Frequency mixing is a key function existing in different systems, especially in mixed photonic-microwave ones. Today, the supremacy of optical networks to carry high bitrate data over large distances motivates the optical implementation of such functions to benefit from the low loss, high bandwidth, low size and weight of optical technologies. In this work, we study a photonic mixer based on a SOA-MZI (Semiconductor Optical Amplifier Mach-Zehnder Interferometer) device and a sampling technique allowing both conversion towards high and low frequencies. The involved mixing principle exploits the spectral characteristics of a sampled signal in which replicas of the original spectrum exist at different other frequencies. Basing the frequency conversion on a sampling technique gives two advantages: the photonic mixer configuration is the same for up and down conversions, and the frequency of the local oscillator can be less than the addressed frequency range.

The implementation of such a sampling technique needs an optically-controlled high-frequency optical switch. As shown in this work, a SOA-MZI can play this role. Depending on the relative phase between its arms, an interferometric structure (MZI) can transmit or cancel an optical input signal. By locating one SOA in each arm of the MZI structure, the cross-phase modulation that exists inside an SOA is exploited to optically control the optical switch state of the MZI. Controlled by an optical pulse source, this optical switch is able to sample an optical input signal carrying complex-modulated data. Frequency conversions of mono and multi-carrier signals in the range 0.5-39.5 GHz have been successfully achieved. By using a differential configuration of the SOA-MZI, both up and down conversions at bitrates up to 1 Gb/s are reached.

Keywords : Photonic mixer - Frequency conversion - Semiconductor Optical Amplifier Mach-Zehnder Interferometer - Radio over Fiber.

Etude d'une technique de conversion vers les hautes et les basses fréquences par échantillonnage tout-optique à base d'un SOA-MZI

Résumé : La conversion de fréquence est une fonction clef présente dans divers contextes, particulièrement dans les systèmes mixtes photoniques-hyperfréquences. Aujourd'hui, la suprématie des réseaux optiques pour le transport de données à haut débit sur de grandes distances incite à l'intégration de telles fonctions dans le domaine optique afin de bénéficier des faibles pertes, larges bandes passantes, faibles poids et tailles propres aux technologies optiques. Dans ce travail, nous étudions un mélangeur tout-optique utilisant un composant SOA-MZI (*Semiconductor Optical Amplifier Mach-Zehnder Interferometer*) et une technique d'échantillonnage permettant la conversion vers les hautes et les basses fréquences. Le principe du mélange exploite les caractéristiques spectrales d'un signal échantillonné pour lequel des répliques du signal d'origine existent à différentes autres fréquences. Utiliser une telle technique pour la conversion de fréquences offre deux avantages : la conversion vers les hautes et les basses fréquences utilise la même configuration du mélangeur et la fréquence de l'oscillateur local peut être inférieure à la gamme des fréquences visées.

L'implémentation d'une telle technique d'échantillonnage nécessite un interrupteur optique contrôlé optiquement. Comme cela est montré dans ce travail, un SOA-MZI peut jouer ce rôle. Selon la phase relative entre ses bras, un interféromètre Mach-Zehnder (MZI) peut transmettre ou non un signal optique d'entrée. En plaçant un SOA dans chaque bras de la structure MZI, la modulation croisée de la phase qui existe au sein d'un SOA est mise à profit pour contrôler l'état de l'interféromètre. Contrôlé par une source impulsionnelle optique, cet interrupteur optique permet d'échantillonner un signal optique porteur de données à modulation complexe. La conversion de fréquence de signaux mono et multi-porteuses dans le domaine 0,5-39,5 GHz a été obtenue avec succès. Par utilisation d'une configuration différentielle du SOA-MZI, des conversions vers les hautes et les basses fréquences jusqu'à un débit de 1 Gb/s ont pu être réalisées.

Mots clefs : Mélangeur tout-optique – Conversion de fréquence – SOA-MZI (Semiconductor Optical Amplifier Mach-Zehnder Interferometer) – Radio sur fibre.